Investigation of Large Protein and Multimeric Protein Complex Structures with Mass Spectrometry Techniques

Kamila Jolanta Pacholarz

Ph.D.

University of Edinburgh

2014

"In wisdom gathered over time I have found
that every experience is a form of exploration"

Ansel Adams

Declaration

This thesis is submitted in part fulfilment of the requirements for the degree of Doctor of Philosophy at the University of Edinburgh. Unless otherwise stated, this work is my own and has not been submitted for any other degree or professional qualification. Work which has formed part of jointly-authored publications has been included; my contribution and contribution of other authors to this work has been explicitly indicated below. Credit has been given within the thesis where reference has been made to the work of others.

Chapter 1:
This chapter includes work published in "*Mass spectrometry based tools to investigate protein-ligand interactions for drug discovery*" Pacholarz, K.J., Garlish, R.A., Taylor, R.J., Barran, P.E. *Chem. Soc. Rev.*, 2012, **41**, 4335-4355. I have surveyed the literature and written the manuscript.

Chapter 3:
This chapter includes work published in "*Dynamics of intact immunoglobulin G explored by drift-tube ion-mobility mass spectrometry and molecular modelling*" Pacholarz, K.J., Porrini, M., Garlish, R.A., Burnley, R.J., Taylor, R.J., Henry, A.J., Barran, P.E. *Angew. Chem., Int. Ed.*, 2014, **53**, 7765-7769. I have designed and carried out all the MS and IM-MS experiments, analysed the data and written the manuscript. Molecular dynamics presented in this publication were performed by Dr Massimiliano Porrini at the Institute Européen de Chimie et Biologie (IECB) in Pessac, France.

Chapter 4:
This chapter includes work submitted for publication entitled "*Distinguishing Loss of Structure from Subunit Dissociation for Protein Complexes: a Gas Phase Route for Microcalorimetry*" Pacholarz, K.J., Barran. P.E. I have designed and carried out all the MS and IM-MS experiments, analysed the data and written the manuscript.

Chapter 6:
This chapter includes work to be submitted for publication entitled "*The application of ion mobility mass spectrometry and hydrogen deuterium exchange mass spectrometry for probing mechanisms of allosteric inhibition of enzymes*" Pacholarz, K.J., Jowitt, T., Burnley, R.J., Ordsmith, V., Porrini, M., Larroy-Maumus, G., Pisco, J.P., Garlish, R.A., Taylor, R.J., de Carvalho, L.P., Barran, P.E.. I have designed and carried out all MS and IM-MS experiments, analysed the data and written the manuscript. Dr Rebecca J. Burnley from UCB has help with set up of HDX-MS experiments and carried out the data analysis. Dr Thomas Jowitt from University of Manchester has performed the AUC experiments. Dr Massimiliano Porrini at the Institute Européen de Chimie et Biologie (IECB) in Pessac, France performed the theoretical CCS calculations.

……………………………..

Kamila J. Pacholarz
December 2014

Acknowledgments

I would firstly like to thank my supervisor Professor Perdita Barran her constant support, help, guidance and opportunities given during the past four years, it has been an exciting journey and I’ve learned lots! I would also like to thank my industrial supervisors Dr Rachel Garlish and Dr Richard Taylor from UCB Pharma for their support and insights into the biopharmaceutical industry.

I would like to thank fellow group members (PBRG!!!) for everyday companionship (well, during the first 3 years), useful discussions, coffee and cake times, PBR(insert appropriate letter) times and continuous efforts to fix the MoQToF together: Jason, Yana, Hattie, Jude, Ewa, Sophie, Alberto, Bex, Jakub, Ashley, Chris, Ellie, Alex and project students, especially Victoria Ordsmith for her great work. Many thanks go to Dr Massimiliano Porrini for running MD and MOBCAL calculations.

As many of the projects I’ve worked on were carried out in collaboration with other institutions, I would like to acknowledge all of the collaborators. Many thanks to Dr Alistair Henry from UCB Pharma for useful discussions, Dr Rebecca Burnley (UCB Pharma) for help with setting up HDX experiments and data analysis, Dr Shirley Peters (UCB Pharma) for providing me with lots of antibody samples and to the entire Physical and Analytical Sciences Group at UCB for their help during my research stays down in Slough. I would also like to thank Dr Luiz Pedro Sório de Carvalho from MRC National Institute of Medical Research for collaboration on the exciting MtATP-PRT project and Dr Thomas Jowitt from University of Manchester for performing the AUC experiments and his contribution to the PRT project. I am also appreciative to Dr Jeff Brown and Dr Kevin Giles from Waters Corporation for the instrument time and help with parameter optimization while working at Waters site in Manchester.

I am also grateful to everyone in the ex-SIRCAMS lab: Logan, Alan, Sophie and Andrew for welcoming me to their office and giving me (and Ultima) space to work in the final year. I would like to acknowledge all technical and administrative support provided by the mechanical workshop, the chemistry electronic workshop, the physics electronic workshop, the IT, the chemistry stores and the admin office.

Finally, I would like to express my gratitude to my parents, grandparents, family and friends for their support over years. Many thanks to my Edinburgh friends (especially Anna) and fellow PhD students as well as my wonderful friends far far away for travels taken together, emails and chats when I needed them the most: Ewa, Pacuś, Nani and Marcelo – thank you!

Abstract

The biophysical properties, biological activity and function of macromolecular systems are highly dependent on their structure. Structure-activity relationships of proteins and their binding partners are critical for drug discovery, biochemical and medical research. While the gas-phase environment might present as an unusual venue from which to explore protein structure, for over the past two decades, nano-electrospray ionization (nESI) coupled to mass spectrometry (MS) has been recognized as having great potential for analysis of protein structure and protein non-covalent complexes. In conjunction with related technique of ion mobility (IM), mass spectrometry (IM-MS) provides insights into protein native-like conformations and any structural changes in may undergo upon ligand binding or alternations induced *via* physical parameters such as temperature, pressure or solution conditions. As most proteins tend to exist as multiple domains; from the distribution of oligomeric states in the Protein Data Base (PDB) 86% of proteins exist as oligomers; the work presented in this thesis focuses on application of MS techniques to probe the tertiary and quaternary structure of various large and multimeric protein complexes, their dynamics and/or conformational changes. Wherever relevant, the gas-phase studies reported here are complemented by other techniques, such as hydrogen deuterium exchange MS (HDX), molecular modelling (MD) and analytical ultracentrifugation (AUC).

Firstly, the dynamics of intact monoclonal antibodies (mAbs) and their fragments are explored with IM-MS. Variations observed in conformational landscapes occupied by two mAb isotypes are rationalized by differences in disulfide linkages and non-covalent interactions between the antibody peptide chains. Moreover, mAb intrinsic flexibility is compared to other multimeric protein complexes in terms of collision cross section distribution span. Secondly, variable temperature MS (VT-MS) and variable temperature IM-MS (IM-MS) are used to probe unfolding and dissociation of four standard multimeric protein complexes (TTR, avidin, conA and SAP) as a function of the of analysis environment temperature. VT-MS is found to allow for decoupling of their melting temperature (T_m) from the protein complex dissociation temperature (T_{GPD}). Whereas, VT-IM-MS is used to investigate structural changes of these protein complexes at elevated temperatures and provide insights into the thermally induced dissociation (TID) mechanism, as well as strength of the non-covalent interactions between subunits. Thirdly, VT-(IM)-MS methodology is applied to study behaviour of three mAbs: IgG1, IgG4 and an engineered IgG4 of increased thermal stability. Such analysis shows to be promising for comparative thermal stability studies for proteins of therapeutic interest. Lastly, the structure of ATP-phosphoribosyltransferase (MtATP-PRT), an enzyme catalysing the first step of the biosynthesis of L-histidine in *Mycobacterium tuberculosis*, is explored. Conformational changes occurring upon feedback allosteric inhibition by L-histidine are probed with MS, IM-MS, HDX-MS and AUC. Reported results serve as the basis for IM-MS/HDX-MS based screening method to be used for screening of a library of novel and promising anti-tuberculosis agents.

Lay summary

Proteins are highly important macromolecules in a living organism, responsible for its proper functioning. Each protein has a specific mission to fulfil in the cell, for instance some proteins form defence against foreign intruders such as bacteria or viruses (antibodies), some catalyze biochemical reactions (enzymes), while others act as molecular carriers (transport proteins) or provide support (structural proteins). The building blocks of proteins, called amino acids, form long chains and depending on their arrangement in the sequence drive protein to fold in a unique way resulting in variety of distinct higher order structures. This three dimensional shape, referred to as conformation, determines the protein function. Often misfolding, over production of certain proteins or their undesired interactions with other molecules may lead to disease. Studying shapes of these macromolecules helps understanding of physiological process related to disease and facilitates design of potential therapeutic drugs.

Researchers use variety of biochemical and biophysical methods as tools to investigate protein structure and obtain a detailed picture their conformations and interactions. One of such tools is mass spectrometry (MS), a method providing mass-to-charge (*m/z*) ratios; experiments can be design to deliver a range of structural, kinetic or dynamics parameters. In conjunction with a hybrid technique of ion mobility (IM), the size of the molecule and any conformational changes it undergoes may be determined. This thesis employs MS and IM-MS as central methodology to probe structures and their changes of several large proteins. Firstly, conformations and flexibility of antibodies - molecules nowadays more commonly serving as templates for design of therapeutics, are studied. Secondly, several protein complexes are exposed to elevated analysis temperature; by disturbing the complex structure, more information about the structure itself can be obtained. Subsequently, the same method is used to probe thermal stability of antibody therapeutics, which some of were designed to have enhanced stability. Lastly, the structure of an enzyme thought to be a promising anti-tuberculosis drug target is investigated. With MS and related techniques, conformational changes the enzyme undergoes upon interaction with a small molecule are probed.

Abbreviations

ADC	antibody-drug conjugate
AmAc	ammonium acetate
AMP	adenosine monophosphate
ATD	arrival time distribution
ATP	adenosine triphosphate
AUC	analytical ultracentrifugation
BPTI	bovine pancreatic trypsin inhibitor
bsAb	bispecific antibody
CCS	collision cross section
CCSD	collision cross section distribution
CD	circular dichroism
CH	constant domain of the heavy chain (Ig)
CID	collision induced dissociation
CL	constant domain of the light chain (Ig)
conA	concanavalin A
CEM	chain ejection model
CRM	charge residue model
CS	charge state
CSD	charge state distribution
CV	collision cell voltage
Da	Dalton
DAR	drug-to-antibody ratio
DC	direct current
DNA	deoxyribonucleic acid
DSB	disulfide bond
DSC	differential scanning calorimetry
DT	drift tube
DTT	dithiothreitol
DV	drift voltage
ECD	electron caption dissociation
EDDA	ethylenediammonium diacetate

EDTA	ethylenediaminetetraacetic acid
EHSS	exact sphere scattering (method)
ELISA	enzyme-linked immunosorbent assay
EM	electron microscopy
ESI	electrospray ionisation
Fab	Fragment antigen binding (Ig)
FAE	Fab arm exchange
FAIMS	field asymmetric waveform ion mobility spectrometry
Fc	Fragment crystallizable (Ig)
FPOP	fast photochemical oxidation of proteins
FT-ICR	Fourier transform ion cyclotron resonance
GPCR	G-protein coupled receptor
IDP	intrinsically disordered protein
Ig	immunoglobulin
IgA	immunoglobulin alpha
IgD	immunoglobulin delta
IgE	immunoglobulin epsilon
IgG	immunoglobulin gamma
IgM	immunoglobulin mu
IMP	integral membrane protein
IR	intrared
IRMPD	infrared multi-photon dissociation
HC	heavy chain (of an Ig)
HDMS	high definition mass spectrometry
HDX	hydrogen deuterium exchange
hGH	human growth hormone
HOS	higher order structure
HSQC	heteronuclear single quantum correlation
IM-MS	ion mobility mass spectrometry
IEM	ion evaporation model
IMS	ion mobility spectrometry
LC	light chain (of an Ig)
m/z	mass to charge ratio
mAb	monoclonal antibody

MALDI	matrix assisted laser desorption ionisation
MCP	microchannel plate
MD	molecular dynamics
MoQToF	modified quadrupole time-of-flight (mass spectrometer)
MS	mass spectrometry
MtATP-PRT	*mycobacterium tuberculosis* ATP-phosphoribosyltransferase
nESI	nanoelectrospray ionisation
nH	Hill number
NHS	*N*-hydroxysuccinimide
NMR	nuclear magnetic resonance (spectroscopy)
NOE	nuclear Overhauser effect
NOESY	nuclear Overhauser enhancement spectroscopy
PA	projection approximation
PDB	protein data bank
PPAR-α	peroxisome proliferator-activated receptor alpha
pI	isoelectic point
PLIMSTEX	protein-ligand interactions by MS, titration and hydrogen/deuterium exchange
PISA	protein interfaces, surfaces and assemblies (online server)
PLGS	ProteinLynx Global Server
PRPP	phosphoribosyl pyrophosphate
PSA	projected superposition approximation
PTM	post transitional modification
Q-ToF	quadrupole time-of-flight
RF	radio frequency
R_g	radius of gyration
RMSD	root mean square deviation
RNA	ribonucleic acid
S/N	signal to noise ratio
SAP	serum amyloid P component
SE	sedimentation equilibrium
SEC	size exclusion chromatography
SID	surface induced dissociation
SIFT-MS	selected ion flow tube mass spectrometry

SIMSTEX	self-association interactions using MS, self-titration and HD exchange
SLS	static light scattering
SPR	surface plasmon resonance
SORI	sustained off-resonance irradiation
SRIG	stacked ring ion guides
SUPREX	stability of unpurified proteins from rates of HD exchange
SV	sedimentation velocity
tATD	total arrival time distribution
TCEP	*tris*(2-carboxyethyl)phosphine
TEA	triethanolamine
TEAA	triethylammonium acetate
TEM	transmission electron microscopy
TIC	total ion count
TID	temperature induced dissociation
TJM	trajectory method
ToF	time of flight
TOCSY	total correlation spectroscopy
TTR	transthyretin
TWIG	travelling wave ion guide
TWIMS	travelling wave ion mobility spectrometry
UPLC	ultra performance liquid chromatography
UV	ultraviolet
VH	variable domain of the heavy chain (Ig)
VL	variable domain of the light chain (Ig)
V_M	Matthews coefficient
V_S	fractional volume of solvent in the lattice structure
VT	variable temperature
WT	wild type
z_{ave}	average charge

Physical Constants and Quantities

a	acceleration
d	distance
e	elementary charge, 1 $e = 1.6021765 \times 10^{-19}$ C
E	electric field strength
f	frictional coefficient
K	mobility
K_0	reduced mobility
k_B	Boltzmann constant, $k_B = 1.3806488(13) \times 10^{-23}$ JK^{-1}
L	drift cell length
m	mass
M_R	relative molecular weight
m/z	mass to charge ratio
N	number density
P	pressure
pI	isoelectric point
q	net charge
S	Svedberg, 1 S = 10^{-13} s
$s_{20,w}$	sedimentation coefficient (in water at 20℃)
T	temperature
t_0	dead time
t_a	arrival time
t_d	drift time
Td	Townsend unit, 1 $Td = 10^{-17}$ Vcm^2
T_{eq}	equilibrium temperature
T_{GPD}	gas phase dissociation temperature
T_m	melting temperature
v	velocity
V	potential difference
v_d	drift velocity
z	nominal charge
μ	reduced mass

ν	radio frequency
ω	angular velocity
Ω	momentum transfer integral

Table of Contents

CHAPTER 2

CHAPTER 3

CHAPTER 4

CHAPTER 5

Probing Antibody Thermal Stability with VT-(IM)-MS - 153 -

CHAPTER 6

Application of MS, IM-MS and HDX-MS for Probing Mechanisms of Allosteric Inhibition of Enzymes - 171 -

CHAPTER 7

APPENDICES

1

Introduction

Protein interactions are a key element of cell signalling and intracellular communication. Loss or change in protein function is associated with disease; hence, studying their structure and interactions is a critical aspect of drug discovery process. For over 20 years, mass spectrometry has gained increased application to study intact bio-macromolecules in a solvent free environment. This chapter discusses the use of native mass spectrometry alone and in conjunction with related techniques such as ion mobility, hydrogen-deuterium exchange or chemical cross-linking, to provide insights into protein structure. Furthermore, fundamental principles of mass spectrometry are explained and other commonly used biophysical techniques are briefly presented.

1.1 Why Study Proteins and Their Structure?

Proteins are highly important macromolecules in living cells, responsible for proper functioning of the host organism. Protein functional classes have specific missions to fulfil in the cell, for instance some proteins form defence against foreign intruders such as bacteria or viruses (antibodies), some catalyze biochemical reactions (enzymes), while others act as molecular carriers (transport proteins) or provide support (structural proteins), among many others.[1,2] The behaviour, biological activity and function of these macromolecular systems is dependent on their structure. Any changes to protein structure, either due to post-translational modifications (PTMs), mutations or protein denaturation might alter protein function and properties, and often leads to disease.[3-5] The structure-function relationship studies are fundamental for drug discovery, biochemical or medical research.[6-8]

Protein interactions represent an attractive axis for therapeutic intervention as targets in drug discovery. Discovery and design of chemical or biological entities that interact with the target proteins is aimed to prevent undesired actions of proteins; done for example by inducing conformational changes and disabling further interactions or blocking binding sites and prohibiting substrate binding involved in the signal cascade. Drug candidates are targeted at variety of proteins such as receptors,[9,10] enzymes,[11,12] ion channels,[13-15] or structural proteins[16,17]. For example, molecules targeted specifically at protein transmembrane receptors - so called G-protein coupled receptors (GPCR) - account for the majority of the best-selling drugs and around 50 % of all prescription pharmaceuticals.[18-20] Moreover, proteins themselves may be used as therapeutics, these entities are known as biologics. The worldwide sales of all biologics approached the $US100 billion in 2010, and it is expected that more than 50 % of new drug approvals by 2015 will be biologics, reaching even 70 % by 2025.[21,22] Progress in drug discovery and development relies, in part, on structural analysis of complexes formed upon introduction of compounds that bind to the protein target in a specific manner as well as the global conformation and stability with regards to protein based therapeutics.

1.1.1 Levels of protein structure

The four levels of protein structure can be distinguished; these are referred to as the primary, secondary, tertiary and quaternary structure. Proteins are biological polymers composed of monomeric units called α-amino acids, which consist of an amino group (-NH_2), a carboxyl group (-COOR), a hydrogen atom (H) and a variable side chain group (R). All eukaryotic proteins are built of combination of amino acids from 20 commonly occurring amino acid with specific R groups. A list of properties and structures of these amino acids are provided in Appendix 1 and 2, respectively. These protein building blocks are held together by covalent peptide bonds to form a polypeptide chain terminated by amino terminus (N-terminus) and carboxyl terminus (C-terminus) on the other site. The unique linear sequence, referred to as the primary structure, folds into highly regular local structures - the secondary structure. This 'local' fold, governed by hydrogen bonds and interactions between closely spaced amino acids, gives rise to α-helices and β-sheets, firstly proposed by Pauling and co-workers in 1951.[23,24] Spatial arrangement of these secondary motifs, gives protein its tertiary structure. This three dimensional structure is maintained by hydrophobic interactions (amino acid with hydrophilic R-groups seek to interact with water molecules, while hydrophobic R-groups avoid contact with aqueous environment and 'hide' towards protein centre), hydrogen bonds, ionic bonds (which form between positively and negatively charged R-groups), and potential disulfide bonds (covalent bonds formed between two cysteine R-groups). If the protein is composed of more than one polypeptide chain, arrangement of there subunits with respect to each other to form a multimer is considered as the quaternary structure. Similarly to tertiary structure, this highest level of spatial organisation in proteins is also stabilized by non-covalent interactions and disulfide bonds. The statistical distribution of quaternary structural types in Protein Data Bank (PDB)[25] shows more than 65 % of proteins exist as multimers (as of August 2014). This underlies need for development of methodologies allowing to preserve weak interactions and probe proteins' highly important architectures.

1.1.2 Why use mass spectrometry to study protein structure?

A range of biophysical techniques are available for investigation of proteins at all structural levels; each possessing certain advantages and some limitations, but when used in combination they can provide a coherent picture of protein structure and properties. Several review articles list and compare these tools, some of which will be briefly introduced later.[26-28] Despite a plethora of available techniques, the gold standard for structural information of protein complexes at atomic resolution remains x-ray crystallography. Improvements in synchrotron radiation facilities and the development of automated data acquisition have left the main challenge in x-ray crystallography to be the sample preparation. Optimisation of protein crystallisation can be a lengthy process, if indeed achievable at all.[29] To date calorimetry and NMR are the methods of choice for data collection in the liquid phase; however, both are time consuming, protein size limited and may only work effectively under solution or substrate concentration conditions that may be unfavourable for the formation of stable protein complexes and which do not mimic physiological conditions.

Mass spectrometry (MS) is a technique which measures the mass to charge ratio (m/z) of ions in the gas-phase; however, it is able to solve protein complexity at various structural levels, addressing questions ranging from protein-ligand binding[30-32] to characterisation of intact therapeutic proteins.[33-38] Its contribution to macromolecular system studies and biological research overall is widely reviewed in the literature.[31,39-44] A great advantage of electrospray ionisation mass spectrometry (ESI-MS) is its non-destructive nature which preserves protein tertiary and quaternary structure and non-covalent interactions with other proteins or molecules. With appropriate sample preparation and suitable tuning of the instrument, it is possible to transfer weakly associated complexes from solution into the gas-phase inside the mass spectrometer source. Analysis of ESI mass spectra obtained under non-denaturing conditions (usually achieved with volatile ammonium acetate or bicarbonate buffers) provide insights into protein topology and stoichiometry. Hence, besides delivering the exact mass measuring of proteins, MS experiments can be designed to obtain an array of information, such as: peptide sequence and protein identification,[45-47] dissociation constants of protein-ligand complexes[48,49]; conformational changes upon binding;[50] location of the binding site;[51] binding stoichiometry and binding specificity;[52] isotopic information such as oxidation states of binding metal ligands;[53] subunit exchange that can occur within multicomponent protein complexes;[54] or protein dynamics[55-58] just to name a few.

In contrast to x-ray crystallography and NMR, mass spectrometry also offers the opportunity for solvent free/independent investigations of interactions that are intrinsic to the given protein system. A gas-phase environment can be in one sense considered more similar to that which certain proteins occupy in biological systems. This is because the dielectric constant of a vacuum ($\varepsilon_{\text{vacuum}} = 1$) is more similar to the membrane receptor environment ($\varepsilon_{\text{peptide/protein}} = 2 – 4$) than for water ($\varepsilon_{\text{water}} = 80$);[59] the gas phase serves as an appropriate medium to study structures of proteins in the conditions more closely resembling their natural membrane habitat.[60] Moreover, MS offers unsurpassed upper mass analysis limit in comparison to the other higher resolution techniques. Minor modifications of commercially available MS instruments[61,62], has been shown to greatly enhance transmission of large ions and permit analysis of mega-Dalton (MDa) complexes such as ribosomes[63], transcriptomes and virus capsids up to 18 MDa[64-68], or even detection of intact viruses as large as 40 MDa.[69]

1.2 Principles of Biological Mass Spectrometry

The history of mass spectrometry goes back to the beginning of 20th century;[70] however, it was in late 1980's when John Fenn's discovery of electrospray ionisation to transfer biological macromolecules into the gas-phase revolutionized the application of mass spectrometry to biological systems.[71] The fate of ions travelling through a mass spectrometer starting from sample preparation to detection is depicted in Figure 1.1. These basic components of a mass spectrometer (highlighted in purple) as well as methods used of conjunction (highlighted in blue) for structural studies of proteins will be discussed in more detail in the following sections.

Prior to mass spectrometry analysis, proteins can be covalently labelled *via* strategies such as hydrogen deuterium exchange (HDX), footprinting or chemical cross-linking. The sample contained in volatile buffer is loaded into a thin glass capillary. Application of a voltage to the capillary allows charging of the molecules and their transfer into the gas phase. Ions travel through vacuum *via* series of focusing lenses and a hexapole to reach further compartments of the mass spectrometer. When conducting an ion mobility experiment, ions will travel through a drift cell where they are separated by charge, shape and size. Subsequently, ions reach mass analyzer where separation is governed by mass to charge (*m/z*) ratio. Here, tandem MS experiments can be performed allowing for dissociation or fragmentation of proteins or protein complexes. Finally, ions hit the detector. The impact of those ions induces an electron cascade and enables to measure the total ion current with is later converted to a spectrum. Example mass spectra of 12.3 kDa cytochrome C (a), 55 kDa tetrameric transthyretin (b) and 148 kDa immunoglobulin G4 (c) are shown in Figure 1.2. Use of volatile buffers and gentle dissolvation techniques allow for transfer of intact complexes in their native-like state.

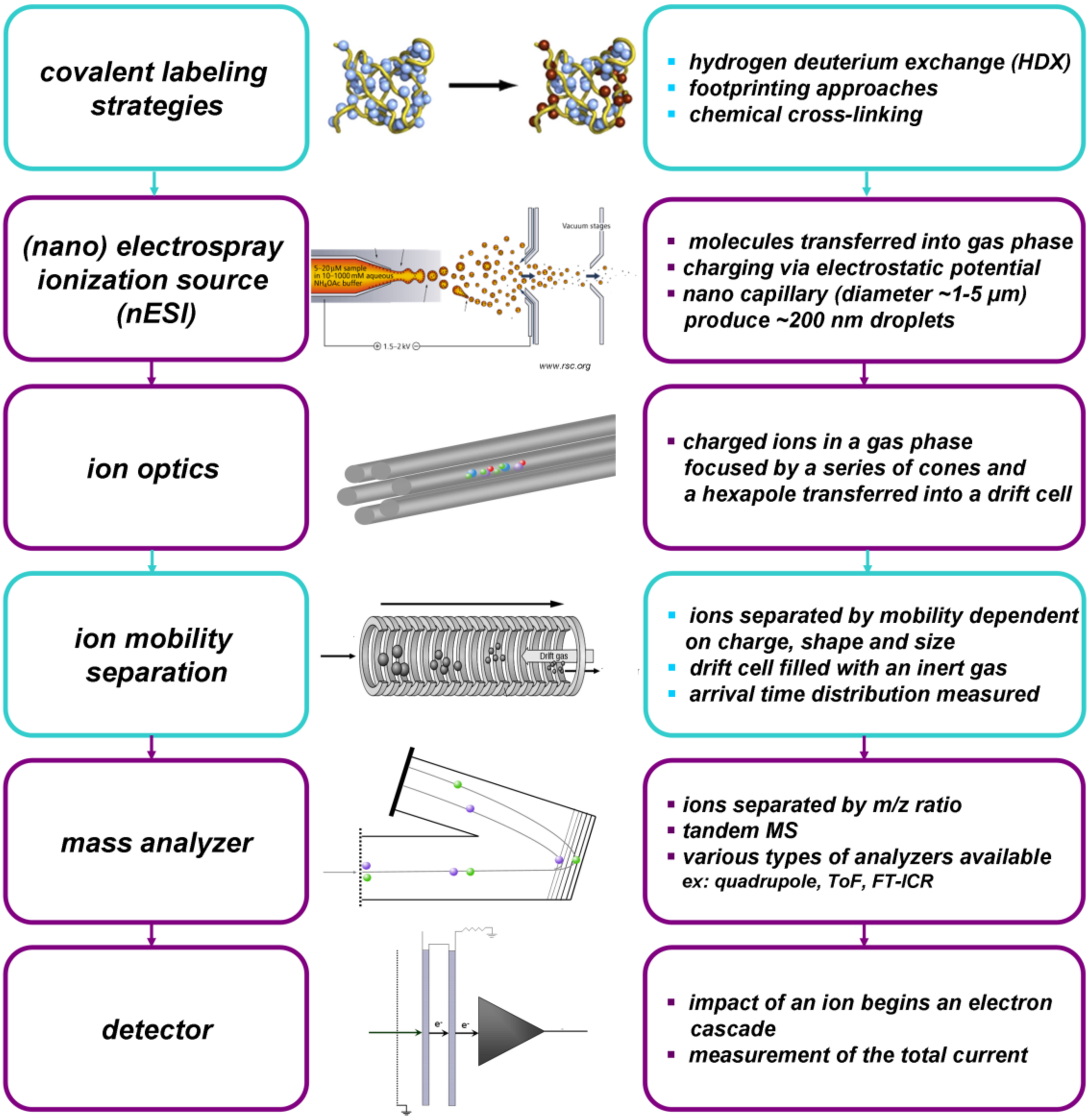

Figure 1.1 Mass spectrometry workflow for structural studies of proteins. Diagram showing ions' path through the basic compartments of a mass spectrometer from sample preparation to the detector.

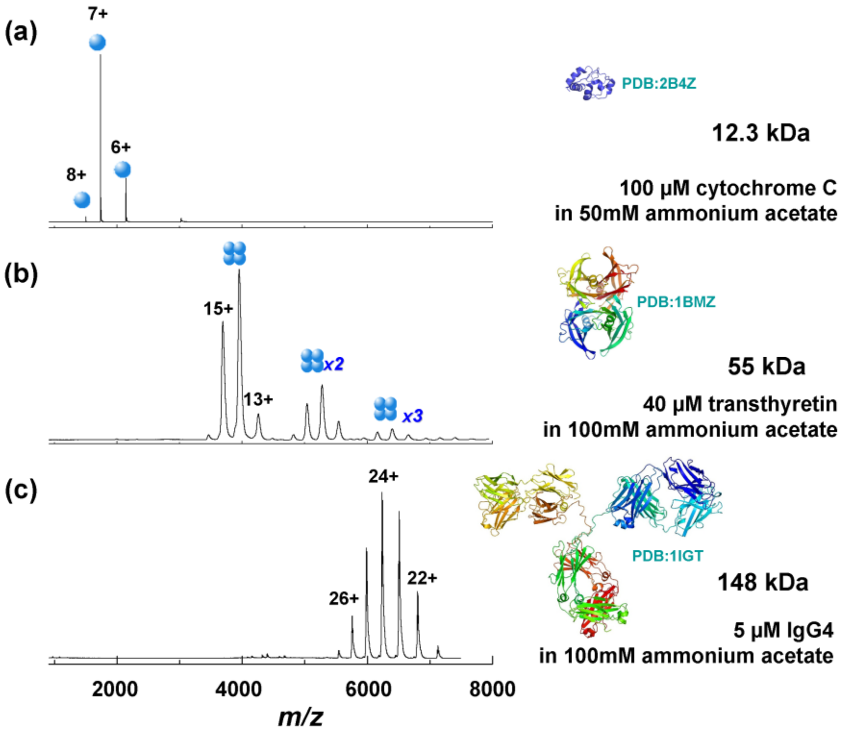

Figure 1.2 Nano-ESI mass spectra of monomeric cytochrome C (a), tetrameric transthyretin (b) and intact immunoglobulin IgG4, along with graphical representation of structures based on the x-ray crystal structures, 2B4Z, 1BMZ and 1IGT, respectively. Use of aqueous buffers, such as ammonium acetate, allow the preservation of non-covalent interactions and native like structure.

1.2.1 Ionisation methods

A crucial step of the MS measurement is ionisation of the analyte. Several methods of sample ionisation exist and are chosen accordingly to the properties of the sample and desired type of information to be obtained. Due to the large number of bonded and non-bonded interactions in proteins, only 'soft' ionisation methods are suitable, namely MALDI (matrix assisted laser desorption ionisation) and ESI. ESI is described in detail, as it is the type of ionisation used for all studies presented in this thesis.

1.2.1.1 Electrospray ionisation

Electrospray ionisation (ESI) is a widely used technique in biological, biochemical, pharmaceutical and medical research, as it allows for fast analysis of various molecules without fragmentation during ionisation. It is a soft ionization technique that can conveniently couple MS to liquid separations and enables MS detection even of large non-volatile molecules such as proteins, producing multiply charged ions. Electrospray ions are commonly formed by addition of a proton $[M+H]^+$, or cations like sodium $[M+Na]^+$, sometimes by removal of a proton $[M-H]^-$.

The initial conception of producing ions by means of electrospray was first proposed by Dole in 1968;[72] however, it was Fenn *et al.* who presented convincing experimental results nearly two decades later and was subsequently awarded a Nobel Prize in 2002 for the application of electrospray to the analysis of biological macromolecules.[71] During the ionisation process, the electrolytic analyte solution is pumped through the conductive end of a capillary, such as coated fused silica or stainless steel emitters with a typical diameter of 100 μm and flow rates 1-100 μL/min.[73,74] Since the solvent volume exiting the emitter is relatively large, a nebuliser gas and/or thermal heating has to be applied for aerosol formation and stable spray sustention; this has to be done especially for highly aqueous liquids. The high potential of a capillary (2-4 kV) induces a strong electric field and draws the liquid towards the inlet; cations move towards the liquid surface and anions move towards the conductive tip. Repulsions between adjacent cations combined with the pull of the cations towards the MS inlet due to the potential difference cause surface to form a Taylor cone, from which droplets with initial diameter of about 1 μm are released.[73] Each droplet is charged due to presence of excess ions that can include H^+, NH_4^+, Na^+ or K^+, or removal of H^+. In order to enhance ionisation efficiency, compounds that increase conductivity (such as formic acid or acetic acid) can be added to the solution. Evaporation of the solvent from the droplets increases charge density. As the Rayleigh limit is passed, where repulsion between cations equals surface tension, Coulomb explosions produce even smaller droplets. Figure 1.3 depicts a nano-ESI (nESI) process, a miniature version of ESI, which will be described later.

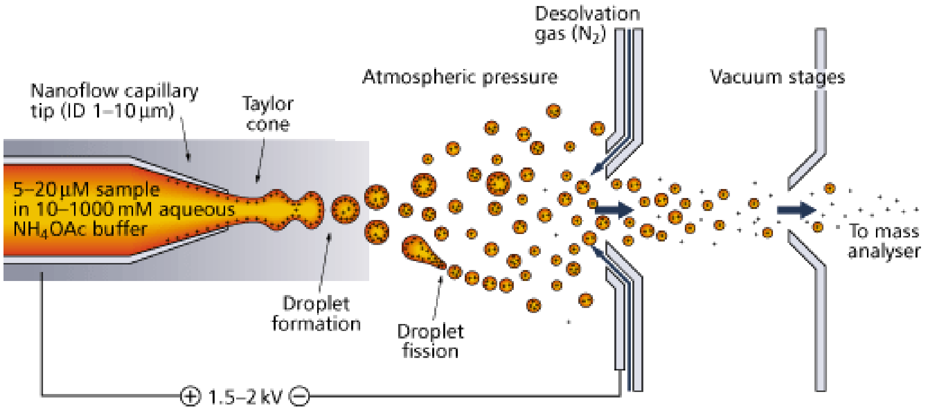

Figure 1.3 Schematic representation of nano-electrospray ionisation in the positive mode, showing Taylor cone formation, production of multiply charged droplets, droplet fission, dissolvation and entry of the ions into the source of a mass spectrometer. Image reproduced from the Royal Society of Chemistry web site.[75]

ESI process can proceed *via* different mechanisms. Currently, three prevailing theories on the gas-phase ion formation are proposed; however, “there is still much debate on the mechanism(s) by which…gaseous ions are formed” (J.Fenn, 2007)[76]. Low molecular weight analytes are thought to follow an Ion Evaporation Model (IEM) (Figure 1.4a).[77] In IEM, droplet reaches a certain radius at which its surface field strength becomes sufficient to support field desorption of solvated ions.[77] The departing ion initially remains connected to the droplet *via* a solvent bridge, which then ruptures as the ion is released.[78] The solvent solute cluster eventually looses its solvation shell as it travels through the source of the mass spectrometer and experiences collisions with background gas ultimately resulting in the solvated ion product.[79]

Large globular species such as folded proteins are charged and released into the gas-phase *via* the Charged Residue Model (CRM) (Figure 1.4b).[72,80-82] Droplets undergo evaporation and fission cycles, producing droplets that finally contain one analyte ion.[72] The solvent shell evaporates to dryness and the charge of the disappearing droplet is transferred to the analyte.[80,82] As the Rayleigh limit is approached, droplets can shed charge upon the shrinkage process by IEM ejection of solvated protons and small ions.[83] It was found that the ESI protonation state predicted by CRM is independent of intrinsic protein charge or amino acid composition.[80,84-87]

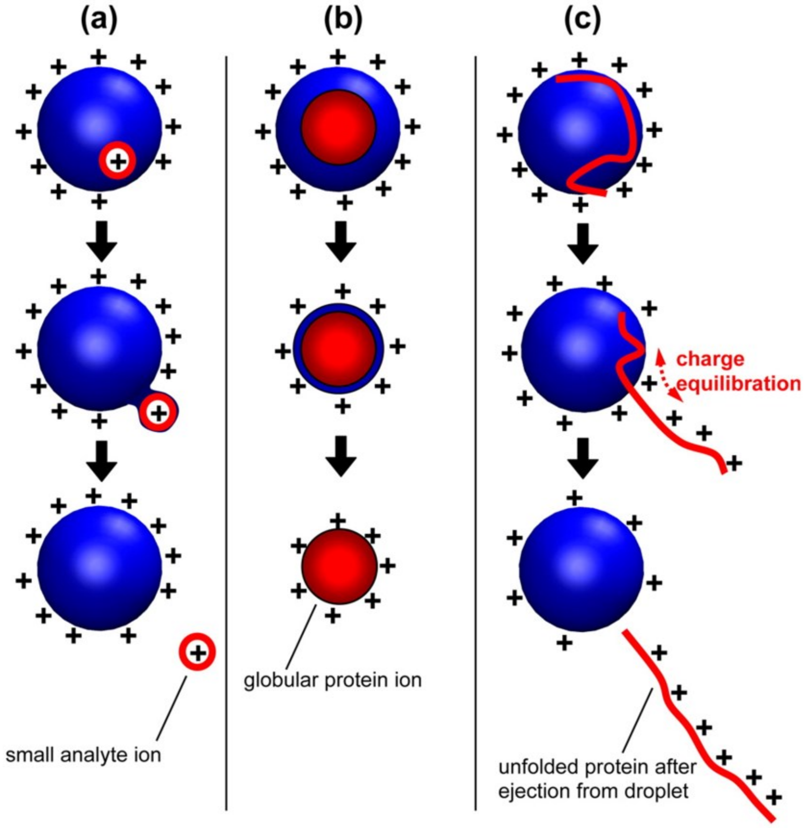

Figure 1.4 Summary of proposed ESI mechanism: (a) IEM – small ion ejection from a charged nanodroplet, (b) CRM – release of a globular protein into the gas phase, (c) CEM – ejection of an unfolded protein. Image adapted with permission from Konermann *et al.*[87] Copyright 2013 American Chemical Society.

The third model, Chain Ejection Model (CEM), has been proposed for disordered polymers (Figure 1.4c).[87] Molecular dynamics (MD) simulations revealed that unfolded protein undergo ESI mechanism somewhat different from the two discussed above.[88,89] Disordered conformations, either intrinsic or solvent triggered, contain solvent accessible non-polar residues with hydrophobic character as opposed to globular proteins where these residues tend to be buried within the hydrophobic core. This makes it unfavourable for the unfolded protein to reside within the droplet and as a result the chain is sequentially ejected from the droplet. CEM ejection of hydrophobic chains occurs on a ns time scale leading to enhanced ion yield and signal intensity as compared ions produced *via* CRM mechanism which is relatively slow and inefficient process occurring on a µs time scale.[88,90-92]

In 1994, Wilm and Mann miniaturised Fenn's ESI technique obtaining improved sensitivity.[73,93] So called nano-ESI (nESI) produces droplets approximately 10 times smaller (about 150 nm) than droplets obtained with the traditional ESI rendering the desolvation process more efficient even under very gentle combinations of applied pressure and temperature. This simple variant of ESI with its much lower potentials between capillary and sampling orifice (1-1.5 kV cf 3-5 kV for ESI) is less destructive to non-covalent interactions. The lower flow rates mean that less sample material is required for analysis allowing interrogation of more limited protein samples, and the potential for multiple high throughput measurements. This invention had a notable impact on mass spectrometry studies of proteins and their complexes.[94]

The purpose of using non-denaturing solution and source conditions is to preserve, as much as possible, the solution phase 'native' conformation of proteins. The effective charge acquired by a compact globular protein when undergoing electrospray ionisation, buffered in an aqueous solution to a suitable pH, close to its isoelectric point, is significantly lower when compared with that presented by the same protein that is electrosprayed from an acidified solution. In the former case there are fewer surface accessible sites available for protonation. This results in native proteins being observed at higher *m/z* ratios and imposes a requirement for mass analyzers with extended *m/z* ranges, particularly for study large multimeric protein complexes. Theoretically, the *m/z* range of time-of-flight (ToF) analyzers is unlimited making them the most appropriate for large native protein studies (often commercially available as quadrupole-ToF hybrids) offering high sensitivity, specificity and rapid analysis.[95,96,97]

Optimisation of several instrument parameters is essential to preserve non-covalent interactions, native conformation and to obtain high transmission efficiency. Adjusting the pressure of the mass spectrometer's interface and accelerating voltage will have an effect on the efficiency of collisions and kinetic energy of the ions in the source of the instrument, this so called collisional cooling, disfavours complex disruption.[98] Bespoke modification of commercial instruments has allowed for better source pressure control and more efficient transmission of large protein complexes.[62,61]

1.2.1.2 MALDI

Matrix assisted laser desorption ionisation (MALDI), a soft ionisation method principally introduced by Karas and Hillenkamp,[99-101] uses UV laser beam to trigger desorption. Samples are mixed in large excess with a small molecule matrix (usually cinnamic aid derivatives for protein analysis), and spotted into a conducting plate. When solid, the mixture is irradiated with a laser under vacuum and sublimates into the gas-phase. The matrix absorbs excess energy protecting protein from fragmentation and also provides protons for ionisation. As this method produces mostly singly charged ions (with a small population of doubly charged species) and uses acidic conditions for sample preparation, it is not a common method of choice for analysis of very large and non-covalent protein complexes. Nevertheless, more recently Zenobi and co-workers have successfully applied MALDI-MS to study high mass non-covalent protein assemblies.[102-105]

1.2.2 Mass analysers

After the ions pass though a series of focusing lenses, the beam enters the mass analyser where ions are separated based on their *m*/*z* ratio. There are several types of mass analysers displaying different properties: compatibility with various *m*/*z* ranges, resolving powers, accuracies, sensitivity, ease of use and operational costs. All advantages and disadvantages should be considered prior to choosing an appropriate type. The following sections will present two types of the mass analysers employed in this work *i.e.* quadrupole mass analyser followed by the time-of-flight (ToF) mass analyser.

1.2.2.1 Quadrupole mass analyser

Quadrupole mass analysers are the most commonly used type due to their relative low cost, easy maintenance and ability to function as both: a mass filter and a full mass analyser. Developed by Paul and Steinwedel in the 1950's, a quadrupole consist of four (usually cylindrical) parallel rods to which a fixed direct current (DC) potential is applied along with an alternating radio frequency (RF) potential (Figure 1.5).[106]

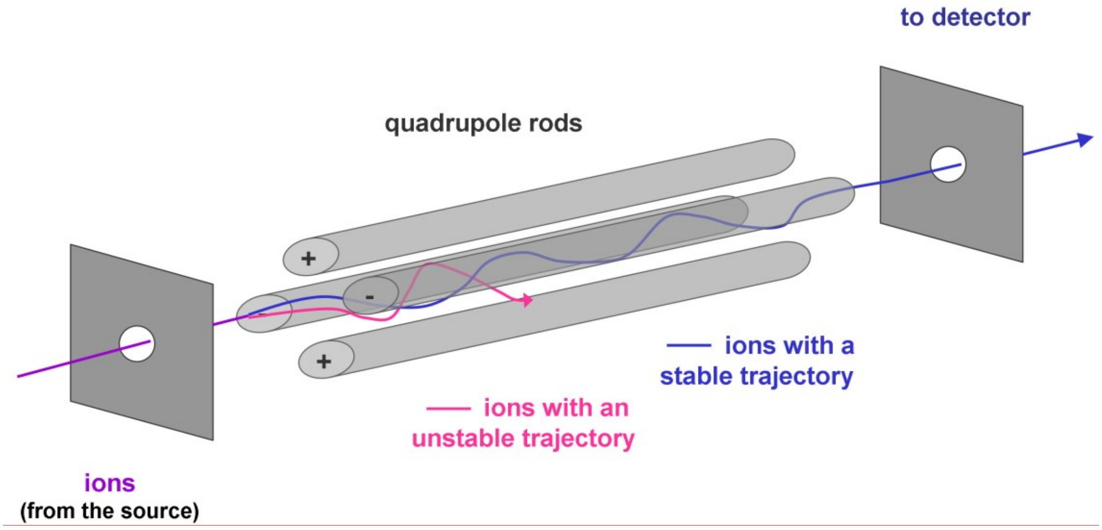

Figure 1.5 Schematic of a quadrupole mass analyser. Opposite rods have the same polarity. The ions with a stable trajectory (blue) are transmitted through the quadrupole and pass further to the detector. The ions with an unstable trajectory (pink) collide with the rods, discharge and are not detected.

The opposite rods are in-phase while the adjacent rod pairs are 180° out-of-phase with respect to their RF field. This produces an oscillating electric field. High frequency polarity switching between adjacent rods, superimposed on the constant electric field, drives ions through the analyser. Ions are drawn towards the oppositely charged rods and change directions upon polarity switching to continue travelling through the analyser. The trajectories of these ions are dependent on the spacing of the rods, the frequency of the RF and the amplitude of the applied potential. These factors determine the influence of the electric field on an ion and can be expressed by the following equations:

$$+\Phi_0 = +(U + V\cos\omega t) \quad \text{and} \quad -\Phi_0 = -(U + V\cos\omega t) \qquad \textit{(Equation 1.1)}$$

where Φ is the total potential on the rods, U is the DC potential, V is the $\mathrm{RF}_{\text{zero-to-peak}}$ voltage, and ω is the angular frequency of the RF (with $\omega = 2\pi v$, v = frequency). For an ion of given m/z there is a set of unique combinations of U, V and ω that will give rise to a stable trajectory allowing it's transmission towards the detector. In Figure 1.5, a schematic of a typical quadrupole is shown; the blue ions are able to oscillate between the rods and reach the detector, whereas the pink ions have an unstable trajectory and discharge during the transmission due to collisions with one of the rods. By fast scanning the RF amplitude, a range of ions with differing *m/z* can follow a stable trajectory resulting in generation of a mass spectrum, where *m/z* values are calculated based on the potential and frequency applied and known geometry of the quadrupole.

Quadrupole analysers are often used as mass filter in tandem mass spectrometers with other types of mass analysers such as time-of-flight (ToF). The ability to select an ion of a specific *m/z* is exploited in the tandem MS experiments, during which the selected precursor is transmitted and subsequently fragmented *via* collision-induced dissociation (CID).

1.2.2.2 Time-of-flight analyser

The time-of-flight (ToF) mass analyser was first described by Stephens[107] in 1946, but it was not until 1955 when Wiley and McLaren demonstrated its practical usage for commercially available instruments.[108] In the ToF instrument, a packet of ions is accelerated by a potential difference and subsequently enters a field-free region and drifts through it at a velocity dependent on the *m*/*z* ratio (Figure 1.6). The *m*/*z* can be easily determined as it is directly proportional to the ions flight time (t_f) through a fixed distance. The relationship between an ion acceleration potential and the flight time can be expressed as following:

$$E_k = \frac{1}{2}mv^2 \qquad \textit{(Equation 1.2)}$$

$$E_k = qV = zeV \qquad \textit{(Equation 1.3)}$$

$$t_f = \sqrt{\frac{m}{z}\left(\frac{d_f^2}{2eV}\right)} \qquad \textit{(Equation 1.4)}$$

where v is the ions velocity, m is mass, E_k is kinetic energy, t_f is flight time, V is acceleration potential, q is the charge on the ion, z is the integer ion charge, e is electron charge, and d_f is flight distance. According to Equation 1.2, for a given kinetic energy, the velocity of an ion is dependent on its mass. Kinetic energy is given to an ion in the acceleration region (pusher) and it varies linearly with the charge as described by Equation 1.3 (the higher the charge the more kinetic energy the ion receives). Combining those two equations results in Equation 1.4, which directly enables to find m/z based on the flight of time (t_f). There is no theoretical upper limit to the mass range which can be analysed by ToF analyser.

The original ToF instruments used linear ToF analyzers (Figure 1.6a); however, nowadays, many instruments are composed of a reflectron ToF analyser (Figure 1.6b), which offers an improved resolution. An ion's proximity to the accelerating voltage can

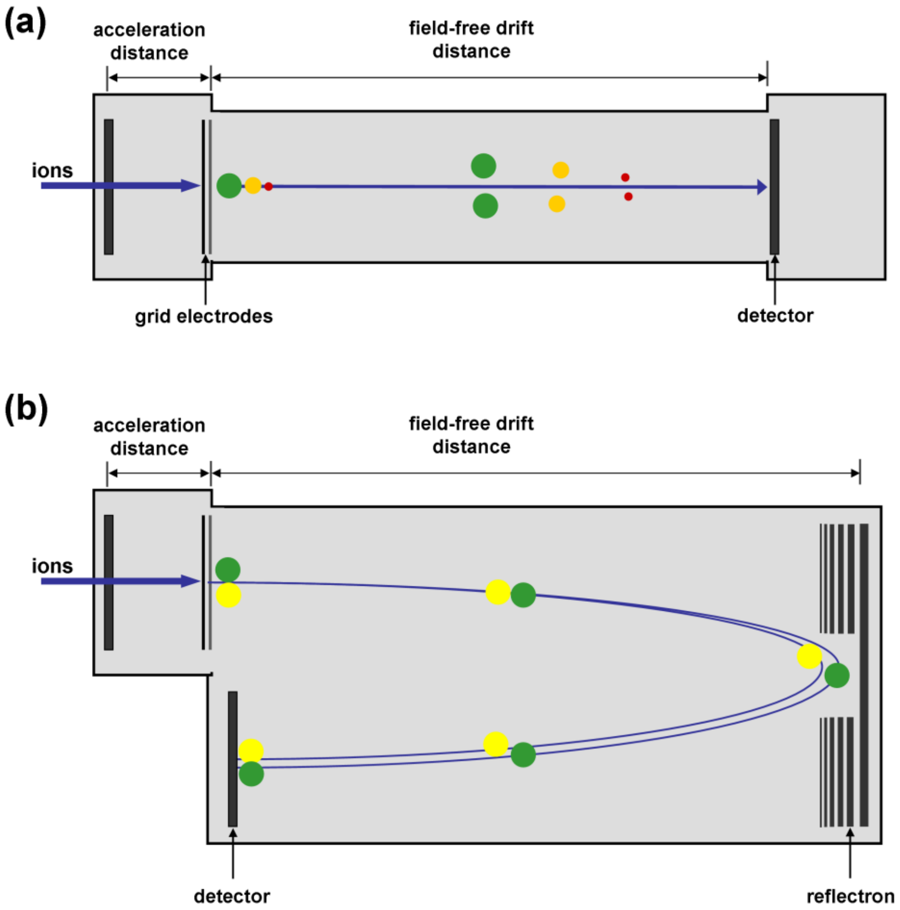

Figure 1.6 Schematic of a linear (a) and a reflectron (b) ToF mass analyser; (a) ions with lower *m/z* are depicted by smaller circles. Ions of the same *m/z* can be distributed along a flight path, broadening the response peak and resulting in poor resolution. (b) Ions of the same *m/z* values are shown, the green ion has higher initial kinetic energy and travels further into the reflectron. Use of this 'ion mirror' enhances analyser resolution by increasing the flight path length and correcting for the initial potential energy differences.

affect the potential difference it experiences; hence, ions of the same *m/z* could enter the field-free drift region with differing kinetic energy causing them to arrive at the detector at slightly different times jeopardizing the resolution. In the 1970's, Mamyrin developed an electrostatic mirror called a reflectron.[109,110] A series of electrostatic lenses deflects ions with a given *m/z* values back towards the detector. Ions with higher kinetic energy penetrate further into the reflectron what allows species of the same *m/z* to arrive at the detector simultaneously, regardless of the initial kinetic energy greatly improving resolution.[111] Figure 1.6 compares both types of these ToF mass analysers. Moreover, a single ToF analyser can be coupled with another ToF analyser (ToF-ToF) or quadrupole (Q-ToF). Often, the first analyser is used to isolate an ion of interest (parent ion) and the second to analyse product ions after induced dissociation or fragmentation.

1.2.3 Detectors

The final stage of a mass spectrometry experiment is ion detection. Most of the MS detectors use incident ions to produce a secondary beam of electrons which is further amplified to create a detectable current. There are three common types of detectors available: electron multiplier, photomultiplier and microchannel plates.

1.2.3.1 Electron multiplier and photomultiplier detectors

Electron multipliers are commonly coupled to quadrupole and ion trap analysers. This type of the detector consists of a series of dynodes held at sequentially increasing potential. Ions from the mass analyser are accelerated and collide with the surface of a first conversion dynode producing electrons which are accelerated further. Collisions with the subsequent dynodes produce more electrons until the final dynode is reached and the signal is detected as an ion current with significant signal amplification (up to 10^6 greater intensity).[112]

The photomultiplier detector operates on a similar principle to the electron multiplier.[113] The ions are incident on a conversion dynode and generate electrons. Subsequently, these electrons collide with a phosphor screen resulting in generation of photons which are then detected by a photomultiplier. If the hybrid Q-ToF instrument used in the ‘quadrupole only’ mode, ions are detected by the photomultiplier on their entry to the ToF tube.

1.2.3.2 Microchannel plates detector

Most ToF instruments are coupled to microchannel plate (MCP) detectors which have a quick time response and high sensitivity (<1 ns and single ion signal of 50 mV).[113] Microchannel plates, firstly implemented in 1960’s, consist of thousands of miniature electron multiplier enabling the detection of large number of ions at the same time.[114] An ion incident on one side of the channel will eject electron upon the collision. This process is repeated inducing a cascade of electrons resulting in measurable current. Figure 1.7, shows a schematic of a microchannel plate (a) and the process of ion detection and signal amplification (b).

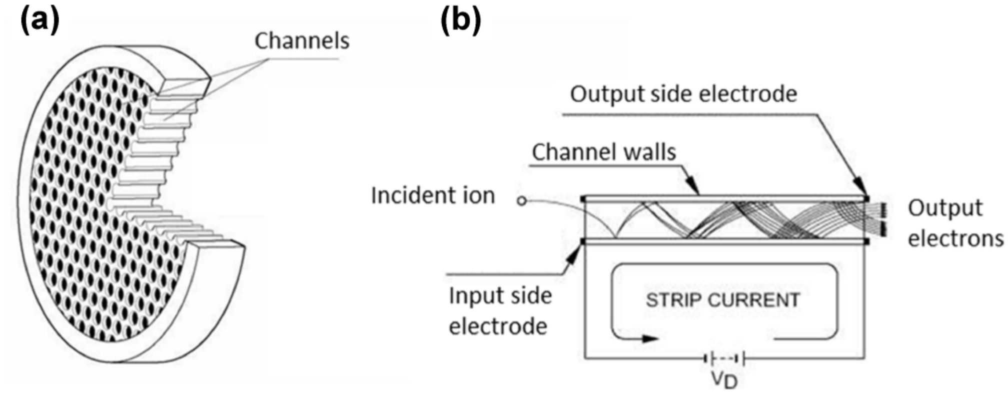

Figure 1.7 Microchannel plate detector (MCP): (a) MCP design featuring an array of channels, (b) MCP in action – an incident ion starts a cascade of electrons upon impact, amplifying the signal. Images adapted from Hamamatsu web site.[115]

.

1.3 Mass Spectrometry Methods for Elucidation of Protein Structure and Interactions

1.3.1 Ion mobility mass spectrometry

Ion mobility mass spectrometry (IM-MS) can provide useful insights into the structures of biological macromolecules and their complexes and has been applied to study peptides and proteins, carbohydrates, lipids, nucleotides as well as other natural products.[28,116] Ion mobility separations performed with an inert background gas are based on the charge, size and shape of an ion and are proportional to the ion surface area *i.e.* to the rotationally averaged collision cross section (CCS). When coupled to a mass spectrometer, separation of ions in the gas-phase becomes two dimensional – based on the mobility (K) and mass to charge ratio m/z. It is possible to separate coincident m/z species based on their oligomeric order and protein conformations as illustrated schematically in Figure 1.8.

Significant developments of IM-MS for biological applications occurred in the mid-1990's, results of the first IM-MS structural studies of peptides were published by Bowers *et al.*[117] and on intact proteins by Jarrold, Clemmer *et al.*[118,119]. About 10 years later, Robinson, Heck, Ashcroft, Loo, Barran, Leary and other groups extended the scope of IM-MS to the study quaternary structure of protein complexes.[120,121-135] Much of this work has been possible due to the remarkable technical developments made by Bateman and co-workers[136,137] in their development of the first commercial IM-MS instruments, which possess a vastly superior transmission efficiency for IM separation, as well as much better m/z resolution compared with most homemade IM-MS devices.

Uetrecht *et al.* have written an excellent review on the application of IM-MS to protein and protein-assembly studies.[138] IM-MS allows the study of protein unfolding and conformational changes upon ligand binding. Protein ions can unfold in the gas phase, most likely driven by Coulombic repulsion. Ions with fewer charges retain more solution-like structure than highly charged ions of the same species.[138] IM-MS is able to resolve distinct conformational families for particular ions and to recognize structural diversity from compact to extended conformational states. For example, Hopper and

Oldham have studied structural stability (unfolding and dissociation) of compact proteins such as the FK-binding protein, lysozyme and myoglobin as a function of ligand binding.[139] IM-MS has also been applied to study 11-membered structure of oligomeric tryptophan RNA binding attenuation protein complex (TRAP) to show retention of its ring-like topography after the electrospray ionisation process and its transition to the gas phase as well as increase of stability upon ligand binding.[121,140]

In comparison to atomic structural resolution methods such as x-ray crystallography or NMR, IM-MS provides relatively low-resolution structural information; however, only small quantities of sample are required, gas phase separations are rapid and solvent effects are not present.[141] Hill *et al*. have prepared an extensive review on milestones in the development of IM-MS.[142] There are three principal types of ion mobility instrumentation that have been successfully coupled with mass spectrometry: drift tube (DT), travelling wave (TWIMS), and field asymmetric waveform ion mobility spectrometry (FAIMS) which will be presented in the following sections.

Despite differences in the configuration of IM-MS instruments; there are some common features. A pulse of ions is injected into a chamber filled with a known inert gas at a known pressure. An electric field is applied across the chamber and the time taken for the ions to travel though is measured. The ions are actively transported through the cell by the electrostatic force; at the same time this force is opposed by collisions of ions with buffer gas. The mobility K is dependent on the molecular shape, charge of the species and the buffer gas pressure. Only DT-IM-MS instruments allow for direct determination of collision cross sections (CCS) by recording the drift velocity of an ion through a linear drift field.[143]

1.3.1.1 Linear DT-IM-MS

Measuring the time it takes for the ions to transverse through a buffer gas (usually helium) filled drift cell under a weak electric field, allows for determination of CCS. The electric field (E) is defined in terms of the length of the drift cell (L) and the voltage applied across the cell (V) by Equation 1.5:

$$E = \frac{V}{L} \qquad \textit{(Equation 1.5)}$$

The ratio of the electric field across the cell (E) to the buffer gas density (N); expressed in Townsend (*Td*); determines the transmission of ions through the cell. Ions align in the electric field and their mobility becomes dependent on E at high E/N values (> 10 *Td*). At lower E/N values (≤ 10 *Td*), known as the low field limit, ion's velocity is constant and linearly proportional to the electric field:

$$v_d = K \cdot E \qquad \textit{(Equation 1.6)}$$

where v_d is the drift velocity and K is the low field mobility. In turn, K is proportional to buffer gas pressure and inversely proportional to Ω. Since K is dependent on N, to decouple it from experimental variables of pressure and temperature, and allow for data comparison, K is converted to reduced mobility K_0 by Equation 1.7; where normalized temperature T_0 is 273.15 K and normalized pressure P_0 is 760 Torr:

$$K_0 = K \frac{P}{P_0} \frac{T_0}{T} \qquad \textit{(Equation 1.7)}$$

The time spent by ions in the drift cell (t_d) can be calculated by:

$$t_d = \frac{L}{v_d} = \frac{L}{K \cdot E} = \frac{P}{V} \frac{L^2 T_0}{K_0 P_0 T} \qquad \textit{(Equation 1.8)}$$

The arrival time (t_a) measured during an IM experiment, is equal to the sum of time taken for the ions to drift through the cell (t_d) and the time ions spent outside the drift cell until detection (dead time, t_0). By maintaining a constant temperature during the measurements, a graph of t_a versus P/V will provide a linear relationship with an intercept equal to t_0. The slope gradient of this line is equal to the inverse of the reduced ion mobility; hence, Ω can be determined using Equation 1.9, which is approximated to the ion's CCS.

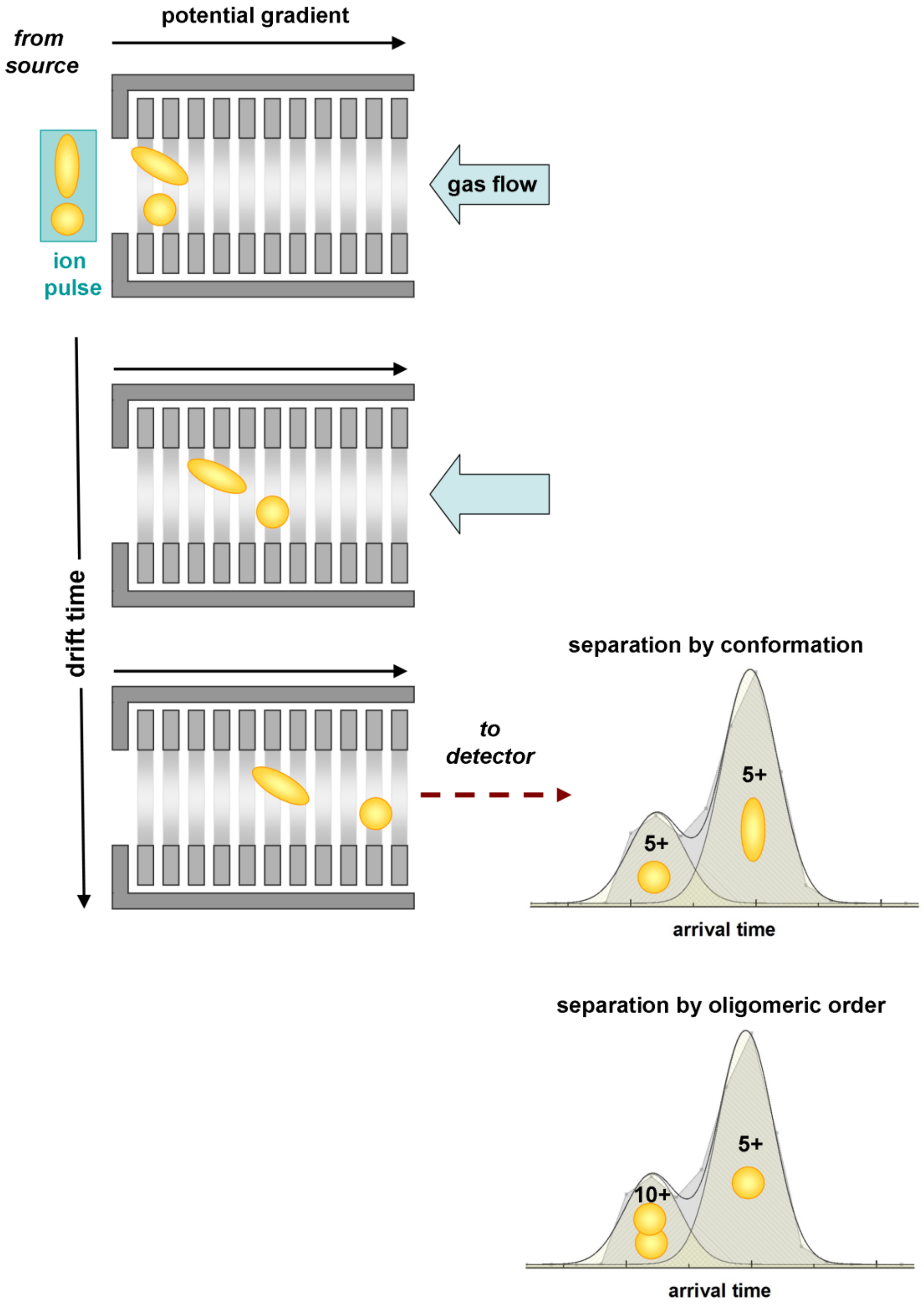

Figure 1.8 Principle of ion mobility separation. Ions are pulsed into the drift cell and travel through a uniform electric DC potential against the gas flow to be separated based on their conformation and charge. Arrival time distributions (ATD) are acquired and can be converted to collision cross sections (CCS).

Mobility K is inversely proportional to CCS according to the following relationship:

$$K_0 = \frac{3ze}{16N}\left(\frac{2\pi}{\mu k_B T}\right)^{1/2}\frac{1}{\Omega} \qquad \textit{(Equation 1.9)}$$

where K_0 is the reduced mobility (the measured mobility K standardized for pressure and temperature to 273.15 K and 760 Torr), z is the ion charge state, e is the elementary charge, N is the gas number density, μ is the reduced mass of the ion-neutral pair, k_B is the Boltzmann constant and T is the gas temperature and Ω is the momentum transfer collision integral (approximated to the CCS of the ion by kinetic theory).

IM allows for separation of coincident *m/z* ions by charge and conformation. As can be seen from Equation 1.9, K and Ω are inversely proportional to each other, hence small and more compact ions (of the same *m/z*) will travel faster through the cell than more extended ions (separation by conformation, Figure 1.8). Whereas, z and Ω are directly proportional, therefore ions carrying more charge will have shorter arrival time than those with less charge but coincident *m/z* value what enables separation by oligomeric order.

1.3.1.2 Travelling wave ion mobility spectrometry (TWIMS)

The application of IM-MS for structural studies of biological macromolecules has greatly increased since the introduction of a commercial quadrupole/travelling wave ion mobility time of flight mass spectrometer.[136] Although the transmission efficiency of ions through a traditional drift cell is low, the physical aspects are well understood.[142,144,145] This is not yet the case for ions transmitted through ion mobility cells with travelling wave technology[136,146] where CCS cannot be directly determined and drift times calibrated for ions of interest against those measured for ions of known Ω values.[120,147,148] Jurneczko *et al.* have compared CCS for several monomeric proteins investigated with different ion mobility techniques and found good agreement, although they also note the consistent reduction in CCS compared to theoretical CCS extrapolated from crystal structure data.[147,149]

The first commercial available integrated IM-MS instrument was introduced by Waters MS Technologies in 2006, and called the Synapt G1 HDMS.[136] Later, upgraded versions of this instrument with improved resolution and sensitivity were released (SynaptG2 in 2009 and G2S in 2012). Synapt HDMS instruments, based on the travelling wave (TWIMS) technology, use stacked ring ion guides (SRIG) for mobility separations located between the quadrupole and the ToF analyser. Ions are released from the first ion guide of T-wave cell as a packet into the IMS T-wave cell filled with nitrogen gas (process analogous to the injection of ions into the drift cell in the DT-IM-MS type instrument). Here however, mobility separation is performed as the repeating DC pulses drive ions through the cell. Application of opposite phases of RF voltage to adjacent rings and superimposed transient DC pulse, creates a moving electric field – the travelling wave, on which ions 'surf'. The ions roll over the wave and the separation occurs based on their mobility and due to collisions with the buffer gas. The fundamentals of travelling wave are not fully understood yet.[146]

A shortcoming in the use of TWIMS-MS devices is that this type of IM-MS device does not directly provide CCS from drift time data. Instead a number of different calibration approaches have been suggested, which all are based on the use of protein standards, whose CCS has been measured in DT-IM-MS instruments.[147,150,151] Whilst this approach has been used to good effect in a number of studies, there are some less satisfactory elements to it. The first is that the DT-IM-MS standards are usually measured with helium as the drift gas, whereas in TWIMS-MS instruments the drift gas is usually nitrogen. This means that TWIMS CCS measurements are made in one gas, but converted to another. For small molecules it is well known that CCS are strongly buffer gas dependent.[152,153] This effect is less for larger macromolecules, but still apparent, which means that standards must be chosen carefully to be 'similar' to the unknown systems under study.

In addition, a problem with applying a calibration method to determine the CCS of an unknown system is that different sampling conditions (including solvent, source temperature, ion transmission settings) all can affect the actual conformation of ions in the mass spectrometer, which in turn may be distorted by the calibration. Further to this there have been reports that the temperature of ions in TWIMS instrumentation may be higher than ambient, whereas for DT-IM-MS, drift cell temperature is a carefully recorded experimental parameter, essential for the evaluation of a CCS from a given ion's mobility (Equation 1.9).[154,155] The ions of course are thermalised in these experiments having undergone many millions of collisions in the first few mm of drift. None-the-less, in the absence of an exact solution for the relationship between the mobilities of ion in TWIMS-MS instruments the calibration methods are still useful, and have produced a number of interesting results. Despite issues with determining absolute CCS from TWIMS-MS data, the ability of these instruments to provide understanding how conformational changes relate to the modulation of protein function is beneficial to structural biology and enabled number of research groups to utilize IM-MS methodology.

1.3.1.3 Field asymmetric waveform ion mobility mass spectrometry (FAIMS)

High-field asymmetric waveform ion mobility spectrometry (FAIMS), also knows as differential mobility, separates ions based on their mobility differences in high and low field at the atmospheric pressure.[156] Because at a high field electric field ($E/N > 10$ *Td*), the mobility of the ion is influenced by the electric field, this method cannot be used to derive CCS. In a FAIMS device, ions drift between two parallel planar electrodes through a buffer gas flowing in the same direction as the ions. One of the electrodes is kept at ground potential, while an alternating electric field (asymmetric wave) is applied to the other electrode consisting of short high-voltage components and long low-voltage component of opposite polarity.[157] The asymmetric wave applied is orthogonal to the gas flow and causes ions to oscillate between the two electrodes moving them towards the detector (analogous to the quadrupole analyser). To prevent ions from discharging against the electrode, a compensation DC voltage is applied to correct their trajectory. Ions of different size and conformation require specific compensation voltage values for successful transmission, hence, it is scanned across a range of values or fixed at a specific value to select a specific ion population (similarly to mass filter approach in quadrupole mass analysers). Use of high fields may cause distortion to conformations and unfolding of labile biomolecules, hence FAIMS is not a method of choice for studies of native-state protein structures. Nevertheless, FAIMS is a powerful tool for the analysis and separation of peptide mixtures[158-161] and also finds vast application in detection of chemical warfare agents and explosives.[142] Commercial instruments were made available by a number of manufacturers, also as a front-end device which can be coupled to a mass spectrometer.

1.3.2 Probing structures via induced dissociation

Information on subunit composition and topology of multimeric protein complexes is often obtained by activating protein ions in the gas-phase to induce structural changes and often dissociation of these subunits. The most commonly used activation method is collision induced dissociation (CID) achieved *via* energetic collisions of the ion with neutral gas. Nevertheless, other activation methods exist, such as *s*urface *i*nduced *d*issociation (SID), *b*lackbody *i*nfrared *r*adiative *d*issociation (BIRD) or the application of elevated injection or acceleration voltages; these methods and their application to study of biomolecules are summarized in Figure 1.9. Since proteins are capable of adopting more compact or extended states both in vivo and also in the gas-phase upon activation, including the IM-MS in this repertoire will provide an experiment that provides conformational information and enables structural changes to be directly followed.

As protein activity is greatly dependent on the solution temperature, several research groups have designed variable temperature nESI (VT-nESI) capillary holders that allow for control of the sample solution temperature. These devices have been applied to address variety of questions and study conformational changes in monomeric proteins such as ubiquitin,[162,163] denaturation of ribonuclease S[164] or DNA destabilization,[165,166] protein-carbohydrate binding,[167,168] unfolding and dissociation of thermally activated proteins such as small heat-shock proteins (sHSPs),[169,170] solution-phase thermal disassembly of co-chaperonins GroES and gp31,[171] or probing early stages of heat-induced protein aggregation[172].

Activation of proteins can be induced not only in-solution prior to transfer into the gas-phase, but also in the vacuum of a mass spectrometer. Raising voltages in the source region of the mass spectrometer, such as cone or extractor cone voltages, affects the acceleration of the ions through the source. Increased collision energy with the background gas is transferred into the internal energy of the sample ion and might

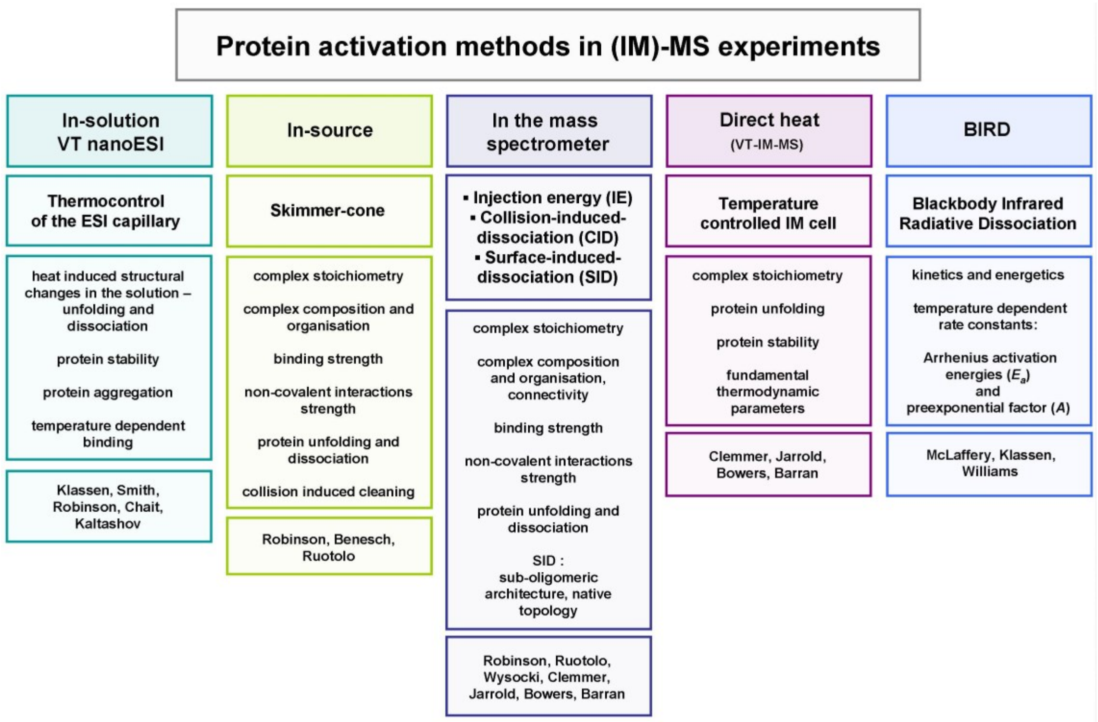

Figure 1.9 Methods of protein activation in an (ion mobility) mass spectrometry experiment. The chart lists MS based techniques used to induce protein activation along with the type of information that can be obtained *via* each method and references to research groups specializing in application of these techniques for studies of protein complexes.

disturb protein structure and induce protein unfolding and protein complex dissociation. With the use of IM, Benesch *et al*., showed how the in-source complex activation affects protein structure.[123] Raising the cone voltage, resulted in an initial decrease in drift time of ions and a subsequent increase in drift time as well as a notable broadening of the arrival time distributions (ATD) for a 197 kDa small heat shock protein Arc1. This was attributed to collision induced reconstructing (collapse of the central cavity) followed by collision induced unfolding.[123] Similar effects have been noted for a ring-shaped tryptophan RNA-binding attenuation protein.[121] Ruotolo *et. al* studied homotetrameric transthyretin (TTR) (56 kDa), and showed how the in-source activated complex undergoes unfolding transition states that are stable on a millisecond time scale prior to dissociation.[122]

Protein dissociation can be induced in the later stages of a mass spectrometer *via* the insertion of a collision cell allowing for collision induced dissociation (CID). In a CID experiment, molecular ions are accelerated by an electric potential to higher kinetic energies. Upon collision with neutral gas molecules, some of the kinetic energy is transferred into internal energy leading to dissociation. CID is a widely used tandem MS method to study protein interactions and arrangement of subunits within a complex. The first reports of CID on tetrameric streptavidin, dimeric cytochrome c or tetrameric TTR, had shown asymmetrical charge partitioning upon dissociation.[173-175] Due to statistical reasons, one subunit might carry slightly more charge than others. This asymmetrical charge partitioning results in a marginally destabilized subunit, resulting from intramolecular Coulombic repulsions.[176] Upon collisional activation of the complex, one or possibly multiple subunits begin to unfold. As the new surface area is exposed, charge migration occurs to that region and drives further unfolding which eventually results in release of highly charged monomer (Figure 1.10).[177] This dissociation pathway is referred to as the ‘typical’ route.[178] The addition of ion mobility separation probed conformational changes that occur during collisional activation process. Several proteins, such as TTR, (and mutants and ligand bound forms) and heat shock protein 16.9 (HSP16.9) have been studied to show a series of conformationally diverse transition states undergoing unfolding prior to dissociation as the CID energy is increased.[124,179,180] Moreover, CID-IM and molecular dynamics (MD) studies on SAP and TTR showed that the protein complex compaction and dissociation are greatly dependent on the charge state, where the highly charged species require less energy to cross the dissociation energy barrier.[179,181] Hall *et al.* reported that high charge states of protein complexes with low subunit flexibility, higher charge densities, fewer salt bridges and smaller interfaces are likely to be involved in promoting dissociation routes without unfolding, the ‘atypical’ dissociation route.[178] Moreover, recent findings show that addition of Hofmeister salt-based solution additives that stabilize the complex, increase the energy dissociation barrier.[182-185]

The multistep protein complex activation occurring on a millisecond time scale in the CID experiment and resulting in asymmetric ejection of unfolded monomer from the complex, might be somewhat limiting the amount of information on the sub-oligomeric architecture.[186,187] Wysocki *et al.* have employed surface induced dissociation (SID) and demonstrated conditions that can achieve dissociation of complexes without any significant unfolding of subunits prior to dissociation (‘atypical’ dissociation).[188-190] Although the concept of SID has been introduced long time ago,[191,192] more recently this

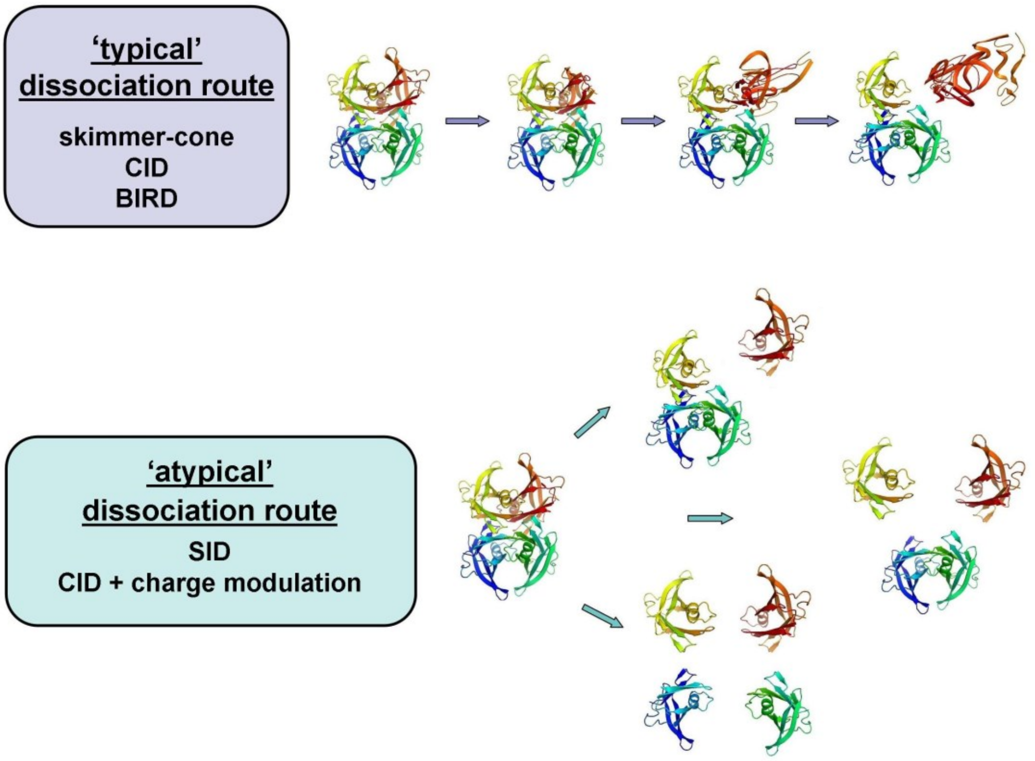

Figure 1.10 The effect of activation techniques on the structure of multimeric proteins. Skimmer-cone, CID and BIRD activation occur on a long time scale and proceed *via* asymmetric charge partitioning followed by subunit unfolding and dissociation - the 'typical' dissociation route. SID activation (occurring at much shorter time scale (ps)) or modulation of charge states in the CID process results in release of compact subunits – the 'atypical' dissociation route. Graphical representation of the activation process is based on a TTR structure, PDB:1BMZ.

method has been used to study dissociation of peptides and non-covalent protein complexes such as TTR, SAP, phosporylase B (PHB) and glutamate dehydrogenase (GDH) or even 801 kDa GroEL. [190,193-198] In a typical CID experiment, energy is deposited into the complex by multiple low-energy collisions, whereas SID deposits energy into the complex by a single collision with a surface on a picosecond time scale. SID experiments show more symmetric charge partitioning upon dissociation and release of compact subunits yielding meaningful information on native-like topology of protein complexes (Figure 1.10).[190,195,196,199,200]

Additionally, in IM-MS experiments, ions can be activated *via* higher energy collisions which occur as ions are injected into the drift cell region of the IM mass spectrometer. High injection energies can induce structural changes and/or fragmentation of the ions if desired. Jarrold *et al.* have first presented this principle on bovine pancreatic trypsin inhibitor (BPTI) and cytochrome *c*.[119] It was found that BPTI retains in its compact form when collisionally activated attributed in part to the presence of three disulfide bridges, unlike cytochrome *c* with no disulfide bridges which gradually unfolds through a series of well defined intermediates.[119] By increasing the ion injection energy, peaks at short arrival times disappear and the intensity shifts to the peak at longer arrival times illustrating the annealing of ions to more open conformations by collisions with the drift gas at the entrance to the drift cell. Injection energy induced unfolding and dissociation has been demonstrated on oligosaccharides, monomeric protein such as ubiquitin, lysozyme and amyloidogenic proteins like *α*-synuclein, amyloid *β*-protein and its aggregates.[201-207] Furthermore, an increase of temperature of the buffer gas during the IM experiments by direct application of heat induces protein unfolding and dissociation, however this method will be discussed in more detail in Chapter 4.[208]

An alternative approach to ion activation is blackbody infrared radiative dissociation (BIRD) technique, which is usually implemented on ion trap type mass spectrometers. In BIRD, isolated ions are activated by absorption of infrared blackbody photons emitted from the walls of a heated vacuum chamber of a Fourier-transform mass spectrometer,[209] enabling the measurement of the temperature dependence of dissociation rate constants and subsequent determination of the Arrhenius activation energy (E_a) and preexponential factor (A) for gaseous ions. Williams and co-workers have widely investigated the dissociation of monomeric proteins,[210-212] and later the first application of BIRD on multimeric protein complexes was reported by Klassen *et al.* on a pentameric Shiga-like Toxin I.[213] Asymmetric dissociation into monomers and tetramers was observed along with remarkably large A, being an indicative of the mechanism proceeding *via* the unfolding of a monomeric subunit prior to dissociation. Further BIRD experiments, found that the dissociation pathway is dependent on temperature, with the loss of a single subunit dominant at higher reaction temperatures, and fragmentation of the backbone dominant at lower reaction temperatures and longer reaction times.[214-216]

1.3.3 Hydrogen deuterium exchange mass spectrometry (HDX)

1.3.3.1 Principles of HDX

Hydrogen deuterium exchange experiments (HDX) are used to examine the structure and dynamics of proteins by replacing a covalently bound hydrogen atom of amides in the backbone of a protein by a deuterium atom and detecting the change spectroscopically in the deuterated form. HDX was explored by a Danish protein scientist Kaj Ulrik Linderstrøm-Langand and it has been used most frequently in conjunction with NMR.[217-220] In 1991, the first successful coupling with a mass spectrometer as the detector was reported by Katta and Chait.[221,222] HDX-MS has been used to study structural changes involved in physiological processes such as viral infections, [223-225] blood coagulation[226-228] or conformational changes in GPCR rhodopsin[229]. Apart from its application in probing binding interaction, HDX-MS has been used mapping unstructured regions of intrinsically disordered proteins (IDP)[230-232], dynamics of enzymes[233,234], or conformations of hydrophobic integral membrane proteins (IMP)[58,235-239]. Furthermore, HDX-MS has been used to investigate protein aggregates associated with formation of amyloid fibrils such as Aβ[240,241], and exploration of the higher order structure and dynamics of protein based therapeutics[242-245].

Some of the protein hydrogen atoms are capable of being replaced by the molecules from the solvent. There are three types of hydrogen atoms in proteins: hydrogen atoms bonded to hetero atoms on side chains with fast forward and backward exchange rates (Type 1), hydrogen atoms on the backbone amide nitrogen that exchange at rates ~100 times slower than those on the side chains (Type 2) and hydrogen atoms covalently bound to carbon that do not exchange (Type 3), these generally occur in aliphatic or aromatic side chain containing amino acids (Figure 1.11).[246] When using deuterium oxide in the solvent system, the heavy deuterium becomes incorporated into the protein and this change can be detected by mass spectrometry. As each amino acid has one Type 2 amide hydrogen (except proline) this method can be used to probe the exchange rates along the entire length of the protein and provide information about protein structure and dynamics.[247,248] The exchange rate of these amide protons is related to the structural characteristics based on the extent to which the exchangeable protons are shielded from the solvent *i.e.* buried in the protein interior, or occluded as part of a

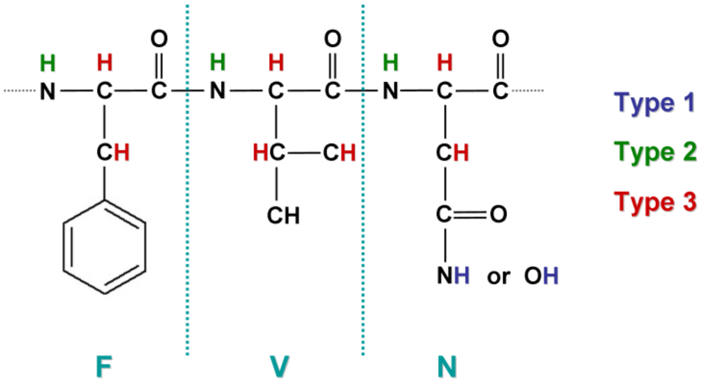

Figure 1.11 Classification of hydrogen atoms in polypeptides: Type 1 - hydrogen atoms (blue) bound to hetero atom undergo rapid reversible exchange under all buffer conditions, Type 2 - hydrogen atoms (green) bound to an amide of the peptide backbone exhibit solvent dependent behaviour (low pH and temperature slow down the exchange rate), Type 3 - aliphatic and aromatic hydrogen atoms (red) show no exchange within the timeframe of an HDX experiment.

surface involved in binding interaction. The location and relative amount of deuterium uptake along the backbone chain can be subsequently determined by digestion of protein and analysis of individual peptides by tandem mass spectrometry (MS-MS). As the hydrogen exchange is acid or base catalyzed, the rate is greatly dependent on the pH. The minimum exchange rate occurs at approximately pH 2.6; therefore, the reaction is quenched by lowering pH to prevent back-exchange and allowing sufficient time for mass spectrometry measurements.[221]

1.3.3.2 Direct HDX

There are two main types of direct HDX experiments that allow investigation of protein conformational changes upon ligand binding: on-exchange and off-exchange experiments.[249] In the on-exchange experiments (Figure 1.12a), HDX is performed on the protein-ligand complex in addition to the unbound protein which acts as a control. Ligand binding is expected to occlude the HDX in specific regions due to steric hindrance at the binding site and resultant changes in conformation (which may be remote from the ligand binding site). After HDX and subsequent reaction quenching to minimize back exchange, proteins are proteolysed and the peptide fragments are analyzed by mass spectrometry. Alignment of the peptides with the primary amino acid sequence of the protein identifies the location of the binding site and any conformational changes from differential mass uptake of deuterium between the complex and the control. This approach has recently been fully automated in a commercial instrument coupling the HD on-exchange experiment with the quenching step, followed by on-line digestion using a pepsin column, chromatographic separation of the resulting peptides and their analysis by MS-MS. In unattended operation this system can generate a time course of deuterium uptake mapped onto the protein sequence to elucidate subtle changes in solvent exposure not just at the ligand binding site but at remote sites subject to conformational changes as a result of binding.

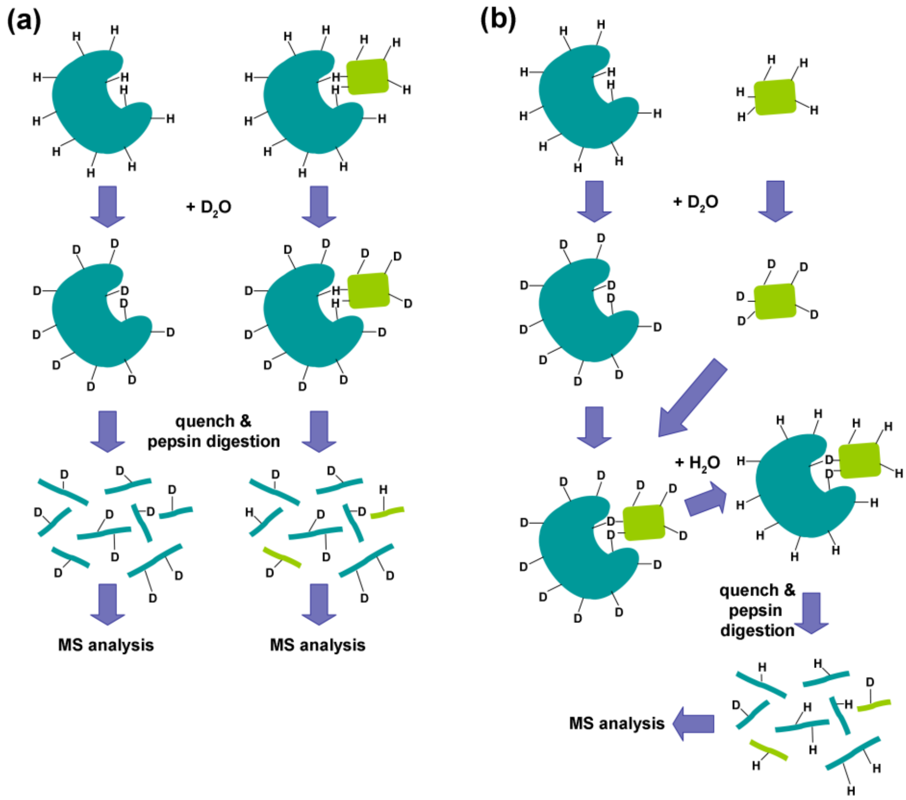

Figure 1.12 Workflow of an HD on-exchange (a) and off-exchange (b) experiments for probing ligand binding sites and any conformational changes induced. Measuring differences in deuterium uptake between apo protein and ligand bound protein helps to map the binding site and probe any conformational changes induced upon ligand binding.

In the off-exchange experiments (Figure 1.12b), protein and ligand hydrogen atoms are allowed to exchange separately with deuterium atoms prior to complex formation. After the time allowed for the complex to form, the deuterium atoms are off-exchanged by dilution with water. Again, the complexes are proteolysed and the peptides analysed with mass spectrometry are compared with those from control experiments performed using each binding partner in isolation. The proteolysed peptides that show extensive residual incorporation of deuterium are assumed to be at the ligand binding interface or involved in conformational changes associated with the binding event. On- and off-exchange experiments have been successfully applied to study inhibition of an essential blood coagulation protein thrombin,[248,250] or structural stability in gas phase of myoglobin,[251] bovine cytochrome *c*[252] and bradykinins[253]. The usefulness of information obtained with HDX on protein-ligand interactions has led to the development of automated HDX-MS systems[254] and semi-automated data processing applications such as *HX-Express*[255], or DynamX from Waters Corporation.

1.3.3.3 PLIMSTEX, SIMSTEX and SUPREX

HDX-MS experiments can be implemented in various ways depending upon the type of information required. Gross *et al*. have developed a LC-MS technique that allows monitoring of protein-ligand interactions termed PLIMSTEX *i.e.* *p*rotein-*l*igand *i*nteractions by *M*S, *t*itration and *h*ydrogen/*d*euterium *e*xchange.[256,257] PLIMSTEX experiments enable the measurement of the binding affinities of protein-ligand complexes. The target protein is equilibrated with an increasing concentration of ligand to create complexes at various protein-ligand ratios. Next, each sample is diluted into deuterated buffer and HDX is allowed to proceed for a set period of time. Samples are cleaned up on-line by reverse-phase chromatography and the amount of deuterium uptake is determined by mass spectrometry.[256,258,259] It is predicted that the difference in mass due to deuterium uptake will be decreasing with an increasing ligand concentration as a result of an increased protection of the backbone amine upon ligand binding. Protein-ligand ratios are plotted against the deuterium uptake where the shape of the curves is directed by binding affinity and stoichiometry.[260] More recently, PLIMSTEX has been adapted for determination of self-association equilibrium constants for proteins. This methodology has been termed SIMSTEX (*s*elf-association *i*nteractions using *M*S, *s*elf-*t*itration and HD *e*xchange) and has been applied to study insulin analogues and is likely to be a valuable tool to study self-assembly of other large proteins.[261]

Fitzgerald *et al.* have also developed an alternative method that uses MALDI-MS and is referred to as SUPREX (*s*tability of *u*npurified *p*roteins from *r*ates of HD *e*xchange) and allows for determination of free energy values (ΔG_u) associated with protein unfolding mechanisms.[262-265] SUPREX uses denaturing agents (such as guanidinium chloride or urea) to measure protein thermodynamic stabilities and as the name suggests it can be applied to protein mixtures. Proteins or protein-ligand complexes are diluted into a series of deuterated HDX buffers containing increasing concentrations of chemical denaturant. After a set incubation time, the mass of each denatured protein sample is determined with MALDI-MS. The number of exchanged hydrogen atoms is plotted versus denaturant concentration resulting in sigmoidal curves reflecting the transition from folded to unfolded protein as more backbone amides are exposed with increasing denaturant concentration. Higher denaturant concentrations are be required to induce unfolding of protein-ligand complex due to its increased stability.[247] Application of the SUPREX protocol can be also expanded to large multimeric protein systems by incorporation of protease digestion step.[266]

As all methodologies, various HDX techniques display advantages and downsides. Continuous HDX experiments might be time consuming and not inherently high-throughput; however, they yield wide range of information on different solution-phase conformations. Recent developments of automated systems have greatly increased the throughput rate. HDX experiments can provide a broad picture of protein dynamics and conformational changes induced by ligand binding, mutation or aggregation. SUPREX experiments provide very little structural information about protein folding and ligand binding in contrast to the continuous HDX; however, they allow for the use of unpurified proteins as long as the other components of the sample mixture do not suppress the signal of protein of interest. This advantage eliminates the need for time-consuming high purity sample preparation and makes SUPPEX more amenable towards high-throughput analysis. Although PLIMSTEX produces much of the same thermodynamic data on protein-ligand binding, it does not involve the use of denaturant which can alter or even prevent ligand binding. In their recent review, Fitzgerald and West, offer more details on those methodologies as well as comparison of the advantages and disadvantages of these approaches.[267]

1.3.4 Chemical cross-linking and mass spectrometry

Chemical cross-linking in combination with mass spectrometry has become a useful tool in the study of protein structures and non-covalent protein complexes. It involves a covalent reaction between complementary functional groups within the protein or between protein and ligand molecules under investigation. The covalently linked proteins and their binding partners are digested and analyzed with mass spectrometry. The location of newly formed cross-linked peptides in the primary amino acid sequence identifies the location of the respective side chains and is useful in structure determination of protein geometry. Top-down and bottom-up approaches and a wide range of available cross-linkers targeted towards certain functional groups, help to map those interactions.[268]

Cross-linking and mass spectrometry have been successfully used to study many non-covalent protein systems such as human serum albumin and its corresponding antibody,[269] calmodulin-melittin,[270] 17*β*-estradiol and estrogen receptor-α,[271] or various peptide ligands with its G protein-coupled receptors[272], or peroxisome proliferator-activated receptor alpha (PPAR-α) and small molecule ligands.[273] This hybrid technique has also been applied to study large protein assemblies and protein-protein interaction networks to understand their physical organisation.[274] Architecture of a signalling complex A-kinase anchoring protein 79[275], RNA polymerase II[276], GroEL-GroES chaperonin complex[277], conformational changes of sugarcane chaperone Hsp70[278], retinal guanylylcyclase-GCAP-2[279] interaction or dynamics of ribosomal protein S1[280] have been successfully probed with cross-linking mass spectrometry. In combination with other techniques such as electron microscopy (EM) or IM-MS, cross-linking data can be integrated to provide insights into interactions between subunits and overall topology to generate three-dimensional models of protein complexes.[281,282]

Moreover, cross-linking has been even used to covalently link binding partners directly in the cell by incorporating the reactive groups into the protein using cell's own biosynthetic mechanisms.[283] A number of reviews have been published either on the cross-linking reagents and protocols[284-286] or protein-protein interaction studies using cross-linking mass spectrometry approach[287-289]. A great advantage of this method is the ability to provide spatial information on proteins and protein complexes that are too large or too flexible for x-ray crystallography or NMR studies.[290] The sections below will briefly describe two different approaches to analysis of cross-linked proteins and protein-ligand complexes as well as types and classification of chemical cross-linking reagents available.

1.3.4.1 Bottom-up and top-down approaches

To perform cross-linking experiments two possible approaches exist: bottom-up and top-down (Figure 1.13). When conducting cross-linking experiments one must know the amino acid sequence of the protein system under investigation as control samples (*i.e.* no cross-linker added) need to be used. In the bottom-up approach, after cross-linking of functional groups, the covalently bound complex is purified by gel electrophoresis or size-exclusion chromatography and enzymatically digested either in-gel or in solution and the resulting proteolytic peptide mixtures are analyzed by MALDI or ESI-MS. Comparison of the mass spectra from cross-linked and non-linked peptide mixtures reveals which individual peptides are cross-linked in the complex providing information on relative spatial orientation of the binding groups. This approach has been successfully applied to study protein interfaces and has been valuable to low-resolution structure determination.[268,288,291, 292]

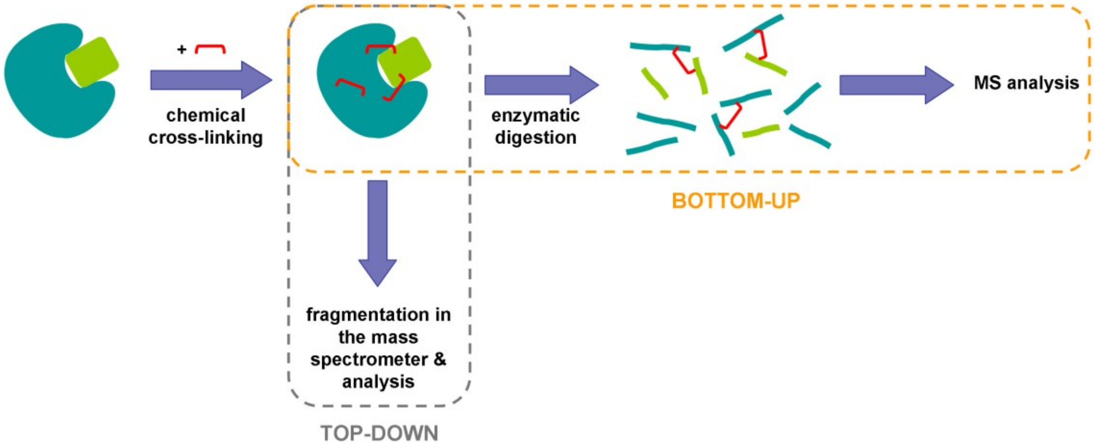

Figure 1.13 Top-down and bottom-up cross-linking approaches. Functional groups within proteins or between proteins and their binding partners are covalently linked *via* cross-linking reagents to provide information on spatial proximity of these groups, hence insights into the structure. Intact proteins are fragmented either *via* enzymatic digestion (bottom-up) or inside of a mass spectrometer (top-down) prior to identification and analysis of resultant peptides.

The top-down approach exploits the capability of a multistage mass spectrometer to fragment intact cross-linked proteins and their complexes.[293] High resolution ESI Fourier transform ion cyclotron resonance mass spectrometry (ESI-FTICR-MS) is the most commonly used tool for this approach. The cross-linking mixture is introduced into the FT-ICR mass spectrometer, isolated in the ICR cell and subsequently fragmented with one of the various fragmentation techniques such as electron caption dissociation (ECD), infrared multi-photon dissociation (IRMPD), or sustained off-resonance irradiation collision-introduced dissociation (SORI-CID). The superior mass accuracy of FT-ICR-MS allows determination of the number of incorporated cross-linkers in the intact protein and the number of possible modifications caused by cross-linking reagents.

This approach has been applied to study for example intramolecular cross-linked products of bovine rhodopsin[294] or ubiquitin[295]. The major advantage of top-down over bottom-up approach is the freedom from a chromatographic separation of the cross-linking mixture prior to mass spectrometric analysis as this is achieved in the mass spectrometer itself. However, FT-ICR-MS becomes less sensitive and lower resolution as the mass of the complex increases; hence, it is challenging to study large protein assemblies using this MS method.

1.3.4.2 Classification of cross-linking reagents

Covalent cross-links can be formed either inter-moleculary between different molecules or intra-moleculary within parts of the same molecule. The cross-linking reagents can be classified either by their reactivities or their functional design. Sinz, in her review, offers an excellent summary on the classification of the many cross-linkers described in the literature. [268,296]

Based on the functional groups, three main types of cross-linkers can be distinguished: amine-reactive, sulfhydryl reactive and photoreactive cross-linkers. *N*-hydroxysuccinimide (NHS) esters, one of the amine-reactive cross-linkers, are most widely used reactive acylating agents. NHS esters react with nucleophiles to produce the NHS group and to subsequently form a stable amide and imide bonds with primary and secondary amines (ex. free *N*-terminus and ε-amino groups in lysine side chains). NHS esters can react with sulfhydryl groups of cysteine, hydroxyl groups of serine or threonine, and imidazole nitrogens of the histadine; however, their reactivity and stability can be influenced by the pH conditions and the solvent system.[268] The other two types of amine-reactive cross-linkers are imidoesters,[297] considered one of the most specific acylating groups, and carbodiimides[298] which form an amide bond between spatially close groups; however, they were found to have only a modest cross-linking efficiency compared to NHS esters.[299]

Sulfhydryl-reactive cross-linkers such as maleimides, are targeted at the SH groups of cysteine residues; unfortunately due to their reductive capabilities, they might have a distorting effect on the protein confirmation. Another large group of cross-linkers are photo-reactive cross-linkers, which react with the target proteins upon irradiation with UV light. Most of these reagents are based on nitrene or carbene chemistry with photolabile presursors such as aryl azides, diazirines and benzophenones. Often those reagents also possess an amide- or sulfhydryl-reactive group.[268] When choosing an ideal photoreagent one should consider its reactivity, stability in the dark and capability to react at the wavelength that does not cause damage to the biological sample.[268]

Cross-linking reagents can be further classified by their functional design into sub classes including homobifunctional, heterobifunctional, trifunctional and zero-length cross-linkers. Homobifunctional cross-linking reagents contain two identical reactive sites and react with the same complementary protein functionality, their proximity being determined by a carbon-chain spacer of a defined length in the cross linker. Similarly, as the name suggests, heterobifunctional reagents incorporate two different reactive groups which react with different functional groups on the proteins and trifunctional cross-linkers acting as heterobifunctional reagents with additional functional group.[300] The smallest available chemical cross-linking reagents called zero-length cross-linkers, mediate a cross-link between two proteins by formation of a bond without an intervening linker; carbodiimides are the most widely used linkers of this type. Despite a large number of cross-linking reagents available there is still need for an improvement and gaining better understanding of their reactivates.

1.4 Selected Complementary Biophysical Techniques to Study Protein Structure

A vast array of biophysical techniques for study of protein structure and interactions is available.[26,28,37,301,302] High resolution techniques like x-ray crystallography and nuclear magnetic resonance (NMR) spectroscopy can provide structural information at the atomic level. Lower resolution techniques such as analytical ultracentrifugation (AUC), electron microscopy (EM), static light scattering (SLS), surface plasmon resonance (SPR), size-exclusion chromatography (SEC), circular dichroism (CD), infrared spectroscopy (IR), ultraviolet (UV) spectroscopy, Raman spectroscopy and others are able to present information on the global structure and properties of proteins and trace any conformational changes. In conjunction with MS, they serve as complementary tools for solving the puzzle of protein structure. Some of these techniques, which have been employed to study biological systems discussed in this thesis, are briefly overviewed below.

1.4.1 Solution-phase techniques

1.4.1.1 NMR spectroscopy

Nuclear magnetic resonance (NMR) spectroscopy is a non-destructive method exploring protein structure and dynamics in their ‘natural’ habitat – the solution-phase.[303-306] Upon exposure to strong magnetic fields and RF signals certain kinds of atomic nuclei (^{1}H, ^{13}C, ^{15}N) absorb the RF radiation. The resonance of each nucleus, represented as a chemical shift, is very sensitive to the local molecular environment and can provide information about covalent and non-covalent protein structure. Peaks observed in an NMR spectrum can split into finer structures (doubles or triplets) as a result of magnetic coupling between adjacent nuclei (J coupling). Furthermore, nuclei can also transfer energy to each other though bonds and though space, a phenomenon known as the nuclear Overhauser effect (NOE), that is used to identify hydrogen atoms in proximity to each other either due to primary sequence or the tertiary protein fold.[307]

Due to a large number of atoms present in a protein molecule, thousands of signals are overlapping and multidimensional experiments must be performed to allow correlating frequencies of distinct nuclei. A series of 2D and 3D NMR experiments are carried out to collect sufficient amount of data so every NMR resonance can be assigned to every NMR detectable atom in a protein. Common homonuclear NMR experiments include: total correlation spectroscopy (TOCSY) allowing identification of individual amino acids by their chemical shifts[308], nuclear Overhauser enhancement spectroscopy (NOESY) detecting interactions between protons within 5 Å of each other[309]; or heteronuclear NMR experiments on isotope-labelled proteins: heteronuclear single quantum correlation (HSQC) correlating nuclei other than ^{1}H; or triple resonance experiments such as HNCO, HN(CA)CO, HNCA, HN(CO)CA, or NHCABA. Detailed description of various NMR experiments can be found elsewhere.[303-305,310] Data are used to derive distances, angles and torsions between atoms and to construct three dimensional models. NMR data can be further used to gain insights into protein interactions and conformational dynamics on a picosecond to second time scale; however, the spectra reveal only the average state of a protein complex.[305,311-313] As NMR spectroscopy is nucleus specific, also HDX experiments can be performed monitoring amide proton exchange and reflecting on the solvent accessible protein regions.[314-317]

As any other technique, NMR spectroscopy presents a number of drawbacks. Firstly, a large quantity of protein sample is required (typically 300-600 µL, concentration of ~1 mM) and the time needed for data acquisition might vary from hours to several days. Additionally, this technique is size limited to small proteins or protein domains and tends not to exceed 100 kDa for atomic resolution[318]; nevertheless, improvements in the method development allowed studying protein complexes such as chaperone GroES-GroEL.[319]

1.4.1.2 Analytical ultracentrifugation (AUC)

Analytical ultracentrifugation (AUC) is a non-destructive low resolution technique measuring the rate at which macromolecules sediment in response to centrifugal force, allowing their hydrodynamic and thermodynamic characterisation in the solution-phase.[320] There are two types of AUC experiments: sedimentation velocity (SV-AUC) based on hydrodynamic theory and used to define the size, shape and interaction of macromolecules; and sedimentation equilibrium (SE-AUC), a thermodynamic method used to determine molecular mass, assembly stoichiometry or association constants.[321-323] AUC methods are used to probe shape and size of large proteins and their complexes within 100 kDa to 10 GDa range, and find application in detection of aggregates or probing of conformational changes.[324-328] Here, the basic principles of SV-AUC will be presented briefly.

In a SV-AUC experiment, the sample is spun at a high velocity (40-60 K rpm) in an analytical centrifuge. The centrifugal force depletes molecules from the meniscus near the centre of the rotor forming a boundary which migrates towards the outside of the rotor. An optical system (absorbance, interference and fluorescence) monitors the concentration distribution across the cell in real time. Proteins can be characterised in their native state under biologically relevant solution conditions at protein concentrations typically of 0.1 to 1 mg mL^{-1}. Additionally, a wide range of pH and ionic strength conditions can be used at temperatures ranging from 4 to 40℃.

Through the SV-AUC experiments sedimentation coefficient (s, expressed in svedberg (1 S = 10^{-13} s)) is determined, which is defined as ratio of a particle's sedimentation velocity (v) to the acceleration (a) that is applied to it:

$$s = \frac{v}{a} \qquad \textit{(Equation 1.10)}$$

The sedimentation coefficient is dependent on the molecular weight and conformation of the protein. This relationship can be expressed by:

$$s = \frac{M_b}{f} \qquad \textit{(Equation 1.11)}$$

where M_b is the buoyant molar mass and f is the frictional coefficient. Derivation of Equation 1.11 can be found elsewhere.[321] Sedimentation coefficients quoted in the literature usually relate to sedimentation in water at 20℃ ($s_{20,w}$). As can be seen from Equation 1.11, s is directly proportional to mass; hence, larger protein species have higher sedimentation coefficient. The sedimentation coefficient is however, inversely proportional to *f*; therefore unfolded proteins or ones with highly elongated conformations will experience more hydrodynamic friction and have smaller sedimentation coefficients than folded, globular proteins of the same molecular weigh

1.4.2 Solid-phase techniques

1.4.2.1 X-ray crystallography

The number of macromolecular structures deposited into the Protein Data Bank (PDB) now exceeds 100 000 with over 88% of them determined using crystallographic methods.[329] X-ray crystallography is a powerful atomic resolution technique considered as the gold standard for protein structure determination. Protein samples are purified and crystallised, then subjected to intense beam of x-ray radiation usually generated by a synchrotron. Electrons in the molecule scatter x-rays to provide a characteristic diffraction pattern. The crystal is gradually rotated to collect multiple data sets with diffraction patterns recorded at every crystal orientation. Due to structural motifs in the unit cell repeating throughout the crystal, the scattering in amplified in selected directions. These patterns are then analysed to provide the electron density map which is used to build a model of protein structure, whose sequence has been determined by other means.[330,331]

X-ray crystallography provides very detailed structural data of proteins along with any other molecules (ligands, ions or inhibitors) that have been incorporated into the crystal. The single electron of the hydrogen atom is always involved in the formation of bonds; therefore, these atoms lack the electronic core and are the weakest x-ray scatterers. For those reasons, hydrogen atoms are often not present in electron density maps and their localisation must be calculated based on the positions of the heavier atoms. Furthermore, as the diffraction pattern is dependent on the formation of highly ordered crystals, this method lacks dynamic information and is challenging with regards to structure determination of flexible and/or disordered protein regions. Although, there is no analyte size limit and large protein assemblies such as viruses can the analysed,[332,333] the crystallisation process can be very demanding if achievable at all in some cases.[334]

1.4.2.2 Electron microscopy

Electron microscopy (EM), a method for structure determination of large macromolecular complexes, uses an electron beam to create molecular images and is particularly useful for studies of difficult to crystallise proteins. The type of EM typically used in life sciences is transmission electron microscopy (TEM).[335] Samples deposited on an EM grid are stained (to enhance contrast by absorbing electrons otherwise projected onto the image), and then exposed to high electron beam. The electron beam that has been partly transmitted through the sample carries structural information with attainable resolution of ~20 Å. Preservation of native-like structure has been a challenge in terms of TEM use for studies of biological macromolecules.

Visualisation of protein molecules became possible with the development of negative stain techniques which aid contrasting and prevent collapse of macromolecules by replacing the surrounding water with dried solution of heavy metal salt.[336] Nevertheless, it can still lead to denaturation of protein structure. Limitations of the technique were solved by introduction of cryo-electron microscopy.[337] In cryo-EM, samples are rapidly frozen in liquid nitrogen-cooled ethane and embedded in a layer of amorphous ice preserving near-native structure in the hydrated state.[338] Multiple copies of cryo-EM images are acquired at low temperatures by low intensity electron exposures, where even resolution of 3.5 Å can be achieved.[339] Furthermore, freeze-trapping allows capturing proteins in different conformational states providing insights into structural dynamics.[340,341] Despite being a time consuming method, EM and cryo-EM are useful options for structure determination of large biomolecules.

1.4.3 Computational methods

Protein behaviour can be studied in solution or *in vacuo* by means on molecular dynamic (MD) simulations. MD enables to follow dynamic evolution of proteins in the gas-phase and the output files are used for determination of theoretical CCS. Information provided by IM-MS can be enhanced with computational approaches and *vice versa*. Experimentally determined CCS can help to discriminate between different predicted models where several structures with similar energy minima are possible. A number of algorithms have been developed using different theoretical assumptions[342-346] however, three of them are commonly used: hard sphere projection approximation (PA)[347], trajectory method (TJM)[348] and exact hard sphere scattering (EHSS)[349,350].

Based on a set of coordinates derived *via* x-ray crystallography, NMR spectroscopy or MD simulations, mobility and buffer gas specific CCS can be calculated using MOBCAL software.[342,348,349,351] The PA treats each molecular atom as a hard sphere, and similarly the interactions between buffer gas and ions are perceived as hard sphere collisions. The resulting CCS is based on averaging the geometric projection areas over all possible orientations of the ion. PA was found to underestimate CCS for large molecules by up to 20 %.[149] The EHSS method is an improved version of PA, which accounts for multiple collisions and scattering but still does not consider the effects of long range potentials between the buffer gas and the ion. For systems with a molecular weight greater than 1.5 kDa the most reliable results can be estimated by a trajectory method calculation.[138,352] The TJM model considers the analyte ion as a collection of molecules, and accounts for possible multiple collisions and the long range interactions which occur between drift gas atoms and the ion. This comprehensive evaluation of the momentum transfer integral that is achieved *via* the TJM method, is computationally very expensive, in addition the code has been found to not scale particularly well for very large extended systems. Recently Bleildholder *et al.* have developed the projected superposition approximation (PSA), a reworked version of the PA which accounts for the dramatic underestimation this rapid method provides.[353-356] By rescaling the CCS of input co-ordinates based on extensive empirical training of this new code, a more computationally amenable answer to translate CCS from crystal structure or NMR co-ordinates of large macromolecular systems is available.

1.5 Conclusions

Mass spectrometry has come of age as a recognised, predictive tool in the analysis of protein structure and protein interactions with certain benefits for structural biology and drug discovery. The molecular weight of proteins can be determined even for very large systems on MDa scale. Intact proteins and their complexes can be analysed and related to data obtained *via* other biophysical techniques and create a fuller picture of their architecture, dynamics and interactions. Recent developments in the use of IM-MS, dissociation techniques, HDX-MS and chemical cross linking mean that mass spectrometry is evolving into a powerful tool for protein structural characterisation.

The work presented in this thesis employs mass spectrometry based methods to probe higher order structure of several large proteins and multimeric protein complexes representing various functional protein classes. Chapter 3 explores flexibility and gas-phase dynamics of therapeutic antibodies; Chapters 4 and 5 set out to probe thermal stability of protein complexes with implication to therapeutic antibodies; whereas Chapter 6 aims to identity and map subtle conformational changes of an enzyme induced by binding of an allosteric inhibitor.

1.6 References

(1) Petsko, G. A.; Ringe, D. *Protein Structure and Function*; New Science Press Ltd: London, UK, 2004.
(2) Buxbaum, E. *Fundamentals of Protein Structure and Function*; Springer Science + Business Media, LLC: New York, USA, 2007.
(3) Jurneczko, E.; Cruickshank, F.; Porrini, M.; Clarke, D. J.; Campuzano, I. D. G.; Morris, M.; Nikolova, P. V.; Barran, P. E. *Angewandte Chemie-International Edition* **2013**, *52*, 4370.
(4) Peters, S. J.; Smales, C. M.; Henry, A. J.; Stephens, P. E.; West, S.; Humphreys, D. P. *Journal of Biological Chemistry* **2012**, *287*.
(5) Ryslava, H.; Doubnerova, V.; Kavan, D.; Vanek, O. *Journal of proteomics* **2013**, *92*, 80.
(6) Taylor, K.; Barran, P. E.; Dorin, J. R. *Biopolymers* **2008**, *90*, 1.
(7) Pedreno, S.; Pisco, J. P.; Larrouy-Maumus, G.; Kelly, G.; de Carvalho, L. P. S. *Biochemistry* **2012**, *51*, 8027.
(8) Sacchi, S.; Caldinelli, L.; Cappelletti, P.; Pollegioni, L.; Molla, G. *Amino Acids* **2012**, *43*, 1833.
(9) Allen, J. A.; Roth, B. L. In *Annual Review of Pharmacology and Toxicology, Vol 51, 2011*; Cho, A. K., Ed. 2011; Vol. 51, p 117.
(10) Wenthur, C. J.; Gentry, P. R.; Mathews, T. P.; Lindsley, C. W. *Annual Review of Pharmacology and Toxicology, Vol 54* **2014**, *54*, 165.
(11) Robertson, J. G. *Biochemistry* **2005**, *44*, 5561.
(12) Yap, T. A.; Molife, L. R.; de Bono, J. S. *Cancer Drug Discovery and Development* **2008**, 135.
(13) Kaczorowski, G. J.; McManus, O. B.; Priest, B. T.; Garcia, M. L. *Journal of General Physiology* **2008**, *131*, 399.
(14) Clare, J. J. *Discovery medicine* **2010**, *9*, 253.
(15) Sun, H.; Li, M. *Acta Pharmacologica Sinica* **2013**, *34*, 199.
(16) Breen, E. C.; Walsh, J. J. *Current Medicinal Chemistry* **2010**, *17*, 609.
(17) Stehn, J. R.; Haass, N. K.; Bonello, T.; Desouza, M.; Kottyan, G.; Treutlein, H.; Zeng, J.; Nascimento, P. R. B. B.; Sequeira, V. B.; Butler, T. L.; Allanson, M.; Fath, T.; Hill, T. A.; McCluskey, A.; Schevzov, G.; Palmer, S. J.; Hardeman, E. C.; Winlaw, D.; Reeve, V. E.; Dixon, I.; Weninger, W.; Cripe, T. P.; Gunning, P. W. *Cancer Research* **2013**, *73*, 5169.
(18) Hoeller, C.; Freissmuth, M.; Nanoff, C. *CMLS Cellular and Molecular Life Sciences* **1999**, *55*, 257.

(19) Overington, J. P.; Al-Lazikani, B.; Hopkins, A. L. *Nature Reviews Drug Discovery* **2006**, *5*, 993.

(20) Chapter, M. C.; White, C. M.; DeRidder, A.; Chadwick, W.; Martin, B.; Maudsley, S. *Pharmacology & Therapeutics* **2010**, *125*, 39.

(21) Walsh, G. *Nature Biotechnology* **2010**, *28*, 917.

(22) Lawrence, S. *Nature Biotechnology* **2007**, *25*, 380.

(23) Pauling, L.; Corey, R. B. *Proceedings of the National Academy of Sciences of the United States of America* **1951**, *37*, 235.

(24) Pauling, L.; Corey, R. B. *Proceedings of the National Academy of Sciences of the United States of America* **1951**, *37*, 729.

(25) Bernstein, F. C.; Koetzle, T. F.; Williams, G. J. B.; Meyer, E. F.; Brice, M. D.; Rodgers, J. R.; Kennard, O.; Shimanouchi, T.; Tasumi, M. *Journal of Molecular Biology* **1977**, *112*, 535.

(26) Vuignier, K.; Schappler, J.; Veuthey, J. L.; Carrupt, P. A.; Martel, S. *Analytical and Bioanalytical Chemistry* **2010**, *398*, 53.

(27) Renaud, J. P.; Delsuc, M. A. *Current Opinion in Pharmacology* **2009**, *9*, 622.

(28) McLean, J. A. *Journal of the American Society for Mass Spectrometry* **2009**, *20*, 1775.

(29) Hassell, A. M.; An, G.; Bledsoe, R. K.; Bynum, J. M.; Carter, H. L.; Deng, S. J. J.; Gampe, R. T.; Grisard, T. E.; Madauss, K. P.; Nolte, R. T.; Rocque, W. J.; Wang, L. P.; Weaver, K. L.; Williams, S. P.; Wisely, G. B.; Xu, R.; Shewchuk, L. M. *Acta Crystallographica Section D-Biological Crystallography* **2007**, *63*, 72.

(30) Maple, H. J.; Garlish, R. A.; Rigau-Roca, L.; Porter, J.; Whitcombe, I.; Prosser, C. E.; Kennedy, J.; Henry, A. J.; Taylor, R. J.; Crump, M. P.; Crosby, J. *Journal of Medicinal Chemistry* **2012**, *55*, 837.

(31) Pacholarz, K. J.; Garlish, R. A.; Taylor, R. J.; Barran, P. E. *Chemical Society reviews* **2012**, *41*, 4335.

(32) Niu, S.; Rabuck, J. N.; Ruotolo, B. T. *Current Opinion in Chemical Biology* **2013**, *17*, 809.

(33) Thompson, N. J.; Rosati, S.; Rose, R. J.; Heck, A. J. R. *Chemical Communications* **2013**, *49*, 538.

(34) Zhang, Z.; Pan, H.; Chen, X. *Mass Spectrometry Reviews* **2009**, *28*, 147.

(35) Beck, A.; Sanglier-Cianferani, S.; Van Dorsselaer, A. *Analytical Chemistry* **2012**, *84*, 4637.

(36) Beck, A.; Wagner-Rousset, E.; Ayoub, D.; Van Dorsselaer, A.; Sanglier-Cianferani, S. *Analytical Chemistry* **2013**, *85*, 715.

(37) Berkowitz, S. A.; Engen, J. R.; Mazzeo, J. R.; Jones, G. B. *Nature Reviews Drug Discovery* **2012**, *11*, 527.

(38) Ezan, E.; Dubois, M.; Becher, F. *Analyst* **2009**, *134*, 825.

(39) Zhou, M.; Robinson, C. V. *Trends Biochem Sci* **2010**, *35*, 522.

(40) Siuzdak, G. *Proceedings of the National Academy of Sciences of the United States of America* **1994**, *91*, 11290.

(41) Akashi, S. *Medicinal Research Reviews* **2006**, *26*, 339.

(42) Papac, D. I.; Shahrokh, Z. *Pharmaceutical Research* **2001**, *18*, 131.

(43) Breuker, K. *International Journal of Mass Spectrometry* **2004**, *239*, 33.

(44) Konermann, L.; Vahidi, S.; Sowole, M. A. *Analytical Chemistry* **2014**, *86*, 213.

(45) Webster, J.; Oxley, D. *Chemical Genomics and Proteomics: Reviews and Protocols* **2012**, *800*, 227.

(46) Bensimon, A.; Heck, A. J. R.; Aebersold, R. *Annual Review of Biochemistry, Vol 81* **2012**, *81*, 379.

(47) Bantscheff, M.; Lemeer, S.; Savitski, M. M.; Kuster, B. *Analytical and Bioanalytical Chemistry* **2012**, *404*, 939.

(48) Zhang, S.; VanPelt, C. K.; Wilson, D. B. *Anal. Chem.* **2003**, *75*, 3010.

(49) Esswein, S. T.; Florance, H. V.; Baillie, L.; Lippens, J.; Barran, P. E. *J Chromatogr A* **2010**, *1217*, 6709.

(50) Berezovskaya, Y.; Armstrong, C. T.; Boyle, A. L.; Porrini, M.; Woolfson, D. N.; Barran, P. E. *Chemical Communications* **2011**, *47*, 412.

(51) Moller, C.; Sprenger, R. R.; Sturup, S.; Hojrup, P. *Analytical and Bioanalytical Chemistry* **2011**, *401*, 1619.

(52) Annis, D. A.; Nazef, N.; Chuang, C. C.; Scott, M. P.; Nash, H. M. *Journal of the American Chemical Society* **2004**, *126*, 15495.

(53) Keith-Roach, M. J. *Analytica Chimica Acta* **2010**, *678*, 140.

(54) Sobott, F.; Benesch, J. L. P.; Vierling, E.; Robinson, C. V. *Journal of Biological Chemistry* **2002**, *277*, 38921.

(55) Pacholarz, K. J.; Porrini, M.; Garlish, R. A.; Burnley, R. J.; Taylor, R. J.; Henry, A. J.; Barran, P. E. *Angewandte Chemie (International ed. in English)* **2014**, *53*, 7765.

(56) Schmidt, C.; Robinson, C. V. *Febs Journal* **2014**, *281*, 1950.

(57) Konermann, L.; Tong, X.; Pan, Y. *Journal of Mass Spectrometry* **2008**, *43*, 1021.

(58) Pan, Y.; Piyadasa, H.; O'Neil, J. D.; Konermann, L. *Journal of Molecular Biology* **2012**, *416*, 400.

(59) Bastug, T.; Kuyucak, S. *Biophysical Journal* **2003**, *84*, 2871.

(60) Barran, P. E.; Polfer, N. C.; Campopiano, D. J.; Clarke, D. J.; Langridge-Smith, P. R. R.; Langley, R. J.; Govan, J. R. W.; Maxwell, A.; Dorin, J. R.; Millar, R. P.; Bowers, M. T. *International Journal of Mass Spectrometry* **2005**, *240*, 273.

(61) van den Heuvel, R. H. H.; van Duijn, E.; Mazon, H.; Synowsky, S. A.; Lorenzen, K.; Versluis, C.; Brouns, S. J. J.; Langridge, D.; van der Oost, J.; Hoyes, J.; Heck, A. J. R. *Analytical Chemistry* **2006**, *78*, 7473.

(62) Sobott, F.; Hernandez, H.; McCammon, M. G.; Tito, M. A.; Robinson, C. V. *Analytical Chemistry* **2002**, *74*, 1402.

(63) Benjamin, D. R.; Robinson, C. V.; Hendrick, J. P.; Hartl, F. U.; Dobson, C. M. *Proceedings of the National Academy of Sciences of the United States of America* **1998**, *95*, 7391.

(64) Lorenzen, K.; Vannini, A.; Crarner, P.; Heck, A. J. R. *Structure* **2007**, *15*, 1237.

(65) Uetrecht, C.; Versluis, C.; Watts, N. R.; Wingfield, P. T.; Steven, A. C.; Heck, A. J. R. *Angewandte Chemie-International Edition* **2008**, *47*, 6247.

(66) Shoemaker, G. K.; van Duijn, E.; Crawford, S. E.; Uetrecht, C.; Baclayon, M.; Roos, W. H.; Wuite, G. J. L.; Estes, M. K.; Prasad, B. V. V.; Heck, A. J. R. *Molecular & Cellular Proteomics* **2010**, *9*, 1742.

(67) Uetrecht, C.; Watts, N. R.; Stahl, S. J.; Wingfield, P. T.; Steven, A. C.; Heck, A. J. R. *Phys Chem Chem Phys* **2010**, *12*, 13368.

(68) Snijder, J.; Rose, R. J.; Veesler, D.; Johnson, J. E.; Heck, A. J. R. *Angewandte Chemie-International Edition* **2013**, *52*, 4020.

(69) Fuerstenau, S. D.; Benner, W. H.; Thomas, J. J.; Brugidou, C.; Bothner, B.; Siuzdak, G. *Angewandte Chemie-International Edition* **2001**, *40*, 542.

(70) Thomson, J. J. *Science* **1913**, *37*, 360.

(71) Fenn, J. B.; Mann, M.; Meng, C. K.; Wong, S. F.; Whitehouse, C. M. *Science* **1989**, *246*, 64.

(72) Dole, M.; Mack, L. L.; Hines, R. L. *Journal of Chemical Physics* **1968**, *49*, 2240.

(73) Wilm, M. S.; Mann, M. *International Journal of Mass Spectrometry* **1994**, *136*, 167.

(74) Karas, M.; Bahr, U.; Dulcks, T. *Fresenius Journal of Analytical Chemistry* **2000**, *366*, 669.

(75) Royal Society of Chemistry website; http://www.rsc.org, 2014.

(76) Nguyen, S.; Fenn, J. B. *Proceedings of the National Academy of Sciences of the United States of America* **2007**, *104*, 1111.

(77) Iribarne, J. V.; Thomson, B. A. *Journal of Chemical Physics* **1976**, *64*, 2287.

(78) Ahadi, E.; Konermann, L. *Journal of the American Chemical Society* **2011**, *133*, 9354.

(79) Daub, C. D.; Cann, N. M. *Analytical Chemistry* **2011**, *83*, 8372.

(80) Peschke, M.; Verkerk, U. H.; Kebarle, P. *Journal of the American Society for Mass Spectrometry* **2004**, *15*, 1424.

(81) Lavarone, A. T.; Williams, E. R. *Journal of the American Chemical Society* **2003**, *125*, 2319.

(82) Iavarone, A. T.; Williams, E. R. *Journal of the American Chemical Society* **2003**, *125*, 2319.

(83) Hogan, C. J., Jr.; Carroll, J. A.; Rohrs, H. W.; Biswas, P.; Gross, M. L. *Analytical Chemistry* **2009**, *81*, 369.

(84) Heck, A. J. R.; van den Heuvel, R. H. H. *Mass Spectrometry Reviews* **2004**, *23*, 368.

(85) de la Mora, J. F. *Analytica Chimica Acta* **2000**, *406*, 93.

(86) Kaltashov, I. A.; Mohimen, A. *Analytical Chemistry* **2005**, *77*, 5370.

(87) Konermann, L.; Ahadi, E.; Rodriguez, A. D.; Vahidi, S. *Analytical Chemistry* **2013**, *85*, 2.

(88) Ahadi, E.; Konermann, L. *Journal of Physical Chemistry B* **2012**, *116*, 104.

(89) Konermann, L.; Rodriguez, A. D.; Liu, J. *Analytical Chemistry* **2012**, *84*, 6798.

(90) Chung, J. K.; Consta, S. *Journal of Physical Chemistry B* **2012**, *116*, 5777.

(91) Patriksson, A.; Marklund, E.; van der Spoel, D. *Biochemistry* **2007**, *46*, 933.

(92) Steinberg, M. Z.; Breuker, K.; Elber, R.; Gerber, R. B. *Physical Chemistry Chemical Physics* **2007**, *9*, 4690.

(93) Wilm, M.; Mann, M. *Analytical Chemistry* **1996**, *68*, 1.

(94) Loo, J. A. *Mass Spectrom Rev* **1997**, *16*, 1.

(95) Ayed, A.; Krutchinsky, A. N.; Ens, W.; Standing, K. G.; Duckworth, H. W. *Rapid Communications in Mass Spectrometry* **1998**, *12*, 339.

(96) Fitzgerald, M. C.; Chernushevich, I.; Standing, K. G.; Whitman, C. P.; Kent, S. B. H. *Proceedings of the National Academy of Sciences of the United States of America* **1996**, *93*, 6851.

(97) Rostom, A. A.; Robinson, C. V. *Current Opinion in Structural Biology* **1999**, *9*, 135.

(98) Sanglier, S.; Atmanene, C.; Chevreux, G.; Van Dorsselaer, A. *Functional Proteomics: Methods and Protocols* **2008**, 217.

(99) Karas, M.; Bachmann, D.; Bahr, U.; Hillenkamp, F. *International Journal of Mass Spectrometry and Ion Processes* **1987**, *78*, 53.

(100) Karas, M.; Hillenkamp, F. *Analytical Chemistry* **1988**, *60*, 2299.

(101) Spengler, B.; Kirsch, D.; Kaufmann, R.; Karas, M.; Hillenkamp, F.; Giessmann, U. *Rapid Communications in Mass Spectrometry* **1990**, *4*, 301.

(102) Pimenova, T.; Pereira, C. P.; Schaer, D. J.; Zenobi, R. *Journal of Separation Science* **2009**, *32*, 1224.

(103) Chen, F.; Maedler, S.; Weidmann, S.; Zenobi, R. *Journal of Mass Spectrometry* **2012**, *47*, 560.

(104) Maedler, S.; Erba, E. B.; Zenobi, R. *Applications of Maldi-Tof Spectroscopy* **2013**, *331*, 1.

(105) Chen, F.; Gerber, S.; Heuser, K.; Korkhov, V. M.; Lizak, C.; Mireku, S.; Locher, K. P.; Zenobi, R. *Analytical Chemistry* **2013**, *85*, 3483.

(106) Paul, W.; Steinwedel, H. S. *Z. Naturforsch* **1957**, *69*, 448.

(107) Stephens, W. E. *Physical Review* **1946**, *69*, 691.

(108) Wiley, W. C.; McLaren, I. H. *Review of Scientific Instruments* **1955**, *26*, 1150.

(109) Karataev, V. I.; Shmikk, D. V.; Mamyrin, B. A. *Soviet Physics Technical Physics-Ussr* **1972**, *16*, 1177.

(110) Mamyrin, B. A.; Karataev, V. I.; Shmikk, D. V.; Zagulin, V. A. *Zhurnal Eksperimentalnoi I Teoreticheskoi Fiziki* **1973**, *64*, 82.

(111) Mamyrin, B. A. *International Journal of Mass Spectrometry* **2001**, *206*, 251.

(112) Suizdak, G. *Mass Spectrometry for Biotechnology*; Academic Press: New York, 1996.

(113) Hoffmann, E. d.; Strooband, V. *Mass Spectrometry: Principles and Applications*; Wiley-Interscience, 2007.

(114) Wiza, J. L. *Nuclear Instruments & Methods* **1979**, *162*, 587.

(115) Hamamatsu website; http://www.hamamatsu.com, 2014.

(116) Konijnenberg, A.; Butterer, A.; Sobott, F. *Biochimica Et Biophysica Acta-Proteins and Proteomics* **2013**, *1834*, 1239.

(117) Vonhelden, G.; Wyttenbach, T.; Bowers, M. T. *Science* **1995**, *267*, 1483.

(118) Clemmer, D. E.; Hudgins, R. R.; Jarrold, M. F. *Journal of the American Chemical Society* **1995**, *117*, 10141.

(119) Shelimov, K. B.; Clemmer, D. E.; Hudgins, R. R.; Jarrold, M. F. *Journal of the American Chemical Society* **1997**, *119*, 2240.

(120) Ruotolo, B. T.; Benesch, J. L. P.; Sandercock, A. M.; Hyung, S. J.; Robinson, C. V. *Nature Protocols* **2008**, *3*, 1139.

(121) Ruotolo, B. T.; Giles, K.; Campuzano, I.; Sandercock, A. M.; Bateman, R. H.; Robinson, C. V. *Science* **2005**, *310*, 1658.

(122) Ruotolo, B. T.; Hyung, S. J.; Robinson, P. M.; Giles, K.; Bateman, R. H.; Robinson, C. V. *Angewandte Chemie-International Edition* **2007**, *46*, 8001.

(123) Benesch, J. L. P. *Journal of the American Society for Mass Spectrometry* **2009**, *20*, 341.

(124) Erba, E. B.; Ruotolo, B. T.; Barsky, D.; Robinson, C. V. *Analytical Chemistry* **2010**, *82*, 9702.

(125) Wang, S. C.; Politis, A.; Di Bartolo, N.; Bavro, V. N.; Tucker, S. J.; Booth, P. J.; Barrera, N. P.; Robinson, C. V. *Journal of the American Chemical Society* **2010**, *132*, 15468.

(126) Lane, L. A.; Fernandez-Tornero, C.; Zhou, M.; Morgner, N.; Ptchelkine, D.; Steuerwald, U.; Politis, A.; Lindner, D.; Gvozdenovic, J.; Gavin, A.-C.; Mueller, C. W.; Robinson, C. V. *Structure* **2011**, *19*, 90.

(127) Lorenzen, K.; Olia, A. S.; Uetrecht, C.; Cingolani, G.; Heck, A. J. R. *Journal of Molecular Biology* **2008**, *379*, 385.

(128) van Duijn, E.; Barendregt, A.; Synowsky, S.; Versluis, C.; Heck, A. J. R. *Journal of the American Chemical Society* **2009**, *131*, 1452.

(129) Uetrecht, C.; Barbu, I. M.; Shoemaker, G. K.; van Duijn, E.; Heck, A. J. R. *Nature Chemistry* **2011**, *3*, 126.

(130) Knapman, T. W.; Morton, V. L.; Stonehouse, N. J.; Stockley, P. G.; Ashcroft, A. E. *Rapid Communications in Mass Spectrometry* **2010**, *24*, 3033.

(131) Woods, L. A.; Platt, G. W.; Hellewell, A. L.; Hewitt, E. W.; Homans, S. W.; Ashcroft, A. E.; Radford, S. E. *Nature Chemical Biology* **2011**, *7*, 730.

(132) Loo, J. A.; Berhane, B.; Kaddis, C. S.; Wooding, K. M.; Xie, Y. M.; Kaufman, S. L.; Chernushevich, I. V. *Journal of the American Society for Mass Spectrometry* **2005**, *16*, 998.

(133) Kaddis, C. S.; Lomeli, S. H.; Yin, S.; Berhane, B.; Apostol, M. I.; Kickhoefer, V. A.; Rome, L. H.; Loo, J. A. *Journal of the American Society for Mass Spectrometry* **2007**, *18*, 1206.

(134) Faull, P. A.; Florance, H. V.; Schmidt, C. Q.; Tomczyk, N.; Barlow, P. N.; Hupp, T. R.; Nikolova, P. V.; Barran, P. E. *International Journal of Mass Spectrometry* **2010**, *298*, 99.

(135) Pukala, T. L.; Ruotolo, B. T.; Zhou, M.; Politis, A.; Stefanescu, R.; Leary, J. A.; Robinson, C. V. *Structure* **2009**, *17*, 1235.

(136) Pringle, S. D.; Giles, K.; Wildgoose, J. L.; Williams, J. P.; Slade, S. E.; Thalassinos, K.; Bateman, R. H.; Bowers, M. T.; Scrivens, J. H. *International Journal of Mass Spectrometry* **2007**, *261*, 1.

(137) Giles, K.; Pringle, S. D.; Worthington, K. R.; Little, D.; Wildgoose, J. L.; Bateman, R. H. *Rapid Communications in Mass Spectrometry* **2004**, *18*, 2401.

(138) Uetrecht, C.; Rose, R. J.; van Duijn, E.; Lorenzen, K.; Heck, A. J. R. *Chemical Society Reviews* **2010**, *39*, 1633.

(139) Hopper, J. T. S.; Oldham, N. J. *Journal of the American Society for Mass Spectrometry* **2009**, *20*, 1851.

(140) Antson, A. A.; Dodson, E. J.; Dodson, G.; Greaves, R. B.; Chen, X. P.; Gollnick, P. *Nature* **1999**, *401*, 235.

(141) Fenn, L. S.; Kliman, M.; Mahsut, A.; Zhao, S. R.; McLean, J. A. *Analytical and Bioanalytical Chemistry* **2009**, *394*, 235.

(142) Kanu, A. B.; Dwivedi, P.; Tam, M.; Matz, L.; Hill, H. H. *Journal of Mass Spectrometry* **2008**, *43*, 1.

(143) McCullough, B. J.; Kalapothakis, J.; Eastwood, H.; Kemper, P.; MacMillan, D.; Taylor, K.; Dorin, J.; Barran, P. E. *Analytical Chemistry* **2008**, *80*, 6336.

(144) Wyttenbach, T.; Bowers, M. T. *Modern Mass Spectrometry* **2003**, *225*, 207.

(145) Bohrer, B. C.; Mererbloom, S. I.; Koeniger, S. L.; Hilderbrand, A. E.; Clemmer, D. E. *Annual Review of Analytical Chemistry* **2008**, *1*, 293.

(146) Shvartsburg, A. A.; Smith, R. D. *Analytical Chemistry* **2008**, *80*, 9689.

(147) Bush, M. F.; Hall, Z.; Giles, K.; Hoyes, J.; Robinson, C. V.; Ruotolo, B. T. *Analytical Chemistry* **2010**, *82*, 9557.

(148) Smith, D. P.; Knapman, T. W.; Campuzano, I.; Malham, R. W.; Berryman, J. T.; Radford, S. E.; Ashcroft, A. E. *European Journal of Mass Spectrometry* **2009**, *15*, 113.

(149) Jurneczko, E.; Barran, P. E. *Analyst* **2011**, *136*, 20.

(150) Scarff, C. A.; Patel, V. J.; Thalassinos, K.; Scrivens, J. H. *Journal of the American Society for Mass Spectrometry* **2009**, *20*, 625.

(151) Clemmer Group Collsion Cross Section Database; http://www.indiana.edu/~clemmer.

(152) Matz, L. M.; Hill, H. H.; Beegle, L. W.; Kanik, I. *Journal of the American Society for Mass Spectrometry* **2002**, *13*, 300.

(153) Campuzano, I.; Bush, M. F.; Robinson, C. V.; Beaumont, C.; Richardson, K.; Kim, H.; Kim, H. I. *Analytical chemistry* **2012**, *84*, 1026.

(154) Morsa, D.; Gabelica, V.; De Pauw, E. *Analytical Chemistry* **2011**, *83*, 5775.

(155) Merenbloom, S.; Flick, T.; Williams, E. *Journal of The American Society for Mass Spectrometry* **2012**, 1.

(156) Purves, R. W.; Guevremont, R.; Day, S.; Pipich, C. W.; Matyjaszczyk, M. S. *Review of Scientific Instruments* **1998**, *69*, 4094.

(157) Purves, R. W.; Guevremont, R. *Analytical Chemistry* **1999**, *71*, 2346.

(158) Shvartsburg, A. A.; Creese, A. J.; Smith, R. D.; Cooper, H. J. *Analytical Chemistry* **2010**, *82*, 8327.

(159) Shvartsburg, A. A.; Tang, K.; Smith, R. D. *Analytical Chemistry* **2010**, *82*, 32.

(160) Xuan, Y.; Creese, A. J.; Horner, J. A.; Cooper, H. J. *Rapid Communications in Mass Spectrometry* **2009**, *23*, 1963.

(161) Venne, K.; Bonneil, E.; Eng, K.; Thibault, P. *Analytical Chemistry* **2005**, *77*, 2176.

(162) Mirza, U. A.; Cohen, S. L.; Chait, B. T. *Analytical Chemistry* **1993**, *65*, 1.

(163) Li, J. W.; Taraszka, J. A.; Counterman, A. E.; Clemmer, D. E. *International Journal of Mass Spectrometry* **1999**, *185*, 37.

(164) Goodlett, D. R.; Loo, R. R. O.; Loo, J. A.; Wahl, J. H.; Udseth, H. R.; Smith, R. D. *Journal of the American Society for Mass Spectrometry* **1994**, *5*, 614.

(165) Mangrum, J. B.; Flora, J. W.; Muddiman, D. C. *Journal of the American Society for Mass Spectrometry* **2002**, *13*, 232.

(166) Frahm, J. L.; Muddiman, D. C. *Journal of the American Society for Mass Spectrometry* **2005**, *16*, 772.

(167) Daneshfar, R.; Kitova, E. N.; Klassen, J. S. *Journal of the American Chemical Society* **2004**, *126*, 4786.

(168) Shoemaker, G. K.; Soya, N.; Palcic, M. M.; Klassen, J. S. *Glycobiology* **2008**, *18*, 587.

(169) Benesch, J. L. P.; Sobott, F.; Robinson, C. V. *Analytical Chemistry* **2003**, *75*, 2208.

(170) Benesch, J. L. P.; Aquilina, J. A.; Baldwin, A. J.; Rekas, A.; Stengel, F.; Lindner, R. A.; Basha, E.; Devlin, G. L.; Horwitz, J.; Vierling, E.; Carver, J. A.; Robinson, C. V. *Chemistry & Biology* **2010**, *17*, 1008.

(171) Geels, R. B. J.; Calmat, S.; Heck, A. J. R.; van der Vies, S. M.; Heeren, R. M. A. *Rapid Communications in Mass Spectrometry* **2008**, *22*, 3633.

(172) Wang, G.; Abzalimov, R. R.; Kaltashov, I. A. *Analytical Chemistry* **2011**, *83*, 2870.

(173) Jurchen, J. C.; Williams, E. R. *Journal of the American Chemical Society* **2003**, *125*, 2817.

(174) Schwartz, B. L.; Gale, D. C.; Smith, R. D.; Chilkoti, A.; Stayton, P. S. *Journal of Mass Spectrometry* **1995**, *30*, 1095.

(175) Sobott, F.; McCammon, M. G.; Robinson, C. V. *International Journal of Mass Spectrometry* **2003**, *230*, 193.

(176) Wanasundara, S. N.; Thachuk, M. *Journal of the American Society for Mass Spectrometry* **2007**, *18*, 2242.

(177) Benesch, J. L. P.; Aquilina, J. A.; Ruotolo, B. T.; Sobott, F.; Robinson, C. V. *Chemistry & Biology* **2006**, *13*, 597.

(178) Hall, Z.; Hernandez, H.; Marsh, J. A.; Teichmann, S. A.; Robinson, C. V. *Structure* **2013**, *21*, 1325.

(179) Pagel, K.; Hyung, S.-J.; Ruotolo, B. T.; Robinson, C. V. *Analytical Chemistry* **2010**, *82*, 5363.

(180) Hyung, S.-J.; Robinson, C. V.; Ruotolo, B. T. *Chemistry & Biology* **2009**, *16*, 382.

(181) Hall, Z.; Politis, A.; Bush, M. F.; Smith, L. J.; Robinson, C. V. *Journal of the American Chemical Society* **2012**, *134*, 3429.

(182) Han, L.; Hyung, S.-J.; Mayers, J. J. S.; Ruotolo, B. T. *Journal of the American Chemical Society* **2011**, *133*, 11358.

(183) Han, L.; Hyung, S.-J.; Ruotolo, B. T. *Angewandte Chemie-International Edition* **2012**, *51*, 5692.

(184) Han, L.; Hyung, S.-J.; Ruotolo, B. T. *Faraday Discussions* **2013**, *160*, 371.

(185) Han, L.; Ruotolo, B. T. *Angewandte Chemie-International Edition* **2013**, *52*, 8329.

(186) Schwartz, B. L.; Bruce, J. E.; Anderson, G. A.; Hofstadler, S. A.; Rockwood, A. L.; Smith, R. D.; Chilkoti, A.; Stayton, P. S. *Journal of the American Society for Mass Spectrometry* **1995**, *6*, 459.

(187) Versluis, C.; van der Staaij, A.; Stokvis, E.; Heck, A. J. R.; de Craene, B. *Journal of the American Society for Mass Spectrometry* **2001**, *12*, 329.

(188) Nikolaev, E. N.; Somogyi, A.; Smith, D. L.; Gu, C. G.; Wysocki, V. H.; Martin, C. D.; Samuelson, G. L. *International Journal of Mass Spectrometry* **2001**, *212*, 535.

(189) Gamage, C. M.; Fernandez, F. M.; Kuppannan, K.; Wysocki, V. H. *Analytical Chemistry* **2004**, *76*, 5080.

(190) Zhou, M.; Dagan, S.; Wysocki, V. H. *Angewandte Chemie-International Edition* **2012**, *51*, 4336.

(191) Cooks, R. G.; Terwilliger, D. T.; Ast, T.; Beynon, J. H.; Keough, T. *Journal of the American Chemical Society* **1975**, *97*, 1583.

(192) Grill, V.; Shen, J.; Evans, C.; Cooks, R. G. *Review of Scientific Instruments* **2001**, *72*, 3149.

(193) Galhena, A. S.; Dagan, S.; Jones, C. M.; Beardsley, R. L.; Wysocki, V. N. *Analytical Chemistry* **2008**, *80*, 1425.

(194) Wysocki, V. H.; Joyce, K. E.; Jones, C. M.; Beardsley, R. L. *Journal of the American Society for Mass Spectrometry* **2008**, *19*, 190.

(195) Zhou, M.; Huang, C.; Wysocki, V. H. *Analytical Chemistry* **2012**, *84*, 6016.

(196) Zhou, M.; Dagan, S.; Wysocki, V. H. *Analyst* **2013**, *138*, 1353.

(197) Zhou, M.; Jones, C. M.; Wysocki, V. H. *Analytical Chemistry* **2013**, *85*, 8262.

(198) Ma, X.; Zhou, M.; Wysocki, V. H. *Journal of the American Society for Mass Spectrometry* **2014**, *25*, 368.

(199) Wysocki, V. H.; Jones, C. M.; Galhena, A. S.; Blackwell, A. E. *Journal of the American Society for Mass Spectrometry* **2008**, *19*, 903.

(200) Beardsley, R. L.; Jones, C. M.; Galhena, A. S.; Wysocki, V. H. *Analytical Chemistry* **2009**, *81*, 1347.

(201) Liu, Y. S.; Valentine, S. J.; Counterman, A. E.; Hoaglund, C. S.; Clemmer, D. E. *Analytical Chemistry* **1997**, *69*, A728.

(202) Liu, Y. S.; Clemmer, D. E. *Analytical Chemistry* **1997**, *69*, 2504.

(203) Wyttenbach, T.; Kemper, P. R.; Bowers, M. T. *International Journal of Mass Spectrometry* **2001**, *212*, 13.

(204) Valentine, S. J.; Anderson, J. G.; Ellington, A. D.; Clemmer, D. E. *Journal of Physical Chemistry B* **1997**, *101*, 3891.

(205) Bernstein, S. L.; Liu, D. F.; Wyttenbach, T.; Bowers, M. T.; Lee, J. C.; Gray, H. B.; Winkler, J. R. *Journal of the American Society for Mass Spectrometry* **2004**, *15*, 1435.

(206) Teplow, D. B.; Lazo, N. D.; Bitan, G.; Bernstein, S.; Wyttenbach, T.; Bowers, M. T.; Baumketner, A.; Shea, J.-E.; Urbanc, B.; Cruz, L.; Borreguero, J.; Stanley, H. E. *Accounts of Chemical Research* **2006**, *39*, 635.

(207) Murray, M. M.; Bernstein, S. L.; Nyugen, V.; Condron, M. M.; Teplow, D. B.; Bowers, M. T. *Journal of the American Chemical Society* **2009**, *131*, 6316.

(208) Mao, Y.; Woenckhaus, J.; Kolafa, J.; Ratner, M. A.; Jarrold, M. F. *Journal of the American Chemical Society* **1999**, *121*, 2712.

(209) Tholmann, D.; Tonner, D. S.; McMahon, T. B. *Journal of Physical Chemistry* **1994**, *98*, 2002.

(210) Price, W. D.; Schnier, P. D.; Jockusch, R. A.; Strittmatter, E. F.; Williams, E. R. *Journal of the American Chemical Society* **1996**, *118*, 10640.

(211) Schnier, P. D.; Price, W. D.; Jockusch, R. A.; Williams, E. R. *Journal of the American Chemical Society* **1996**, *118*, 7178.

(212) Jockusch, R. A.; Schnier, P. D.; Price, W. D.; Strittmatter, E. F.; Demirev, P. A.; Williams, E. R. *Analytical Chemistry* **1997**, *69*, 1119.

(213) Felitsyn, N.; Kitova, E. N.; Klassen, J. S. *Analytical Chemistry* **2001**, *73*, 4647.

(214) Felitsyn, N.; Kitova, E. N.; Klassen, J. S. *Journal of the American Society for Mass Spectrometry* **2002**, *13*, 1432.

(215) Sinelnikov, I.; Kitova, E. N.; Klassen, J. S. *Journal of the American Society for Mass Spectrometry* **2007**, *18*, 617.

(216) Kitova, E. N.; Sinelnikov, I.; Deng, L.; Klassen, J. S. *International Journal of Mass Spectrometry* **2013**, *345*, 97.

(217) Englander, S. W.; Mayne, L.; Bai, Y.; Sosnick, T. R. *Protein Science* **1997**, *6*, 1101.

(218) Schellman, J. A.; Schellman, C. G. *Protein Science* **1997**, *6*, 1092.

(219) Benson, E. E.; Linderstromlang, K. *Biochimica Et Biophysica Acta* **1959**, *32*, 579.

(220) Linderstromlang, K. *Biochimica Et Biophysica Acta* **1955**, *18*, 308.

(221) Englander, S. W. *Journal of the American Society for Mass Spectrometry* **2006**, *17*, 1481.

(222) Katta, V.; Chait, B. T. *Rapid Communications in Mass Spectrometry* **1991**, *5*, 214.

(223) Morton, V. L.; Burkitt, W.; O'Connor, G.; Stonehouse, N. J.; Stockley, P. G.; Ashcroft, A. E. *Phys Chem Chem Phys* **2010**, *12*, 13468.

(224) Lam, T. T.; Lanman, J. K.; Emmett, M. R.; Hendrickson, C. L.; Marshall, A. G.; Prevelige, P. E. *Journal of Chromatography A* **2002**, *982*, 85.

(225) Lanman, J.; Lam, T. T.; Barnes, S.; Sakalian, M.; Emmett, M. R.; Marshall, A. G.; Prevelige, P. E. *Journal of Molecular Biology* **2003**, *325*, 759.

(226) Turner, B. T.; Maurer, M. C. *Biochemistry* **2002**, *41*, 7947.

(227) Mandell, J. G.; Baerga-Ortiz, A.; Akashi, S.; Takio, K.; Komives, E. A. *Journal of Molecular Biology* **2001**, *306*, 575.

(228) Mandell, J. G.; Falick, A. M.; Komives, E. A. *Analytical Chemistry* **1998**, *70*, 3987.

(229) Lodowski, D. T.; Palczewski, K.; Miyagi, M. *Biochemistry* **2010**, *49*, 9425.

(230) Balasubramaniam, D.; Komives, E. A. *Biochimica Et Biophysica Acta-Proteins and Proteomics* **2013**, *1834*, 1202.

(231) Goswami, D.; Devarakonda, S.; Chalmers, M. J.; Pascal, B. D.; Spiegelman, B. M.; Griffin, P. R. *Journal of the American Society for Mass Spectrometry* **2013**, *24*, 1584.

(232) Keppel, T. R.; Howard, B. A.; Weis, D. D. *Biochemistry* **2012**, *51*, 7812.

(233) Tang, L.; Coales, S. J.; Morrow, J. A.; Edmunds, T.; Hamuro, Y. *Chembiochem* **2012**, *13*, 2243.

(234) Pan, J.; Han, J.; Borchers, C. H. *International Journal of Mass Spectrometry* **2012**, *325*, 130.

(235) West, G. M.; Chien, E. Y. T.; Katritch, V.; Gatchalian, J.; Chalmers, M. J.; Stevens, R. C.; Griffin, P. R. *Structure* **2011**, *19*, 1424.

(236) Parker, C. H.; Morgan, C. R.; Rand, K. D.; Engen, J. R.; Jorgenson, J. W.; Stafford, D. W. *Biochemistry* **2014**, *53*, 1511.

(237) Orban, T.; Jastrzebska, B.; Gupta, S.; Wang, B.; Miyagi, M.; Chance, M. R.; Palczewski, K. *Structure* **2012**, *20*, 826.

(238) Rey, M.; Forest, E.; Pelosi, L. *Biochemistry* **2012**, *51*, 9727.

(239) Mehmood, S.; Domene, C.; Forest, E.; Jault, J.-M. *Proceedings of the National Academy of Sciences of the United States of America* **2012**, *109*, 10832.

(240) Zhang, Y.; Rempel, D. L.; Zhang, J.; Sharma, A. K.; Mirica, L. M.; Gross, M. L. *Proceedings of the National Academy of Sciences of the United States of America* **2013**, *110*, 14604.

(241) Pan, J.; Han, J.; Borchers, C. H.; Konermann, L. *Biochemistry* **2012**, *51*, 3694.

(242) Wei, H.; Mo, J.; Tao, L.; Russell, R. J.; Tymiak, A. A.; Chen, G.; Iacob, R. E.; Engen, J. R. *Drug Discovery Today* **2014**, *19*, 95.

(243) Zhang, A.; Hu, P.; MacGregor, P.; Xue, Y.; Fan, H.; Suchecki, P.; Olszewski, L.; Liu, A. *Analytical Chemistry* **2014**, *86*, 3468.

(244) Pan, L. Y.; Salas-Solano, O.; Valliere-Douglass, J. F. *Analytical Chemistry* **2014**, *86*, 2657.

(245) Mo, J.; Tymiak, A. A.; Chen, G. *Drug Discovery Today* **2012**, *17*, 1323.

(246) Clarke, J.; Itzhaki, L. S. *Current Opinion in Structural Biology* **1998**, *8*, 112.

(247) Konermann, L.; Pan, J. X.; Liu, Y. H. *Chemical Society Reviews* **2011**, *40*, 1224.

(248) Garcia, R. A.; Pantazatos, D.; Villarreal, F. J. *ASSAY and Drug Development Technologies* **2004**, *2*, 81.

(249) Sinz, A. *Chemmedchem* **2007**, *2*, 425.

(250) Mandell, J. G.; Falick, A. M.; Komives, E. A. *Proceedings of the National Academy of Sciences of the United States of America* **1998**, *95*, 14705.

(251) Buijs, J.; Ramstrom, M.; Danfelter, M.; Larsericsdotter, H.; Hakansson, P.; Oscarsson, S. *Journal of Colloid and Interface Science* **2003**, *263*, 441.

(252) McLafferty, F. W.; Guan, Z. Q.; Haupts, U.; Wood, T. D.; Kelleher, N. L. *Journal of the American Chemical Society* **1998**, *120*, 4732.

(253) Freitas, M. A.; Marshall, A. G. *International Journal of Mass Spectrometry* **1999**, *182*, 221.

(254) Chalmers, M. J.; Busby, S. A.; Pascal, B. D.; He, Y. J.; Hendrickson, C. L.; Marshall, A. G.; Griffin, P. R. *Analytical Chemistry* **2006**, *78*, 1005.

(255) Weis, D. D.; Engen, J. R.; Kass, I. J. *Journal of the American Society for Mass Spectrometry* **2006**, *17*, 1700.

(256) Zhu, M. M.; Rempel, D. L.; Du, Z. H.; Gross, M. L. *Journal of the American Chemical Society* **2003**, *125*, 5252.

(257) Zhu, M. M.; Chitta, R.; Gross, M. L. *International Journal of Mass Spectrometry* **2005**, *240*, 213.

(258) Sperry, J. B.; Shi, X. G.; Rempel, D. L.; Nishimura, Y.; Akashi, S.; Gross, M. L. *Biochemistry* **2008**, *47*, 1797.

(259) Zhu, M. M.; Rempel, D. L.; Zhao, J.; Giblin, D. E.; Gross, M. L. *Biochemistry* **2003**, *42*, 15388.

(260) Zhu, M. M.; Rempel, D. L.; Gross, M. L. *Journal of the American Society for Mass Spectrometry* **2004**, *15*, 388.

(261) Chitta, R. K.; Rempel, D. L.; Grayson, M. A.; Remsen, E. E.; Gross, M. L. *Journal of the American Society for Mass Spectrometry* **2006**, *17*, 1526.

(262) Hopper, E. D.; Roulhac, P. L.; Campa, M. J.; Patz, E. F.; Fitzgerald, M. C. *Journal of the American Society for Mass Spectrometry* **2008**, *19*, 1303.

(263) Dai, S. Y.; Fitzgerald, M. C. *Journal of the American Society for Mass Spectrometry* **2006**, *17*, 1535.

(264) Powell, K. D.; Ghaemmaghami, S.; Wang, M. Z.; Ma, L. Y.; Oas, T. G.; Fitzgerald, M. C. *Journal of the American Chemical Society* **2002**, *124*, 10256.

(265) Powell, K. D.; Fitzgerald, M. C. *Biochemistry* **2003**, *42*, 4962.

(266) Tang, L. J.; Roulhac, P. L.; Fitzgerald, M. C. *Analytical Chemistry* **2007**, *79*, 8728.

(267) Fitzgerald, M. C.; West, G. M. *Journal of the American Society for Mass Spectrometry* **2009**, *20*, 1193.

(268) Sinz, A. *Mass Spectrometry Reviews* **2006**, *25*, 663.

(269) Nazabal, A.; Wenzel, R. J.; Zenobi, R. *Analytical Chemistry* **2006**, *78*, 3562.

(270) Schulz, D. M.; Ihling, C.; Clore, G. M.; Sinz, A. *Biochemistry* **2004**, *43*, 4703.

(271) Hah, S. S. *Analytical Sciences* **2009**, *25*, 731.

(272) Umanah, G. K. E.; Huang, L. Y.; Ding, F. X.; Arshava, B.; Farley, A. R.; Link, A. J.; Naider, F.; Becker, J. M. *Journal of Biological Chemistry* **2010**, *285*, 39425.

(273) Muller, M. Q.; de Koning, L. J.; Schmidt, A.; Ihling, C.; Syha, Y.; Rau, O.; Mechtler, K.; Schubert-Zsilavecz, M.; Sinz, A. *Journal of Medicinal Chemistry* **2009**, *52*, 2875.

(274) Stengel, F.; Aebersold, R.; Robinson, C. V. *Molecular & Cellular Proteomics* **2012**, *11*.

(275) Gold, M. G.; Stengel, F.; Nygren, P. J.; Weisbrod, C. R.; Bruce, J. E.; Robinson, C. V.; Barford, D.; Scott, J. D. *Proceedings of the National Academy of Sciences of the United States of America* **2011**, *108*, 6426.

(276) Chen, Z. A.; Jawhari, A.; Fischer, L.; Buchen, C.; Tahir, S.; Kamenski, T.; Rasmussen, M.; Lariviere, L.; Bukowski-Wills, J.-C.; Nilges, M.; Cramer, P.; Rappsilber, J. *Embo Journal* **2010**, *29*, 717.

(277) Trnka, M. J.; Burlingame, A. L. *Molecular & Cellular Proteomics* **2010**, *9*, 2306.

(278) Tiroli-Cepeda, A. O.; Lima, T. B.; Balbuena, T. S.; Gozzo, F. C.; Ramos, C. H. I. *Journal of Proteomics* **2014**, *104*, 48.

(279) Pettelkau, J.; Schroeder, T.; Ihling, C. H.; Olausson, B. E. S.; Koelbel, K.; Lange, C.; Sinz, A. *Biochemistry* **2012**, *51*, 4932.

(280) Lauber, M. A.; Rappsilber, J.; Reilly, J. P. *Molecular & Cellular Proteomics* **2012**, *11*, 1965.

(281) Taverner, T.; Hernandez, H.; Sharon, M.; Ruotolo, B. T.; Matak-Vinkovic, D.; Devos, D.; Russell, R. B.; Robinson, C. V. *Accounts of Chemical Research* **2008**, *41*, 617.

(282) Politis, A.; Park, A. Y.; Hyung, S.-J.; Barsky, D.; Ruotolo, B. T.; Robinson, C. V. *PLoS One* **2010**, *5*, e12080.

(283) Sinz, A. *Analytical and Bioanalytical Chemistry* **2010**, *397*, 3433.

(284) Brunner, J. *Annual Review of Biochemistry* **1993**, *62*, 483.

(285) Kluger, R.; Alagic, A. *Bioorganic Chemistry* **2004**, *32*, 451.

(286) Melcher, K. *Current Protein & Peptide Science* **2004**, *5*, 287.

(287) Back, J. W.; Notenboom, V.; de Koning, L. J.; Muijsers, A. O.; Sixma, T. K.; de Koster, C. G.; de Jong, L. Z. *Analytical Chemistry* **2002**, *74*, 4417.

(288) Sinz, A. *Journal of Mass Spectrometry* **2003**, *38*, 1225.

(289) Trakselis, M. A.; Alley, S. C.; Ishmael, F. T. *Bioconjugate Chemistry* **2005**, *16*, 741.

(290) Sriswasdi, S.; Harper, S. L.; Tang, H.-Y.; Gallagher, P. G.; Speicher, D. W. *Proceedings of the National Academy of Sciences of the United States of America* **2014**, *111*, 1801.

(291) Young, M. M.; Tang, N.; Hempel, J. C.; Oshiro, C. M.; Taylor, E. W.; Kuntz, I. D.; Gibson, B. W.; Dollinger, G. *Proceedings of the National Academy of Sciences of the United States of America* **2000**, *97*, 5802.

(292) Sinz, A. *Analytical and Bioanalytical Chemistry* **2005**, *381*, 44.

(293) Kelleher, N. L.; Lin, H. Y.; Valaskovic, G. A.; Aaserud, D. J.; Fridriksson, E. K.; McLafferty, F. W. *Journal of the American Chemical Society* **1999**, *121*, 806.

(294) Novak, P.; Haskins, W. E.; Ayson, M. J.; Jacobsen, R. B.; Schoeniger, J. S.; Leavell, M. D.; Young, M. M.; Kruppa, G. H. *Analytical Chemistry* **2005**, *77*, 5101.

(295) Kruppa, G. H.; Schoeniger, J.; Young, M. M. *Rapid Communications in Mass Spectrometry* **2003**, *17*, 155.

(296) Hermanson, G. T. *Bioconjugate techniques*; 2nd ed.; Academic Press, 2008.

(297) Hartman, F. C.; Wold, F. *Journal of the American Chemical Society* **1966**, *88*, 3890.

(298) Ghosh, S. S.; Kao, P. M.; McCue, A. W.; Chappelle, H. L. *Bioconjugate Chemistry* **1990**, *1*, 71.

(299) Dihazi, G. H.; Sinz, A. *Rapid Communications in Mass Spectrometry* **2003**, *17*, 2005.

(300) Fujii, N.; Jacobsen, R. B.; Wood, N. L.; Schoeniger, J. S.; Guy, R. K. *Bioorganic & Medicinal Chemistry Letters* **2004**, *14*, 427.

(301) Fioroni, M.; Dworeck, T.; Rodriguez-Ropero, F.; Fioroni, M.; Dworeck, T.; RodriguezRopero, F. *Beta-Barrel Channel Proteins as Tools in Nanotechnology: Biology, Basic Science and Advanced Applications* **2014**, *794*, 41.

(302) Laurence, J. S. *Molecular Pharmaceutics* **2012**, *9*, 695.

(303) Wang, X.; Lee, H.-W.; Liu, Y.; Prestegard, J. H. *Journal of Structural Biology* **2011**, *173*, 515.

(304) Wishart, D. *Current Pharmaceutical Biotechnology* **2005**, *6*, 105.

(305) Bangerter, B. W. *Nuclear magnetic resonance*, 1995.

(306) Breukels, V.; Konijnenberg, A.; Nabuurs, S. M.; Doreleijers, J. F.; Kovalevskaya, N. V.; Vuister, G. W. *Current protocols in protein science* **2011**, *Chapter 17*, Unit17.5.

(307) Wuthrich, K. *Journal of Biological Chemistry* **1990**, *265*, 22059.

(308) Braunschweiler, L.; Bodenhausen, G.; Ernst, R. R. *Molecular Physics* **1983**, *48*, 535.

(309) Basus, V. J. *Methods in Enzymology* **1989**, *177*, 132.

(310) Breukels, V.; Konijnenberg, A.; Nabuurs, S. M.; Doreleijers, J. F.; Kovalevskaya, N. V.; Vuister, G. W. *Current protocols in protein science; editorial board, John E. Coligan,* **2011**, *Chapter 17*, Unit17.5.

(311) Kleckner, I. R.; Foster, M. P. *Biochimica Et Biophysica Acta-Proteins and Proteomics* **2011**, *1814*, 942.

(312) Mittermaier, A. K.; Kay, L. E. *Trends in Biochemical Sciences* **2009**, *34*, 601.

(313) Tossavainen, H.; Kukkurainen, S.; Maatta, J. A. E.; Kahkonen, N.; Pihlajamaa, T.; Hytonen, V. P.; Kulomaa, M. S.; Permi, P. *PloS one* **2014**, *9*, e100564.

(314) Chandak, M. S.; Nakamura, T.; Makabe, K.; Takenaka, T.; Mukaiyama, A.; Chaudhuri, T. K.; Kato, K.; Kuwajima, K. *Journal of Molecular Biology* **2013**, *425*, 2541.

(315) Vilar, M.; Wang, L.; Riek, R. *Amyloid Proteins: Methods and Protocols, Second Edition* **2012**, *849*, 185.

(316) Greene, L. H.; Li, H.; Zhong, J.; Zhao, G.; Wilson, K. *European Biophysics Journal with Biophysics Letters* **2012**, *41*, 41.

(317) Cook, G. A.; Opella, S. J. *Biochimica Et Biophysica Acta-Biomembranes* **2011**, *1808*, 1448.

(318) Jehle, S.; Falb, M.; Kirkpatrick, J. P.; Oschkinat, H.; van Rossum, B.-J.; Althoff, G.; Carlomagno, T. *Journal of the American Chemical Society* **2010**, *132*, 3842.

(319) Fiaux, J.; Bertelsen, E. B.; Horwich, A. L.; Wuthrich, K. *Nature* **2002**, *418*, 207.

(320) Lebowitz, J.; Lewis, M. S.; Schuck, P. *Protein Science* **2002**, *11*, 2067.

(321) Cole, J. L.; Lary, J. W.; Moody, T. P.; Laue, T. M. In *Biophysical Tools for Biologists: Vol 1 in Vitro Techniques*; Correia, J. J., Detrich, H. W., Eds. 2008; Vol. 84, p 143.

(322) Howlett, G. J.; Minton, A. P.; Rivas, G. *Current Opinion in Chemical Biology* **2006**, *10*, 430.

(323) Laue, T. M. *Energetics of Biological Macromolecules* **1995**, *259*, 427.

(324) Laue, T. *Current Opinion in Structural Biology* **2001**, *11*, 579.

(325) Laue, T. M.; Stafford, W. F. *Annual Review of Biophysics and Biomolecular Structure* **1999**, *28*, 75.

(326) Krayukhina, E.; Uchiyama, S.; Nojima, K.; Okada, Y.; Hamaguchi, I.; Fukui, K. *Journal of Bioscience and Bioengineering* **2013**, *115*, 104.

(327) Gabrielson, J. P.; Arthur, K. K.; Stoner, M. R.; Winn, B. C.; Kendrick, B. S.; Razinkov, V.; Svitel, J.; Jiang, Y.; Voelker, P. J.; Fernandes, C. A.; Ridgeway, R. *Analytical Biochemistry* **2010**, *396*, 231.

(328) Andya, J. D.; Liu, J.; Shire, S. J. *Analysis of Irreversible Aggregation, Reversible Self-association and Fragmentation of Monoclonal Antibodies by Analytical Ultracentrifugation*, 2010; Vol. 11.

(329) Berman, H. M.; Westbrook, J.; Feng, Z.; Gilliland, G.; Bhat, T. N.; Weissig, H.; Shindyalov, I. N.; Bourne, P. E. *Nucleic Acids Research* **2000**, *28*, 235.

(330) Wlodawer, A.; Minor, W.; Dauter, Z.; Jaskolski, M. *Febs Journal* **2008**, *275*, 1.

(331) Ilari, A.; Savino, C. In *Methods in Molecular Biology:Volume I: Data, Sequence, Analysis and Evolution*; Keith, J. M., Ed. 2008; Vol. 452, p 63.

(332) Verdaguer, N.; Garriga, D.; Fita, I. *Sub-cellular biochemistry* **2013**, *68*, 117.

(333) Govindasamy, L.; Agbandje-McKenna, M.; McKenna, R. *Structural Virology* **2011**, 100.

(334) Grey, J. L.; Thompson, D. H. *Expert Opinion on Drug Discovery* **2010**, *5*, 1039.

(335) Ruprecht, J.; Nield, J. *Progress in Biophysics & Molecular Biology* **2001**, *75*, 121.

(336) Ohi, M.; Li, Y.; Cheng, Y.; Walz, T. *Biological Procedures Online* **2004**, *6*, 23.

(337) Adrian, M.; Dubochet, J.; Lepault, J.; McDowall, A. W. *Nature* **1984**, *308*, 32.

(338) Jonic, S.; Venien-Bryan, C. *Current Opinion in Pharmacology* **2009**, *9*, 636.

(339) Henderson, R.; Baldwin, J. M.; Ceska, T. A.; Zemlin, F.; Beckmann, E.; Downing, K. H. *Journal of Molecular Biology* **1990**, *213*, 899.

(340) Bongini, L.; Fanelli, D.; Piazza, F.; De los Rios, P.; Sandin, S.; Skoglund, U. *Proceedings of the National Academy of Sciences of the United States of America* **2004**, *101*, 6466.

(341) Miyazawa, A.; Fujiyoshi, Y.; Unwin, N. *Nature* **2003**, *423*, 949.

(342) Clemmer, D. E.; Jarrold, M. F. *Journal of Mass Spectrometry* **1997**, *32*, 577.

(343) Scarff, C. A.; Thalassinos, K.; Hilton, G. R.; Scrivens, J. H. *Rapid Communications in Mass Spectrometry* **2008**, *22*, 3297.

(344) Vonhelden, G.; Hsu, M. T.; Gotts, N.; Bowers, M. T. *Journal of Physical Chemistry* **1993**, *97*, 8182.

(345) Wyttenbach, T.; Witt, M.; Bowers, M. T. *Journal of the American Chemical Society* **2000**, *122*, 3458.

(346) Shvartsburg, A. A.; Hudgins, R. R.; Dugourd, P.; Jarrold, M. F. *Chemical Society Reviews* **2001**, *30*, 26.

(347) Wyttenbach, T.; vonHelden, G.; Batka, J. J.; Carlat, D.; Bowers, M. T. *Journal of the American Society for Mass Spectrometry* **1997**, *8*, 275.

(348) Shvartsburg, A. A.; Schatz, G. C.; Jarrold, M. F. *Journal of Chemical Physics* **1998**, *108*, 2416.

(349) Shvartsburg, A. A.; Jarrold, M. F. *Chemical Physics Letters* **1996**, *261*, 86.

(350) Shvartsburg, A. A.; Smith, R. D. *Journal of the American Society for Mass Spectrometry* **2008**, *19*, 1286.

(351) Mesleh, M. F.; Hunter, J. M.; Shvartsburg, A. A.; Schatz, G. C.; Jarrold, M. F. *Journal of Physical Chemistry* **1996**, *100*, 16082.

(352) Shvartsburg, A. A.; Hudgins, R. R.; Dugourd, P.; Jarrold, M. F. *Journal of Physical Chemistry A* **1997**, *101*, 1684.

(353) Bleiholder, C.; Wyttenbach, T.; Bowers, M. T. *International Journal of Mass Spectrometry* **2011**, *308*, 1.

(354) Bleiholder, C.; Contreras, S.; Do, T. D.; Bowers, M. T. *International Journal of Mass Spectrometry* **2013**, *345*, 89.

(355) Anderson, S. E.; Bleiholder, C.; Brocker, E. R.; Stang, P. J.; Bowers, M. T. *International Journal of Mass Spectrometry* **2012**, *330*, 78.

(356) Bleiholder, C.; Contreras, S.; Bowers, M. T. *International Journal of Mass Spectrometry* **2013**, *354*, 275.

2

Experimental Methods

Instruments used in experiments presented in the following chapters are described here, along with typical tuning parameters. An example of ion mobility mass spectrometry data acquisition and processing is provided. Information on nano-electrospray conditions, reagents, general sample preparation procedure and mass calibration is presented.

2.1 Biological Mass Spectrometry

All of the mass spectra presented in this thesis were obtained using quadrupole time-of-flight mass spectrometers: either Ultima API US (Waters, Manchester, UK); in-house modified IM-Q-ToF 1; Synapt G2 HDMS or Synapt G2S HDMS (Waters, Manchester, UK); with nano-electrospray ionisation source.

2.1.1 Reagents and general sample preparation

Intact IgG and Fc-hinge fragment samples, used in experiments presented in Chapter 3 and Chapter 5, were provided by UCB Pharma. Antibody-drug-conjugates (ADC) were provided by Piramal Healthcare. Standard protein complexes studied in Chapter 4 *i.e.* avidin from egg white (A9275) was obtained from Sigma Aldrich (St. Louis, MO, USA), concanavalin A from *Canavalia ensiformis* (C2010) was obtained from Sigma Aldrich (St. Louis, MO, USA), human TTR was obtained from SCIPAC (Sittingbourne, UK); and human SAP was obtained from CalBioChem (Darmstadt, Germany). ATP-phosphoribosyltransferase investigated in Chapter 6, was provided by Dr. Luiz Pedro Sório de Carvalho from MRC National Institute for Medical Research (London, UK). Detailed information on sample preparation, concentration and conditions can in found in the relevant chapters.

Ammonium acetate (AmAc) was obtained from Fisher Scientific (Loughborough, UK). On the day of analysis, buffer was exchanged to ammonium acetate (Fisher Scientific, Loughborough, UK) using micro Bio-Spin Chromatography columns (Micro Bio-Spin 6 Columns, Tris) following the instructions specified by the manufacturer. The desalting procedure was performed one to four times to achieve desired sample purity. The majority of experiments were carried out at pH 6.8 (pI of all proteins are provided in the Appendix 3). Otherwise (Chapter 6), pH of the buffer was adjusted with hydrochloric acid or ammonia supplied by VWR International Ltd (UK). Solution pH readings were taken using a pH meter (Jenway 3305). High purity water was obtained from an Arium 611 water purification unit (Sartorius, Göttingen, Germany) fitted with a 0.2 µm filter or supplied by Fisher Scientific Ltd (Loughborough, UK). Solids were weighed with a Mettler AC100 balance to an accuracy of ± 0.0001 g. Charge reduction experiments were carried out by addition of 10% (v) triethylammonium acetate buffer (TEAA) (Fluka, Steinheim, Switzerland) prior to MS analysis.

2.1.2 Nano-electrospray ionisation and sample introduction

All MS and IM-MS instruments utilized in the presented studies were fitted with nESI sources. Samples were ionised using nESI method, where protein species were charged and transferred from solution into the gas phase. NanoESI capillaries were prepared in-house from thin-walled borosilicate capillaries (inner diameter 0.9 mm, outer diameter 1.2 mm, World Precision Instruments, Stevenage, UK) using a Flaming/Brown P-97 micropipette puller (Sutter Instrument Company, Novato, CA, USA). These were then filled with sample using micro-loading tips (Eppendorf, Hamburg, Germany). A positive voltage was applied to the solution via 0.125 mm platinum wire (Goodfellow Cambridge Ltd., Huntingdon, UK) inserted into the capillary. Capillary voltage applied *via* platinum wire was adjusted to give optimum spraying conditions and ranged from 1.0 to 2.0 kV which was dependent on the solvent composition and protein species under investigation, as well as tip geometry.

2.1.3 Ion transfer, mass analysis and detection

Ions generated by the nESI enter the mass spectrometer *via* a ‘Z-spray’ source. The axis of the sample capillary is orthogonal to the sampling orifice *i.e.* the cone, which in turn is perpendicular to the following extractor cone, as shown in Figure 2.1. This architecture results in increased sensitivity by allowing transmission of ions and reduction in transmission of neutral species. To aid the desolvation process, the temperature of the source region may be increased. For work presented in Chapters 3-5, the source temperature was set to 80 °C, unless otherwise stated. The work presented in Chapter 6, required application of lower source temperatures (30 °C) to prevent aggregation of protein species in the glass capillary.

Post the extractor cone, ions travel through a transfer hexapole. On the Ultima API US instrument, this region has been modified to include a flow-resisting sleeve.

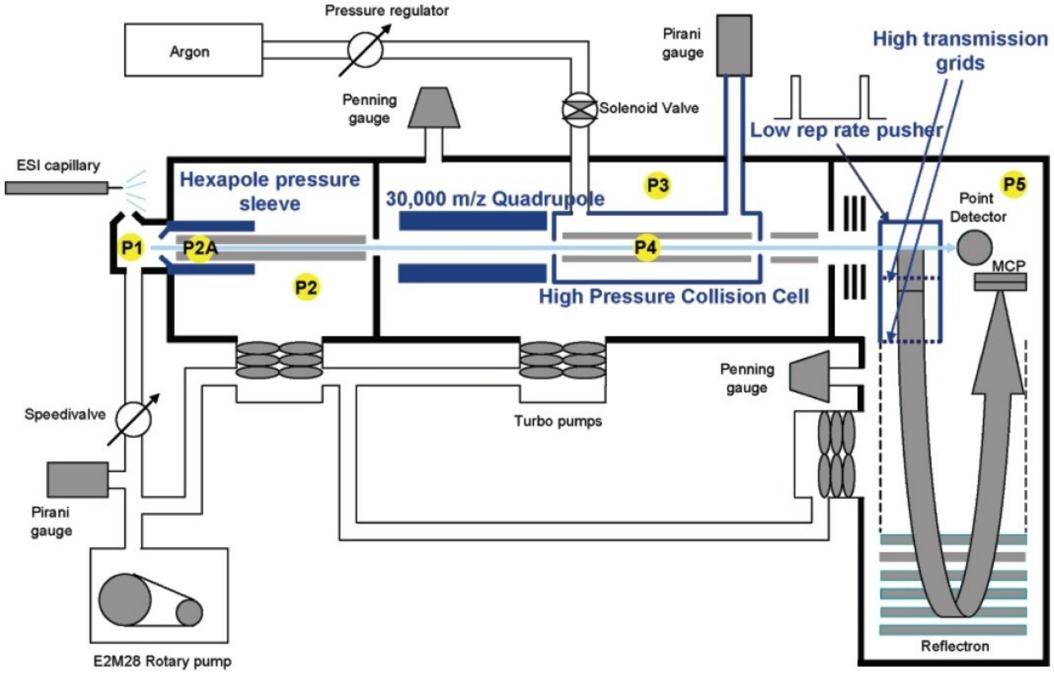

Figure 2.1 Schematic representation of a Waters Quadrupole Time of Flight (Q-ToF) mass spectrometer modified for analysis of large molecules; modification carried out by MS Vision. Inclusion of the hexapole pressure sleeve allows for use of increased pressure and enhances the transfer of large molecular species to the mass analyser. Items indicated in dark blue are modifications included. Yellow circles indicate differential pressure stages: P1 – regulated by the pumping efficiency of the rotary pump to 9 × 10^{-1} mBar; P2A - hexapole pressure within a flow-restricting sleeve estimated to be about 8 × 10^{-3} mBar; P2 – pressure in the hexapole chamber maintained ~4 × 10^{-3} mBar; P3 – pressure in the quadrupole chamber ~7 × 10^{-3} mBar; P4 – pressure in the collision cell ~2 × 10^{-2} mBar; and P5 – pressure in the ToF chamber ~3 ×10^{-7} mBar. The image has been reproduced from van den Heuvel *et al*. 2006.[1]

It has been shown, that the application of increased pressure in the first and second vacuum chamber of the mass spectrometer is a requirement for the analysis or large proteins. [1-6] Increased pressure leads to collisional cooling and focusing of large ions in the ion guides, hence improved transmission to the quadrupole analyser and later ToF. Pressure can be controlled with two Speedivalves (Edwards, West Sussex, UK), located along the vacuum line between the source rotary backing pump and the source block. Partially closing the Speedivalve, and throttling the source backing pump, enables the source pressure to rise. Source pressure used typically varied from 3 and 9 × 10^{-1} mBar dependent on the species under investigation and these values will be reported in the relevant chapters. The instrument modification has been carried out by MS Vision (The Netherlands).

Eventually, ions reach the quadrupole analyser. Here, collision-induced dissociation (CID) can be performed by selecting ions of a particular *m/z* and increasing the kinetic energy by collisions with an inert gas such as argon, causing complex dissociation or fragmentation as described in Chapter 1. The Ultima API US instrument has been modified to allow for ion selection up to *m/z* 30374. Moreover, the quadrupole can be used as a mass filter where ions are not subjected to high collision energies what allows for preservation of intact species, as it has been done for the majority of experiments presented in this work. Post the collision cell, ions pass though a transfer hexapole into the ToF region. Here, the pusher accelerates the ions into the ToF tube until they reach the reflectron where they are refocused and reflected back towards the microchannel plate (MCP) detector. The velocity of each ion is inversely proportional to its *m/z*. Ion signals are converted by a 1 GHz time-to-digital converter, resulting in a total ion count (TIC) chromatogram which can be deconvoluted into a mass spectrum using MassLynx software (Waters, Manchester, UK).

A typical QToF mass spectrometer has three stages of differential pumping: the source, the quadrupole analyser and the ToF chamber; to create a decreasing gradient along the length of the instrument. Each compartment is kept under vacuum by a turbomolecular pump, backed by a rotary pump. Typical pressure values for the QToF Ultima API US in each region are as follows: source ~ $2\text{-}9 \times 10^{-1}$ mBar (regulated with the Speedivalve), analyser ~7×10^{-3} mBar; and ToF ~3×10^{-7} mBar.

2.1.4 Mass calibration

External mass calibration was carried out using a 2 mgmL^{-1} solution of caesium iodide (Sigma Aldrich, Dorset, UK) in 49.5 % water, 49.5 % isopropanol and 1 % formic acid. The metal salt calibrant provides a series of monoisotopic cluster peaks corresponding to $Cs_{n+1}I_n$ ions, covering an appropriate *m/z* range.

2.1.5 Typical instrumental parameters

Typical instrument settings for Ultima API US used in the presented work are shown in Table 2.1. Optimisation of the source parameters is crucial for preservation of non-covalent complexes. Particular attention must be paid to the influence of the source pressure on the ion transmission and to the cone voltage effecting protein tertiary and quaternary structure and non-covalent interactions.

Table 2.1 Typical instrumental parameters for the Q-ToF Ultima API US in the positive mode.

Parameter	Value	Comment
Capillary /kV	1.0 – 2.0	
Cone /V	20 – 200	adjusted accordingly to the sample and experimental design
Extractor /V	1.0 – 3.0	
RF Lens1 /V	2.0	
Apperture1 /V	5.0	
RF Lens2 /V	0.0	
Source Temperature /°C	25 – 80	adjusted accordingly to the sample
LM Resolution /V	5.0	
HM Resolution /V	5.0	
Collision Energy /V	10	raised stepwise for CID
Ion Energy /V	1.0	
Steering /V	-1.10	
Entrance /V	65.0	
Pre-filter /V	4.0	
Transport /V	5.0	
Aperture3 /V	15.0	
Acceleration /V	200	
Focus /V	0	
Tube Lens /V	60	
Offset1 /V	0	
Offset2 /V	0	
Pusher /V	980	
ToF /kV	9.10	
Reflectron /V	35.0	
Pusher Cycle Time / µs	70 – 200	adjusted accordingly to *m/z* range
Multiplier /V	650	
MCP /V	2000- 2400	

2.1.6 Use of buffers to reduce charge

Application of elevated voltages in the source region of a mass spectrometer to aid desolvation process may lead to non-covalent complex dissociation and/or structure perturbation. Addition of different buffer salts, such as triethylammonium acetate (TEAA) to the sample buffer, has been reported not only to reduce the charge of the ions but also to increase the stability of protein complexes in the gas phase.[7-9] The charge-reducing nature of alkylated ammonium ions is mainly based on its higher gas-phase basicity relative to ammonium acetate, which is commonly used as a buffer in the native MS experiments. The gas-phase basicity of the ionic species present in the solution controls how much charge is emitted during the electrospray process. Small ionic electrolytes with higher gas-phase basicity will compete for charges with ionized sites of the protein and effectively remove the charge from protein species.[10-13] Moreover, reducing the charge increases the energy barrier of unfolding and subsequent complex dissociation.[9,14] Even with use of an elevated acceleration voltages in the source region, non-covalent complexes may remain intact in the presence of such additives.

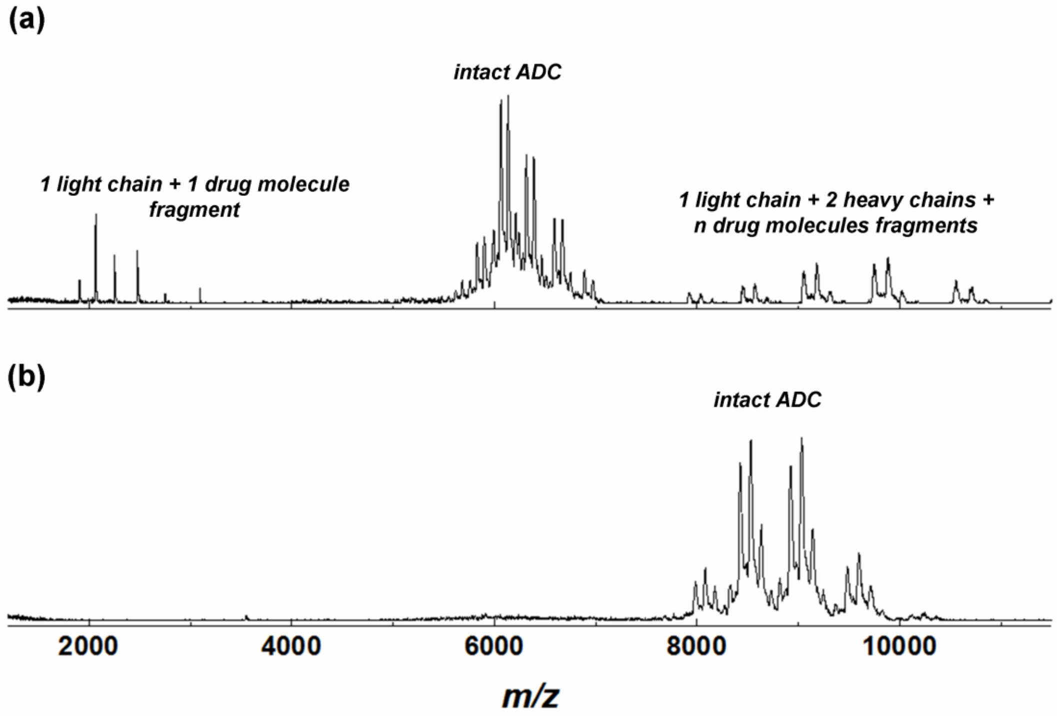

Figure 2.2 Use of charge reducing agents, such as TEAA, not only decreases the charge of ions detected but also helps to preserve non-covalent interactions. Antibody-drug-conjugates (ADC) can undergo dissociation when high acceleration voltages are applied to aid desolvation for enhanced resolution (a). Addition of 10 % TEAA to the sample buffer (b) helps to keep these non-covalent complexes intact making the drug-to-antibody ratio (DAR) determination simpler. Both mass spectra shown here were acquired under identical instrumental conditions.

Figure 2.2 illustrates how addition of TEAA to the sample helps to preserve non-covalent interactions by using an antibody-drug-conjugate (ADC) as an example.

ADCs are a new class of anticancer biopharmaceutical drugs composed of an antibody (also know as immunoglobulin) linked *via* a stable chemical linker to a biologically active cytotoxic small molecule drug.[15,16] One of the most important properties of an ADC is the average number of drug molecules attached to an antibody as it determines the amount of drug delivered to the tumour cells and affects safely and efficacy. Mass spectrometry is currently emerging as a tool of choice for drug-to-antibody ratio (DAR) determination.[17-20] The immunoglobulins of the G isotype (IgG), which are commonly used as templates for ADCs, are ~150 kDa protein complexes composed of two light chains and two heavy chains covalently linked though disulfide bonds (for details see Chapter 3). When the cytotoxic drug is being conjugated *via* the cysteine of the interchain disulfide bond, the ADC molecule becomes a non-covalent tetramer as the disulfide bridges are broken. Since the mass of the drug conjugate and its linker is relatively small (~1 kDa) in comparison to the antibody molecule, high acceleration voltages are applied to aid desolvation process and enhance the resolution at higher *m/z* to allow accurate peak assignment and mass determination. Often, use of elevated acceleration voltages leads to dissociation of non-covalent complexes. In Figure 2.2a, an experimental ADC provided by Piramal Healthcare, was sprayed from 100 mM AmAc with the sample cone held at 200 V potential. Peaks corresponding to an intact ADC are observed in the ~ *m/z* 5500 – 7000 region; however, there is a significant amount of dissociation products present: one light chain + 1 drug molecule fragment (*m/z* 1800 – 3500) and two heavy chains + one light chain + n drug molecules fragment (*m/z* 7800 - 11000), making the DAR determination challenging. As 10 % (by volume) of TEAA is added to the sample (Figure 2.2b), only the intact ADC species are observed (*m/z* 7800 - 10500) as the complex does not undergo dissociation. Moreover, charge reduction shifts the peaks to a higher *m/z* region and as a consequence spectra interpretation and DAR derivation is rendered more straight forward.

2.2 Ion Mobility Mass Spectrometry (IM-MS)

Ion mobility mass spectrometry (IM-MS) experiments presented in this work were performed on an in-house modified Q-ToF 1 (Waters, Manchester, UK), known as the ‘MoQToF’[21] and on Synapt G2 HDMS and Synapt G2S HDMS instruments (Waters, Manchester, UK). Samples for IM-MS measurements were ionised by nESI in positive mode as described in section 2.1.2. A description of these instruments, as well as data acquisition and analysis of ‘MoQToF’ data is described in the subsequent sections.

2.2.1 Linear drift tube IM-MS – MoQToF

2.2.1.1 Instrument description

The linear drift tube IM-MS instrument (MoQ-ToF) is an in-house modified Q-ToF 1 which contains a 51 mm copper drift cell with temperature control capabilities. The drift chamber filled with a buffer gas is situated between the first transfer hexapole and the quadrupole analyser as highlighted in yellow in Figure 2.3. Typically, the drift cell is filled with helium gas at a pressure of 3.2 – 4.0 Torr (4.3 – 5.3 mBar) and a weak electric field is applied to propel the ions through the cell. The MoQ-ToF instrument can be operated either in MS or IM-MS mode. In the MS mode, ions formed in the nESI source are guided through a series of ion lenses and the drift cell towards the detector. In the IM-MS mode, analysis relies on trapping and then injection a pulse of ions to drift through the cell. A continuous beam of ions is produced by nESI source, the DC voltage on the ‘top hat’ ion gate lens (*d* in Figure 2.3) is raised to trap ions which are then pulsed out of hexapole in discrete “ion packets”. At regular intervals, this trapping voltage is lowered for several microseconds (40-100 μs) to inject the pulse into the drift cell. The frequency of this pulse is set using a Stanford DG535 digital delay generator (Stanford Systems, Sunnyvale, CA, USA) and is dependent on the ToF pusher period which in turn is dependent on *m*/*z* required for the ion species. For example, a pusher period of 160 μs is used to cover *m/z* range up to 8000. Therefore, any two mobility events occur every 200 x 160 μs = 32 ms, or at a frequency of 31.3 Hz (v = 1/t = 1/32 ms = 31.3 Hz). Ions drift through the cell and separate due to mobility. The small compact ions traverse faster than the large extended ions. On exiting of the drift cell, ions are refocused in the post-cell hexapole and travel though the quadrupole mass analyser to the ToF analyser and the MCP detector. Ion arrival time distributions (ATD) *i.e.* mobility spectra are recorded by synchronized release of ions into the drift cell, with one mobility separation event sampled 200 times *i.e.* pushes by the ToF.

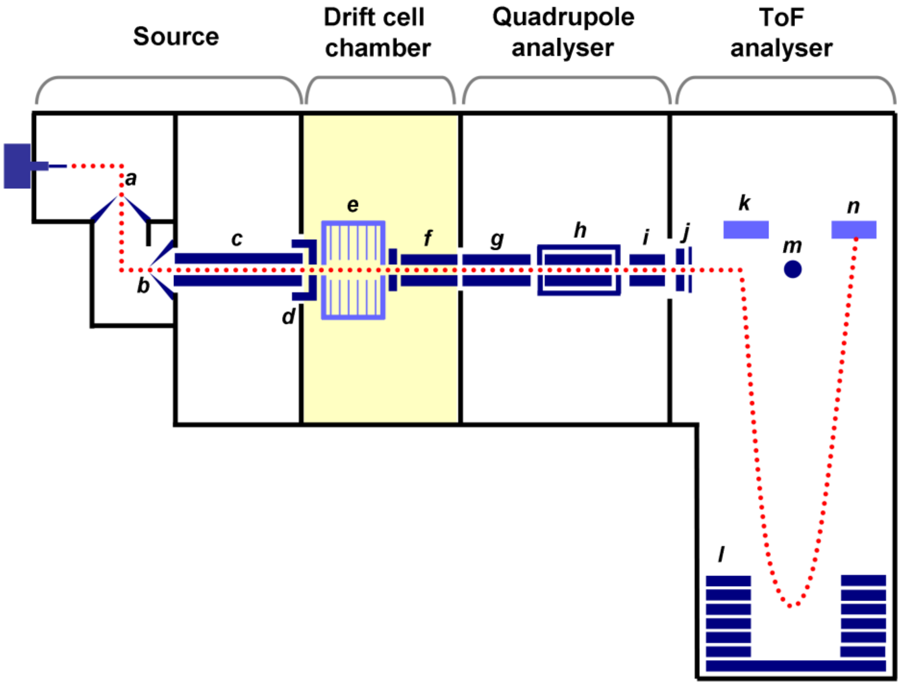

Figure 2.3 **Schematic of the linear drift tube ion mobility mass spectrometer 'MoQToF' illustrating the source region, the drift chamber, the quadrupole and the time-of-flight analysers. The drift chamber, highlighted in yellow, has been modified in-house to include the linear drift cell (e). The ion flight path is shown in red dotted line. Labelled instrument elements are: *a* - sample cone, *b* – extractor cone , *c* – pre-cell hexapole, *d* – top hat lens, *e* – drift cell, *f* – post-cell hexapole, *g* – quadrupole, *h* – collision cell, *i* – post-collision cell hexapole, *j* – acceleration and focusing lenses, *k* – pusher, *l* – reflectron, *m* – point detector (for quadrupole analyser), and *n* – MCP detector (for ToF analyser).**

The drift chamber is filled with the CP Grade helium gas (99.999%, BOC Speciality Gases Ltd, Guildford, UK) at a pressure of ~3.75 ± 0.02 Torr measured using a MKS Barotron (MKS Instruments, Andover, Massachusetts, USA). A precise pressure is recorded at the start and end of each measurement and is used in the calculations of CCS (± 5 % error). In addition to the differential pumping regions as in the Q-ToF Ultima API US described in the section 2.1.3., the MoQToF contains an additional vacuum chamber pumped by a 500 Ls^{-1} Pfeiffer TMH520 pump (Pfeiffer Vacuum Ltd., Newport Pagnell, UK), backed by a dual state Edwards E2M40 rotary pump (Edwards Vacuum, Crawley, UK) and an additional mechanical booster pump when the drift cell is filled with gas. Optimisation of pressure in the source region for improved transmission of large molecules, is achieved by throttling of the source rotary pump (Edwards E28) and the introduction of argon gas (99.998 %, BOC Speciality Gases Ltd, Guildford, UK) to the pre-cell hexapole chamber and control of its flow with a metering bellows-sealed valve. The typical pressures in each region, with the buffer gas in the cell, are: source ~ 3-8 × 10^{-1} mBar (adjusted by controlling the argon flow), analyser ~ 3 × 10^{-3} mBar, ToF ~ 5 × 10^{-7} mBar.

2.2.1.2 The drift cell and the temperature control of the drift cell region

The design of the drift cell is based on the previously reported by Bowers *et al*. at the University of California Santa Barbara, CA, USA.[22-24] The cell contains five copper drift rings separated by ceramic spacers housed within a copper block and the end cap which is also separated by a ceramic space ring (Figure 2.4). A potential difference between those elements is applied to achieve a linear drift field with a total drift length of 51 mm. Ions enter and exit the drift cell though 0.8 mm orifices in molybdenum discs enclosed on each site of the cell.

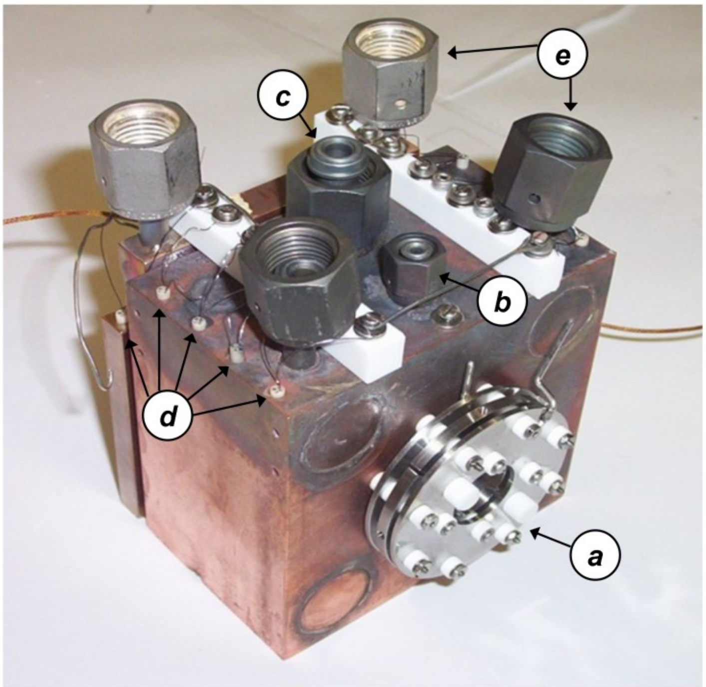

Figure 2.4 A photograph of the MoQToF drift cell showing: *a* - the Einzel lens stack, *b* – the buffer gas inlets, *c* – the buffer gas outlet, *d* – the ceramic heaters and *e* – the cooling lines.

The design of the drift cell allows for temperature control of the buffer drift gas and determination of temperature dependant absolute CCS. The cell can be heated up to 700 K *via* tantalum wire (0.25 mm diameter, Goodfellow Cambridge Ltd., Huntingdon, UK) wound ceramic rods (Kimball Physics Inc., Wilton, NH, USA) located in both the cell body (8 heaters) and the end cap (2 heaters). A current is supplied to the heaters by two external variable transformers, resulting in resistive heating of the cell copper block. Cooling of the cell is accomplished by passing chilled nitrogen gas though the channels inside the copper block. The nitrogen gas is cooled by passing it though a stainless steel tubular coil contained in a thermally insulated Dewar flask filled with liquid nitrogen. The temperature of the drift cell is carefully monitored using three k-type thermocouples (one situated on the cell body and two on the end cap) read on an Omega CN1001TC thermocouple controller. Temperature is recorded before and after each measurement, and the average value is used in the calculations of CCS.

The voltages applied to the drift cell and associated optics (Figure 2.5a) are supplied *via* an in-house build power supply. As the ions are pulsed from the ‘top hat’ (TH1) lens, they are focused into the entrance orifice of the cell *via* a stack of three stainless steel cylindrical lenses (L1, L2 and L3) referred to as the Einzel lens stack. The pre-drift cell lenses (H1, TH1, L1, L2 and L3) are referenced to ‘cell body voltage 1’ (C1), whereas

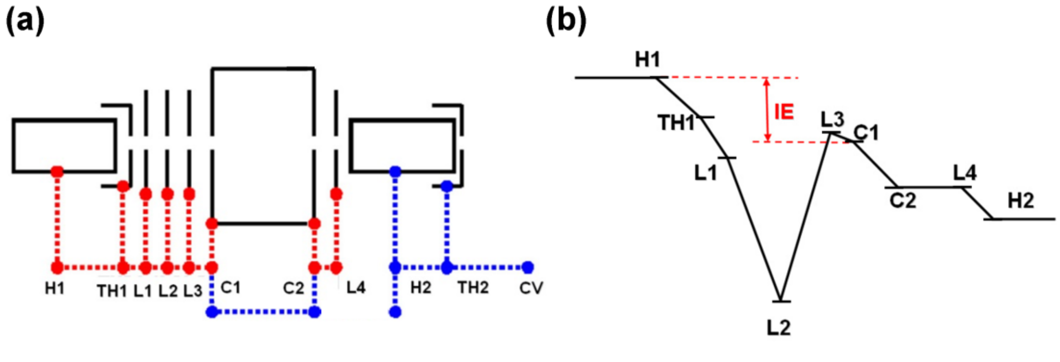

Figure 2.5 (a) Schematic of the MoQToF drift cell with surrounding lenses. H1 – the pre-cell hexapole, H2 – the post-cell hexapole, TH1 – the pre-cell ‘top hat’ lens, TH2 – the post-cell ‘top-hat’ lens, L1, L2 and L3 – the pre-cell lenses, L4 – the post-cell lens, C1 – the ‘cell body one’, C2 – the cell body two – end cap. (b) The potential gradient along the drift cell and associated optics. The potential difference between H1 and C1 is the energy with which ions are injected into the drift cell (IE) indicated here with a red double-headed arrow.

the post-drift cell lens L4 is referenced to the end cap voltage (C2). H2 and TH2 float above the collision cell voltage (CV) which is set from the instrument tuning page in the MassLynx software; C2 and H1 are referenced to this and the source, respectively. Typically used drift cell voltages and their working ranges are reported in Table 2.2 below.

Table 2.2 Voltage requirements and typical drift cell lens stack settings used in a IM-MS experiments on the MoQToF instrument. *The C1 voltage is decreased in 5-10 V intervals to acquire IM data at several distinct drift voltages.

Lens	Voltage range	Potential *wrt.* C1 or C2* / V	Actual voltage/ V
H1	0 to 200	30 - 35	C1 + H1
TH1	0 to 200	2 - 30	C1 + TH1
L1	0 to -350	-50 - (-5)	C1 + L1
L2	0 to -350	-180 - (-80)	C1 + L2
L3	+50 to -50	23 - 30	C1 + L3
C1*	0 to 200	70	C1
C2	0 to 75	10*	C2
L4	+50 to -50	-4 – 5*	C2 + L4

The kinetic energy with which ion are injected into the drift cell in defined as the potential difference between the pre-cell hexapole (H1) and the first drift cell lens, depicted in red arrow (IE) in Figure 2.5b. This energy can be varied within 25 V to 54 V, and is adjusted dependent on the ion species analyzed and experimental design. The injection energy is kept low to preserve the native protein structure and to minimise the shortening of the drift region as ions injected from higher energies will penetrate deeper into the drift cell before starting to drift. In the work presented here the values were kept between 31-36 V dependent on the ion species.

2.2.1.3 Typical instrumental parameters

The typical instrumental settings used in the work presented in this thesis are tabulated in Table 2.3.

Table 2.3 Typical instrumental parameters for the MoQToF IM-MS instrument in the positive mode.

Parameter	Value	Comment
Capillary /kV	1.3 – 2.0	
Cone /V	40 – 200	adjusted accordingly to the sample and experimental design
Extractor /V	110-140	at the drift voltage of 60 V (this value is decreased as the DV is lowered during the IM-MS experiment)
RF Lens /V	2.40	
Source Temperature /°C	25 – 80	adjusted accordingly to the sample
LM Resolution /V	4.4	
HM Resolution /V	4.4	
Collision Energy /V	4.0	
Ion Energy /V	0.5	
Steering /V	-2.0	
Entrance /V	43.3	
Pre-filter /V	5.0	
Transport /V	3.0	
Aperture2 /V	5.7	
Acceleration /V	200	
Focus /V	0	
Tube Lens /V	90	
Guard /V	44.1	
ToF /V	7.20	
Reflectron /V	35.00	
Pusher Cycle Time / µs	70 – 200	adjusted accordingly to *m/z* range
Multiplier/ Hz	6250	at pusher cycle time = 160 µs
MCP /V	2400 or 3000*	* higher MCP voltage used prior to the instrument maintenance service
TDC Start /mV	300	
TDC Stop /mV	40	
TDC Threshold	0.00	

2.2.1.4 Data acquisition and analysis: an example

The following IM-MS experiment is provided as an example of data acquisition and data analysis obtained from the in-house modified MoQToF instrument. An Fc-hinge fragment of an immunoglobulin G4, IgG4 (~54 kDa) was analysed by ion-mobility mass spectrometry. In-depth description of immunoglobulin classification and structure can be found in Chapter 3. The protein sample was kindly provided by UCB Pharma, and on the day of analysis the sample buffer was exchanged to 100 mM ammonium acetate, pH 6.8. 40 µM IgG4 Fc-hinge sample was ionised by nESI as described in section 2.1.2. The mass spectrum shown in Figure 2.6, displays a narrow charge state distribution centred at the 13+ charge state (*m/z* 4130).

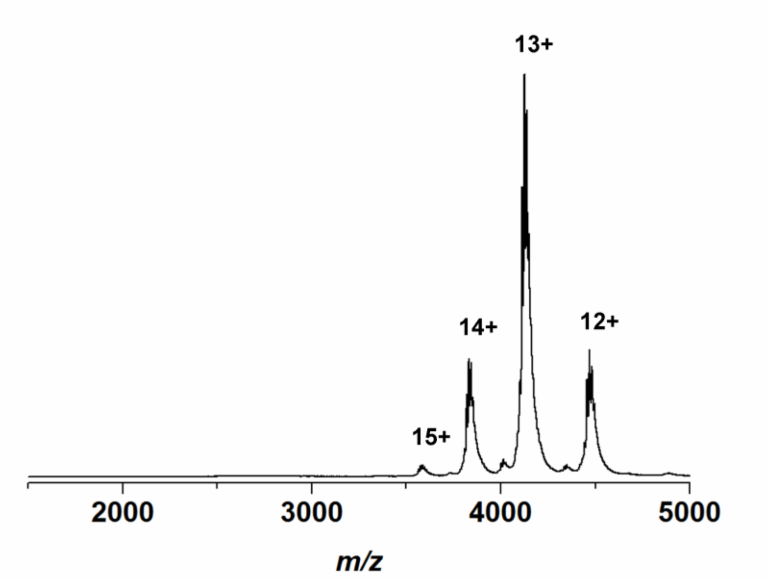

Figure 2.6 nESI mass spectrum of 40 µM IgG4 Fc-hinge fragment in 100 mM ammonium acetate at pH 6.8, acquired on MoQToF instrument at 300 K. The theoretical mass calculated based on the amino acid sequence is 52 167 Da, measured mass is 53 454 Da; the deviation from the theoretical mass can be assigned to the presence of two *N*-glycans and residual solvent.

In the IM-MS experiment, a total arrival time distribution (tATD), corresponding to one mobility separation, is generated every 200 MS scans (Figure 2.7). Spectra are acquired for at least fifteen pulses per each drift voltage. Some ion species, usually large molecules with poorer transmission, require more pulses to be collected for enhanced signal intensity once summed. Several IM experiments are performed at various drift voltages applied across the drift cell, ranging from 60 to 15 V in 5-10 V intervals, typically measurements are carried out at 60, 45, 35, 30, 25, and 15 V. As the drift voltage is lowered, the extractor cone voltage is adjusted by the same number of volts to preserve the field integrity between source and drift cell. Along with tATD, pressure and temperature is recorded at the start and end of each set of scans and averaged for further calculations as will be described below.

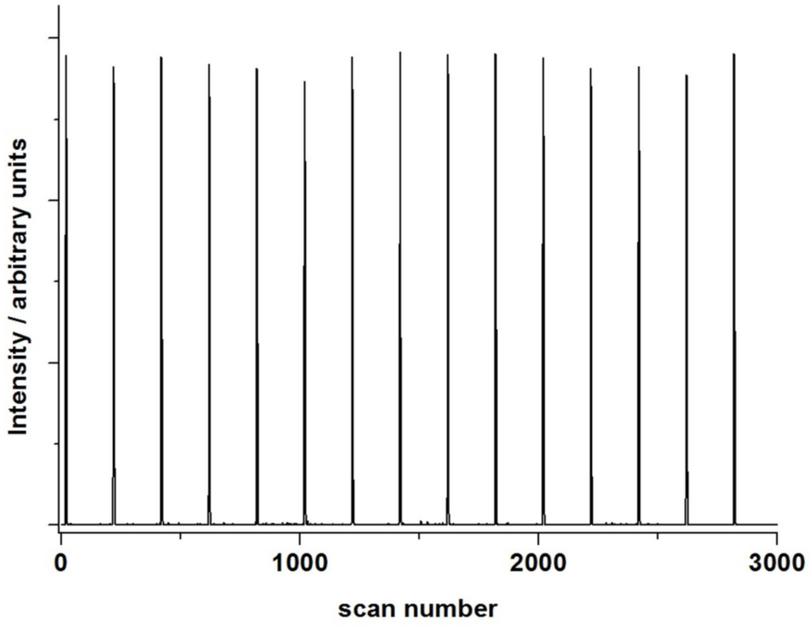

Figure 2.7 Total ion ATD at a drift voltage of 35 V for the IgG4 Fc-hinge fragment. Each peak is a collection of 200 scans.

From the tATD, a mass spectrum can be generated and a deconvoluted ATD for each *m/z* peak can be extracted. Deconvoluted ATD peaks are summed to enhance data quality. An ATD extracted for the most intense charge state (13+) of the IgG4 Fc-hinge fragment is shown in Figure 2.8a. The average scan number is calculated in Origin 8.5.1 graphing software (OriginLab, Northampton, MA, USA) by fitting a Gaussian distribution and determining the midpoint value. For many species, especially the dynamic and flexible systems, the individual ATD are broad and peaks are not base line resolved indicating the presence of potential multiple closely related conformers. The Gaussian function is used:

$$y = y_0 + \frac{A}{w\sqrt{\frac{\pi}{2}}} e^{-2\frac{(x-x_c)^2}{w^2}} \qquad (\textit{Equation 2.1})$$

where offset $y_0 = 0$, A is the area, x_c is the centre of the fitted peak and w is the peak width; to resolve these distributions. The maxima values for the resulting peaks are used for further calculations (Figure 2.8b).

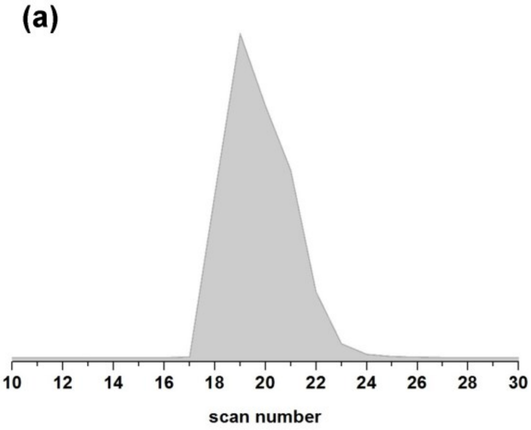

Figure 2.8 The 'raw' ATD extracted for the +13 charge state of the IgG4 Fc-hinge fragment [M+13H]$^{13+}$ (~*m/z* 4130) at 300 K and DV – 35V (a), along with the Gaussian fitting to the ATD data points to elucidate average ATD for population of ions (b); the cumulative peak fit (blue line) is the sum of the Gaussian fits (red and green lines) and closely approximates the experimental ATD data.

An average arrival time (t_a) is obtained by multiplication of the average scan number (x_c from Equation 2.1) by the MS pusher period used in the experiment. Average arrival time (t_a) corresponds to the time ions take to travel through the drift cell (the drift time, t_d) plus the time ions spent outside the drift cell (known as the dead time, t_0). Next, the arrival time (t_a) is plotted as function of pressure over drift voltage (P/V) and a linear fit to the data-points is made (Figure 2.9), which should have a high R^2 value (> 0.999). The y-intercept of this fitted line provides the instrumental 'dead time' (t_0), and the slope of the gradient is inversely proportional to the reduced mobility (K_0) in the following way:

$$t_d = t_a - t_0 = \frac{L^2 T_0 P}{K_0 T P_0 V} \qquad (\textit{Equation 2.2})$$

where L is the length of the tube (0.051 m), V is the drift voltage, P is the pressure, P_0 is 760 Torr, T is the temperature and T_0 is 273.15 K. The rotationally-averaged collision cross section (Ω) can be then calculated from K_0 knowing that:

$$\Omega = \frac{3ze}{16N}\left(\frac{2\pi}{\mu k_B T}\right)^{1/2}\frac{1}{K_0} \qquad (Equation\ 2.3)$$

where z is the integer ion charge, e is electron charge (1.602×10^{-19} C), N is the number density of the buffer gas, μ is the reduced mass of the analyte (in kg) and the buffer gas and k_B is the Boltzmann constant (1.381×10^{-23} J K^{-1}). Each complete IM-MS experiment is performed at least twice and the average collision cross sections are calculated for each charge state.

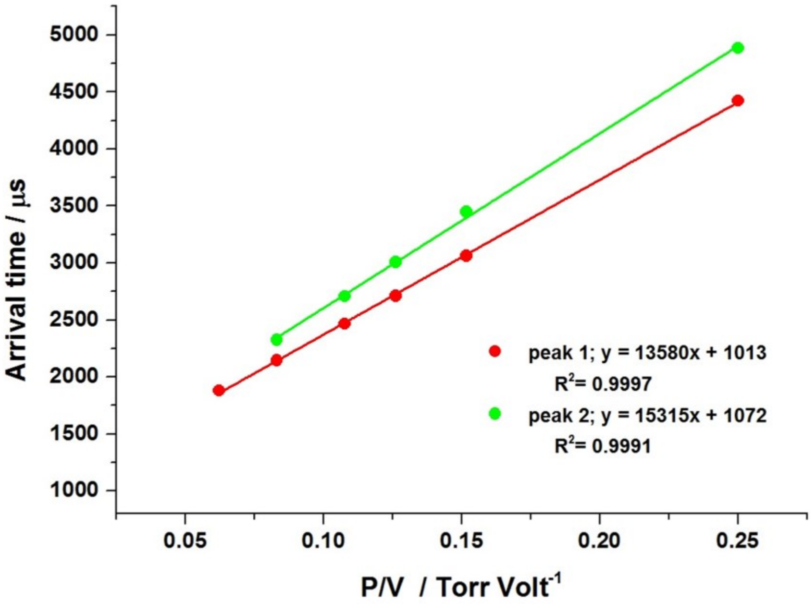

Figure 2.9 Plot of average arrival times (µs) versus *P/V* (Torr Volt^{-1}) for the IgG4 Fc-hinge fragment [M+13H]$^{13+}$ ion at 300 K. The slope of the linear fit is inversely proportional to the reduced mobility K_0, and the intercept gives the instrument dead time, t_d.

Protein complexes investigated in the work presented in this thesis are large and/or multimeric dynamic systems displaying broad ATD. In the literature, CCS are often reported as discrete values. Here however, the resulting ATD show broad and complex profile due to presence of a number of closely related dynamic conformational families not resolvable at this experimental time scale and temperature. Assigning two or more discrete arrival time maxima (hence CCS) would not reflect the experimentally observed conformation occupancy and would risk biasing interpretation towards the presence of more defined structures. Instead experimental results are reported as the entire arrival distributions acquired for each charge state. To make comparison of the results obtained at different experimental conditions possible, ATD are converted into CCS distribution profiles (CCSD). To make such conversion possible, the instrumental dead time (t_o) needs to be known. Instead of using the strategy described earlier of fitting individual Gaussian peaks to match the cumulative peak with the experimental data to obtain the maxima for each conformational family, a median scan number value of the total distribution is used to determine t_o from the P/V plot . Next, all the experimental data points recorded are converted into CCS using Equation 2.3, to yield the CCSD profiles.

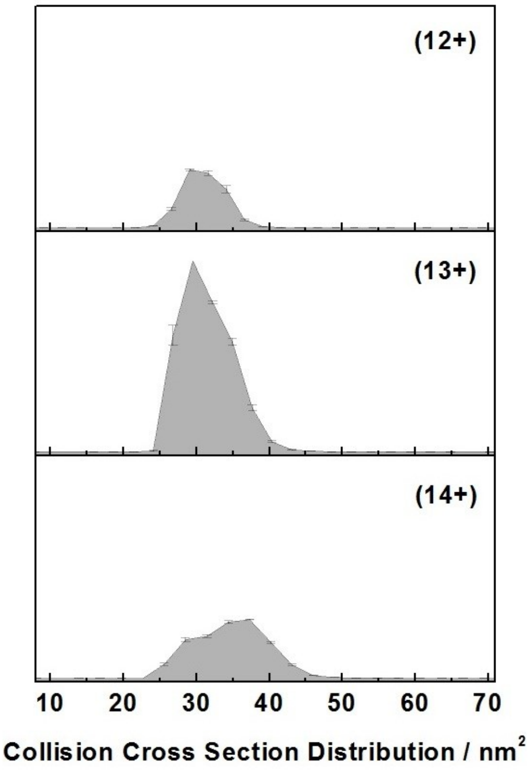

Figure 2.10 Collision cross section distribution profiles (CCSD in nm^2) for the three charge states of highest intensity for the IgG4 Fc-hinge fragment acquired at 300 K, DV = 35 V, and normalized to the spectral intensity.

Figure 2.10 shows such CCSD for three charge states of the IgG4 Fc-hinge fragment. Immunoglobulins are known to be highly dynamic molecules somewhat hindering full structural characterization using classical methods such as NMR spectroscopy (due the size of the intact molecule) or x-ray crystallography (due to the need for sample crystallisation). IM-MS provides shape defining parameters, a very high mass limit of the analyte and no need for crystallisation, rendering it highly suitable to study the higher order structure of large dynamic proteins such as IgGs. Gas-phase conformations of the IgG4 Fc-hinge fragment probed with linear DT-IM-IM show broad CCSD populated from ~22 to 46 nm^2 suggesting multiple indistinguishable conformations, and/or dynamics in the time scale of the experiment. In comparison to other proteins of similar size, the CCSD width is significantly broader for the Fc-hinge fragments as well as the intact IgG molecules. Insights into antibody gas-phase dynamics from IM-MS and molecular dynamics (MD) as well as the effect of the buffer gas temperature on the CCSD of intact IgGs will be discussed in Chapters 3 and 5, respectively.

2.2.2 Travelling wave IM-MS – Synapt G2 HDMS

TWIM-IM-MS experiments on ATP-phosporibosyltransferase presented in Chapter 6, were performed on Synapt G2Si HDMS (at Waters Corporation, Floats Road, Manchester, UK) and Synapt G2 HDMS (at the Manchester Institute of Biotechnology, Manchester, UK). Samples for IM-MS measurements were ionised by nESI in positive mode as described in section 2.1.2.

2.2.2.1 Instrument layout and operation

In 2006, Waters Micromass Technologies introduced the first commercially available ion-mobility mass spectrometer called the Synapt HDMS. In the subsequent years, upgraded versions of the higher resolution instrument mediated by an altered drift cell with higher pressure and drift voltage by inclusion of a helium-filled entry cell prior to the T-wave IMS cell (Synapt G2 HDMS, Figure 2.11) and the StepWave device (Synapt G2S, Figure 2.13) were released. Synapt HDMS instruments have hybrid quadrupole/IM/ToF geometry where the T-wave *i.e.* travelling wave ion guide (TWIG) technology is used to separate ions based on their conformations. Unlike the MoQToF described above the TWIG is located after quadrupole analyser. Ions generated using nESI pass *via* a ‘Z-spray’ and are subsequently transferred though a T-wave ion guide and a quadrupole mass filter to the IM section of the instrument composed of three travelling wave ion guides. The first compartment, the trap T-wave, accumulates ions as the previous mobility separation is taking place. Next, the ions are released in a packet into the IMS T-wave filled with nitrogen gas as visualized in Figure 2.12.

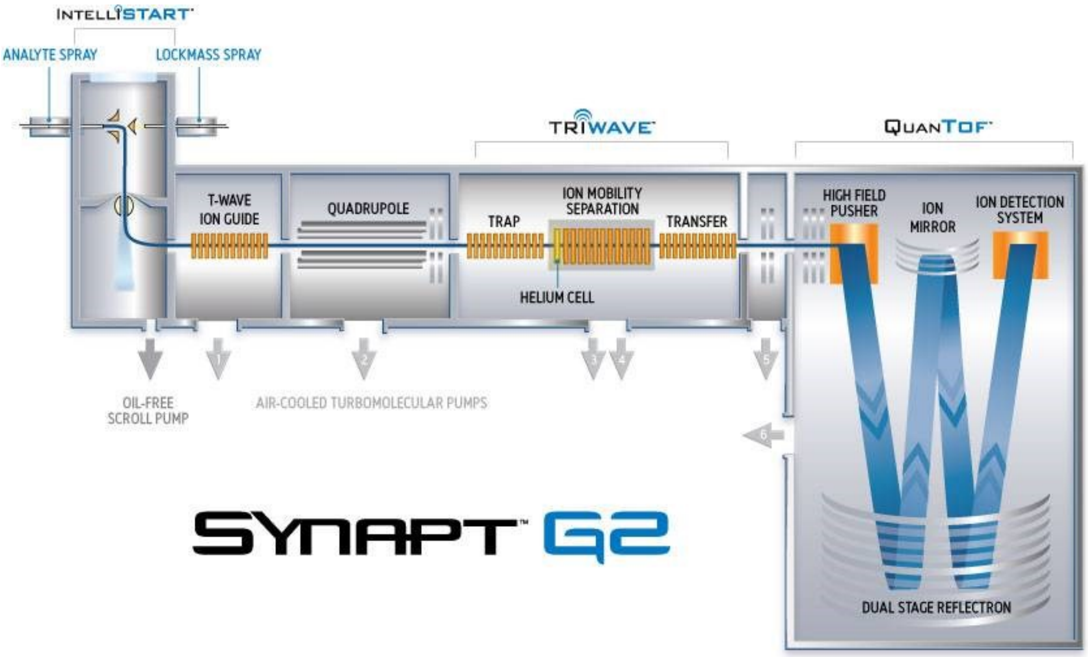

Figure 2.11 Schematic of the Waters Synapt G2 HDMS instrument. Image adapted from the Waters web page [25].

This event is analogous to the injection of ions from the pre-cell hexapole into the drift cell on the MoQToF instrument. Here however, the following mobility separation is performed as the repeating DC pulses drive ions through the cell. Increased mobility resolution can be achieved by use of higher N_2 pressure and higher T-wave pulse amplitudes. Nevertheless, increasing the pressure alone might lead to reduction in signal intensity, fragmentation of molecules or distortion of structure while working with native state proteins. For those reasons, the second generation Synapt G2 HDMS (Figure 2.11) has been implemented with an interface high pressure helium-filled cell situated just in front of the IMS cell. The helium-filled cell balances N_2 pressure in the main cell, maximizes the transmission of ions into the mobility cell and promotes ion cooling. From there mobility separated ions are delivered to the ToF mass analyzer though the transfer T-wave. As in the MoQToF instrument, ion arrival time distributions are recorded *via* synchronised mass spectral acquisition with the gated release of ions from the trap T-wave cell. Ion detection is accomplished by a system combining ultrafast electron multiplier and with a novel analog-to-digital conversion (ADC) detector electronics.

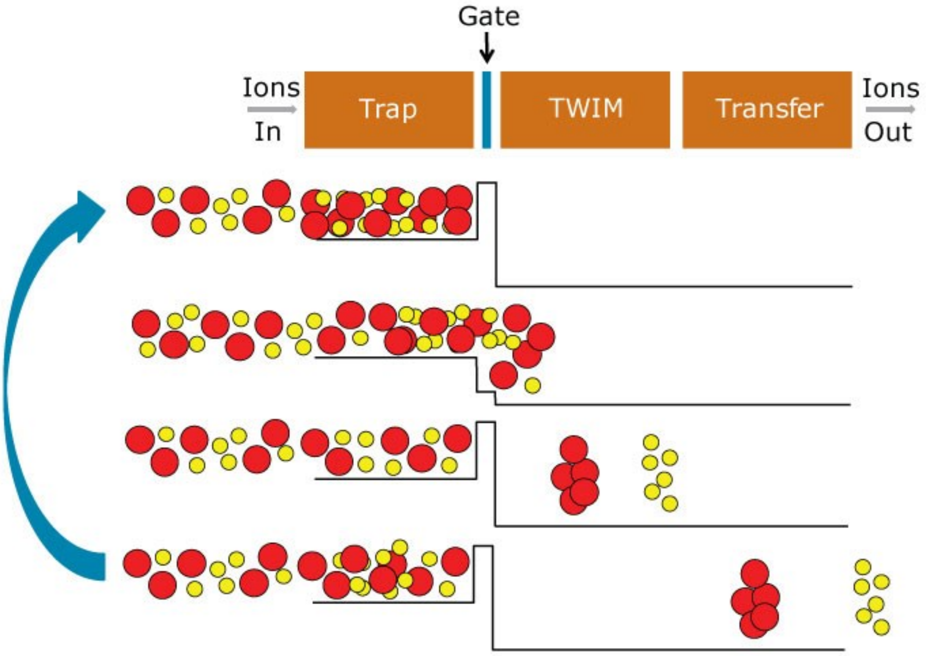

Figure 2.12 During the ion mobility experiment on a Synapt HDMS instrument, ions are accumulated in the trap T-wave cell and subsequently gate released in ion pockets into the TWIM IMS cell, where the mobility separation occurs. Mobility separated ions are further transferred to the ToF mass analyser *via* transfer T-wave. This process is continually repeated on a ten of millisecond time scale. Image adapted from one found on the Waters web site [25].

Further increase in instrument sensitivity has been achieved with the new off-axis ion guide design in the source region, the StepWave introduced with the Synapt G2S HDMS instrument. The new design, based on stacked ring ion guide technology, actively extracts the ion beam (indicated in yellow in Figure 2.13) into the upper stage,

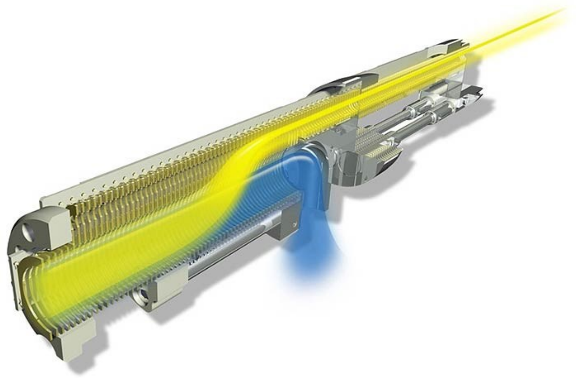

Figure 2.13 Illustration of the StepWave device implemented on the Waters Synapt G2S HDMS instrument. The off-axis ion source technology was designed to maximise ion transmission from the source to the mass analyser. Image adapted from one found on the Waters web site [25].

and allows for removal of neutral species and excess solvent to the exhaust (in blue). This feature not only maximises ion transmission from the source to the mass analyser but also increases method robustness as the upper ion guide is protected from the majority of contaminants.

Unlike the linear DT based arrival times, the physical relationship between T-wave based drift time and CCS have not been fully understood yet and the fundamentals of TWIMS have been explained only qualitatively.[26] Data obtained from Synapt HDMS instrument are commonly externally calibrated against the DT-IM-MS data of molecules with similar arrival times and masses.[27-29] Normalised CCS for charge and reduced mass are plotted versus arrival times (excluding time spent outside of the TWIMS region) creating power-series fit calibration curve. The calibration is valid given that the mobilities *i.e.* corrected arrival times lie within the mobility range observed for the calibrant.

The main parameters that allow successful ion transport through the IMS cell are wave height (V) and wave velocity (ms^{-1}). These experimental parameters affect the measured CCS.[30] In the work presented in Chapter 6, CCS have been determined based on MoQToF measurements; whereas T-wave IMS based data is presented in terms of arrival time and comparison among the samples is made based on data acquired under identical experimental conditions and instrumental parameters.

2.2.2.2 Travelling wave ion guide technology

Synapt HDMS instruments use stacked ring ion guides (SRIG) located between the quadrupole and the ToF analyser. The T-wave device, shown in Figure 2.14a, is composed of a series of ring-shaped electrodes which are supported on printed circuit boards supplying radio frequency (RF) and direct current (DC) voltages. The ions are radially confined within the device by application of opposite phases of RF voltage to adjacent rings, as they progress along the axis (Figure 2.14b)[31]. The ions 'surf' though the IMS cell due to application of transient DC pulse superimposed on the RF voltage, what creates a moving electric field – the travelling wave. At elevated N_2 gas pressure (~0.5 mBar in the first generation and ~2.5 mBar in the second generation instruments),

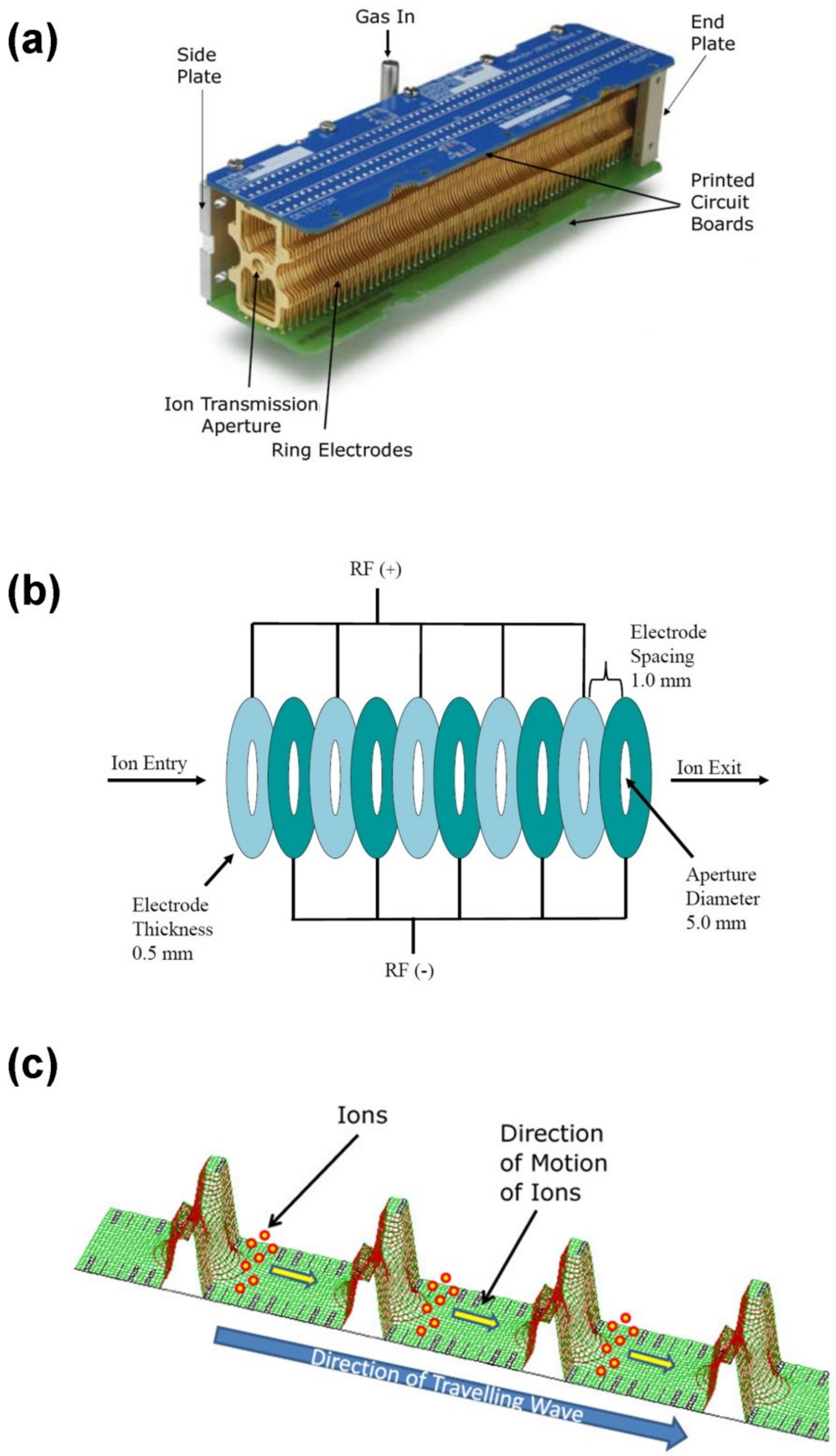

Figure 2.14 (a) A photograph of the T-wave device consisting of series of transmission ring electrodes; image adapted from the Waters web page[25]; (b) Schematic diagram of an RF-only stacked ring ion guide (SRIG); image adopted from Giles *et al.*, 2004[32]; (c) ions 'surfing' on the travelling wave shown with a computer simulation in SIMION software, image reproduced from one found on the Waters web site[25].

ion separation occurs based on their mobility and due to collisions with the buffer gas. The ions roll over the wave as shown in Figure 2.14c; species with higher mobility roll over the wave less often in comparison to ions with lower mobility; and are propelled through the device with shorter drift times. Ions with lower mobility are displaced over the wave crest to the previous potential well, and remain there until the next wave carries them forward.

2.2.2.3 Typical instrumental parameters

As with any other nESI-MS instrumentation, optimisation of source parameters (capillary and cone voltage) as well as bias potential is essential for preservation of native-like protein structures and non-covalent complexes. As previously, the optimisation of source pressure helps the transmission of large ions. The main parameters allowing successful ion transport through the cell are wave height (V), wave velocity (ms^{-1}) and gas pressure. Optimization of the gas flow ratio between the He-filled pre-cell and N_2 IMS cell gas flow allows for improved mobility separation.[33] Table 2.4, lists the typical experimental settings employed in experiments performed on the Synapt G2 HDMS and Synapt G2S HDMS instruments. The experimental parameters were screened to achieve an optimum signal and prevent any instrument-induced structural rearrangements.

Table 2.4 Typical instrumental parameters for Synapt G2 HDMS and Synapt G2S HDMS instruments in the positive mode.

Parameter	Synapt G2 HDMS	Synapt G2S HDMS
Capillary / kV	1.66	1.67
Cone /V	99	99
Extractor /V	3.0	2.5
Source Temperature /°C	20	20
LM Resolution /V	2.0	4.9
HM Resolution /V	15.0	15.3
Aperture1	0.0	0.0
Pre-filter /V	2.0	2.0
Ion energy /V	1.0	1.0
Trap Collision Energy* /V	10.0	5.6
Transfer Collision Energy /V	0.0	2.0

Parameter	Synapt G2 HDMS	Synapt G2S HDMS
Source Gas Flow / mL/min	0.0	0.0
Trap Gas Flow / mL/min	0.40	5.0
He Gas Flow / mL/min	180.0	180.0
IMS Gas Flow / mL/min	90.0	90.0
Detector	2875	2700
Collision Energy /V	4.0	4.0
Acceleration1	70.0	70. 0
Acceleration2	200.0	200.0
Aperture2	40.0	70.0
Transport1	70.0	70.0
Transport2	70.0	70.0
Steering	0.0	0.00
Tube Lens	45	75
Pusher	1900.0	1900.0
Puller	1370.0	1370.0
Collector	50	50
Collector Pulse	10.0	10.0
Entrance	55	62
Flight Tube /kV	10.00	10.00
Reflectron /kV	3.780	3.780
Trap DC Bias	45.0	60.1
Trap DC Exit	3.0	-4.9
IMS DC Entrance	25.0	20.0
He Cell DC	35.0	50.0
He Cell Exit	-5.0	-20.0
IMS Bias	3.0	5.0
IMS DC Exit	0.0	0.0
Transfer DC Entrance	4.0	5.0
Transfer DC Exit	5.0	15.0
Trap Wave Velocity/ m/s	508	311
Trap Wave Height /V	8.0	7.0
IMS Wave Velocity / m/s	550	617
IMS Wave Height /V	40.0	40.0
Transfer Wave Velocity / m/s	508	75

Parameter	Synapt G2 HDMS	Synapt G2S HDMS
Transfer Wave Height /V	0.1	5.0
Step Wave 1 In Velocity / m/s	NA	300.0
Step Wave 1 In Height /V	NA	10.0
Step Wave 1 Out Velocity m/s	NA	300.0
Step Wave 1 Out Height /V	NA	1.0
Step Wave 2 Velocity/ m/s	NA	300.0
Step Wave 2 Height /V	NA	0.0
Backing Pressure /mBar	7.53	8.90
Source Pressure /mBar	3.86×10^{-3}	4.42×10^{-3}
Trap Pressure /mBar	2.74×10^{-2}	2.39×10^{-2}
He Cell Pressure /mBar	1.41×10^{3}	1.32×10^{3}
IMS Pressure /mBar	3.65	1.91
Transfer Pressure /mBar	1.00×10^{-6}	2.15×10^{-2}
ToF Pressure /mBar	1.03×10^{-6}	1.51×10^{-6}

* increased stepwise in 10 V intervals for the CID experiments

2.3 Computational Techniques: Molecular Dynamics and Estimation of CCS from PDB Structures

All MD calculations and estimation of CCS from the PDB structures presented in this thesis were performed by Dr Massimiliano Porrini at the Institute Européen de Chimie et Biologie (IECB) in Pessac, France.

The experimentally derived DT-IM-MS based CCS can be compared to the theoretical CCS of protein structures obtained *via* other biophysical methods such as NMR spectroscopy, x-ray crystallography, electron microscopy or molecular dynamics.[34] The input x-ray crystallography structure coordinate files of intact IgGs (1IGT, 1IGY and 1HZH – work presented in Chapter 3) and MtATP-phosporibosyltransferase (1NH7 and 1NH8 – work presented in Chapter 6) were taken from the online database - the Protein Data Bank (PDB)[35].

X-ray crystallography usually cannot resolve positions of hydrogen atoms. As the structure and function of proteins and peptides is highly dependent on the protonation state of its amino acid building blocks, position of all hydrogen atoms and any protons needs to be assigned prior to any molecular modeling. This can be achieved by using platforms such as the H++ server [36-39], or Amber molecular modeling package[40] by predicting the protonation state (pK) of ionisable groups within the molecule. Protons are added to the output files which are then used for further molecular modeling.

For the MD results reported in Chapter 3, after adding hydrogen atoms, structures are minimized *in vacuo* with the sander module of Amber11[40], implementing a radial cut-off of 999 Å and Amber99SB-ILDN force field.[41] Theoretical CCS are calculated with each of the three methods described in Chapter 1, implemented in the MOBCAL code[42,43], with the trajectory method (TJM)[44] appropriately modified to handle large systems such as these studied in this thesis. The less accurate methods: the projection approximation (PA)[45] and the exact sphere scattering (EHSS)[43,46] are included in this work for comparison with other more approximate methods; results from TJM are most reliable and most robust with respect to comparison to the coordinates.[47] To follow the evolution of dynamics in the gas-phase, the structures are firstly gradually heated up to 300 K, utilizing a Langevin thermostat (damping coefficient of 2 ps^{-1}) with a time-step of 1.0 fs, and then subjected to a constant temperature (300 K) molecular dynamics (MD) run of 10 ns, again with Langevin thermostat. Damping coefficient, radial cut-off, force field and time-step were the same as these described above, and the simulation software package utilized was NAMD 2.9.[48] The observables are computed to follow conformational rearrangements of the proteins studied are the backbone root mean square deviation (RMSD), the radius of gyration (R*g*) and the rotationally averaged CCS. The latter are calculated with a simulation time increment of every few ns intervals to follow the gas-phase dynamics.

2.4 Hydrogen Deuterium Exchange Mass Spectrometry (HDX-MS)

Even though x-ray crystallography and cryo-electron microscopy provide invaluable snapshots of static structures; a complementary method reflecting structural dynamics in physiologically relevant solvent environment is needed to fully understand protein behaviour. HDX is a chemical phenomenon in which labile hydrogen atoms at backbone amide positions in the protein exchange with deuterium atoms in a surrounding solvent or gas and these changes can be measured with MS, as it was described in Chapter 1.[49] HDX-MS has been successfully used to study higher order structure of biopharmaceuticals,[50] epitope mapping,[51,52] conformational changes,[53,54] protein dynamics[55,56] or allosteric interactions.[57,58]

Experimental data presented in Chapter 6 of this thesis was collected on the Waters HDX module with nanoAcquity UPLC and Synapt G2 mass spectrometer, equipped with a LEAP-PAL robotics system at UCB Pharma, Slough, UK. Data analysis was performed using the ProteinLynx Global Server (PLGS) v2.5 and DynamX Data Analysis software v2.0 (Waters Corporation, Manchester, UK). The deuterium update protein maps were created in the PyMOL Molecular Graphics System, V1.5.0.4 (Schrödinger, LLC., Portland, OR, USA). Experimental set-up and data analysis were performed with help of Dr Rebecca J Burnley from UCB Pharma.

2.4.1 Instrumental set-up

An automated workflow, from sample preparation to data processing, results in optimal use of experimental time. An automated sample injection system (LEAP-PAL robotics system) for sample labeling, quenching and digestion on a pepsin column, schedules the experiments and allows for three replicas to be run overnight on a protein even of 200 kDa size, significantly reducing the human labour required. The workflow of a typical HDX experiment using Waters HDX automated system is shown in Figure 2.15. Proteins are prepared in the aqueous buffers at a desired pH (usually pH 7 and above), then diluted 20 fold into phosphate buffer in H_2O (for undeuterated analysis) or D_2O (for deuterated analysis), with use of the robotics system. Next, mixtures are incubated at

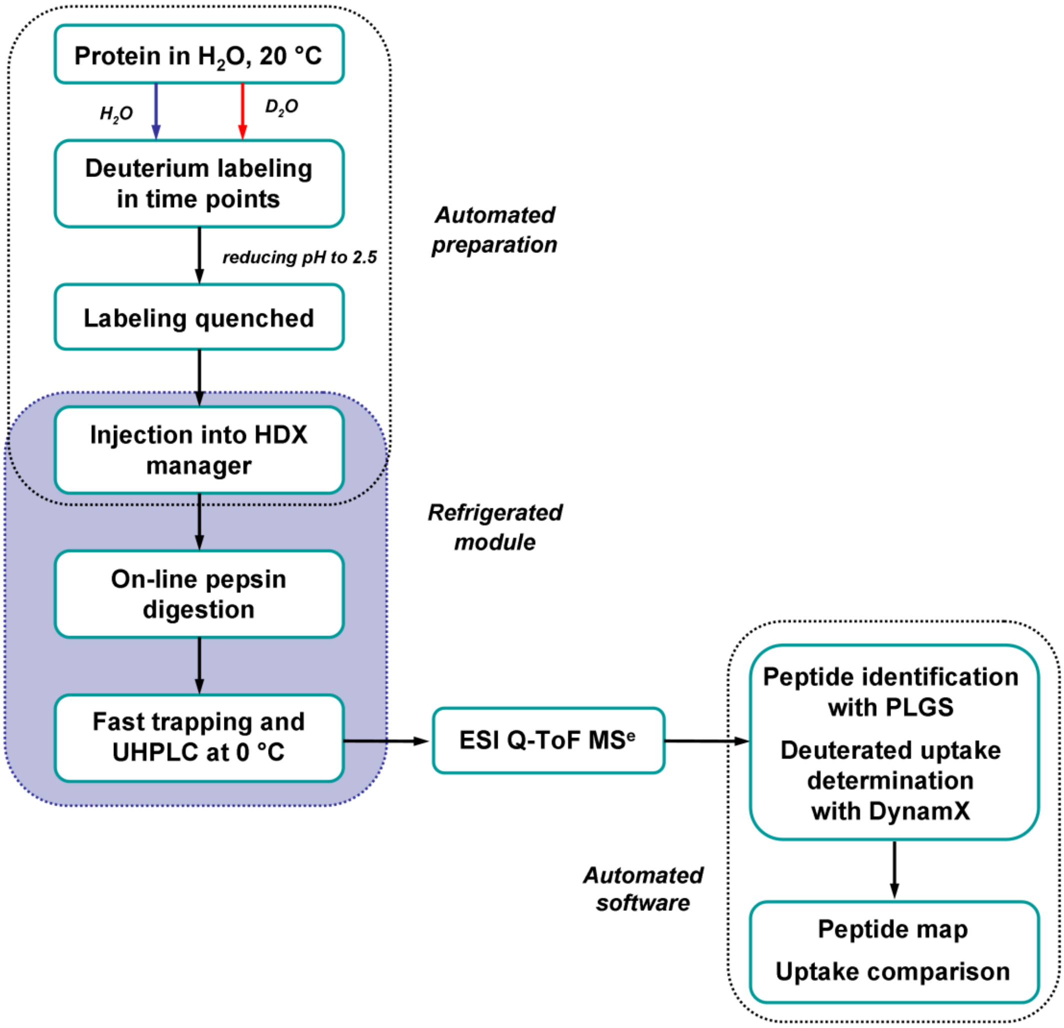

Figure 2.15 Workflow of a hydrogen-deuterium exchange mass spectrometry (HDX-MS) experiment using the Waters nanoACQUITY UPLC system with HDX technology.

20°C in the deuterated buffer for a specified amount of time to produce a labeling time-course. The labeling reaction is quenched at various time points by reducing the pH to 2.5. Next, the denaturing agents guanidine chloride (Gdn-HCl) and *tris*(2-carboxyethyl)phosphine (TCEP) are added to reduce the disulfide bonds. Once the HDX reaction is chemically quenched, the HDX Manger injects samples into the pepsin column for peptic digestion; here everything is performed under properly controlled temperature and pH conditions. If intact analysis *i.e.* global HDX data is required, the sample bypasses the pepsin column and proceeds directly onto the trapping column and then analytical column. The non-specific cleaving nature of pepsin produces overlapping peptides and increases the sequence coverage of the studied protein. Maintaining temperatures at 0 ± 1 °C assures that the back-exchange is kept to an absolute minimum. Resulting peptides are separated by UPLC and further fragmented and identified in the mass spectrometer. If necessary, IM separation can be used to provide additional, orthogonal separation to chromatography and mass dimensions for overlapping ion species. Peptides are identified and the deuterium update is determined using the PLGS database search and the DynamX Data Analysis software (Waters Corporation, Manchester, UK), respectively. Each experiment is performed in triplicate and the average values are reported.

2.4.2 Data analysis using PLGS and DynamX software

Manual analysis of HDX-MS data produced across multiple time points, multiple species and few replicas is a time consuming task. Deuterium uptake at a peptide level needs to be determined for hundreds of peptides. With the use of automated PLGS search and DynamX software, the data processing time is reduced.

Firstly, peptides are identified with the PLGS database search and the output files are created. These output files and the raw MS data are imported into the DynamX software. DynamX software determines deuterium uptake of each peptide from the undeuterated data versus the deuterated data at various time-points. Deuterium update of each peptide identified is plotted as a function of exposure time to create the uptake curves. To ensure consistency in monitoring HDX, the software tracks all peptides reproducibly found in experimental replicates. Now, the data can be visualized by means of ‘butterfly charts’, difference plots and heat maps (Figure 2.16).

Figure 2.16 shows a workflow of an HDX data analysis in the DynamX software. The list of peptides identified through a PLGS search of a sample protein is displayed (Figure 2.16a). The uptake curves (upper right hand corner panel of Figure 2.16a) for the selected peptide shows how the extent of deuterium uptake changes with respect to the incubation time, as well as the differences between relative deuterium uptake between ligand-free (red curve) and ligand-bound (blue curve) species, if such experiment was performed. A spectrum of the selected peptide at a specified incubation time point (lower right hand corner panel of Figure 2.16a) can be also viewed. Here, the raw spectrum is shown in red, and the blue lines are overlaid centroid data identified though the PLGS search and matched to the peptide. The data can be also displayed as stacked

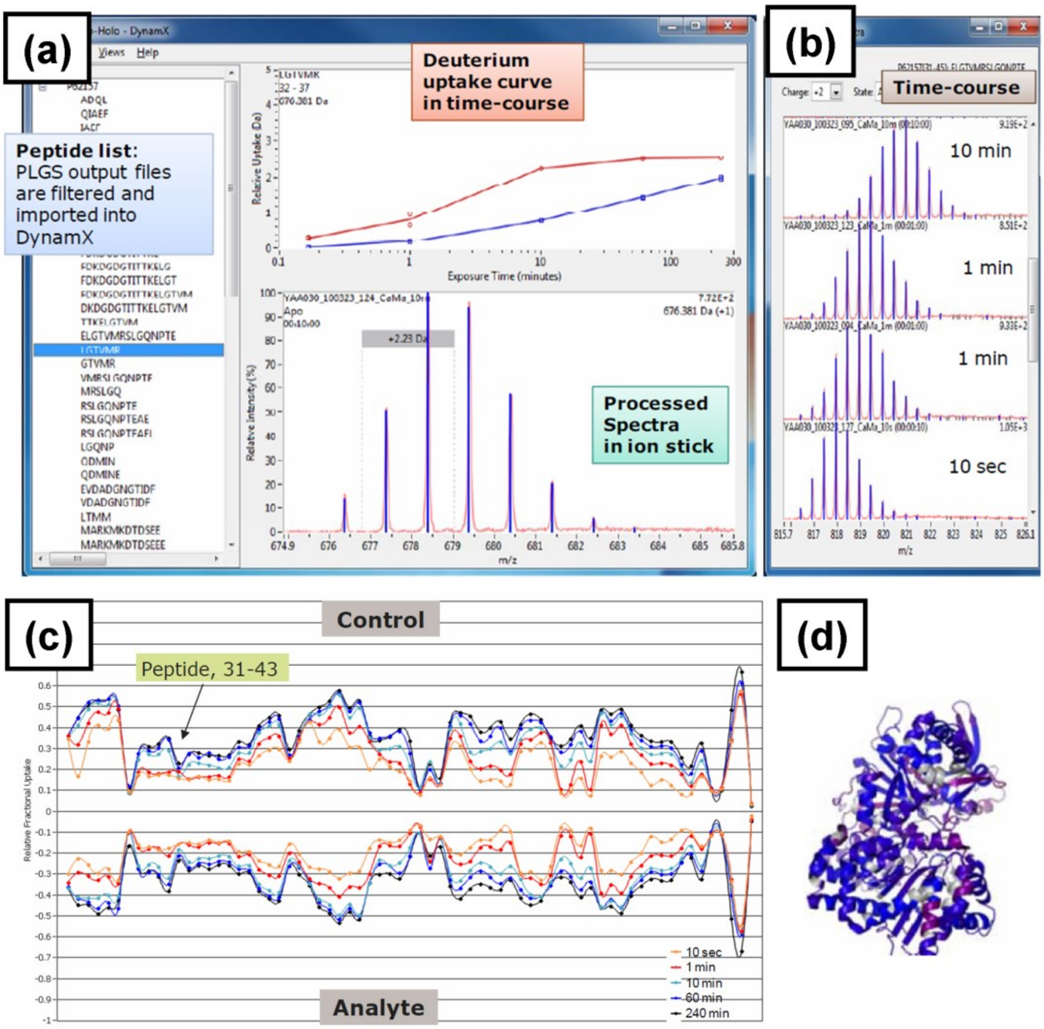

Figure 2.16 An HDX data analysis and visualisation in the Waters DynamX software. (a) main window of the DynamX software showing the list of identified peptides through the PLGS search (LHS), deuterium uptake curves (upper RHS) and a mass spectrum of a selected peptide at a selected incubation time point; (b) the stacked mass spectra of a selected peptide in a time-course; (c) a ‘butterfly chart’ comparing relative fractional deuterium uptake between two protein batches at various incubation time points; and (d) HDX data visualized as a colour coded heat map created in PyMOL Molecular Graphics System. Images obtained from Water Corporation web page.[25]

spectra in a given time-course (Figure 2.16b) showing the mass shift due to deuterium incorporation as a function of incubation time.

To cope with the burden of data processed, results are often presented as a ‘butterfly chart’ (Figure 2.16c).[59] Here as an example, two different batches of protein sample are compared in relative fractional uptake. Each point along the x-axis corresponds to a peptide identified through the PLGS search. The plot shows relative fractional update at specified labeling time-points indicated in different colours. Such visualisation helps to spot any differences in HOS between the protein batches. Moreover, when concerned with conformational changes due to ligand binding or environmental changes, differences in deuterium uptake will help to differentiate between solvent accessible regions of the protein and those where uptake is reduced due to structural rearrangements or ligand binding. If structural data obtained *via* other biophysical techniques exists and the atom coordinate file is available, HDX data can be further visualised by exporting the deconvoluted data for each residue into PyMOL Molecular Graphics System to build a colour coded heat map as the one shown in Figure 2.16d.

2.5 References

(1) van den Heuvel, R. H. H.; van Duijn, E.; Mazon, H.; Synowsky, S. A.; Lorenzen, K.; Versluis, C.; Brouns, S. J. J.; Langridge, D.; van der Oost, J.; Hoyes, J.; Heck, A. J. R. *Analytical Chemistry* **2006**, *78*, 7473.

(2) Tahallah, N.; Pinkse, M.; Maier, C. S.; Heck, A. J. R. *Rapid Communications in Mass Spectrometry* **2001**, *15*, 596.

(3) Chernushevich, I. V.; Thomson, B. A. *Analytical Chemistry* **2004**, *76*, 1754.

(4) Schmidt, A.; Bahr, U.; Karas, M. *Analytical Chemistry* **2001**, *73*, 6040.

(5) Sobott, F.; Hernandez, H.; McCammon, M. G.; Tito, M. A.; Robinson, C. V. *Analytical Chemistry* **2002**, *74*, 1402.

(6) Heck, A. J. R.; van den Heuvel, R. H. H. *Mass Spectrometry Reviews* **2004**, *23*, 368.

(7) Pagel, K.; Hyung, S.-J.; Ruotolo, B. T.; Robinson, C. V. *Analytical Chemistry* **2010**, *82*, 5363.

(8) Zhou, M.; Dagan, S.; Wysocki, V. H. *Angewandte Chemie-International Edition* **2012**, *51*, 4336.

(9) Hall, Z.; Politis, A.; Bush, M. F.; Smith, L. J.; Robinson, C. V. *Journal of the American Chemical Society* **2012**, *134*, 3429.

(10) Catalina, M. I.; van den Heuvel, R. H. H.; van Duijn, E.; Heck, A. J. R. *Chemistry-a European Journal* **2005**, *11*, 960.

(11) Lemaire, D.; Marie, G.; Serani, L.; Laprevote, O. *Analytical Chemistry* **2001**, *73*, 1699.

(12) Hogan, C. J., Jr.; Carroll, J. A.; Rohrs, H. W.; Biswas, P.; Gross, M. L. *Analytical Chemistry* **2009**, *81*, 369.

(13) Hogan, C. J., Jr.; Carroll, J. A.; Rohrs, H. W.; Biswas, P.; Gross, M. L. *Journal of the American Chemical Society* **2008**, *130*, 6926.

(14) Wanasundara, S. N.; Thachuk, M. *Journal of Physical Chemistry A* **2009**, *113*, 3814.

(15) Chari, R. V. J.; Miller, M. L.; Widdison, W. C. *Angewandte Chemie* **2014**, *53*, 3796.

(16) Beck, A. *mAbs* **2014**, *6*, 30.

(17) Beck, A.; Wagner-Rousset, E.; Ayoub, D.; Van Dorsselaer, A.; Sanglier-Cianferani, S. *Analytical Chemistry* **2013**, *85*, 715.

(18) Thompson, N. J.; Rosati, S.; Heck, A. J. R. *Methods* **2014**, *65*, 11.

(19) Wakankar, A.; Chen, Y.; Gokarn, Y.; Jacobson, F. S. *Mabs* **2011**, *3*, 161.

(20) Chen, J.; Yin, S.; Wu, Y.; Ouyang, J. *Analytical Chemistry* **2013**, *85*, 1699.

(21) McCullough, B. J.; Kalapothakis, J.; Eastwood, H.; Kemper, P.; MacMillan, D.; Taylor, K.; Dorin, J.; Barran, P. E. *Analytical Chemistry* **2008**, *80*, 6336.

(22) Kemper, P. R.; Bowers, M. T. *Journal of the American Society for Mass Spectrometry* **1990**, *1*, 197.

(23) Wyttenbach, T.; von Helden, G.; Bowers, M. T. *International Journal of Mass Spectrometry* **1997**, *165*, 377.

(24) Wyttenbach, T.; Kemper, P. R.; Bowers, M. T. *International Journal of Mass Spectrometry* **2001**, *212*, 13.

(25) Waters Corporation website, http://www.waters.com, 2014.

(26) Shvartsburg, A. A.; Smith, R. D. *Analytical Chemistry* **2008**, *80*, 9689.

(27) Ruotolo, B. T.; Benesch, J. L. P.; Sandercock, A. M.; Hyung, S. J.; Robinson, C. V. *Nature Protocols* **2008**, *3*, 1139.

(28) Leary, J. A.; Schenauer, M. R.; Stefanescu, R.; Andaya, A.; Ruotolo, B. T.; Robinson, C. V.; Thalassinos, K.; Scrivens, J. H.; Sokabe, M.; Hershey, J. W. B. *Journal of the American Society for Mass Spectrometry* **2009**, *20*, 1699.

(29) Bush, M. F.; Hall, Z.; Giles, K.; Hoyes, J.; Robinson, C. V.; Ruotolo, B. T. *Analytical Chemistry* **2010**, *82*, 9557.

(30) Michaelevski, I.; Eisenstein, M.; Sharon, M. *Analytical Chemistry* **2010**, *82*, 9484.

(31) Gerlich, D. *Advances in Chemical Physics* **1992**, *82*, 1.

(32) Giles, K.; Pringle, S. D.; Worthington, K. R.; Little, D.; Wildgoose, J. L.; Bateman, R. H. *Rapid Communications in Mass Spectrometry* **2004**, *18*, 2401.

(33) Atmanene, C.; Petiot-Bécard, S.; Zeyer, D.; Van Dorsselaer, A.; Hannah, V. V.; Cianférani-Sanglier, S. *Analytical Chemistry* **2012**, *84*, 4703.

(34) Jurneczko, E.; Barran, P. E. *Analyst* **2011**, *136*, 20.

(35) Berman, H. M.; Westbrook, J.; Feng, Z.; Gilliland, G.; Bhat, T. N.; Weissig, H.; Shindyalov, I. N.; Bourne, P. E. *Nucleic Acids Research* **2000**, *28*, 235.

(36) H++ server, http://biophysics.cs.vt.edu/H++, 2014.

(37) Anandakrishnan, R.; Aguilar, B.; Onufriev, A. V. *Nucleic Acids Research* **2012**, *40*, W537.

(38) Myers, J.; Grothaus, G.; Narayanan, S.; Onufriev, A. *Proteins-Structure Function and Bioinformatics* **2006**, *63*, 928.

(39) Gordon, J. C.; Myers, J. B.; Folta, T.; Shoja, V.; Heath, L. S.; Onufriev, A. *Nucleic Acids Research* **2005**, *33*, W368.

(40) Case, D. A.; Darden, T. A.; III, T. E. C.; Simmerling, C. L.; Wang, J.; Duke, R. E.; Luo, R.; Walker, R. C.; Zhang, W.; Merz, K. M.; Roberts, B.; Wang, B.; Hayik, S.; Roitberg, A.; Seabra, G.; Kolossvary, I.; F.Wong, K.; Paesani, F.; Vanicek, J.; Liu, J.; X.Wu; Brozell, S. R.; Steinbrecher, T.; H. Gohlke; Cai, Q.; Ye, X.; Wang, J.; Hsieh, M.-J.; Cui, G.; Roe, D. R.; Mathews, D. H.; Seetin, M. G.; Sagui, C.; Babin, V.; Luchko, T.; Gusarov, S.; Kovalenko, A.; Kollman, P. A. University of California, San Francisco, 2010.

(41) Lindorff-Larsen, K.; Piana, S.; Palmo, K.; Maragakis, P.; Klepeis, J. L.; Dror, R. O.; shaw, D. E. *Proteins-Structure Function and Bioinformatics* **2010**, *78*, 1950.

(42) Mesleh, M. F.; Hunter, J. M.; Shvartsburg, A. A.; Schatz, G. C.; Jarrold, M. F. *Journal of Physical Chemistry* **1996**, *100*, 16082.

(43) Shvartsburg, A. A.; Jarrold, M. F. *Chemical Physics Letters* **1996**, *261*, 86.

(44) Shvartsburg, A. A.; Schatz, G. C.; Jarrold, M. F. *Journal of Chemical Physics* **1998**, *108*, 2416.

(45) Wyttenbach, T.; vonHelden, G.; Batka, J. J.; Carlat, D.; Bowers, M. T. *Journal of the American Society for Mass Spectrometry* **1997**, *8*, 275.

(46) Shvartsburg, A. A.; Smith, R. D. *Journal of the American Society for Mass Spectrometry* **2008**, *19*, 1286.

(47) Bleiholder, C.; Contreras, S.; Do, T. D.; Bowers, M. T. *International Journal of Mass Spectrometry* **2013**, *345*, 89.

(48) Phillips, J. C.; Braun, R.; Wang, W.; Gumbart, J.; Tajkhorshid, E.; Villa, E.; Chipot, C.; Skeel, R. D.; Kale, L.; Schulten, K. *Journal of Computational Chemistry* **2005**, *26*, 1781.

(49) Hvidt, A.; Linderstromlang, K. *Biochimica Et Biophysica Acta* **1954**, *14*, 574.

(50) Wei, H.; Mo, J.; Tao, L.; Russell, R. J.; Tymiak, A. A.; Chen, G.; Iacob, R. E.; Engen, J. R. *Drug Discovery Today* **2014**, *19*, 95.

(51) Zhang, Q.; Willison, L. N.; Tripathi, P.; Sathe, S. K.; Roux, K. H.; Emmett, M. R.; Blakney, G. T.; Zhang, H.-M.; Marshall, A. G. *Analytical Chemistry* **2011**, *83*, 7129.

(52) Ahn, J.; Engen, J. R. *Chimica Oggi-Chemistry Today* **2013**, *31*, 25.

(53) Wei, H.; Ahn, J.; Yu, Y. Q.; Tymiak, A.; Engen, J. R.; Chen, G. *Journal of the American Society for Mass Spectrometry* **2012**, *23*, 498.

(54) Sowole, M. A.; Alexopoulos, J. A.; Cheng, Y.-Q.; Ortega, J.; Konermann, L. *Journal of Molecular Biology* **2013**, *425*, 4508.

(55) Hentze, N.; Mayer, M. P. *Journal of visualized experiments : JoVE* **2013**, e50839.

(56) Pan, Y.; Piyadasa, H.; O'Neil, J. D.; Konermann, L. *Journal of Molecular Biology* **2012**, *416*, 400.

(57) Iacob, R. E.; Zhang, J.; Gray, N. S.; Engen, J. R. *Plos One* **2011**, *6*, e15929.

(58) Zhang, J.; Adrian, F. J.; Jahnke, W.; Cowan-Jacob, S. W.; Li, A. G.; Iacob, R. E.; Sim, T.; Powers, J.; Dierks, C.; Sun, F.; Guo, G.-R.; Ding, Q.; Okram, B.; Choi, Y.; Wojciechowski, A.; Deng, X.; Liu, G.; Fendrich, G.; Strauss, A.; Vajpai, N.; Grzesiek, S.; Tuntland, T.; Liu, Y.; Bursulaya, B.; Azam, M.; Manley, P. W.; Engen, J. R.; Daley, G. Q.; Warmuth, M.; Gray, N. S. *Nature* **2010**, *463*, 501.

(59) Houde, D.; Berkowitz, S. A.; Engen, J. R. *Journal of Pharmaceutical Sciences* **2011**, *100*, 2071.

3

Dancing Antibodies: Exploring the Dynamics of Immunoglobulin G with DT-IM-MS and MD

Monoclonal antibodies (mAb) are a rapidly growing group of biopharmaceuticals. Due to their intrinsic flexibility, intact mAbs provide a challenge with regards to higher order structure characterization. Intact mAbs and their fragments are explored here using the DT-IM-MS and were found to be far more dynamic in the gas-phase than proteins of comparable size. This is rationalised with MD simulations, which revealed dynamics between linked folded domains of mAbs.

3.1 Introduction

3.1.1 Immunoglobulins – function, classification and structure

Immunoglobulins (Ig), also known as antibodies, are glycoproteins employed by the immune system for binding to antigens.[1] Antibodies are produced by plasma cells and are secreted in response to non-self antigens, often produced by bacteria or viruses, in order to bind and remove these intruders. Antibodies exist in various isoforms which differ in their biological function, structure, distribution in the body and antigen responses. These 'Y' shaped molecules are composed of four polypeptide chains, with the atom density distributed almost evenly into three globular domains linked *via* a flexible stretch of polypeptide chain referred to as the hinge region. Each of the Ig isoforms consists of one or more replicas of the 'Y' shaped unit. In mammals, five different isoforms (also known as classes) are identified: gamma (IgG), mu (IgM), alpha (IgA), delta (IgD) and epsilon (IgE), shown in Figure 3.1. These are classified based on differences in the amino acid sequence.[2] In this chapter, the IgG isotype is investigated which constitutes to about 75% of serum immunoglobulins in humans and is commonly used as a template for therapeutic modalities.[3]

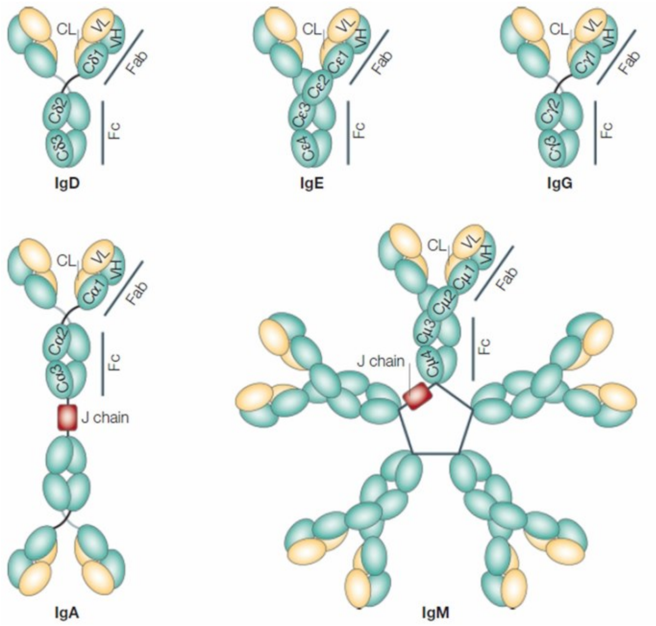

Figure 3.1 Five isoforms of mammalian immunoglobulins IgD, IgE, IgG, IgA and IgM and their main components: constant (C) and variable (V) regions of heavy (H, teal) and light chains (L, yellow) and the J chains (red) which merge 'Y' subunits in IgA and IgM isoforms. Image reproduced from Rojas, R. et al., 2002.[4]

From a structural point of view, all the isoforms share several similar features: each 'Y' unit consists of two identical heavy chains (HC) with covalently attached oligosaccharide groups, and two identical non-glycosylated light chains (LC). There are two isoforms of LC, lambda (λ) and kappa (κ), which have not been found to be functionally different and can be found in any of the isotypes.[5] The two identical half-molecules, each composed of one HC and one LC, are joined *via* disulfide bonds. The isotype and effector function of an antibody is determined by the sequence of the HC, specifically the Fc portion. Here, the IgG isoform is investigated, hence further description of the structural characteristics will be based on this.

A schematic representation of an IgG molecule is shown in Figure 3.2. An IgG is about 150 kDa with each HC ~50 kDa and each LC ~25 kDa. All chains consist of a series of amino acid sequences folded into discrete compact regions known as domains each of about 110 amino acids.[6,7] Each of the four chains has a variable domain (VL and VH) at the N-terminal, which is responsible for the antigen binding. As the nomenclature suggests, the amino acid sequence of these regions varies across antibodies accordingly to the antigen binding specificity. The remaining domains are referred to as 'constant' domains; the light chain constant domain (CL) domain and heavy chain consisted of three constant domains: CH1, CH2 and CH3 (Figure 3.2).

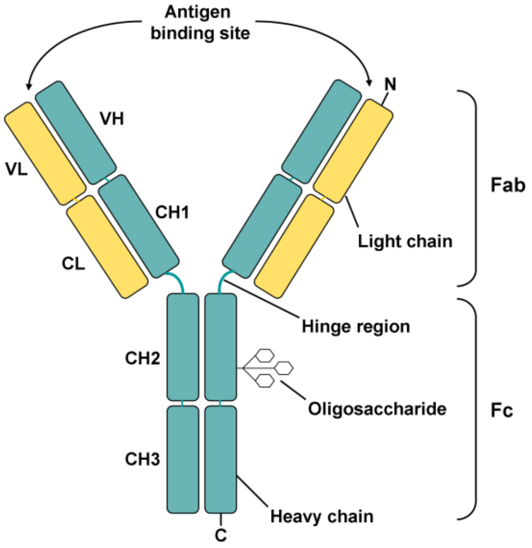

Figure 3.2 A schematic representation of the immunoglobulin gamma structure. Each IgG consists of two light chains (yellow) and two heavy chains (teal) joined at the hinge region *via* disulfide bonds. The Fab arms of an antibody recognize and bind to an antigen, while the Fc region interacts with the cell surface receptors.

Antibody molecule structure can be divided into two functionally distinct regions. The two identical ‘arms’ of the ‘Y’ shaped structure which recognise and bind to an antigen are named Fab fragments (Fragment antigen binding). Each Fab arm is composed of the LC and VH and CH1 domains. The CH2 and CH3 domains contained within the tail of the ‘Y’ unit are termed as the Fragment crystallizable (Fc), with its name originating from an early observation of ready crystallization.[8,9] This region has no reported antigen binding activity; instead it interacts with the cell surface receptors and complement proteins.[8,9] The CH3 domains are non-covalently bonded as oppose to the non interacting CH2 domains which in turn contain N-linked glycans situated within the cavity between the two HCs.[10]

Furthermore, IgGs are categorized into subclasses: IgG1, IgG2, IgG3 and IgG4 (in humans) as shown in Figure 3.3. Apart from variation in the amino acid sequence, the most distinct difference among the IgG subclasses is the location and the number of disulfide bonds (DSB) in the hinge region.[11-15] All IgGs poses twelve conserved intra-chain disulfide bonds buried within the structure and associated with an individual folded domain.[16] More importantly, it is the number and properties of the inter-chain disulfide linkages that allocate IgGs into various subclasses.[17] The two HC are covalently associated in the hinge region by two DSB in IgG1 and IgG4, four DSB in IgG2 and eleven DSB in IgG3.

More recently, IgG2 and IgG4 subclasses were found to have an alternative DSB linkage in the hinge region. The classical DBS organization in IgG2 referred to as IgG2-A, has four inter-chain linkages connecting two half molecules.[14] In the non-classical arrangement of IgG2-B and IgG2-A/B, one of the inter-chain DSB is linked to a cysteine residue located in the CH1 domain instead to a cysteine in the hinge region, either for one half molecule or both, respectively.[18-21] Distribution of these DSB isoforms is directed by the type of light chain present; λ LC constitutes to formation of the IgG2-A, κ LC favours the IgG2-B, while IgG2-A/B is considered as a structural intermediate between both.[19] Likewise, IgG4 subclass also displays non-classical linkage system. It is capable of forming a stable intra-chain DSB in the hinge region allowing for the antibody to part into two half-molecules.[22-24] This dissociation is recognized as the first step in the Fab arm exchange (FAE) process during which an IgG4 exchanges half-molecules with another IgG4 of different antigen binding specificity to form a bispecific

IgG4 (bsAb).[24-27] An additional structural difference among the IgG subclasses, setting IgG1 apart from other isoforms, is the location of the disulfide bonds between the LC and HC. In IgG1, the C-terminal cysteine residue of the LC is linked to the fifth cysteine residue of the HC. In case of the IgG2, IgG3 and IgG4 subclasses, the LC is linked to the third cysteine residue of the HC located in the Fab portion of the antibody near the N-terminal of the CH1 disulfide loop.[28]

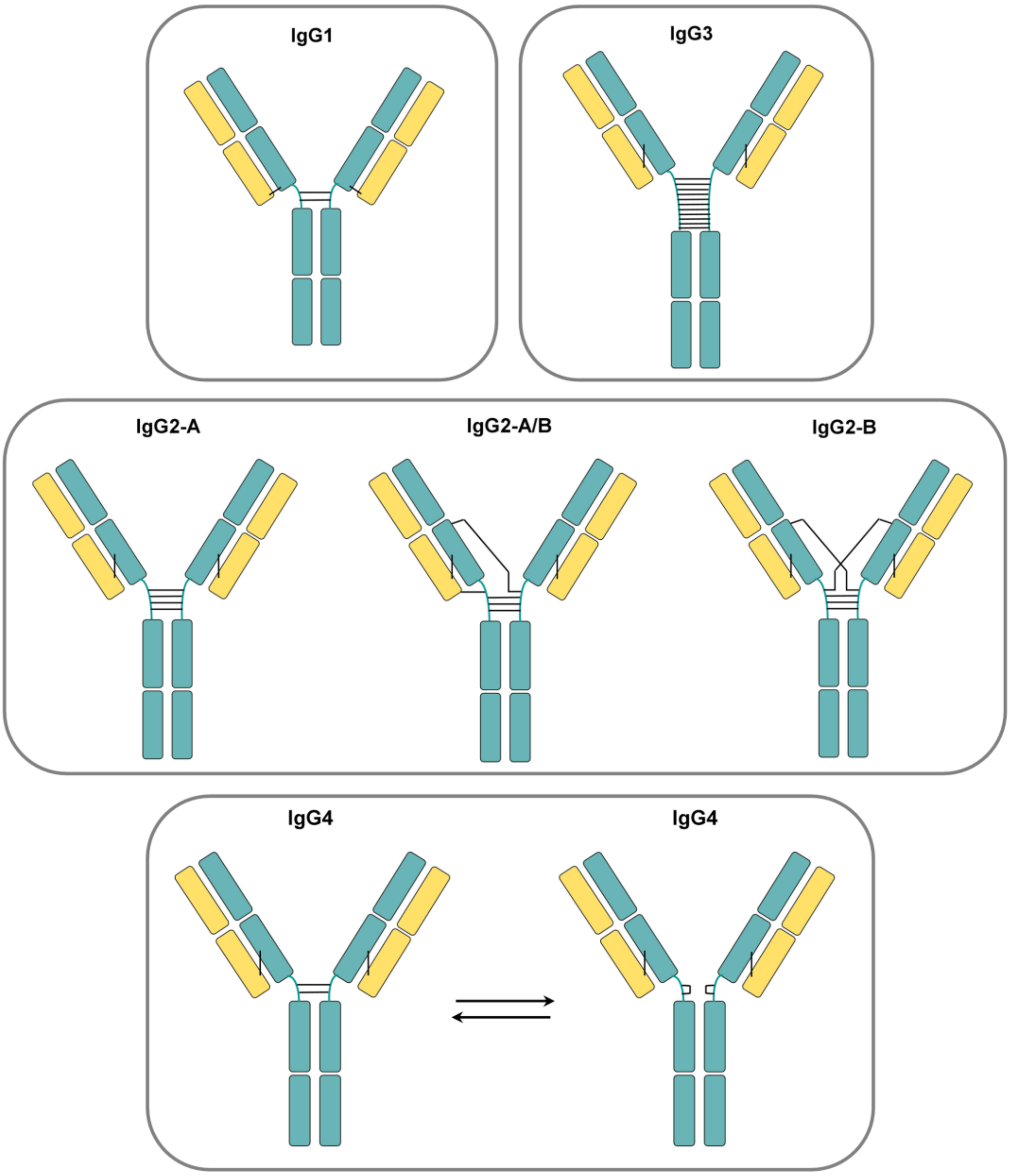

Figure 3.3 Schematic representations of four IgG subclasses: IgG1, IgG2, IgG3 and IgG4, showing the major differences location and number of the inter-chain disulfide bonds among the subclasses (marked as solid black lines). The IgG4 subclass is capable of forming inter-chain and intra-chain DSB in the hinge region. The IgG2 subclass consists of further three disulfide bond isoforms.

Early studies on antibody structure have indicated immunoglobulins to be highly flexible and dynamic molecules.[29-34] This segmental flexibility allows antibodies to fulfil their biological function and effectively extend their arms to identify and bind to the target. The upper hinge region allows Fab arms to adopt variable angles with respect to each other (Fab-Fab flexibility also know as Fab arm waving)[29,35], moreover it also enables rotational flexibility of each individual Fab (Fab arm rotation).[36-38] The lower hinge segment governs the position of the Fab arms relative to the Fc region (Fab-Fc flexibility known as Fc wagging).[35,37,38] Additional molecular movement, so called Fab elbow bending, is observed between the variable domain (VL and VH) and the CL and CH1 domains.[39]

The degree of flexibility depends upon the length of the hinge, the number and properties of inter heavy chain DSBs present within that region. In decreasing order, the relative flexibility of the hinge regions of the IgG subclasses has been classified as follows: IgG3 > IgG1 > IgG4 > IgG2. Mean Fab-Fab angles were reported to be 136 ± 53° for IgG3, 117 ± 43° for IgG1, 128 ± 39° for IgG4 and 127 ± 32° for IgG2, where the large standard deviations are attributed to a high degree of flexibility.[35] In IgG3, the elongated hinge gives the molecules a greater flexibility and range of motions, whereas flexibility of IgG2 is restricted by a shorter hinge from any other subclass, presence of a rigid poly-proline double helix and stabilizing four DSB.[40] The hinge of IgG4 is shorter than that of IgG1 and places its flexibility as intermediate between that of IgG1 and IgG2. Such flexibility provides a challenge for full structural characterisation of intact antibodies.

3.1.2 mAbs as therapeutics

Monoclonal antibodies (mAb) and related products form the fastest growing class of therapeutic agents with application in the treatment of diseases including cancer, immunological and neurodegenerative disorders, and other pathologies.[41-49] In the past three decades, more than 40 mAbs and their derivatives have been approved for use in various indications, and currently many more are in research and pre-clinical trials.[50,51] The approved entities, include not only the ‘naked’ antibodies but also radio-immunoconjugates,[52,53] antibody-drug conjugates (ADCs),[54-57] bispecific antibodies (bsAbs),[58-61] immunocytokines,[59,62,63] Fab fragments,[64] and Fc-fusion protein/peptides[65,66]. Between 2006 and 2010, 13 new mAbs were approved as therapeutics, representing over a half of genuinely new biopharmaceuticals to come on market in that period.[67] The worldwide sales for all biologics *i.e.* mAbs and other protein based therapeutics, is expected to approach US$150 billion mark by 2015, rising further to US$170 billion by 2025.[67,68]

Along with the development of these new biopharmaceuticals, there is a need for rapid, sensitive and robust analytical methods for detailed characterization of these complex and flexible biological structures. Additionally, as these therapeutics begin to come off patent, opportunities are rising for production of generic copies of these drugs known as biosimilars.[69,70] Being far larger, naturally more heterogeneous, and produced as a result of batch fermentation, protein based drugs provide a significant regulatory challenge compared to small molecules. Regulatory authorities have identified three critical characteristics of any protein biopharmaceutical which must be monitored and controlled during the development process: post-translational modifications (PTMs), three-dimensional structure and protein aggregation.[69,71] A characterization tool that can address all of those needs is mass spectrometry which allows us to probe mAbs at a primary and higher order structural level. MS based approaches are used to provide insights into molecular composition, PTMs, glycosylation patterns, mixture characterization, oligomerisation and aggregation, conformational changes, DSB scrambling, antibody-antigen binding or epitope mapping.[69,71-78]

3.1.3 Native IM-MS studies of intact immunoglobulins

Ion mobility mass spectrometry (IM-MS) facilitates study of protein higher order structure and provides shape defining parameters for each mass (and charge) selected species termed their collision cross sections (CCS). Moreover, since IM-MS is an isolated molecule technique, it can delineate structural changes that occur upon antigen binding or environmental change, which can be compared with theoretical values derived from structures solved with other methods. Despite an increasing application of IM-MS for structural studies, as of now, there is just handful of reports available in the literature on use of this technique to study intact mAbs.

Application of IM-MS to probe higher order structure of intact mAbs was first reported by Schnier and co-workers.[79] TWIM-IM-MS was applied to resolve disulfide structural isoforms of IgG2 mAbs. IM-MS revealed presence two to three gas-phase conformer populations related to disulfide bond heterogeneity among the IgG2 subclasses (described in section 3.1.1, Figure 3.3), as opposed to a single gas-phase conformer observed for IgG1 and C232S IgG2 mutant both of which are homogenous with respect to the DSB heterogeneity. Later, Gross *et al.* used combination of IM-MS, top-down fragmentation and protein footprinting to characterize conformational differences among IgG2 isoforms and several IgG2 mutants with altered S-S bonding.[80] IM-MS studies verified that the WT IgG2 presents itself in two major conformations, while the mutants display more compact CCSD than the dominant WT component. Utilization of fast photochemical oxidation of proteins (FPOP) approach provided residue-level information for the entire mAb also locating the conformational differences determined by IM-MS and identifying the hinge region as the origin of these differences.

IM-MS was used to investigate conformation dependent binding of a reference protein standard to a specific mAb commonly used in ELISA assays.[81] Under native conditions, human growth hormone (hGH) was present across two conformational families, while additionally two more extended forms were revealed under reduced conditions. Upon addition of the rhGH-specific mAb, none of the most compact rhGH conformer was observed in the free rhGH detected in the presence of mAb. The authors suggested, that although extended forms of the protein seemed to be not directly involved in binding with mAb, they might constitute an intermediate conformer necessary for mAb-rhGH binding rather than the mAb binding exclusively to the compact form of rhGH. Furthermore, the rhGH mAb was found to exist in three monomer conformations with median CCS values ranging from 61 to 76 nm^2 and ~80 % of the mAb sitting primarily in the monomer 2 conformation centred at 68 nm^2.

Recently, Debaene *et al.* applied native MS and time resolved TWIM-MS to monitor Fab arm exchange (FAE) between two humanized IgG4 and the subsequent formation of bsAb.[82] Differences observed in the drift time between the mAbs and bsAb are believed to arise from the structural differences rather than mass difference which in turn affects the drift time. The FAE process was monitored as a function of time in the presence and absence of a reducing agent to demonstrate how IM-MS can differentiate between mAbs and the newly formed bsAb. This chapter presents application of drift tube ion mobility mass spectrometry (DT-IM-MS) supported by molecular dynamics (MD) simulations to probe both structure and dynamics of two IgG1 and two IgG4 mAbs of different antigen binding specificity.

3.2 Methodology

3.2.1 *Sample preparation*

Four intact IgG samples and two Fc-hinge fragments were provided by UCB Pharma; protein samples were expressed and purified by Dr Shirley Peters. Two types of IgG1 and IgG4 antibodies of different antigen binding specificity examined in this chapter are denoted here as A and B; the amino acid sequences are available in the Appendix 3. Samples were stored in 50 mM sodium acetate (NaOAc) : 125 mM sodium chloride (NaCl) at 4 °C. On the day of analysis, samples were diluted to the concentration of 40µM and the buffer was exchanged to 100 mM, 200 mM or 500 mM ammonium acetate (Fisher Scientific, Loughborough, UK) pH 6.8, using micro Bio-Spin Chromatography columns (Micro Bio-Spin 6 Columns, Tris) following the instructions specified by the manufacturer. The desalting procedure was performed twice to achieve desired sample purity. High purity water was obtained from an Arium 611 water purification unit (Sartorius, Göttingen, Germany) fitted with a 0.2 µm filter. Charge reduction experiments were carried out by addition of 10 % (v) triethylammonium acetate buffer (TEAA) (Fluka, Steinheim, Switzerland) prior to MS analysis.

3.2.2 *Mass spectrometry*

Mass spectra were recorded on a Q-ToF mass spectrometer (Ultima API US, Waters, Manchester, UK). 5 µM samples were ionized using positive nESI as described in Chapter 2, section 2.1.2. Source voltages and pressures were tuned to enable maximum ion transmission. The source backing pressure was elevated to 5×10^{-1} mBar. The capillary potential was held at 1.6 kV, the source temperature was set to 80 °C, and the cone voltage was varied between 60 and 200 V; low voltages were used for preservation of native-like structure, while high cone voltages were applied in experiments aimed at mass determination. Other instrumental settings for the Ultima API US mass spectrometer are listed in Chapter 2, Table 2.1

3.2.3 Ion mobility mass spectrometry

40 μM samples were ionised using positive nESI as described in Chapter 2, section 2.1.2. The IM-MS data were acquired on the MoQToF, quadrupole time-of-flight mass spectrometer, detailed in section 2.2.1.[83] The capillary potential was held at 1.5 - 1.8 kV, the source temperature was set to 80 °C, and the cone voltage was set to 80 V. The injection energy used was between 31 and 33 V. Other instrumental settings for the MoQToF IM mass spectrometer are listed in Chapter 2, Table 2.3. The drift cell was filled with helium gas at a pressure of 3.7 – 3.8 Torr at temperature of 302 ± 2 K. The electric potential across the cell was varied from 60 to 20 V for intact IgG samples; and 60 to 15 V for the Fc-hinge fragments, with measurements taken at six different drift voltages. The rotationally-averaged collision cross-sections (CCS) were determined from a plot of arrival time versus P / T and the CCSD were determined as described in Chapter 2, section 2.2.1.4. Each experiment was repeated in triplicate and the average values are reported.

3.2.4 Molecular dynamics

The MD simulations, estimation of theoretical CCS and calculation of the secondary structure content presented in this chapter were performed by Dr Massimiliano Porrini at the Institute Européen de Chimie et Biologie (IECB) in Pessac, France.

The input coordinates files were those taken from the crystallographic structures, PDB identifiers 1IGT and 1IGY for: IgG2a and IgG1, respectively. After adding hydrogen atoms, the X-ray structures of the two antibodies were minimized *in vacuo* with the sander module of Amber11[84], implementing a radial cut-off of 999 Å and Amber99SB-ILDN force field[85]. The theoretical collision cross sections (CCS) were calculated with each of the three methods implemented in the MOBCAL code[86] with the trajectory method appropriately modified to handle large systems such as mAbs studied here. The less accurate methods PA and EHSS are included here for comparison with other more approximate methods; results from TJM are most reliable and most robust with respect to comparison to the co-ordinates.[87] To follow the dynamic evolution in gas phase, the antibodies were firstly gradually heated up to 300 K, utilizing a Langevin thermostat (damping coefficient of 2 ps^{-1}) with a time-step of 1.0 fs, and then subjected to a constant temperature (300 K) molecular dynamics (MD) run of 10 ns, again with Langevin thermostat. The damping coefficient, radial cut-off, force field and time-step were the same as these described above, and the simulation software package utilized was NAMD 2.9.[88] The observables computed to follow the conformational rearrangements of the antibodies were the backbone root mean square deviation (RMSD), the radius of gyration (R*g*), and the rotationally averaged CCS. The latter was calculated with a simulation time increment of 0.5 ns (plus one computation at 0.25 ns), except for which additional random evaluations were done. The content of the secondary structure was determined using AmberTools13 (module cpptraj), which implements the algorithm DSSP.[89]

The Matthews coefficients and solvent content of the asymmetric units were calculated using an online Matthews Coefficient Calculator.[90]

3.3 Results and Discussion

3.3.1 Mass spectrometry of intact IgGs

Two types of IgG1 and IgG4 antibodies of different antigen binding specificity examined in this chapter, are denoted here as A and B. nESI-MS of 5 μM IgG1 A, IgG4 A, IgG1 B and IgG4 B in 100 mM ammonium acetate at pH 6.8 acquired on the Ultima API US Q-ToF mass spectrometer are shown in Figure 3.4. Mass spectra present narrow charge state distributions diagnostic of the native-like nESI-MS conditions. Peaks corresponding to the intact IgG are observed in the ~5700 – 7200 *m/z* range; with the charge state envelope ranging from 21+ to 27+ charge state, centred at the 24+ charge state.

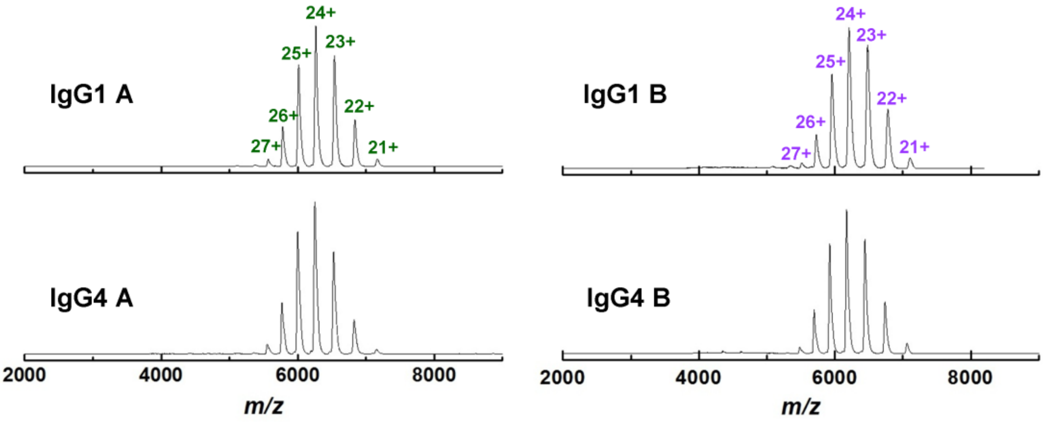

Figure 3.4 nESI mass spectra of intact IgG1 A and IgG4 A (left), IgG1 B and IgG4 B (right) in 100 mM ammonium acetate at pH 6.8 acquired on the Ultima API US Q-ToF mass spectrometer at a sample cone potential of 200 V.

For mass determination experiments, high cone voltages (200 V) were applied. Raising voltages in the source region of the mass spectrometer, such as sample cone or extractor cone voltage, affects the acceleration of the ions through the source. The measured mass of protein complexes in the gas phase tends to be higher than the mass derived from the sequences of their components.[91,92] Theoretical monoisotopic masses based on the amino acid sequence of the IgG1 A, IgG4 A, IgG1 B and IgG4 B are 147106.78 Da, 146776.18 Da, 145246.13 Da and 144915.53 Da, respectively (sequences available in the Appendix 3). The theoretical masses reported here, do not include the mass of two *N*-glycans attached at the Fc domain, each of ~1400-1700 Da. Measured masses at lower acceleration voltages (sample cone 50 V) were found to be 150450 ± 67 Da, 151486 ± 162 Da, 148908 ± 60 Da and 148442 ± 56 Da for IgG1 A, IgG4 A, IgG1 B and IgG4 B, respectively. Measured masses at high acceleration voltage (sample cone 200 V) decreased further to 149666 ± 28 Da, 149837 ± 138 Da, 147978 ± 17 Da and 147578 ± 31 Da for IgG1 A, IgG4 A, IgG1 B and IgG4 B, respectively. The 2.6 - 3.0 kDa deviation from the theoretical mass can be assigned due to the presence of two *N*-glycans. Upon gentle increase of the accelerating voltage, the peak width decreases along with a variation from the theoretical mass, attributed to the loss of residual solvent and salt bound to the protein complex. This collision-induced cleaning is often used to improve the mass spectrum quality and parameters are optimized to find a balance between preventing in-source dissociation and achieving adequate, well resolved protein ion signal.[93,94]

Increasing collision energy with the background gas transfers energy to the sample ion and can disturb protein structure and induce protein unfolding and protein complex dissociation. Therefore for structural studies, such as those presented in the next section, care was taken in the optimization of those crucial parameters.

3.3.2 Conformational landscapes occupied by intact IgG explored with DT-IM-MS

3.3.2.1 Differences in CCSD among IgG isoforms

nESI-IM-MS of 40 μM IgG1 A, IgG4 A, IgG1 B and IgG4 B in 100 mM ammonium acetate at pH 6.8 were acquired on the MoQ-ToF ion mobility mass spectrometer. Source conditions were optimized and low acceleration voltages were applied to preserve protein native-like structure. Arrival time distributions (ATDs) were recorded following mobility separation at 300 K and converted into CCSD as described in Chapter 2 section 2.2.1.4. Figure 3.5 shows the CCSD of four intact mAbs, normalized to spectra intensity, where the CCSD are outlined in different colours for different charge states observed. Across the four antibodies investigated, all appear flexible with very broad ATDs describing CCS landscapes populated from ~50 to 100 nm^2. Only CCSD obtained for the most populated charge states, z = 22+ to 26+, are shown (Figure 3.5) as the intensity of the lowest (21+) and the highest (27+) charge states observable in the MS mode was not sufficient in IM mode.

In Table 3.1, median CCS values from the total occupied space for each charge state are reported. Whilst the trends for each antibody are similar, the range of CCS presented over the charge states observed differ. For the 22+ charge state, the median CCS found for IgG1 and IgG4 are the same (~61-62 nm^2) as is the width of the ATD, suggesting indistinguishable conformations. As the charge state increases so does the median CCS for each mAb. For the two highest charge states of significant intensity (25+ and 26+), the observed median CCS for IgG4 molecules are larger than the equivalent for the IgG1 mAbs. The median CCS of the 26+ charge state of IgG4 is significantly larger (82-83 nm^2) than CCS of the same charge state of IgG1 (76-77 nm^2). The change in median CCS across the charge state range is 15 nm^2 for both IgG1s and 20 nm^2 for both IgG4s; hence the conformers adopted by the different isotypes of mAb appear to be distinguishable by IM-MS.

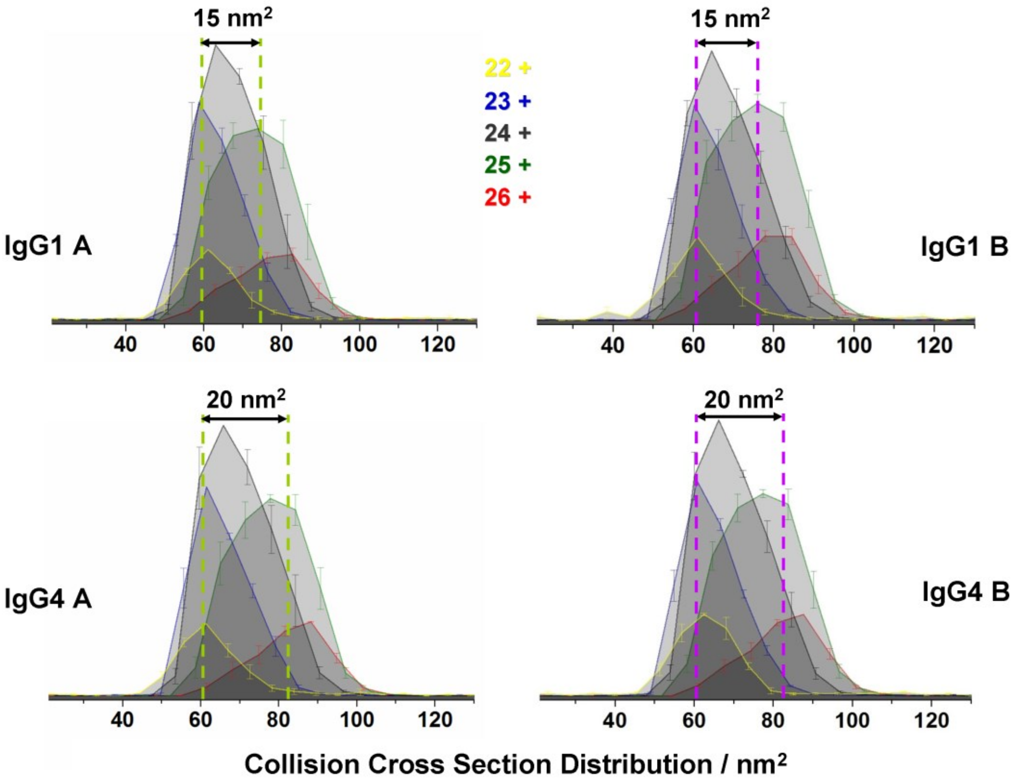

Figure 3.5 Conformational space occupied by intact IgG1 A, IgG4 A, IgG1 B and IgG4 B across the charge states in terms of collision cross sections (CCS). Data shown here was acquired at 300 K and at a fixed drift voltage of 35 V and was normalized to the spectral intensity.

Table 3.1 Median collision cross section (CCS) values along with the standard deviation values derived from three experimental replicas; for each charge state of IgG1 A, IgG4 A, IgG1 B and IgG4 B reported in nm^2 across detected charge states.

charge state	IgG1 A / nm^2	IgG1 B / nm^2
22 +	61.7 ± 1.1	61.1 ± 1.6
23 +	62.5 ± 1.6	63.3 ± 1.0
24 +	65.9 ± 1.3	66.7 ± 1.3
25 +	71.7 ± 0.6	73.9 ± 2.6
26 +	76.1 ± 1.1	77.4 ± 3.9

charge state	IgG4 A / nm^2	IgG4 B / nm^2
22 +	61.8 ± 1.6	61.8 ± 1.4
23 +	64.7 ± 1.4	64.1 ± 0.9
24 +	68.6 ± 0.5	68.4 ± 0.5
25 +	76.8 ± 1.9	75.6 ± 1.1
26 +	83.2 ± 0.6	82.2 ± 0.8

3.3.2.2 DT-IM based CCS vs. TWIM based CCS

The median CCS determined with the linear DT-IM-MS on our MoQToF instrument, correspond well with the TWIM-MS based CCS reported in the literature. Ashcroft's group found the rhGH-specific mAb monomer (IgG1) to be present in three conformations with median CCS values ranging from 61 to 76 nm^2 and ~80 % of the mAb sitting primarily in the monomer 2 conformation centred at 68 nm^2.[81] The span of TWIM based median CCS observed for these IgG1s correlates with DT-IM based CCS of both IgG1s investigated in this chapter. Additionally, Debaene *et al*. reported TWIM based CCS of two IgG4 mAbs undergoing Fab-arm exchange (FAE) to be 69.6 ± 0.4 nm^2 and 65.9 ± 0.3 nm^2 and the resulting bispecific antibody (bsAb) to have an intermediate CCS of 66.9 ± 0.1 nm^2.[82] Only CCS for the most intense charge states were reported. The observed differences between values reported in this thesis and the reported by Debaene *et al.* could originate from the differences in the amino acid composition of these mAbs as well as differences in the experimental procedure, instrumentation and CCS determination protocol.

3.3.2.3 The effect of buffer composition on the CCSD of intact mAbs

Aqueous ammonium acetate buffer is the most commonly chosen buffer for protein analysis in their native state by MS. Nevertheless, the concentration of the buffer needs to be chosen carefully depending on the target protein. Non MS compatible storage buffer of IgG1 A was exchanged to 100 mM, 200 mM and 500 mM ammonium acetate to investigate the effect on buffer ionic strength on mAb charge state distribution and CCSD. Figure 3.6a shows spectra of mAbs contained in the above mentioned buffers. No change in charge state distribution was observed; however, increasing the buffer strength resulted in broadening of peaks and reduction of S/N ratio. IM experiments showed no differences in CCSD of IgG1 A among the three ammonium acetate buffers tested as shown in Figure 3.6b using the most abundant 24+ charge state. Since increased buffer strength was demonstrated not to have an effect on the conformational space occupied by IgG1 A and only contributed to lower the signal quality, the 100 mM AmAc was chosen as an optimum buffer strength and was used in all experiments reported in this chapter.

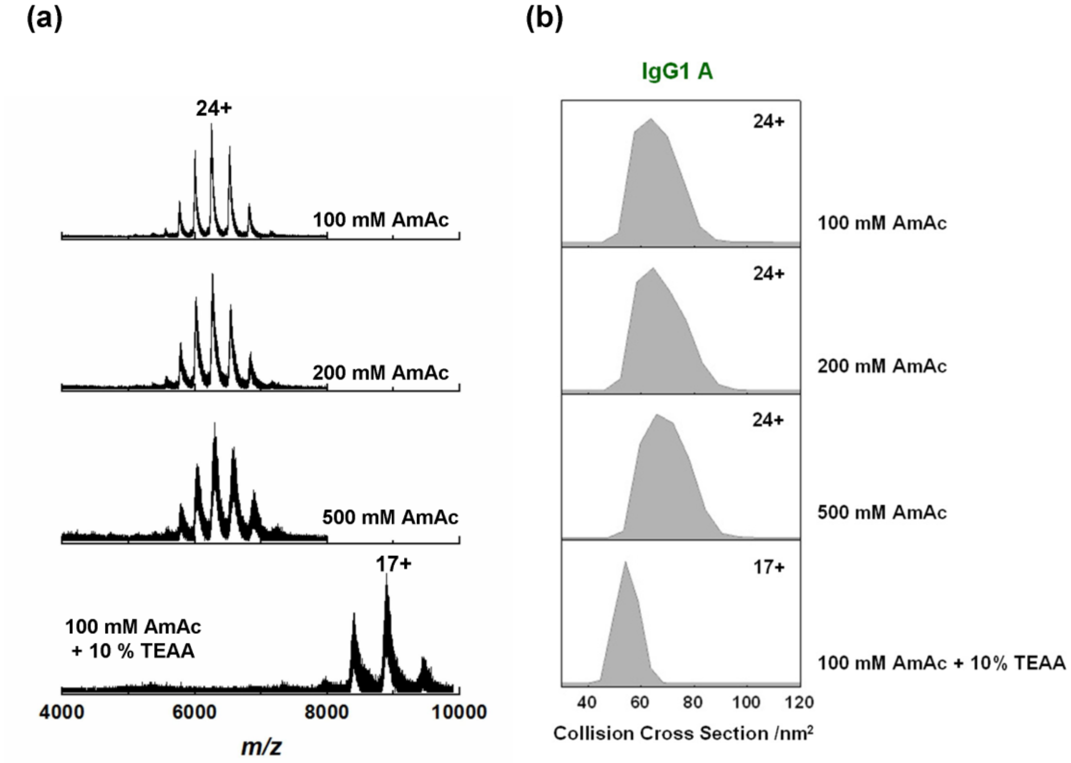

Figure 3.6 (a) Mass spectra of IgG1 A in 100 mM AmAc, 200 mM AmAc, 500 mM AmAc and 100 mM AmAc + 10 % TEAA (from top to bottom). Upon the addition of a charge reducing agent, TEAA, the charge state envelope shifts it's centre from 24+ to 17+ ions. (b) Conformational space occupied by the IgG1 A (149 kDa) in 100 mM AmAc, 200 mM AmAc, 500 mM AmAc and 100 mM AmAc + 10% triethylammonium acetate (TEAA) (from top to bottom) in terms of collision cross sections (CCS). When in the ammonium acetate buffer, IgG1 A 24+ displays the same CCS profile regardless of the buffer strength. Upon the addition of TEAA; charge state shift is noted, however no structural stabilization is observed but even further decrease in the CCS. Data shown here was acquired at 300 K and 35 V drift voltage.

Use of charge reducing agents may help to stabilize protein structure and preserve non-covalent protein complexes in the gas phase.[95,96] The effect of triethylammonium acetate (TEAA) on the IgG structure was investigated. Upon the addition of 10% TEAA, IgG1 A experiences a charge state envelope shift by 7 charge states; from 24+ to 17+ as the most abundant state. Nevertheless, addition of this charge modulator does not induce structural stabilization. Furthermore, the antibody undergoes significant compaction with a central CCS of ~55 nm^2 for the 17+ charge state (Figures 3.6).

3.3.2.4 mAb flexibility and CCSD

CryoEM and TEM studies have indicated that IgGs are flexible, dynamic molecules, capable of Fab arm waving and rotation, as well as Fab elbow bending or Fc wagging.[36] Mean Fab-Fab angles have been previously reported to be 117 ± 43° for IgG1 and 128 ± 39° for IgG4, where the large standard deviations on these values are attributed to a high degree of flexibility.[35] Considering this, the wide CCSD observed for mAbs could be attributed to a large number of closely related conformational families present in the gas phase with dynamic flexibility that cannot be resolved by room temperature ion mobility measurements. Whilst some features (notably the tail on the left hand side for the 26+ species) suggests states with very different conformations, the lack of baseline resolution means we can surmise that the mAbs present interconverting conformers.

It can be speculated as to why the IgG4 subclass can occupy more space in the gas-phase than IgG1. The hinge region of the IgG1 subclass is known to be more flexible in comparison to the hinge of the IgG4 subclass. [30,35,97] The structure and stability of IgG antibodies has been shown to be affected by differences in the inter- and intra-disulfide bonds. The non-classical structure of the IgG2 B has been shown to be more compact than that of IgG2 A by SEC and AUC.[19] These isoforms have previously been also resolved by TWIM-IM-MS.[79] Moreover, the disulfide linkages between the HC and LC vary among the IgG subclasses resulting in structural differences. This bond links the carboxy-terminal of the LC with the cysteine residue at position 220 in IgG1 and at position 131 in IgG2, IgG3 and IgG4 of the CH1 sequence of the HC. The LC of IgG4 being linked further from the centre of mass, will allow for more 'movement' and have more accessible space dynamics which will display broader CCDS as shown experimentally.

3.3.3 Fc-hinge fragment CCSD profiles further emphasize differences in gas-phase conformations among the IgG subclasses

To test whether the broadness of CCSD of intact mAbs is only attributed to the movement of Fab arms with respect to the Fc domain or whether there are other factors controlling the conformational diversity, the Fc-hinge fragments of both IgG1 and IgG4, were studied with DT-IM-MS. nESI-IM-MS of 40 μM Fc-hinge mAb fragments in 100 mM ammonium acetate at pH 6.8 were acquired on the MoQ-ToF ion mobility mass spectrometer. Source conditions were optimized and low acceleration voltages were applied to preserve protein native-like structure. ATD were recorded following mobility separation at 300 K and converted into CCSD as described in Chapter 2 section 2.2.1.4. Mass spectra of both Fc-hinge fragments (Figure 3.7a) display narrow charge state distribution centred at the 13+ charge state. Fc-hinge fragments of both mAbs present broad CCSD. Similarly, as in case of intact mAbs, no striking differences are noted in CCSD for the 12+ charge states as shown in Figure 3.7b. The CCSD of 13+ charge state of the IgG4 Fc-hinge appears to be slightly broader than the one of the IgG1 Fc-hinge fragment. Interestingly, the highest 14+ charge state of IgG4 Fc-hinge displays two conformational families, with the larger one centred at 37.5 nm^2 being more abundant as opposed to the IgG1 Fc-hinge fragment with majority of species centred at 31.6 nm^2.

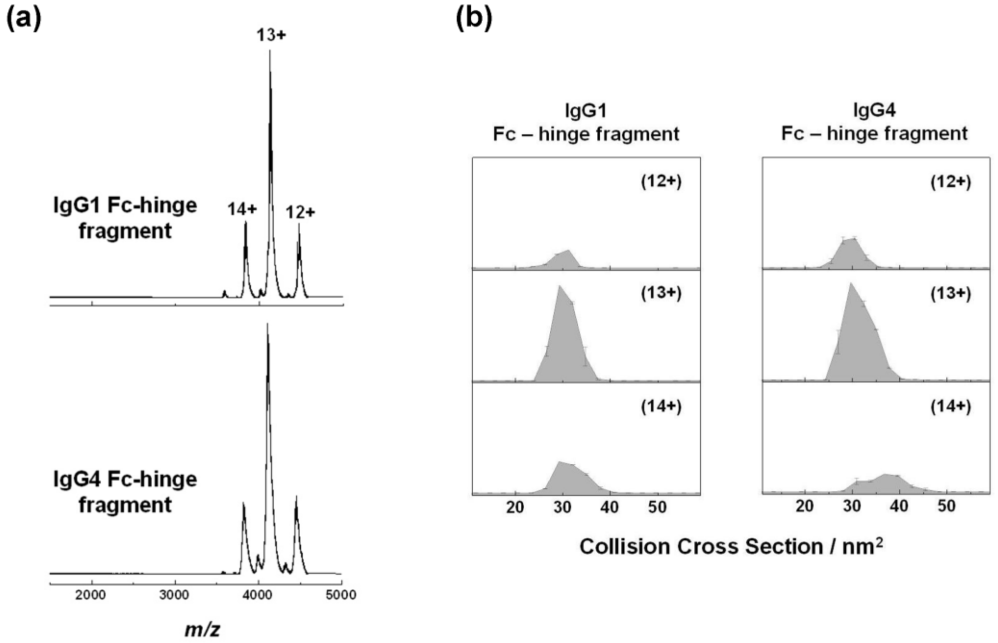

Figure 3.7 (a) Mass spectra of the IgG1 Fc-hinge fragment (top) and the IgG4 Fc-hinge fragment (bottom) in 100 mM ammonium acetate. (b) Conformational space occupied by the IgG1 Fc-hinge fragment (left) and IgG4 Fc-hinge fragment (right). Data shown here was acquired at 300 K and 35 V drift voltage and was normalized to spectral intensity. *CCSD of IgG4 Fc-hinge fragment have been already shown in Chapter 2, Figure 2.10; here it is shown again to ease the comparison and pinpoint differences in CCSD between IgG1 Fc-hinge fragment and IgG4 Fc-hinge fragment.

It can be speculated that the distinct features in the hinge region and the non-covalent interactions between the CH3-CH3 domains are potentially responsible for the experimentally observed differences.[98-100] These and/or other interactions may dictate how the intrinsic flexibility varies in the absence of solvent. The characteristic core sequence of the IgG4 hinge (residues 226-230 of the HC) and presence of a serine rather than a proline at position 228 permits formation of intra- and inter- HC disulfide bonds (a process essential for FAE to occur); whereas an arginine at position 409 at the CH3-CH3 interface weakens the non-covalent association between these domains. Both of these features are prerequisite for the FAE process in which IgG4 dissociates into half-molecules and re-assembles with half-molecule of another IgG4 of different specificity to form a bsAb.[25,98,101-103] Recently Davies *et al*. presented the first high-resolution crystal structures of recombinant and serum-derived IgG4-Fc fragments.[100] The study revealed how Arg409 can adopt two different conformations affecting the stability of the CH3 interface. One of these conformations is similar to those observed in IgG1, whereas the other conformation weakens the interface by disrupting the water molecule network resulting in reduced hydrogen bonding what might also be an early snapshot to the dissociation process. Only the latter conformation was observed in the CH3 domain crystal structure; however, authors believe that the two conformers are equally populated. Similar conclusions can be draw from the DT-IM-MS experiments presented here. Over 60 % of the 14+ charge state of the IgG4 Fc-hinge fragment populates the larger conformational family of the two observed. Larger CCS would suggest the structure to be more open and hence could be corresponding to the conformation with destabilised interactions between the CH3 domains of the HC described by Davies *et al*..[100] In contrast, the 14+ charge state of the IgG1 Fc-hinge fragment occupies mainly one – the smaller conformational family centred at 31.6 nm^2, hinting at the presence of a more compact structure held tightly *via* strong CH3-CH3 interactions.[27]

3.3.4 Comparison of mAb's CCSD to CCSD of other protein complexes as a measure of structural flexibility

The conformational spread observed for mAbs was compared to that found for similarly sized proteins (Figure 3.8). The CCSD of both, IgG1 and IgG4 as well as the Fc-hinge fragments were compared to those of several multimeric protein complexes, namely: tetrameric transthyretin (TTR, ~55 kDa), tetrameric concanavalin A (ConA, ~102 kDa), pentameric human serum amyloid P component (SAP, ~128 kDa) and hexameric ATP-phosporibosyltransferase (ATP-PRT, ~190 kDa) (these complexes will be further described in the following chapters). In Figure 3.8, the CCSD are plotted as a function of molecular mass (kDa); coloured blocks are used to represent the span of baseline CCSD observed, whereas points represent the median CCS determined for each of the charge states observed. As expected, the median CCS increase with increasing protein mass, however IgGs display a notably wider range of conformations, which can be attributed to dynamic and flexible structures. Whilst, the 24+ IgG species with a median CCS of ~65.9 - 68.6 nm^2 follow a trend line set by other multimeric protein complexes, it is the higher charge states ($z > 24$) that deviate significantly.

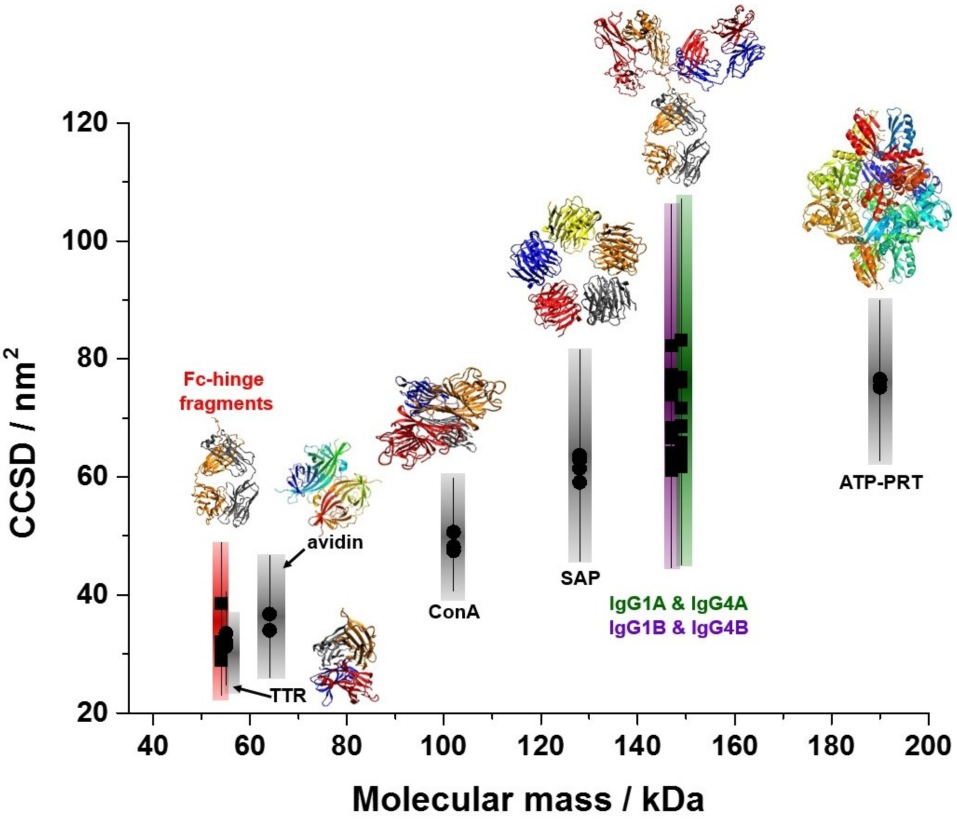

Figure 3.8 Collision cross sections distributions (CCSD) of the detected charge states vs. molecular mass of mAb Fc-hinge fragments, transthyretin (TTR, PDB:1BMZ), avidin (PDB:AVE), concanavalin A (ConA, PDB:1DQ0), human serum amyloid P component (SAP, PDB:1SAC), IgG1s and IgG4s (PDB:1IGY), and MtATP-phosporibosyltransferase (ATP-PRT, PDB:1NH7) along with structures based on crystal data deposited into the Protein Data Bank. The coloured blocks represent CCSD width, and points represent median CCS determined for charge states observed for each protein complex; ▲ are used to represent the IgG1 subclass and ■ for the IgG4 subclass.

This deviation can also be illustrated by comparing the CCS profiles of each protein. Figure 3.9a, shows CCSD for the most abundant charge state of each of protein complexes considered here. Clearly, the intact IgG1 and IgG4 present significantly wider CCSD and populate more conformational space than other multimeric complexes. The CCSD width of Fc-hinge fragments (~54 kDa) is slightly broader than the one of similarly sized tetrameric TTR (~55 kDa). The 24+ charge state of intact mAbs (~147 - 149 kDa) display considerably larger CCSD than 128 kDa SAP or 190 kDa ATP-PRT. When CCSD width is plotted in function of molecular mass, mAbs and their fragments are clear outliners from the trend set by other complexes (Figure 3.9b).

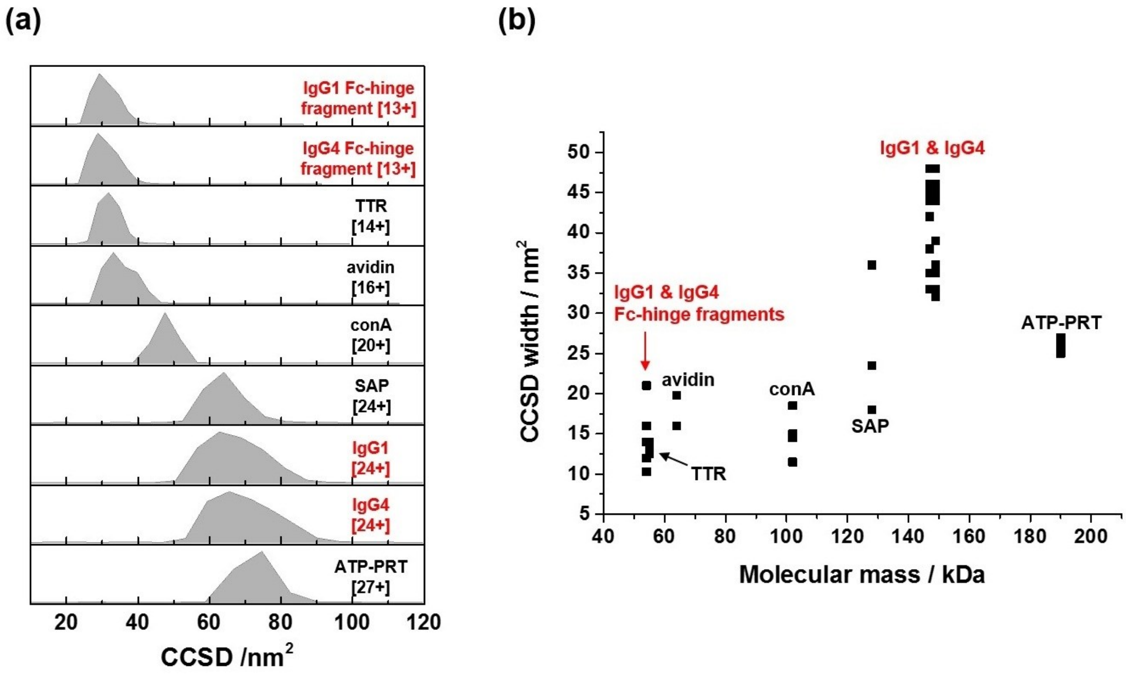

Figure 3.9 (a) Conformational space occupied by the most intense charge states of IgG1 Fc-hinge, IgG4 Fc-hinge, transthyretin (TTR), avidin, concanavalin A (ConA), serum amyloid P component (SAP), IgG1, IgG4 and ATP-PRT protein complexes. Both, intact IgGs and Fc-hinge fragments present considerably broader CCSD containing closely related conformational families. Data shown here was acquired at 300 K and 35 V drift voltage. (b) Collision cross section distribution (CCSD) widths across charge states of IgG1 Fc-hinge, IgG4 Fc-hinge, transthyretin (TTR), concanavalin A (ConA), serum amyloid P component (SAP), IgG1, IgG4 and ATP-PRT plotted as a function of molecular mass. Both, Fc-hinge fragments and intact IgGs are outliers from the other protein complexes investigated.

It is worth mentioning that the CCSD profile of avidin appears to be slightly broader in comparison to proteins of alike size. Similarly to intact IgGs and their Fc-hinge fragments, avidin is a glycoprotein what suggest that presence of glycans could be contributing to broader CCSD profiles. Performing IM-MS experiments on deglycosylated IgGs and Fc-hinge fragments would help to predict how much of the CCSD peak width can be attributed to presence of glycans. At the same time, deglycosylation of IgGs could lead to collapse of intra-cavity between CH2 domains and contradict the idea of probing native-like structures. In conclusion, IM-MS reveals the intact mAbs to be more structurally dynamic than proteins of comparable size which can be attributed to their intrinsic flexibility.

3.3.5 In vacuo molecular dynamics simulations tracing gas-phase behaviour of intact IgGs

3.3.5.1 Estimation of theoretical CCS and in vacuo MD simulations

Full structural characterization of antibodies has been hindered by their flexibility causing the crystallization step to be a major challenge.[32,35] Most of the hundreds of IgG structures available at the Protein Data Bank (PDB) are merely fragments of antibodies, typically only the Fab arm or the isolated Fc domains. There are to date just three x-ray crystallography based structures of intact IgG molecules deposited into PDB, namely: human IgG1 b12 (1HZH), IgG2a (1IGT) and IgG1 (1IGY).[28,104,105] For comparison of the DT-IM-MS based CCS and the theoretical CCS, the available structures were protonated, minimized *in vacuo* to reach the lowest energy state structure, and theoretical CCS were calculated with the trajectory method (TJM) implemented in the MOBCAL code.[86] Calculated CCS were found to be 100.3 nm^2, 105.6 nm^2 and 100.8 nm^2 for 1HZH, 1IGT and 1IGY, respectively. Experimentaly determined CCS are significanlty smaller than the theoretically derived CCS, thus indicating that the protein might have collapsed somewhat in the gas-phase in comparison to the x-ray structure. It is important to keep in mind that x-ray crystallography provides only a snapshot of a ‘frozen’ protein conformation. Antibodies being flexible and dynamic molecules display closely related conformations, as shown by IM-MS, that x-ray crystallography as a solid state technique cannot necessarily capture all. It can be envisaged that the three atom dense linked domains of an IgG *i.e.* two Fab arms and the Fc, might rearrange to a lower energy gas-phase structure.

To follow the dynamic evolution of intact mAbs in the gas-phase and gain further insights into the IM-MS results, *in vacuo* molecular dynamic (MD) simulations on the crystal structures were performed. The 1HZH structure was discounted as the deposited coordinates have several residues missing including some in the hinge region which play a crucial role in mAb flexibility and the range of adopted conformations. Antibodies were first gradually heated up to 300 K, and then subjected to molecular dynamics (MD) for 10 ns. The conformational changes are reported with respect to simulation time in terms of the CCS of each mAb using three approximation methods: the projection approximation (PA)[106], the trajectory method (TJM)[107], and the exact hard sphere scattering (EHSS)[108] with the results listed in Table 3.2. Whilst the CCS values from the PA method appear to agree with experimental measurements, this method is known to underestimate the CCS for coordinates from molecules larger than 3 kDa.[87,109] The most robust method is TJM and only the results from that will be discussed here.

At t = 0, theoretical CCS calculated with the trajectory method are found to be 105.6 nm^2 and 100.8 nm^2 for 1IGT and 1IGY, respectively. The MD simulations support the speculated mAb *in vacuo* structural collapse; over only 2 ns of MD both antibodies undergo a significant compaction. Change in CCS with respect to simulation time is shown in Figure 3.10a. After 10 ns of *in vacuo* MD simulations, theoretical CCS calculated with TJM decreased to 86.5 nm^2, and 84.1 nm^2 for 1IGT, and 1IGY, respectively. These CCS are still a little higher than median experimental values, although Figure 3.5 shows that around 20% of the conformational occupancy of the mAbs is at or above these t = 10 ns theoretical values. Since the millisecond time scale of the ion mobility experiments greatly exceeds the simulation time (ions take ~12 - 24 ms to transverse MoQToF's drift cell), further structural compaction is anticipated with longer time *in vacuo*.

During it's gas-phase evolution represented as a red line in Figure 3.10, 1IGT undergoes the highest degree of compaction; from the initial CCS of 105.6 nm^2 to 86.5 nm^2 after 10 ns of MD simulation *i.e.* 18.1 % reduction in CCS. This very high conformational rearrangment is depicted also from the backbone root-mean-square deviation (RMSD) trend which plateaus at ~17 Å and again increases after 6 ns to reach ~20 Å after 10 ns, suggesting further structural rearangments to be taking place (Figure 3.10b). RMSD measures the average distance between the backbone atoms of superimposed protein

Table 3.2 Theoretical collision cross sections (CCS) of 1IGT and 1IGY at various time points (up to 10 ns) resulting from the *in vacuo* molecular dynamic simulations. Reported CCS were calculated with the trajectory method (TJM), the exact hard sphere scattering method (EHSS) and the projection approximation method (PA).

	TJM CCS /nm^2		EHSS CCS /nm^2		PA CCS /nm^2	
time /ns	1IGT	1IGY	1IGT	1IGY	1IGT	1IGY
0	105.57	100.84	104.61	98.60	82.03	76.30
0.156	-	-	-	-	-	-
0.250	94.91	87.31	98.28	90.07	75.79	68.60
0.380	-	-	-	-	-	-
0.464	-	90.16	-	89.39	-	68.06
0.500	95.41	90.05	95.96	89.58	74.23	68.12
1.000	93.26	87.6	93.75	87.37	72.17	66.28
1.182	91.3	-	93.31	-	71.84	-
1.496	90.63	-	91.85	-	70.44	-
1.500	92.94	84.96	92.05	84.90	70.75	64.30
1.860	-	85.17	-	85.00	-	64.39
2.000	89.43	83.77	89.62	84.76	68.52	64.27
2.500	89.50	83.86	89.39	84.94	68.37	64.35
3.000	88.26	86.60	89.49	84.93	68.63	64.28
3.500	91.69	85.50	89.42	84.61	68.25	64.30
4.000	86.63	84.23	89.14	84.43	68.13	63.88
4.500	89.88	83.70	89.31	84.17	68.28	63.71
5.000	88.48	85.34	89.10	84.84	68.17	64.15
5.500	87.54	84.20	88.96	84.34	68.02	63.86
6.000	86.37	85.79	88.41	84.15	67.69	63.74
6.500	88.24	85.00	87.54	84.16	66.78	63.88
7.000	87.57	85.33	87.31	84.01	66.83	63.72
7.500	89.15	82.72	87.40	83.23	66.68	63.21
8.000	88.95	83.27	87.00	83.01	66.59	63.08
8.500	87.00	83.55	86.74	83.36	66.28	63.26
9.000	86.67	82.69	87.10	83.21	66.40	63.09
9.500	85.25	83.95	86.35	83.55	65.85	63.31
10.000	86.49	84.13	87.00	83.77	66.40	63.40

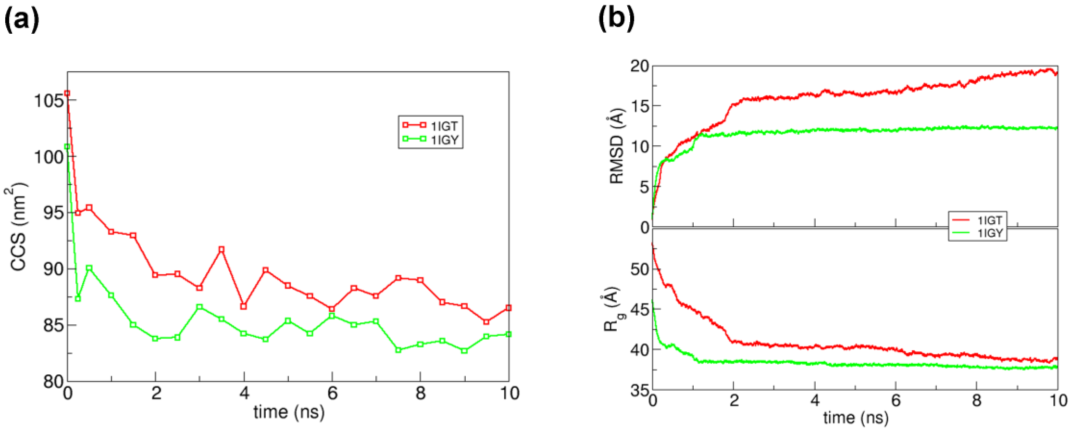

Figure 3.10 (a) Theoretical TJM based CCS in nm^2 of 1IGT (red) and 1IGY (green) subjected to molecular dynamics (MD) to investigate the *in vacuo* behaviour of the IgGs. Significant collapse of 1IGT and 1IGY is observed only after 0.25 ns. The points represent calculated CCS values reported in Table 3.2. (b) Backbone RMSD (Å) and R_g (Å) recorded during the 10 ns *in vacuo* MD of 1IGT (red) and 1IGY (green).

structures over the simulation time and indicates divergance among the aligned structures, hence larger values correlate to greater structural changes. The root mean square distance from each atom of the protein to the centriod expressed as radius of gyration (R_g), changes in a similar fashion throughout the simulation of 1IGT. A sharp decrease between 0 ns and 2 ns and subsequent gentle decrease between 2 ns and 10 ns is observed as seen in the bottom panel of Figure 3.10b. The 1IGY mAb (green line in Figure 3.10), shows 16.6 % decrease in CCS after 10 ns and its RMSD plateaus at ~12 Å. Although changes in CCS, RMSD and R_g are lesser, 1IGY collapses faster in comparison to 1IGT; within the first nanosecond it reaches a conformation stable up to 10 ns, whereas the compaction of 1IGT occurs within a double time scale (~2 ns) to conformation that is stable up to 6 ns and experiences further collapse afterwards. This gradual collapse of 1IGT is visualized in Figure 3.11, showing snapshots from the MD simulation at t = 0 ns, t = 1 ns and t = 10 ns. The contraction of three linked domains (two Fab arms and Fc fragment) is mainly observed around the hinge region. Furthermore it is worth noting that for each antibody, the CCS do not simply decrease as the simulation time progresses but fluctuate, being an indicative of flexible molecules, present over many interconverting conformers. This conclusion is also supported by wide ATD and the corresponding large CCSD across the narrow charge state range compared with that found for other protein complexes as discussed in the previous section (Figures 3.8 and 3.9).

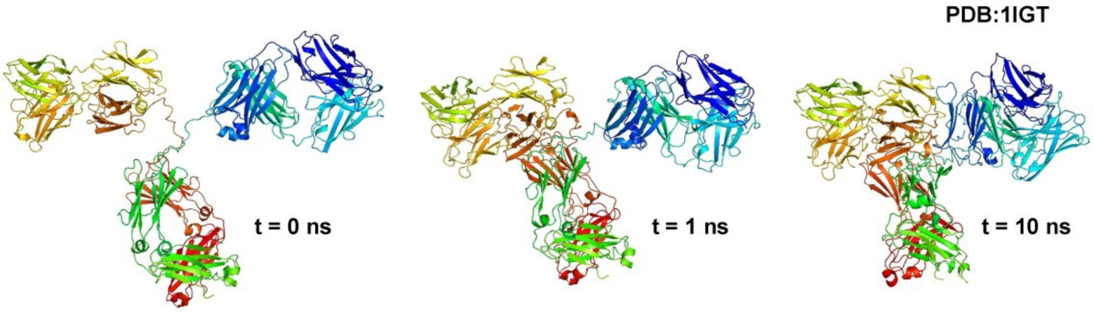

Figure 3.11 Snapshots from an *in vacuo* MD simulation at t = 0 ns, t = 1 ns and t = 10 ns presenting gradual contraction of an intact IgG2a (PDB:1IGT). Structural collapse can be mainly observed around the hinge region, whereas the folded domain regions remain well preserved.

3.3.5.2 Solvent content and secondary structure content

A significant amount of the volume of a protein crystal is occupied by solvent. An estimation of the number of molecules contained within a crystallographic asymmetric unit was first achieved by Matthews in 1968.[110] Matthews defined V_M, now known as the Matthews coefficient, as the crystal volume per unit of protein molecular weight expressed in Å^{3}Da^{-1}, which can be calculated using the following relationship:

$$V_M = \frac{V}{nM} \qquad (\textit{Equation 3.1})$$

where V is the volume of the unit cell, n is the number of asymmetric units and M is molecular weight of contents of the asymmetric unit. Moreover, it was shown that V_M has a straightforward relationship to the fractional volume of solvent (V_S) in the crystal and can be calculated *via*:

$$V_S = 1 - \frac{1.23}{V_M} \qquad (\textit{Equation 3.2})$$

V_M values for 1IGY and 1IGT were calculated to be 2.99 $Å^3Da^{-1}$ and 3.39 $Å^3Da^{-1}$ respectively, using an online Matthews Probability Calculator.[90] The solvent content (V_S), based on the Matthews coefficient, was found to be 59 % and 64 % for 1IGY and 1IGT, respectively. In each case this is higher than the average protein crystal structure solvent content of ~47% as calculated based on a survey of 10,471 entities in PDB.[111] As the mAbs desolvate, they lose both solvent and stabilising buffer interactions. Based on the high solvent content of the unit cells used here as a comparator, one would predict structural contraction that is experimentally observed. The 1IGT mAb having a higher solvent content is also seen to experience higher degree of compaction during the 10 ns MD simulation. Whilst these mAbs are not identical to the mAb studied experimentally, structural homology allows us to predict which regions of a mAb will contract and also which are unchanged *in vacuo*.

Despite a significant change in the theoretical CCS, the secondary structure content does not change drastically along the MD simulation time. This content was determined using AmberTools13 (module cpptraj), which implements the algorithm DSSP.[89] The percentage of secondary structure elements *i.e.* coils, turns, β-sheets and helices present at 2 ns intervals of the MD run is reported in Table 3.3 for both mAbs. After 10 ns of *in vacuo* MD simulation on the 1IGT crystal structure, the total helical content decreases from 7.1 % to 6.2 % and the total β-sheet content decreases from 47.3 % to 41.7 %. Similarly in case of the 1IGY crystal structure, the total helical content decreases from 6.2 % to 5.0 % and the total β-sheet content decreases from 43.3 % to 35.8 %. It can be seen in Figure 3.11, that structural contraction occurs mainly around the hinge region and the antigen binding region remains still well preserved *in vacuo*. The MD simulation shown how the linked folded domains of mAbs ‘dance’ in the absence of solution as they do in the condensed phase.[30,35,97]

Table 3.3 Secondary structure content and theoretical CCS (TJM based) of 1IGT and 1GTY prior to and at 2 ns intervals of *in vacuo* MD simulation.

1IGT						
Simulation time / ns	0	2	4	6	8	10
TJM based CCS / nm^2	106	89	87	86	89	86
Coil	34.42	37.92	39.82	42.48	40.20	41.95
Turn	11.25	11.32	10.79	11.63	10.87	10.11
Parallel-β-sheet	2.13	2.05	2.13	1.52	1.98	1.67
Anti-parallel-β-sheet	45.14	41.64	40.88	39.29	41.11	40.05
3_{10}-helix	3.50	3.57	3.80	2.66	3.50	3.80
α-helix	3.57	3.12	3.20	2.05	1.82	2.28
$\pi_{(3-14)}$-helix	0.00	0.38	0.38	0.38	0.53	0.15

1GTY						
Simulation time / ns	0	2	4	6	8	10
TJM based CCS / nm^2	101	84	84	86	83	84
Coil	39.57	47.30	46.83	45.52	44.36	47.06
Turn	10.97	11.90	10.66	11.67	12.67	12.13
Parallel-β-sheet	2.01	1.47	1.62	1.39	1.39	1.39
Anti-parallel-β-sheet	41.27	34.54	35.01	35.94	35.63	34.39
3_{10}-helix	3.94	3.17	4.40	3.63	4.48	4.02
α-helix	2.24	1.62	1.47	1.85	1.47	1.00
$\pi_{(3-14)}$-helix	0.00	0.00	0.00	0.00	0.00	0.00

3.4 Conclusions

IM-MS has revealed intact mAbs to be more structurally dynamic than proteins of comparable size which is attributed to their intrinsic flexibility. This flexibility of mAbs is reflected by broad CCSD landscapes and the lack of baseline resolution is an indicative of closely related interconverting conformational families present. Moreover, the distinct features in the hinge region and the non-covalent interactions at the CH3-CH3 interface are potentially responsible for the experimentally observed differences in CCSD of intact IgG1 and IgG4 as well as their Fc-hinge fragments.

The MD simulations indicate that desolvation causes a contraction in the hinge region and loss of the cavities between the folded domains of mAbs; however, still preserves much of the secondary structure as well as the tertiary fold. The subtle differences in IM-MS data from the two IgG subclasses, with IgG1 less flexible than IgG4 in the absence of solvent, these contrasts with solution evidence which shows the IgG4 hinge to be more rigid than that of IgG1, and raises interesting caveats about the use of mass spectrometry to probe higher order structure in flexible proteins such as mAbs or biosimilars. Nevertheless, IM-MS and MD simulations have shown that the linked folded domains proteins 'dance' in the absence of solution as they do in the condensed phase. In future, 'freezing' molecules in the gas-phase by use of low temperature IM-MS and preferably instruments with higher mobility separation capabilities, could provide insights into the conformational diversity of mAbs.

3.5 References

(1) Litman, G. F.; Anderson, M. K.; Rast, J. *Annual Review of Immunology* **1999**, *17*, 109.
(2) Amzel, L. M.; Poljak, R. J. *Annual Review of Biochemistry* **1979**, *48*, 961.
(3) Junqueira, L. C.; Carneira, J.; Kelley, R. O. *Basic Histology*; McGraw-Hill Publishing Co, 1998.
(4) Rojas, R.; Apodaca, G. *Nature Reviews Molecular Cell Biology* **2002**, *3*, 944.
(5) Janeway, C. A.; Travers, P.; Walport, M.; Shlomchik, M. J. *Immunobiology: The Immune System in Health and Disease*; Garland Publishing: New York, 2001.
(6) Schiffer, M.; Girling, R. L.; Ely, K. R.; Edmundso.Ab *Biochemistry* **1973**, *12*, 4620.
(7) Poljak, R. J.; Amzel, L. M.; Avey, H. P.; Chen, B. L.; Phizacke.Rp; Saul, F. *Proceedings of the National Academy of Sciences of the United States of America* **1973**, *70*, 3305.
(8) Porter, R. R. *Biochemical Journal* **1959**, *73*, 119.
(9) Porter, R. R. *Nature* **1958**, *182*, 670.
(10) Arnold, J. N.; Wormald, M. R.; Sim, R. B.; Rudd, P. M.; Dwek, R. A. *Annual Review of Immunology* **2007**, *25*, 21.
(11) Pink, J. R. L.; Milstein, C. *Nature* **1967**, *216*, 941.
(12) Frangion, B.; Milstein, C. *Journal of Molecular Biology* **1968**, *33*, 983.
(13) Pink, J. R. L.; Milstein, C. *Nature* **1967**, *214*, 92.
(14) Milstein, C.; Frangion, B. *Biochemical Journal* **1971**, *121*, 217.
(15) Liu, H.; May, K. *Mabs* **2012**, *4*, 17.
(16) Frangion, B.; Milstein, C.; Franklin, E. C. *Biochemical Journal* **1968**, *106*, 15.
(17) Frangion, B.; Milstein, C. *Nature* **1967**, *216*, 939.
(18) Wypych, J.; Li, M.; Guo, A.; Zhang, Z.; Martinez, T.; Allen, M. J.; Fodor, S.; Kelner, D. N.; Flynn, G. C.; Liu, Y. D.; Bondarenko, P. V.; Ricci, M. S.; Dillon, T. M.; Balland, A. *Journal of Biological Chemistry* **2008**, *283*, 16194.
(19) Dillon, T. M.; Ricci, M. S.; Vezina, C.; Flynn, G. C.; Liu, Y. D.; Rehder, D. S.; Plant, M.; Henkle, B.; Li, Y.; Deechongkit, S.; Varnum, B.; Wypych, J.; Balland, A.; Bondarenko, P. V. *Journal of Biological Chemistry* **2008**, *283*, 16206.

(20) Martinez, T.; Guo, A.; Allen, M. J.; Han, M.; Pace, D.; Jones, J.; Gillespie, R.; Ketchem, R. R.; Zhang, Y.; Balland, A. *Biochemistry* **2008**, *47*, 7496.

(21) Liu, Y. D.; Wang, T.; Chou, R.; Chen, L.; Kannan, G.; Stevenson, R.; Goetze, A. M.; Jiang, X. G.; Huang, G.; Dillon, T. M.; Flynn, G. C. *Molecular Immunology* **2013**, *54*, 217.

(22) Schuurman, J.; Perdok, G. J.; Gorter, A. D.; Aalberse, R. C. *Molecular Immunology* **2001**, *38*, 1.

(23) Schuurman, J.; Van Ree, R.; Perdok, G. J.; Van Doorn, H. R.; Tan, K. Y.; Aalberse, R. C. *Immunology* **1999**, *97*, 693.

(24) Aalberse, R. C.; Schuurman, J. *Immunology* **2002**, *105*, 9.

(25) Kolfschoten, M. v. d. N.; Schuurman, J.; Losen, M.; Bleeker, W. K.; Martinez-Martinez, P.; Vermeulen, E.; den Bleker, T. H.; Wiegman, L.; Vink, T.; Aarden, L. A.; De Baets, M. H.; van De Winkel, J. G. J.; Aalberse, R. C.; Parren, P. W. H. I. *Science* **2007**, *317*, 1554.

(26) Rispens, T.; Ooijevaar-de Heer, P.; Bende, O.; Aalberse, R. C. *Journal of the American Chemical Society* **2011**, *133*, 10302.

(27) Rispens, T.; Davies, A. M.; Ooijevaar-de Heer, P.; Absalah, S.; Bende, O.; Sutton, B. J.; Vidarsson, G.; Aalberse, R. C. *The Journal of biological chemistry* **2014**, *289*, 6098.

(28) Saphire, E. O.; Parren, P.; Pantophlet, R.; Zwick, M. B.; Morris, G. M.; Rudd, P. M.; Dwek, R. A.; Stanfield, R. L.; Burton, D. R.; Wilson, I. A. *Science* **2001**, *293*, 1155.

(29) Roux, K. H. *International Archives of Allergy and Immunology* **1999**, *120*, 85.

(30) Dangl, J. L.; Wensel, T. G.; Morrison, S. L.; Stryer, L.; Herzenberg, L. A.; Oi, V. T. *Embo Journal* **1988**, *7*, 1989.

(31) Sandin, S.; Ofverstedt, L. G.; Wikstrom, A. C.; Wrange, O.; Skoglund, U. *Structure* **2004**, *12*, 409.

(32) Bongini, L.; Fanelli, D.; Piazza, F.; De los Rios, P.; Sandin, S.; Skoglund, U. *Proceedings of the National Academy of Sciences of the United States of America* **2004**, *101*, 6466.

(33) Noelken, M. E.; Nelson, C. A.; Buckley, C. E.; Tanford, C. *Journal of Biological Chemistry* **1965**, *240*, 218.

(34) Yguerabi.J; Epstein, H. F.; Stryer, L. *Journal of Molecular Biology* **1970**, *51*, 573.

(35) Roux, K. H.; Strelets, L.; Michaelsen, T. E. *Journal of Immunology* **1997**, *159*, 3372.

(36) Brekke, O. H.; Michaelsen, T. E.; Sandlie, I. *Immunology Today* **1995**, *16*, 85.

(37) Kim, H.; Matsunaga, C.; Yoshino, A.; Kato, K.; Arata, Y. *Journal of Molecular Biology* **1994**, *236*, 300.

(38) Schumaker, V. N.; Phillips, M. L.; Hanson, D. C. *Molecular Immunology* **1991**, *28*, 1347.

(39) Huber, R.; Bennett, W. S. *Nature* **1987**, *326*, 334.

(40) Abramov, V. M.; Arkhangelskaya, Z. A.; Zavyalov, V. P. *Biochimica Et Biophysica Acta* **1983**, *742*, 295.

(41) Presta, L. G. *Current Opinion in Immunology* **2008**, *20*, 460.

(42) Carter, P. J. *Experimental Cell Research* **2011**, *317*, 1261.

(43) Caravella, J.; Lugovskoy, A. *Current Opinion in Chemical Biology* **2010**, *14*, 520.

(44) Dimitrov, D. S. *Mabs* **2010**, *2*, 347.

(45) Scott, A. M.; Wolchok, J. D.; Old, L. J. *Nature Reviews Cancer* **2012**, *12*, 278.

(46) Scott, A. M.; Allison, J. P.; Wolchok, J. D. *Cancer Immunity* **2012**, *12*, 14.

(47) Chan, A. C.; Carter, P. J. *Nature Reviews Immunology* **2010**, *10*, 301.

(48) Valera, E.; Masliah, E. *Pharmacology & Therapeutics* **2013**, *138*, 311.

(49) Goetz, J.; Ittner, A.; Ittner, L. M. *British Journal of Pharmacology* **2012**, *165*, 1246.

(50) Beck, A.; Wurch, T.; Bailly, C.; Corvaia, N. *Nature Reviews Immunology* **2010**, *10*, 345.

(51) Reichert, J. M. *Mabs* **2010**, *2*, 84.

(52) Steiner, M.; Neri, D. *Clinical Cancer Research* **2011**, *17*, 6406.

(53) Hess, C.; Venetz, D.; Neri, D. *Medchemcomm* **2014**, *5*, 408.

(54) Beck, A.; Haeuw, J.-F.; Wurch, T.; Goetsch, L.; Bailly, C.; Corvaia, N. *Discovery Medicine* **2010**, *53*, 329.

(55) Chari, R. V. J.; Miller, M. L.; Widdison, W. C. *Angewandte Chemie* **2014**, *53*, 3796.

(56) Drachman, J. G.; Senter, P. D. *Hematology-American Society of Hematology Education Program* **2013**, 306.

(57) Lianos, G. D.; Vlachos, K.; Zoras, O.; Katsios, C.; Cho, W. C.; Roukos, D. H. *Oncotargets and Therapy* **2014**, *7*, 491.

(58) Beck, A.; Reichert, J. M. *Mabs* **2011**, *3*, 221.

(59) Fournier, P.; Schirrmacher, V. *Biodrugs* **2013**, *27*, 35.

(60) May, C.; Sapra, P.; Gerber, H.-P. *Biochemical Pharmacology* **2012**, *84*, 1105.
(61) Kontermann, R. E. *Mabs* **2012**, *4*, 182.
(62) Pasche, N.; Neri, D. *Drug Discovery Today* **2012**, *17*, 583.
(63) List, T.; Neri, D. *Clinical pharmacology : advances and applications* **2013**, *5*, 29.
(64) Nelson, A. L. *Mabs* **2010**, *2*, 77.
(65) Beck, A.; Reichert, J. M. *Mabs* **2011**, *3*, 415.
(66) Wu, B.; Sun, Y.-N. *Journal of Pharmaceutical Sciences* **2014**, *103*, 53.
(67) Walsh, G. *Nature Biotechnology* **2010**, *28*, 917.
(68) Erickson, B. E. *Chemical & Engineering News* **2010**, *88*, 25.
(69) Berkowitz, S. A.; Engen, J. R.; Mazzeo, J. R.; Jones, G. B. *Nature Reviews Drug Discovery* **2012**, *11*, 527.
(70) Beck, A. *Mabs* **2011**, *3*, 107.
(71) Beck, A.; Wagner-Rousset, E.; Ayoub, D.; Van Dorsselaer, A.; Sanglier-Cianferani, S. *Analytical Chemistry* **2013**, *85*, 715.
(72) Thompson, N. J.; Rosati, S.; Rose, R. J.; Heck, A. J. R. *Chemical Communications* **2013**, *49*, 538.
(73) Zhang, Z.; Pan, H.; Chen, X. *Mass Spectrometry Reviews* **2009**, *28*, 147.
(74) Ezan, E.; Dubois, M.; Becher, F. *Analyst* **2009**, *134*, 825.
(75) Rosati, S.; van den Bremer, E. T. J.; Schuurman, J.; Parren, P. W. H. I.; Kamerling, J. P.; Heck, A. J. R. *Mabs* **2013**, *5*, 917.
(76) Rosati, S.; Thompson, N. J.; Barendregt, A.; Hendriks, L. J. A.; Bakker, A. B. H.; de Kruif, J.; Throsby, M.; van Duijn, E.; Heck, A. J. R. *Analytical Chemistry* **2012**, *84*, 7227.
(77) Beck, A.; Sanglier-Cianferani, S.; Van Dorsselaer, A. *Analytical Chemistry* **2012**, *84*, 4637.
(78) Richter, V.; Kwiatkowski, M.; Omidi, M.; Robertson, W. D.; Schlueter, H. *Pharmaceutical Bioprocessing* **2013**, *1*, 381.
(79) Bagal, D.; Valliere-Douglass, J. F.; Balland, A.; Schnier, P. D. *Analytical Chemistry* **2010**, *82*, 6751.
(80) Jones, L. M.; Zhang, H.; Cui, W.; Kumar, S.; Sperry, J. B.; Carroll, J. A.; Gross, M. L. *Journal of the American Society for Mass Spectrometry* **2013**, *24*, 835.
(81) Pritchard, C.; O'Connor, G.; Ashcroft, A. E. *Analytical chemistry* **2013**, *85*, 7205.
(82) Debaene, F.; Wagner-Rousset, E.; Colas, O.; Ayoub, D.; Corvaia, N.; Van Dorsselaer, A.; Beck, A.; Cianferani, S. *Analytical Chemistry* **2013**, *85*, 9785.
(83) McCullough, B. J.; Kalapothakis, J.; Eastwood, H.; Kemper, P.; MacMillan, D.; Taylor, K.; Dorin, J.; Barran, P. E. *Analytical Chemistry* **2008**, *80*, 6336.
(84) Case, D. A.; Darden, T. A.; III, T. E. C.; Simmerling, C. L.; Wang, J.; Duke, R. E.; Luo, R.; Walker, R. C.; Zhang, W.; Merz, K. M.; Roberts, B.; Wang, B.; Hayik, S.; Roitberg, A.; Seabra, G.; Kolossvary, I.; F.Wong, K.; Paesani, F.; Vanicek, J.; Liu, J.; X.Wu; Brozell, S. R.; Steinbrecher, T.; H. Gohlke; Cai, Q.; Ye, X.; Wang, J.; Hsieh, M.-J.; Cui, G.; Roe, D. R.; Mathews, D. H.; Seetin, M. G.; Sagui, C.; Babin, V.; Luchko, T.; Gusarov, S.; Kovalenko, A.; Kollman, P. A. University of California, San Francisco, 2010.
(85) Lindorff-Larsen, K.; Piana, S.; Palmo, K.; Maragakis, P.; Klepeis, J. L.; Dror, R. O.; shaw, D. E. *Proteins-Structure Function and Bioinformatics* **2010**, *78*, 1950.
(86) Shvartsburg, A. A.; Schatz, G. C.; Jarrold, M. F. *Journal of Chemical Physics* **1998**, *108*, 2416.
(87) Bleiholder, C.; Contreras, S.; Do, T. D.; Bowers, M. T. *International Journal of Mass Spectrometry* **2013**, *345*, 89.
(88) Phillips, J. C.; Braun, R.; Wang, W.; Gumbart, J.; Tajkhorshid, E.; Villa, E.; Chipot, C.; Skeel, R. D.; Kale, L.; Schulten, K. *Journal of Computational Chemistry* **2005**, *26*, 1781.
(89) Kabsch, W.; Sander, C. *Biopolymers* **1983**, *22*, 2577.
(90) Rupp, B.; Matthews Probabilities Calculator; http://www.ruppweb.org/mattprob/default.html ed. 2005-2014.
(91) Smith, R. D.; Loo, J. A.; Barinaga, C. J.; Edmonds, C. G.; Udseth, H. R. *Journal of the American Society for Mass Spectrometry* **1990**, *1*, 53.
(92) Sobott, F.; Robinson, C. V. *International Journal of Mass Spectrometry* **2004**, *236*, 25.
(93) Benesch, J. L. P. *Journal of the American Society for Mass Spectrometry* **2009**, *20*, 341.
(94) Kitova, E. N.; Sinelnikov, I.; Deng, L.; Klassen, J. S. *International Journal of Mass Spectrometry* **2013**, *345*, 97.

(95) Zhou, M.; Dagan, S.; Wysocki, V. H. *Angewandte Chemie-International Edition* **2012**, *51*, 4336.

(96) Hall, Z.; Politis, A.; Bush, M. F.; Smith, L. J.; Robinson, C. V. *Journal of the American Chemical Society* **2012**, *134*, 3429.

(97) Oi, V. T.; Vuong, T. M.; Hardy, R.; Reidler, J.; Dangl, J.; Herzenberg, L. A.; Stryer, L. *Nature* **1984**, *307*, 136.

(98) Labrijn, A. F.; Rispens, T.; Meesters, J.; Rose, R. J.; den Bleker, T. H.; Loverix, S.; van den Bremer, E. T. J.; Neijssen, J.; Vink, T.; Lasters, I.; Aalberse, R. C.; Heck, A. J. R.; van de Winkel, J. G. J.; Schuurman, J.; Parren, P. W. H. I. *Journal of Immunology* **2011**, *187*, 3238.

(99) Rispens, T.; Ooievaar-De Heer, P.; Vermeulen, E.; Schuurman, J.; Kolfschoten, M. v. d. N.; Aalberse, R. C. *Journal of Immunology* **2009**, *182*, 4275.

(100) Davies, A. M.; Rispens, T.; Heer, P. O.-d.; Gould, H. J.; Jefferis, R.; Aalberse, R. C.; Sutton, B. J. *Journal of Molecular Biology* **2014**, *426*, 630.

(101) Rispens, T.; Ooijevaar-de Heer, P.; Bende, O.; Aalberse, R. C. *Journal of the American Chemical Society* **2011**, *133*.

(102) Rose, R. J.; Labrijn, A. F.; van den Bremer, E. T. J.; Loverix, S.; Lasters, I.; van Berkel, P. H. C.; van de Winkel, J. G. J.; Schuurman, J.; Parren, P. W. H. I.; Heck, A. J. R. *Structure* **2011**, *19*, 1274.

(103) Davies, A. M.; Rispens, T.; den Bleker, T. H.; McDonnell, J. M.; Gould, H. J.; Aalberse, R. C.; Sutton, B. J. *Molecular Immunology* **2013**, *54*, 1.

(104) Harris, L. J.; Skaletsky, E.; McPherson, A. *Journal of Molecular Biology* **1998**, *275*, 861.

(105) Harris, L. J.; Larson, S. B.; Hasel, K. W.; McPherson, A. *Biochemistry* **1997**, *36*, 1581.

(106) Wyttenbach, T.; vonHelden, G.; Batka, J. J.; Carlat, D.; Bowers, M. T. *J Am Soc Mass Spectr* **1997**, *8*, 275.

(107) Mesleh, M. F.; Hunter, J. M.; Shvartsburg, A. A.; Schatz, G. C.; Jarrold, M. F. *Journal of Physical Chemistry* **1996**, *100*, 16082.

(108) Shvartsburg, A. A.; Jarrold, M. F. *Chemical Physics Letters* **1996**, *261*, 86.

(109) Jurneczko, E.; Barran, P. E. *Analyst* **2011**, *136*, 20.

(110) Matthews, B. W. *Journal of Molecular Biology* **1968**, *33*, 491.

(111) Kantardjieff, K. A.; Rupp, B. *Protein Science* **2003**, *12*, 1865.

4

Variable Temperature (IM)-MS: Unfolding and Dissociation of Multimeric Protein Complexes

Proteins and protein complexes undergo structural changes depending on the surrounding environment, in turn affecting their biological function. Here, VT-MS is applied to study four multimeric protein complexes and allow for decoupling of their melting temperature (T_m) from the protein complex dissociation temperature (T_{GPD}). VT-IM-MS is used to investigate structural changes of these proteins at elevated temperatures and provide insight into the thermally induced dissociation (TID) mechanism, as well as strength of the non-covalent interactions between subunits.

4.1 Introduction

The biophysical properties, biological activity and function of macromolecular systems are highly dependent on their structure. In turn structure-function analyses are critical for drug discovery, biochemical or medical research.[1-3] Changes to protein structure, either due to post-translational modifications (PTMs), mutations or protein denaturation can alter both the function and the biophysical properties of a given protein.[4-6] The structure of these large complex molecules is not only greatly dependent on their amino acid sequence, but also on their surrounding environment, and can be altered by changes in solution conditions (pH, ionic strength) or by physical parameters like temperature and pressure. Understanding the molecular basis of thermodynamic stability of proteins is a fundamental problem with clear practical applications. Nowadays, with an emerging market for protein based therapeutics, improving protein stability has a tangible benefit.[7,8] Thermal stability is an indicative of global protein stability and is traditionally probed using circular dichroism and/or calorimetry techniques such as differential scanning calorimetry (DSC).[9-11] Data obtained from such analysis can also delineate other properties of proteins such as their ease of crystallization for further structural studies.[12]

4.1.1 Variable temperature IM-MS studies: past and present

Jarrold *et al*. were the first to report variable temperature (VT) IM-MS to probe temperature dependent conformations adopted by proteins in the gas phase. Their initial study revealed that the effect of increased temperature on the CCS of cytochrome *c* ions was charge state dependent.[13,14] Measurements were performed at various temperatures over the range 273-573 K; it was reported that lower charge states (5+ and 6+) show little change in CCS over the temperature range, whereas higher charge states (7+) demonstrate dramatic changes in the CCS attributed to a series of unfolding transitions as the temperature is raised. Later, Bowers and co-workers applied VT-IM-MS to study unfolding and dissociation of amyloid *β*-protein peptide multimers.[15] Last year, the Barran group reported on the effect of the salt on the conformations of model monomeric proteins (BPTI, ubiquitin and cytochrome *c*) at temperatures ranging from 260 to 360 K.[16] The study showed that thermally induced unfolding is minimized in the presence of adducted iodide to monomeric proteins, and that at relatively low temperatures, native proteins can unfold.

Currently, there is no commercially available instrument suitable for analysis of large biomolecules that would allow drift gas temperature control and variation. Even though, variable temperature technique of selected ion flow tube MS (SIFT-MS) exists, it is applied for the study of ion-molecule reaction kinetics in the gas phase yielding reaction rate coefficients; this type of instrumentation is commonly used for volatile compounds and is not suitable for large protein work.[17-19] Our in-house modified linear drift tube ion mobility mass spectrometer[20] features heating and cooling capabilities and allows for control of the buffer gas temperature within 200 – 600 K range. Several other IM-MS instruments with temperature control exist, allowing for work either at cryogenic or elevated temperatures. Often, the mass working range is limited and the above mentioned instruments have predominantly been used to study small molecules, peptides or monomeric proteins.[21,22-25] Recently, Russell *et al*. reported on capturing hydrated peptide ions in their linear drift tube VT-IM mass spectrometer with cryogenic capabilities designed for non-covalent complexes and weakly bound cluster ions.[26] Using low temperature (~80 K) in the drift region allowed for preservation of short lived hydrated gramicidin S and bradykinin ions. The results suggested that the number of water clusters retained and hydration process might be peptide specific.[26] Studies as such, illustrate the importance of VT-MS and VT-IM-MS experiments and how these new approaches can be used to address fundamental questions related to gas phase biomolecules.

The focus of the work presented in this chapter is to extend the capabilities of VT-IM-MS methodology to the study of multimeric protein complexes. The motivation to do so is based on the fact that most proteins tend to exist as multiple domains; from the distribution of oligomeric states in the Protein Data Base (PDB), 86% of proteins exist as oligomers.[27] The behavior of four commercially available model protein complexes: transthyretin (TTR), avidin, concanavalin A (conA) and human serum amyloid P component (SAP) was probed at temperatures from 300 K up to 550 K and traced thermally induced dissociation (TID) of subunits in the gas-phase with IM-MS. Unlike, solution studies, TID enables the protein complex melting temperature (T_m) to be decoupled from the complex dissociation temperature (T_{GPD}). Moreover, the conformational changes occurring during the dissociation process are revealed. This approach provides fundamental insights into protein folding, subunit interactions and could be adapted to derive fundamental thermodynamic parameters.

4.2 Methodology

4.2.1 Sample preparation

Ion species selected for this study were four commercially available multimeric protein complexes: human transthyretin (TTR, 55kDa), avidin (64 kDa), concanavalin A (conA, 103 kDa), human serum amyloid P component (SAP, 128 kDa). Avidin from egg white (A9275) and concanavalin A from *Canavalia ensiformis* (C2010) were obtained from Sigma Aldrich (St. Louis, MO, USA). Human TTR was obtained from SCIPAC (Sittingbourne, UK); human SAP was obtained from CalBioChem (Darmstadt, Germany). Amino acid sequences of all four complexes are available in the Appendix 3. Ammonium acetate (AmAc) was obtained from Fisher Scientific (Loughborough, UK). 40μM protein complex solutions (avidin, conA and SAP) were prepared in 200 mM AmAc (pH 6.8) and stored at -25℃. The buffer was exchanged to 100 mM AmAc on the day of analysis, using micro Bio-Spin Chromatography columns (Micro Bio-Spin 6 Columns, Tris) following the instructions specified by the manufacturer. The desalting procedure was performed twice to achieve desired sample purity. High purity water was obtained from an Arium 611 water purification unit (Sartorius, Göttingen, Germany) fitted with a 0.2 μm filter.

4.2.2 Variable temperature mass spectrometry and variable temperature ion mobility mass spectrometry

30 μM samples were ionised using positive nESI as described in Chapter 2, section 2.1.2. IM-MS data were acquired on the MoQToF, quadrupole time-of-flight mass spectrometer modified in-house to include 5.1 cm drift cell, detailed in section 2.2.1.[20] Voltages along the mass spectrometer were adjusted to preserve non-covalent

interactions and native like structures. The capillary potential was held at 1.5 - 1.8 kV, the source temperature was set to 80 °C, and the cone voltage was set to 80 V. The injection energy used was between 31 and 36 V. Other instrumental settings for the MoQToF IM mass spectrometer are listed in Chapter 2, Table 2.3. The drift cell was filled with helium as the buffer gas at a pressure of 3.7 – 3.8 Torr and the pressure measured using a capacitance manometer (MKS Instruments, UK); the precise pressure was recorded for each and every drift voltage and used in the calculations of CCS. Ion mobility experiments were carried out at several drift cell temperatures ranging from 300 K to 550 K, as discussed in the results section. The cell was heated *via* tantalum wire wound ceramic heaters located in both the cell body (8 heaters) and in the end cap (2 heaters) driven by variable transformers (Variacs). The temperature of the drift cell was monitored using three k-type thermocouples and recorded for each data set. The electric potential across the cell was varied from 60 to 15 V with measurements taken at six different drift voltages. In cases, when the signal intensity was low (SAP, at $T \geq 450$ K) 20 V instead of 15 V was used as the sixth drift voltage data point. The rotationally-averaged collision cross-sections (CCS) were determined from a plot of arrival time versus P / T and the CCSD were determined as described in Chapter 2, section 2.2.1.4. Data was processed using Mass Lynx V.4.1 Build 10, Microsoft Excel 2003 and Origin 8.5.1 graphing software (OriginLab, Northampton, MA, USA). The VT-MS experiments were repeated in triplicate and the average values are reported. VT-IM-MS experiment on TTR, SAP and avidin (only at 475 K) were performed twice. Experiments on avidin at the remaining temperatures and concanavalin A were performed once.

4.2.3 Calculations of the surface interface area, number of hydrogen bonds and salt bridges

Calculations on the surface interface area, possible number of hydrogen bonds and salt bridges of TTR and avidin were carried out using the online ‘Protein interfaces, surfaces and assemblies’ service PISA at the European Bioinformatics Institute website (http://www.ebi.ac.uk/pdbe/prot_int/pistart.html).[28,29] Three structures of TTR (PDB: 1BMZ, 1DVQ, 3U2I) and avidin (PDB: 1AVE, 1VYO, 1RAV) deposited in the Protein Data Bank were used and the average values for each protein are reported.

4.3 Results and Discussion

4.3.1 Probing dissociation of protein complexes with VT-MS

VT-MS experiments were performed on four protein complexes shown in Figure 4.1: tetrameric transthyretin (TTR, 55 kDa), avidin (64 kDa) and concanavalin A (conA, 103 kDa) and a pentameric human serum amyloid P component (SAP, 128 kDa). 30 µM protein samples in 100 mM ammonium acetate at pH 6.8 were ionised using nESI and data were acquired on the in-house modified IM-MS instrument (MoQToF) shown in Figure 2.3. The selected model protein complexes have been well studied *via* mass spectrometry by other groups,[30-38] are commercially available, have easy preparation requirements, yield a constant spray, and have been proposed as suitable calibrants for TWIMS mass spectrometers.[39] In order to preserve complexes' quaternary structure, key source parameters were optimized, in particular the capillary, sample and extractor cone and injection energy voltages.

Mass spectra of complexes under investigation present relatively narrow charge state distributions indicating well preserved gas-phase structures (Figure 4.2). The temperature of the drift cell helium gas was raised *via* ten tantalum wire wound ceramic heaters driven by two external variable transformers and the temperature was closely monitored by the capacitance manometer. Mass spectra were recorded at temperatures ranging from 300 K to 550 K at 20-50 K intervals. The time ions spend in the temperature controlled region of MoQToF is dependent on the ions' mass, charge and the electric potential applied across the drift cell. In the experiment at 300 K presented here, this time varied from 1.8 ms to 4.2 ms for the 55 kDa TTR where z = 15+ charge and from 2.2 ms to 5.2 ms for the 128 kDa SAP where z = 22+ charge, where the potential difference across the drift cell ranging from 60 to 15 V. The experimental time frame does vary somewhat with temperature, however, this was minimised by adjusting the pressure as a function of temperature to match the drift time at 300 K.

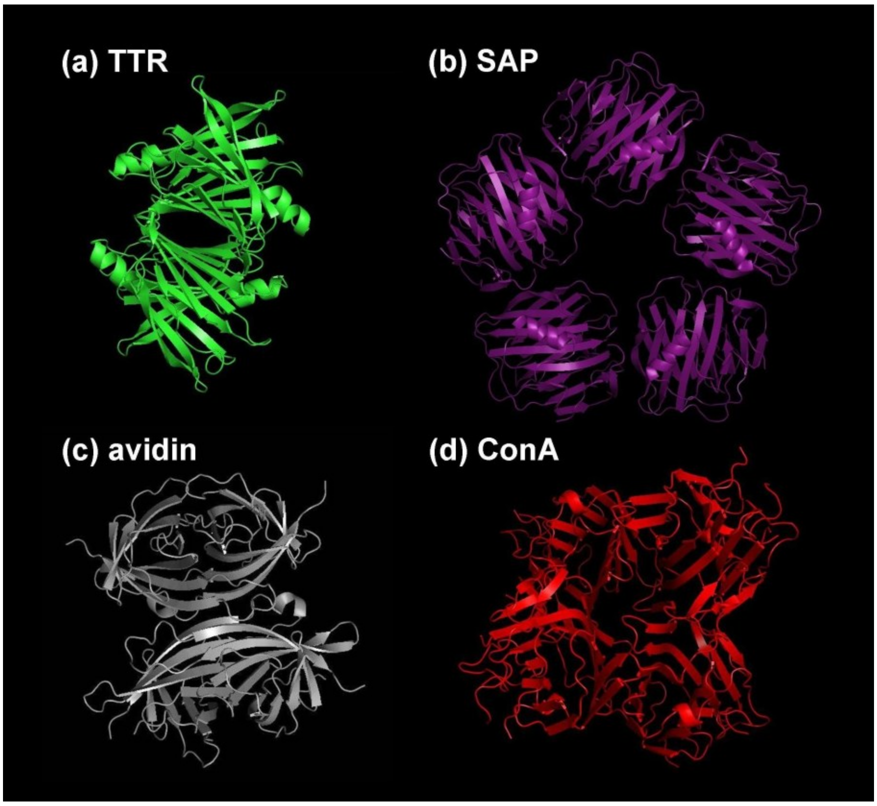

Figure 4.1 Structure of (a) TTR tetramer, (b) SAP pentamer, (c) avidin and (d) concanavalin A based on the x-ray crystal structures available in PDB: 1BMZ, 1SAP, 1AVE and 1DQ2 respectively.

Mass spectra of TTR, SAP, avidin and conA at progressively higher temperatures are shown in Figure 4.2. TTR, a 55 kDa homotetrameric protein, is present in a narrow charge state distribution centred at 14+ charge state (~*m/z* 3950). A minor amount of a higher order species *i.e.* a dimer of tetramer, is also observed around *m/z* 5000. A range of sample concentrations and buffer strengths were examined prior to choosing the most suitable experimental conditions. Upon the increase of temperature up to 400 K, the TTR complex remains intact as a tetramer in the 1.7 – 4.1 ms (at 60 – 15 V drift voltage) it spends in the high temperature environment of the drift cell. Above 450 K, dissociation of this tetrameric complex into monomers is observed. Several monomeric species are now present in the *m/z* 1200 – 2400 region of the mass spectrum, with 8+ charge state (~ *m/z* 1735) being the most abundant. Above 550 K, higher order species are no longer detected and only small amount of tetrameric species remains. As can be seen in the top mass spectrum in Figure 4.2a, is dominated by 10+ to 6+ TTR monomers. Moreover, low charge intermediate trimers, centred on a 6+charge state (~ *m/z* 5900), are present.

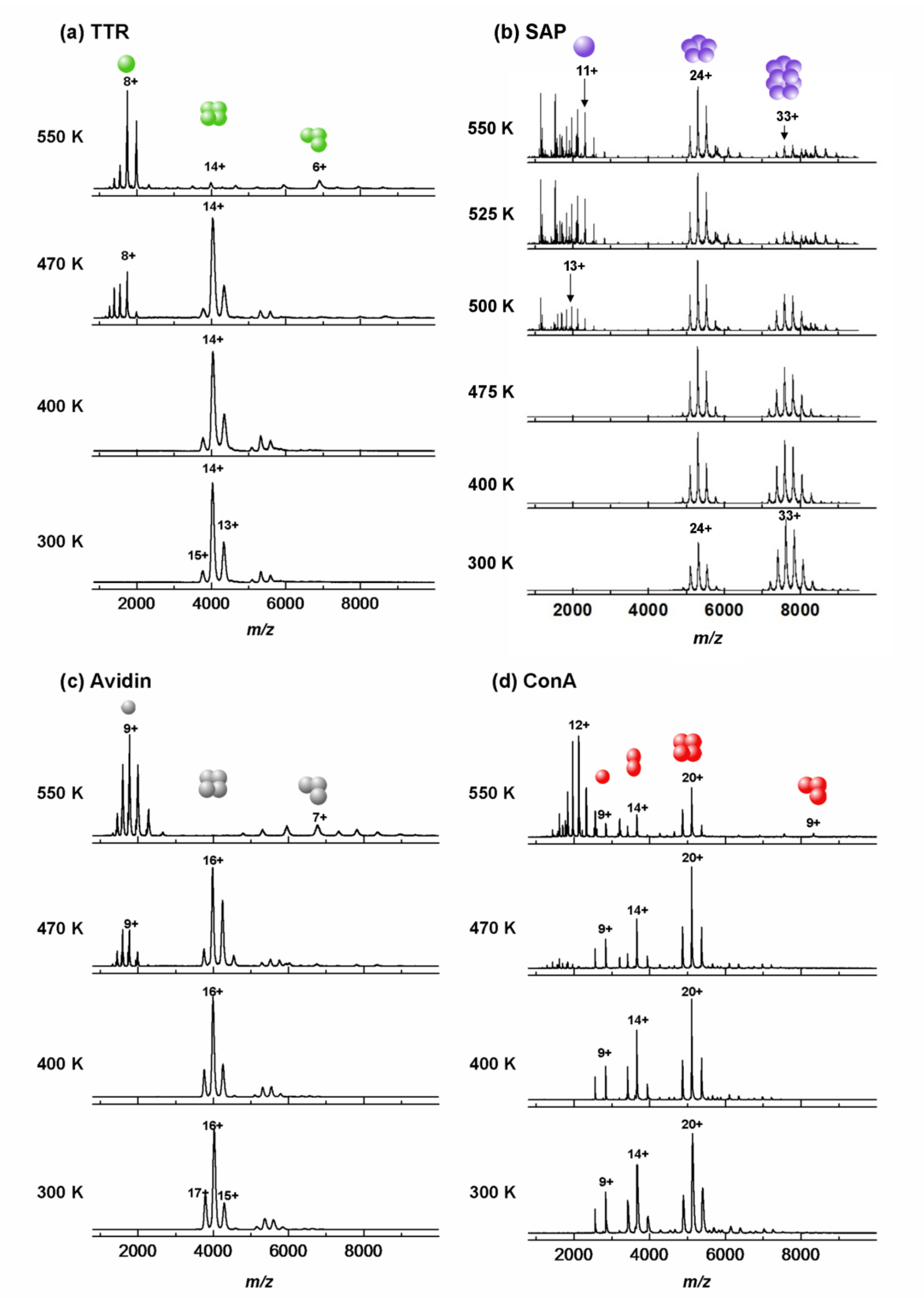

Figure 4.2 Mass spectra acquired at 300 - 550 K for (a) transthyretin (TTR), (b) human serum amyloid P component (SAP) (c) avidin and (d) concanavalin A (ConA) illustrating thermally induced dissociation (TID) of in the gas-phase. As the temperature is increased, the m/z peaks become narrower which is attributed to more efficient stripping of salt adducts.

At 300 K, the charge is more or less evenly distributed among the subunits at 300 K; however, at elevated temperatures when the dissociation occurs, the ejected monomer carriers over 50 % of the total charge. This 'asymmetric' charge partitioning suggests that the subunit undergoes unfolding prior to dissociation as observed in the CID experiments in the past, following the 'typical' dissociation route.[40]

SAP requires higher temperature for the onset of dissociation into monomers to take place. The 128 kDa SAP presents a slightly broader charge state distribution than TTR, present in the *m/z* 4900 – 5900 region and centred on the 24+ charge state (~ *m/z* 5330). Even with the relatively low 30 μM sample concentration a significant amount decamer is present.[41] These higher order species remain observable until above 550 K (Figure 4.2b). Mass spectra acquired at temperatures between 300 K and 500 K, show a gradual decrease of decameric SAP population. No dissociation of SAP into monomers is observed below 500 K. Above 500 K, SAP begins to dissociate into monomeric species centred on the 11+ charge state, ~*m/z* 2320, as shown in the top spectrum in Figure 4.2b. Due to the instrumental layout (drift cell prior to quadrupole analyzer), it is not possible to mass select ion species to determine whether the majority of dissociated monomer is ejected from SAP pentamer or decamer. As for TTR, asymmetric charge partitioning is observed, implying unfolding of the subunit(s) prior to complex dissociation. Furthermore, at temperatures at which dissociation into monomers occurs, additional peaks are observed at ~*m/z* 1147 and ~*m/z* 1529 corresponding to a peptide with mass of ~4.58 kDa. Intensity of those peaks increases as the buffer gas temperature is raised. Detected peptide is most likely originating from SAP monomer backbone fragmentation, however, further CID experiments have not been carried out to determine its sequence.

Similar unfolding and dissociation trends are observed for tetrameric avidin shown in Figure 4.2c. Avidin, a 64 kDa homotetrameric protein, is present in a narrow charge state distribution (*m/z* 3700 – 4300) centred at 16+ charge state, ~ *m/z* 3990. A minor amount of higher order species *i.e.* a dimer of tetramers, is also observed around *m/z* 5500, likely due to the sample concentration. Upon the increase of temperature up to 400 K, the avidin complex remains intact as a tetramer. Similarly to TTR, it is above 450 K, when the dissociation into monomers is observed. Dissociation produces monomeric species with 9+ charge state (~ *m/z* 1775) being the most abundant. Above 550 K, mass spectrum is dominated by 11+ to 7+ avidin monomers; however, there are still some low charge intermediate trimers, centred at 7+ charge state (~ *m/z* 6860), present.

Concanavalin A requires higher temperature for the onset of dissociation (Figure 4.2d). Under physiological conditions, conA exists as a tetramer (103 kDa), dimer and monomer. The tetrameric population is centred on the 20+ charge state (~*m/z* 5130), dimeric population is centred on the 14+ charge state (~*m/z* 3670), and monomeric population is centred on 9+ charge state (~*m/z* 2850). Mass spectra acquired at 300 K and 400 K, do not show significant differences apart from narrowing of the tetramer peaks at higher temperature due to salt clean up. Above 470 K, onset of dissociation into highly charged monomers centred at 12+ charge state (~*m/z* 2140) is observed. Dissociation increases at temperatures above 500 K. The mass spectra acquired at 550 K, still contain significant amounts of intact tetramer and as well as lower charge state solution present dimers and monomers. Data obtained from VT-MS experiments gives insight into gas-phase dissociation of multimeric complexes into subunits and the results are compared to in-solution complex dissociation data reported in the literature.

4.3.2 Gas-phase protein complex dissociation curves and determination of T_{GPD}

The extent of dissociation into monomeric species was observed to vary with the drift time. Figure 4.3, shows time dependent dissociation of TTR at 475 K. As the drift voltage (DV) across the drift cell is lowered, ions take longer to transverse the drift cell and complexes undergo dissociation to greater extend. For example, change of the DV from 60 V to 15 V results in increase of drift time from 1.75 ms to 4.26 ms for the 14+ TTR charge state, and significantly affects the dissociation ratio.

From the previous reports of others[42] and VT-IM-MS experiments presented in the following sections, it is apparent that the amount of energy required to break the dissociation energy barrier is dependent on the ion charge state. Highly charged ions are susceptible to more Coulombic repulsion than lower charge states, and as a result dissociate more readily, despite the relatively low Δz across these native nESI charge state distributions. Considering this fact, summed intensities over all the presented

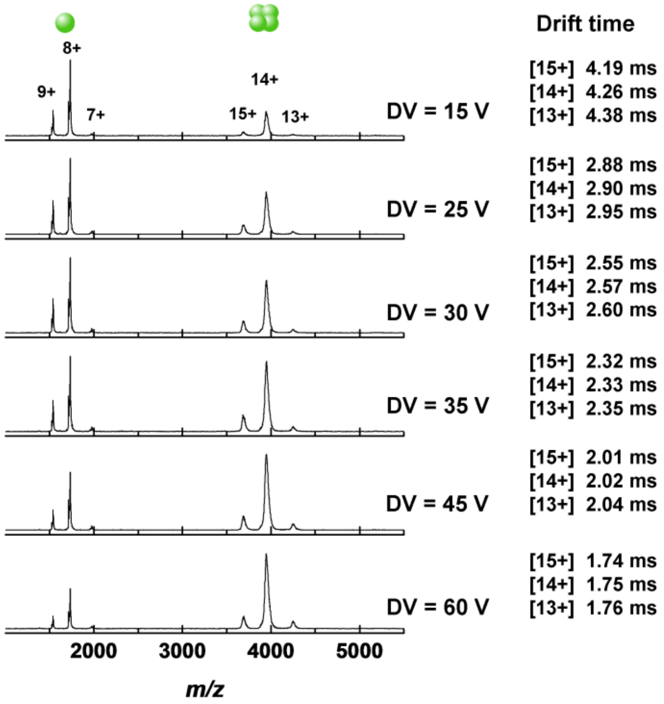

Figure 4.3 Time dependent dissociation of TTR at 475 K. Mass spectra acquired DV = 60, 45, 35, 30, 25 and 15 V on the MoQToF mass spectrometer.

charge states were used to construct dissociation curves such as these shown in Figure 4.4, to reflect the majority of ion population. The ratio of the summed intensities of charge states corresponding to the intact complex [$I_{complex}$] over the sum of the summed intact complex charge state intensities and summed intensities of monomer charge states resulting from the thermal dissociation [$I_{complex}$ + $I_{monomer}$] was plotted as a function of buffer gas temperature for each protein investigated and the data points were fitted with a Boltzmann function (Figure 4.4). For protein complexes requiring temperatures exceeding the instrument capabilities to reach a complete dissociation *i.e.* conA and SAP, the fit was extended for the dissociation ratio to approach 0. The dissociation process occurs in the drift cell region of the instrument, and any detector response factor differences between monomers and multimers have been neglected. The gas-phase dissociation temperature (T_{GPD}) for each complex is reported; here, the T_{GPD} is defined as the temperature at which 50 % of the complex population has dissociated into monomeric species as a result of increased temperature of analysis environment. T_{GPD} were determined at several DV and plotted as function of drift time (Figure 4.5). The T_{GPD} decreases with longer drift times. Data points were fitted with an exponential decay function to determine the dissociation equilibrium temperature (T_{eq}) for each

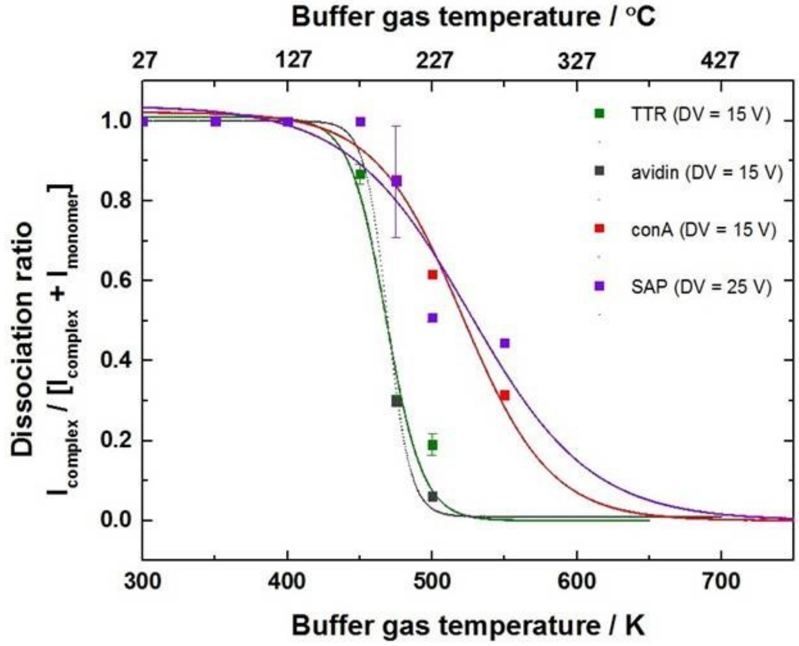

Figure 4.4 Temperature induced dissociation (TID) curves of avidin (grey), TTR (green), conA (red), and SAP (purple) used for determination of T_{GPD}, determined near the equilibrium drift time (DV = 15 V for TTR, avidin and conA; DV = 25 V for SAP).

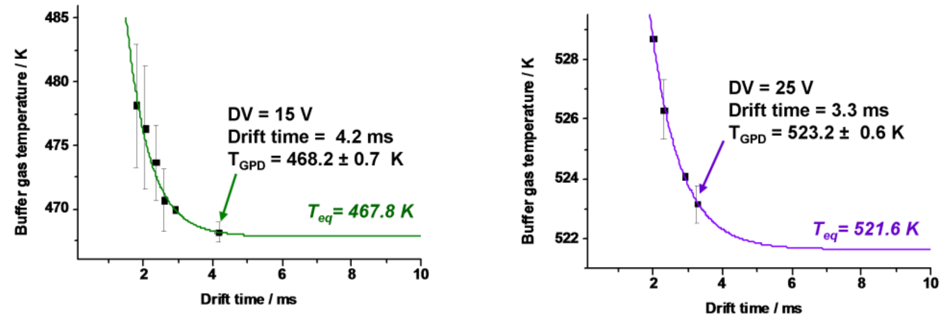
(a) TTR

(b) SAP

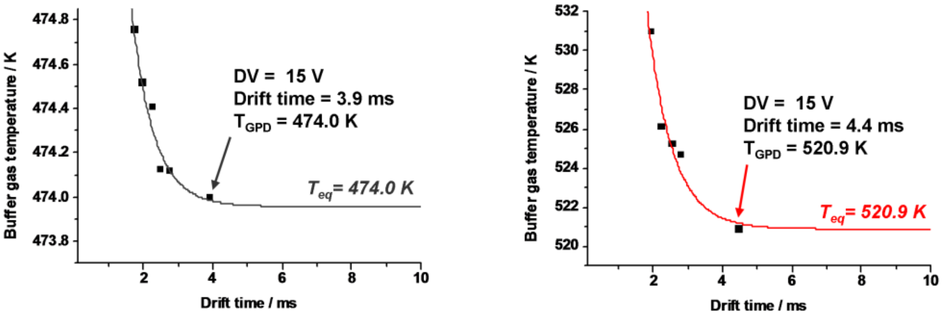
(c) avidin

(d) conA

Figure 4.5 Determination of the dissociation equilibrium temperature (T_{eq}). The gas-phase dissociation temperature (T_{GPD}) of (a) TTR, (b) SAP, (c) avidin and (d) conA versus drift time (ms) at corresponding DV. Results for TTR and SAP are based on two repeats, and a single repeat for avidin and conA.

complex. Measurements taken at the lowest DV are the closest to the T_{eq} as can be achieved with the current instrumentation. Data acquired at these low DV was used to construct the dissociation curves shown in Figure 4.4. Table 4.1 lists T_{GPD} at various drift times. Solution thermal stability techniques, such as differential scanning calorimetry (DSC), provide one with the T_m, a melting temperature at which 50 % of the protein has undergone a transition which is attributable to loss of structure. From thermal dissociation VT-MS measurements, gas-phase dissociation temperatures (T_{GPD}) are determined for four protein complexes and compared to T_m values based on DSC measurements (Table 4.1).

The T_{GPD} of TTR was determined to be 468.2 ± 0.7 K. Notably, the literature value of T_m for TTR is significantly lower (by 21 %) than T_{GPD}. The reported literature T_m of TTR is 370.95 K as determined by DSC,[43] which is almost 100 K lower than T_{GPD} determined VT-MS experiments. T_{GPD} increases for complexes with higher molecular mass which in similar fashion were determined to be 474.0 K, 520.9 K and 523.2 ± 0.6 K for avidin, conA and SAP respectively. This increase is only partially correlated to molecular mass. As conA is known to exist in equilibrium with its dimeric and monomeric form, for the purpose of calculating the dissociation ratios only the 15+ to 11+ monomers (~*m/z* 1715 – 2340) produced during the TID were considered, as opposed to the naturally occurring 10+ to 8+ monomers (~*m/z* 2560 –3200) (Figure 4.2d). Moreover, the T_{GPD} is not only dependent on the mass of the complex, but appears to be dependent by the strength on the non-covalent interactions between subunit interfaces as will be discussed later.

The protein complex structure is perturbed at the raised temperatures. In-solution studies allow the measurement of T_m *i.e.* the protein transformation; however, they cannot distinguish between loss of structure and complex dissociation, nor do they distinguish in detail the route by which structure is lost. With use of VT-MS, the T_{GPD} can be determined, and we can also differentiate between two competing processes: loss of structure and dissociation. The difference between T_m and T_{GPD} was about 100 K for the protein complexes investigated here, illustrating a significant difference in the amount of energy required for loss of structure vs. complex dissociation. In other words, the unfolding energy barrier and dissociation energy barrier can be decoupled in the gas-

Table 4.1 Average drift time across charge states of for TTR, avidin, conA and SAP at various drift voltages; gas-phase dissociation temperature (T_{GPD}) determined at each DV; the equilibrium temperature (T_{eq}) and the literature in-solution melting temperature T_m.

Protein complex	Drift time/ms	T_{GDP} /K	T_{eq} /K	T_m /K
TTR	1.8	478.2 ± 4.9		
	2.1	476.6 ± 4.8		
	2.6	473.7 ± 2.9		
	2.6	470.7 ± 2.5		
	2.9	470.0 ± 0.0		
	4.2	**468.2 ± 0.7**	**467.8**	**370.9**[43]
Avidin	1.7	474.8		
	2.0	474.5		
	2.2	474.4		
	2.5	474.1		
	2.7	474.1		
	3.9	**474.0**	**474.0**	**356.7**[44]
ConA	1.9	531.0		
	2.2	526.1		
	2.5	525.3		
	2.8	524.7		
	3.1	527.8		
	4.5	**520.9**	**520.9**	**338.0 ± 6.5**[45]
SAP	2.0	528.7 ± 0.1		
	2.3	526.3 ± 1.0		
	2.9	524.1 ± 0.0		
	3.3	**523.2 ± 0.6**	**521.6**	**359.2 – 363.2**

phase by VT-MS. Moreover, VT-MS allows the decoupling of extrinsic (solvent) from intrinsic factors on thermal stability of protein complexes.

The TID charge state dissociation profile of TTR (Figure 4.2a), matches the dissociation profile from CID experiments reported by Pagel *et al.*[32]. The TTR tetramer displays a narrow charge state distribution centred at 14+ charge state (~*m/z* 3950). Upon complex activation, either by CID or TID, a highly charged monomer carrying approximately

50 % of overall charge (here, 8+ (~ *m/z* 1735) being the most abundant dissociated monomer) is released from the complex. CID and TID mass spectra of SAP, avidin and ConA, display similar dissociation pattern.[34,37] Based on the matching charge state profiles and IM-MS data, it may be postulated that CID and TID activate the complexes in a very similar fashion. Currently, TID experiments can only be performed using custom modified mass spectrometers that allow for control and monitoring of the temperature within the instrument. CID is a widely available technique featured in many mass spectrometers. Correlating TID temperatures and CID energies could serve as a framework for thermal stability screening, especially useful when the amount of sample material is limited to perform the classical DSC measurements. Here, for example about 725 eV (E_{lab}, based on data reported by Pagel *et al.*[32]) is required to achieve 50 % dissociation of TTR 14+ tetramer occurring at about 468 K as determined *via* the TID experiments. Moreover, the TID data could also be used to obtain thermodynamic parameters (enthalpy (ΔH) and entropy (ΔS)) on the interactions between subunits.

4.3.3 Investigating the TID mechanism with VT- IM-MS

The in-house modified linear DT-IM mass spectrometer allows not only for the determination of T_{GPD} but also enables investigation of structural changes of proteins that might occur prior to dissociation as the buffer gas temperature is increased in the drift cell. IM-MS experiments, for the complexes studied here, were carried out at temperatures ranging from 300 K to 500 K or 550 K, dependent on the T_{GPD} determined earlier. CCS distributions (CCSD) and their transformations, derived from arrival time distributions (ATD) of TTR and SAP acquired at a range of temperatures are presented in Figure 4.6. CCSD of avidin and conA at a range of temperatures are available in the Appendix 4. Changes in the CCS and width of CCSD are clearly visible, indicating significant structural changes as an effect of increased analysis environment temperature. IM data acquired at 350 K and 400 K show a minor decrease in the CCS of TTR and SAP in comparison to CCS determined at 300 K, suggesting a structural collapse. The greatest shift towards larger CCS is observed at and above the T_{GPD} determined with VT-MS. In Figure 4.7, median CCS (nm^2) of each protein and their dissociated subunits, as well the naturally occurring dimers and monomers of conA, are plotted versus buffer gas temperature (K).

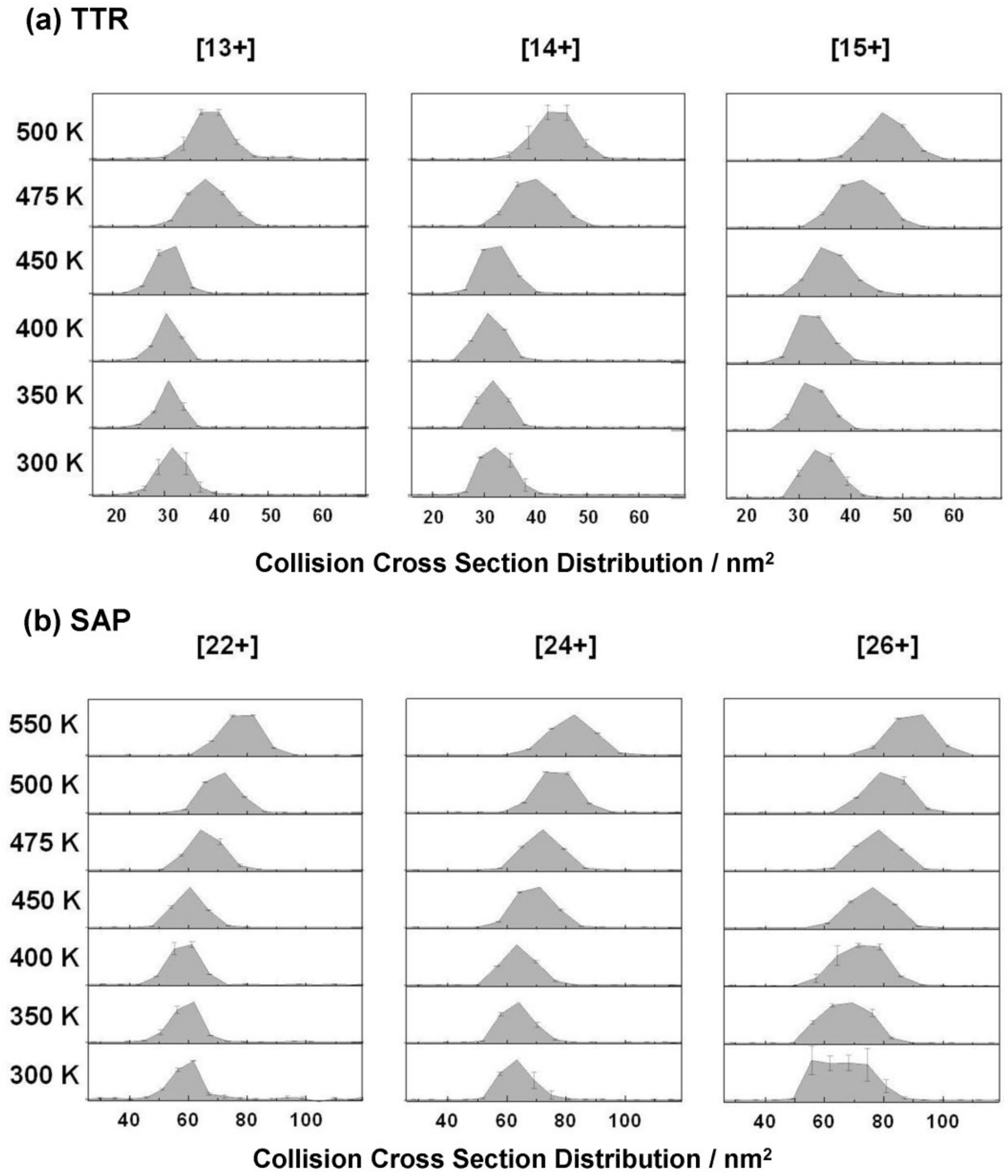

Figure 4.6 Collision cross section distributions (CCSD) of TTR (13+,14+ and 15+ charge states) and SAP (22+,24+ and 26+ charge states) acquired at DV=35 V and buffer gas temperatures ranging from 300 to 500 K and 550 K, respectively. CCSD of avidin and conA are available in the Appendix 4.

The range of TTR tetramer median CCS across charge states decreases from 31.3 - 33.5 nm^2 to 30.7 - 32.3 nm^2 at 350 K and further to 30.5 - 32.3 nm^2 at 400 K (the list of all median CCS values is available in the Appendix 5). The extent of the collapse was noted to be greater for higher charge states (Figure 4.7a). As the buffer gas temperature is increased to 450 K, the median CCS of higher charge states increase as the subunits begin to unfold; however, the 13+ charge state remains still somewhat compact. Around

TTR's T_{GPD}, a significant increase in CCS is observed and the median CCS range across charge states increases to 38.3 - 42.0 nm^2 at 475 K and further to 39.5 - 47.0 nm^2 at 500 K. The relative change in median CCS with respect to CCS at 300 K is more extensive for higher charge states reaching +40.3 % for the 15+ charge state. Moreover, the CCS of the expelled highly charged monomer has been calculated at temperatures near T_{GPD} and above. It was found that the dissociated monomer has a large CCS (16.8 - 22.6 nm^2 at 475 K) similar to the CCS of a CID dissociated monomer,[32,35] suggestive of extensive subunit unfolding prior to dissociation in the TID process. It has been previously reported that highly charged TTR monomers (7+ to 9+) expelled from the complex during the CID process, adopt CCS in the range of about 17 nm^2 to 27 nm^2, or even up to 30 nm^2. [32,33,35]

The SAP pentamer follows a similar pathway of compaction, unfolding and dissociation. At 350 K and 400 K a minor decrease in the median CCS is observed for the 22+ to 25+ charge states. The range of the median CCS for the SAP pentamer across charge states changes from 59.1 - 63.7 nm^2 to 58.9 - 66.4 nm^2 at 350 K, with -3.65 % reduction in median CCS for 22+ charge state and only -0.39 % reduction for 25+ charge state. The compaction progresses further at 400 K to 58.8 - 71.9 nm^2. In contrast to TTR, lower charge states experience a greater degree of compaction; the 26+ charge state does not experience any compaction and the CCS begins to increase already at 350 K (+2.71 %) and further at 400 K, where up to +8.20 % change in CCS is noted. As reported before, the compaction behaviour might originate from a collapse of the units of SAP into the central cavity.[33] This path is likely to be controlled by the subtle stabilizing or destabilizing effects of charge interactions on the protein ion's surface and collapse of high charge states might be mitigated by dominating Coulombic repulsions and/or by the loss of buffer salts or water.[33,37] The CCS for all SAP charge states detected, continues to increase above 450 K and the median CCS range reaches 77.4 – 89.7 nm^2 at 550 K (*i.e.* an increase of +31.2 % for 22+ charge state CCS and of +44.2 % for the 26+ charge state CCS). CCS of the highly charged ejected monomer is again similar to the one determined through CID experiments on SAP, ranging from 25.7 – 34.2 nm^2 at 500 K for 10+ - 13+ charge states.[35]

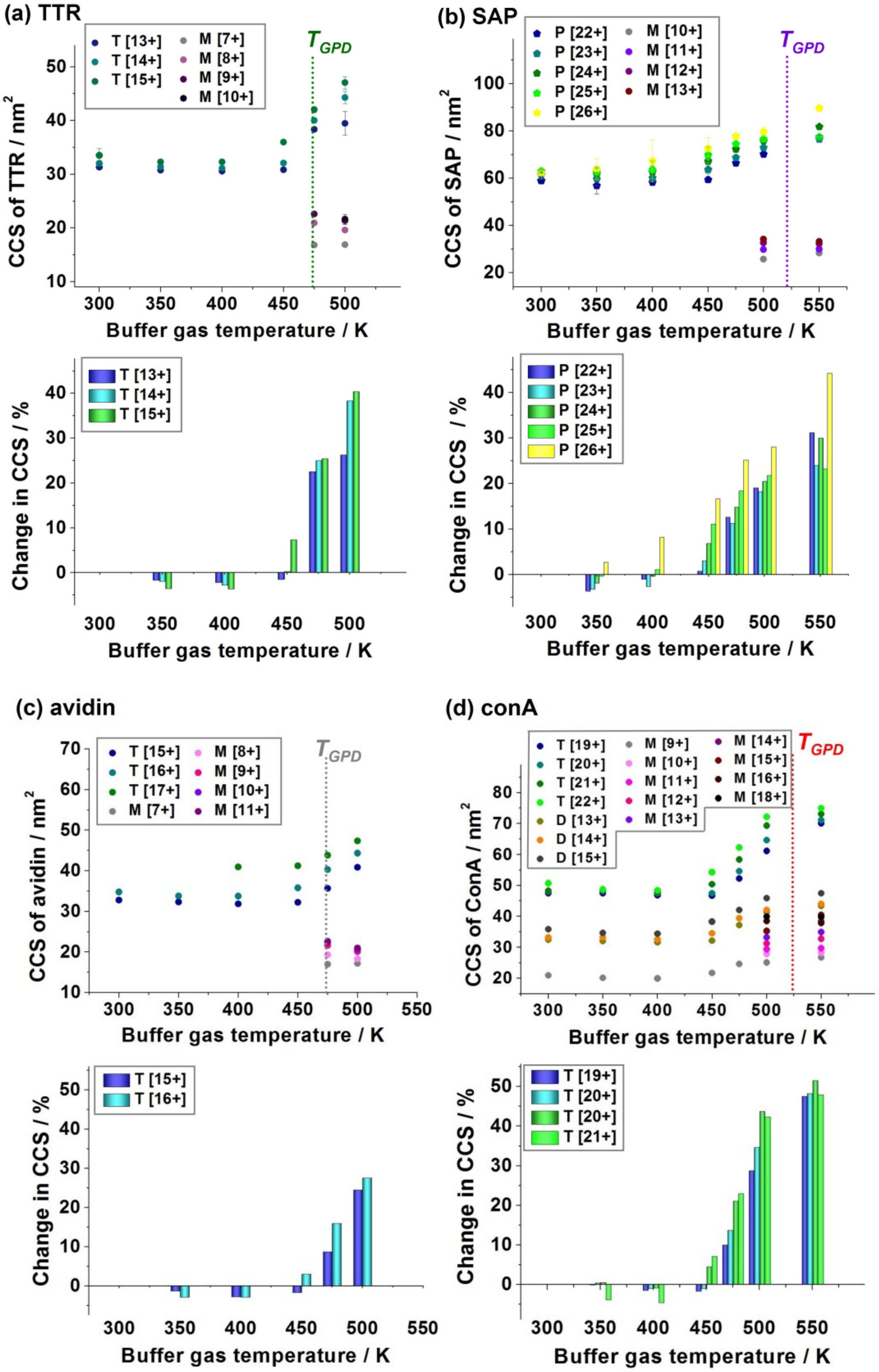

Figure 4.7 Median CCS and percentage change in CCS with respect to CCS at 300 K of (a) TTR, (b) SAP, (c) avidin, and (d) conA in function of buffer gas temperature. VT-IM-MS measurements illustrate an initial decrease in the CCS associated with complexes' minor collapse and latter significant increase in CCS as protein subunits begin to unfold and subsequently dissociate. M = monomer, D = dimer, T = tetramer and P = pentamer.

Similarly to TTR and SAP, avidin experiences compaction at 350 K and 400 K and subsequent unfolding at temperatures above 450 K shown by the increase in the CCS. The range of avidin tetramer median CCS across charge states decreased from 32.8 – 34.8 nm^2 (15+ and 16+ charge states) to 32.3 – 46.3 nm^2 (15+ to 17+ charge states) at 350 K and further to 31.9 – 41.0 nm^2 at 400 K. As for TTR, the initial compaction is more extensive for the higher charge states, and so is unfolding. As the buffer gas temperature is increased to 450 K, the CCS of higher charge states are increasing as the subunits begin to unfold; however, the 15+ charge state remains still somewhat compact. Around avidin's T_{GPD}, a significant increase in CCS is observed and the median CCS range across charge states increases to 35.6 – 43.8 nm^2 at 475 K and further to 40.8 – 47.3 nm^2 at 500 K. Relative change in median CCS with respect to CCS at 300 K is more extensive for higher charge states and reaches +27.5 % for the 16+ charge state at 500 K. Moreover, CCS of the ejected highly charged monomer near T_{GPD} was found to be in range of 17.0 – 22.4 nm^2 (at 475 K).

The ConA tetramer follows a similar dissociation pathway. The range of conA tetramer median CCS across charge states decreased from 47.5 – 50.6 nm^2 (19+ to 22+ charge states) to 47.4 – 48.7 nm^2 at 350 K and further to 46.8 – 48.3 nm^2 at 400 K. The extent of the collapse was noted to be greater for the higher charge states. As the buffer gas temperature is increased to 450 K, median CCS of higher charge states are increasing as the subunits begin to unfold; however, the 19+ and 20+ charge states remain still compact. The CCS for all conA tetramer charge states detected, continue to increase above 450 K and the median CCS range reaches 70.0 – 74.9 nm^2 at 550 K (*i.e.* +47.5 % increase in 19+ charge state CCS and +47.9 % in 22+ charge state CCS). As conA exists in dimeric and monomeric forms even before the application of external energy, changes in these structures at elevated temperatures were also investigated. Both, conA dimer and conA monomer experience a minor compaction at 350 K and 400 K; this compaction is more extensive for higher charge states of dimer, just as for tetrameric conA (for median CCS values, see Appendix 5). At 450 K and above, median CCS begin to increase as the protein unfolds and continues to do so up to 550 K. Interestingly, the naturally occurring monomer follows the same pathway of collapse (at 350 K and 400 K) and unfolding above 450 K, like multimeric systems, suggesting that the collapse is not only originating from intra-subunit cavity collapse but also from significant compaction within each subunit. CCS of the highly charged ejected monomer is again similar to the one determined through CID experiments on conA, ranging from 28.2 – 37.8 nm^2 at 550 K for 10+ - 16+ monomers.

The collected IM data shows that protein complexes undergo initial compaction upon temperature increase and subsequent unfolding prior to dissociation similarly to the CID process. As reported by others, the CID process occurs by initial compaction of the complex and subsequent unfolding of subunits following the 'typical' dissociation route.[33,46] VT-IM-MS data acquired at 350 K and 400 K displays a minor decrease in CCS of all four protein complexes in comparison to CCS determined at 300 K, suggesting a structural compaction. This decrease in CCS is associated with initial loss of structure and originates from the collapse of structure into the intra-subunit cavities as well as the collapse of the subunits within themselves. The temperature at which maximum compaction occurs is comparable to the T_m obtained from the in-solution studies.

As the temperature is increased to 450 K and higher, an extensive increase in CCS is noted associated with subunit unfolding. The CCS increases accordingly with the energy input, either by TID or CID. Due to statistical reasons, one subunit might carry slightly more charge than others. This asymmetrical charge partitioning results in a marginally destabilized subunit, resulting from intramolecular Coulombic repulsions.[47] Upon collisional activation of the complex, one or possibly multiple subunits begin to unfold. As the new surface area is exposed, charge migration occurs to that region and drives further unfolding which eventually results in release of highly charged monomer which further supports the resemblance of TID mechanism to CID mechanism.[48]

Here as an example, the CCS of TTR at 300 K was found to be in a range of 31.3 - 33.5 nm^2 and in close agreement with that reported by Pagel *et al.* (~31 nm^2).[32] At 500 K, a temperature at which only marginal amount of TTR tetrameric species were detectable, CCS has increased to 39.5 – 47.0 nm^2 for 13+ - 15+ charge states, which again is in close agreement with the most extensive conformations measured for TTR tetramer activated by CID (40 - 45 nm^2)[32]. Moreover, the CCS of the ejected highly charged monomers were calculated at temperatures near T_{GPD} and above. It was found that the dissociated monomers of all protein complexes studied here, have large CCS similar to those CCS of monomers produced *via* CID.[35] Comparison of computationally determined CCS of monomers clipped from a complex x-ray crystal structures, showed that CID produced monomers are in their unfolded state.[35]

Although, observed trends are similar among different protein complexes, the degree of compaction and unfolding varies across charge states. Past the compaction stage, as the subunits begin to unfold, a gradual increase in CCS is noted across all charge states. Some complexes experience close to a 50 % increase in CCS in comparison to those found at 300 K. A common trend was seen; higher charge states experience greater degree of extension and require less energy to initiate unfolding. This phenomenon is believed to be influenced by Coulombic effects and has been reported previously for monomeric proteins such as cytochrome c and lysozyme, or complexes like SAP. [33,49,50]

The degree of compaction varied among the protein complexes. Low charge states of SAP, a complex with relatively large internal cavity, experience greater compaction, in agreement with MD and CID experiments reported by Hall *et al.*.[37] At the same time, the highest charge state did not undergo any compaction. The compaction pathway is believed to be suppressed due to competing effects from Coulombic repulsion for the high charge states; whereas, the lower charge states collapse only presumably into the internal cavity. The other three complexes studied here, display an opposite trend *i.e.* greater extent of compaction for higher charge states. These complexes have significantly smaller intra-subunit cavities in relation to SAP. It can be speculated that the majority of compaction observed must be coming from a collapse/loss of structure within the subunits themselves. An alternative explanation is that lower charge states are already quite compact at 300 K, hence the relative decrease appears less extensive. Upon exposure to higher temperature, the total change for the lower charge state is relatively low whereas higher charge states with marginally larger CCS at 300 K, collapse to the same extent as lower charge states; however, the relative change observed is greater.

4.3.4 Broadening of the CCSD width as an indicator of multiple closely related conformational families

The CCS discussed in the previous section were the median CCS. When acquiring IM data, one does not simply record a narrow peak corresponding to a precise CCS value, especially when dealing with large multimeric protein complexes, as can be seen in Figure 4.6. The CCSD derived from the experimental ATD provide details on protein flexibility and the amount of closely related or interconverting conformations as had been shown for immunoglobulins in Chapter 3. In Figure 4.8 the baseline width of the CCSD for all four protein complexes is plotted versus buffer gas temperature ranging from 300 K to 550 K. It is clearly visible, that the higher the charge state, the broader the CCSD becomes and the width also varies with the temperature.

For the 13+ charge state of TTR, the CCSD becomes narrower at temperatures between 350 K and 450 K (Figure 4.8a). This correlates with the decrease in the median CCS associated with structural compaction. As the complexes attempts to adopt the most compact structure, a limited range of conformational combinations is reflected by a narrow CCSD. The width of the other two charge states fluctuates slightly within the discussed temperature range. At 475 K, a temperature near TTR's T_{GPD} at which 50 % of the complex has dissociated, the CCSD of all three charge states increases significantly and nearly doubles for the 13+ charge state. As the complex dissociates, the protein subunits unfold prior to their ejection. After crossing the temperature associated with the dissociation energy barrier, the CCSD begins to decline again (at 500 K).

Unlike TTR, the CCSD of SAP pentamer does not decrease within the 350 K and 400 K range (Figure 4.8b). The CCSD for the 22+ and 24+ charge states increases gradually with temperature and peaks around 550 K *i.e.* near SAP's T_{GPD}. Due to the instrument limitations, it was not possible to perform experiments at higher temperatures to determine the CCSD widths at temperatures much higher than T_{GPD} energy barrier. The 26+ charge state behaves somewhat differently and a decrease in CCSD width is observed at 450 K. As 26+ charge state is the most prone to unfolding, it can be speculated that it reaches the dissociation energy barrier at lower temperature after which a decrease in CCSD is observed. It has been shown by Hall *et al.*[33], that lower energies in CID experiments are required for higher charge states of SAP to induce unfolding.

The CCSD width of avidin lower charge states (15+ and 16+) experience narrowing of the CCSD at 350 K and 400 K, similarly to TTR (Figure 4.8c). Past the T_{GPD} energy barrier and the maximum CCSD width, the values begin to decline. The highest charge state (17+) CCSD width does not decrease significantly until passing the T_{GPD} barrier.

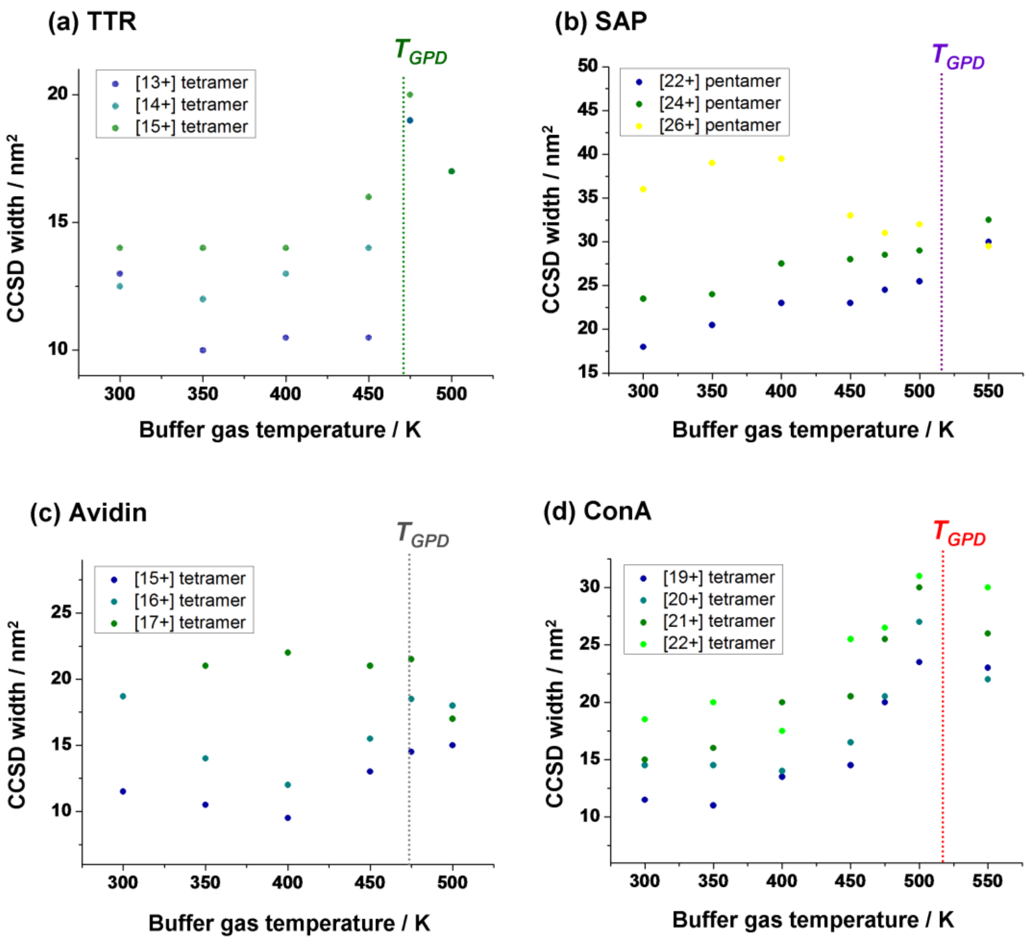

Figure 4.8 Baseline width of collision cross section distributions (CCSD) of (a) TTR, (b) even charge states of SAP (c) avidin, and (d) conA acquired at buffer gas temperatures ranging from 300 K to 550 K. It is shown, how the CCSD width is dependent on the charge state with higher charge states having broader CCSD. The width of CCSD changes significantly with the temperature of analysis environment, as well. In the TTR plot (a), CCSD width data points at 475 K for 13+ and 14+ are overlapping; as are CCSD width data points at 500 K for all TTR charge states.

All conA charge states experience mostly gradual broadening of CCSD (Figure 4.8d). This increase becomes steeper at temperatures above 450 K, and values gently decline pass the T_{GPD} of conA.

The observed broadening of the CCSD along with increasing buffer gas temperature is an indicative for presence of multiple closely related conformers produced upon complex dissociation. For all four complexes, it was noted that the higher the charge state, the broader the CCSD becomes and the width also varies with the temperature of buffer gas. Some of these differences should be attributed to diffusion; however, temperature *i.e.* amount of energy supplied, plays the most important role in the observed CCSD trends.

At 350 K and 400 K, the CCSD either slightly decreases or remains almost constant. At these temperatures, each protein complex is losing its quaternary structure, collapsing into its internal cavity, adopting a minimum energy gas phase conformation. The structure becomes ‘locked’ and has minimum number of conformers present. When the subunits begin to unfold at 450 K and higher temperatures, there is now a significant increase in the CCSD width. Various subunits are unfolding and/or remaining collapsed to a diverse extent, this results in many closely related conformational families. Pagel *et al*. reported on the presence of five intermediate conformers of TTR at various CID activation energies.[32] After reaching the T_{GPD} energy barrier and the widest CCSD, the values begin to decline.

4.3.5 The TID mechanism might be adopting a more ‘atypical’ dissociation route as the analysis temperature increases

Ejection of a highly charged monomer, initial collapse of the complex structure followed by subunit unfolding and presence of unfolding intermediates reflected by broad baseline CCSD are all supportive of the ‘typical’ dissociation route.[34] An interesting observation was made, as the analysis temperature is increased during the VT-(IM)-MS experiment, the average charge state (z_{ave}) of the ejected monomer decreases accordingly. The z_{ave} values for all four complexes were calculated across temperatures at which the dissociation into subunits is observed *i.e.* 450 – 550 K for TTR, avidin and conA and 475 – 550 K for SAP (Figure 4.9). The z_{ave} decreases from 8.8 ± 0.3 to 7.9 ± 0.1 for TTR ($\Delta z = 0.91$), from 10.6 ± 0.1 to 8.6 ± 0.01 for avidin ($\Delta z = 2.01$), from 18.8 ± 0.2 to 12.8 ± 0.06 for con A ($\Delta z = 6.06$) and from 13.26 ± 0.23 to 12.00 ± 0.01 for SAP ($\Delta z = 1.27$). The charge of conA monomers undergoes greatest change; however, this value is likely affected by the presence of monomeric conA species existing already at the physiological conditions. Nevertheless, dissociation of all four complexes at increasing temperature results in decreased z_{ave} suggesting that the process might be adapting more ‘atypical’ dissociation route.[35,36] Lower z_{ave} would be reflective of less asymmetrical charge partitioning during the charge migration as the monomer experiences less unfolding. Additionally, the median CCS of high charge state monomers were found to be smaller at 500 K than median CCS at 475 K (Figure 4.7, Appendix 5). It can be

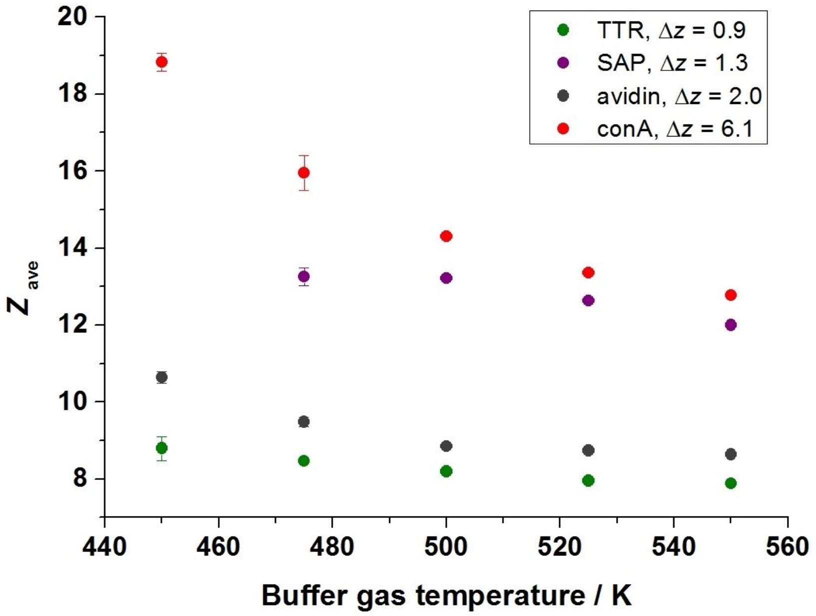

Figure 4.9 The average charge state (z_{ave}) of the ejected monomer of TTR (green), SAP (purple), avidin (grey) and conA (red) versus buffer gas temperature (in K). z_{ave} is noted to decrease at higher buffer gas temperatures suggesting that the dissociation mechanism might be on a route to resembling SID-like dissociation at very high temperatures.

speculated that at the higher buffer gas temperatures, the dissociation process occurs at a shorter time scale leading to ejection of slightly less unfolded monomer with lower z_{ave}, especially for highly charged species where the dissociation energy barrier is lower.[33,34]

Moreover, baseline width of CCSD of the ejected monomer decreases at higher temperature. Figure 4.10 presents CCSD of the ejected TTR monomers with charge states 7+, 8+ and 9+ at 475 K and 500 K. It can be clearly seen how the CCSD becomes narrower at 500 K in comparison to CCSD at 475 K, especially for the 8+ and 9+ charge states. Narrower CCSD indicate a lesser amount of conformationally related species present; here in particular, a lesser amount of monomers unfolded to a various extent.

Currently, the upper temperature working range of the MoQToF instrument is limited to about 550 – 600 K, nevertheless it would be interesting to perform experiments at buffer gas temperatures above 550 K to determine whether: (a) the z_{ave} of the ejected monomer decreases further as the analysis temperature raises – suggestive of more symmetrical charge partitioning during charge migration, (b) the CCS of the ejected monomer decreases further as the analysis temperature raises – suggestive of ejection of slightly

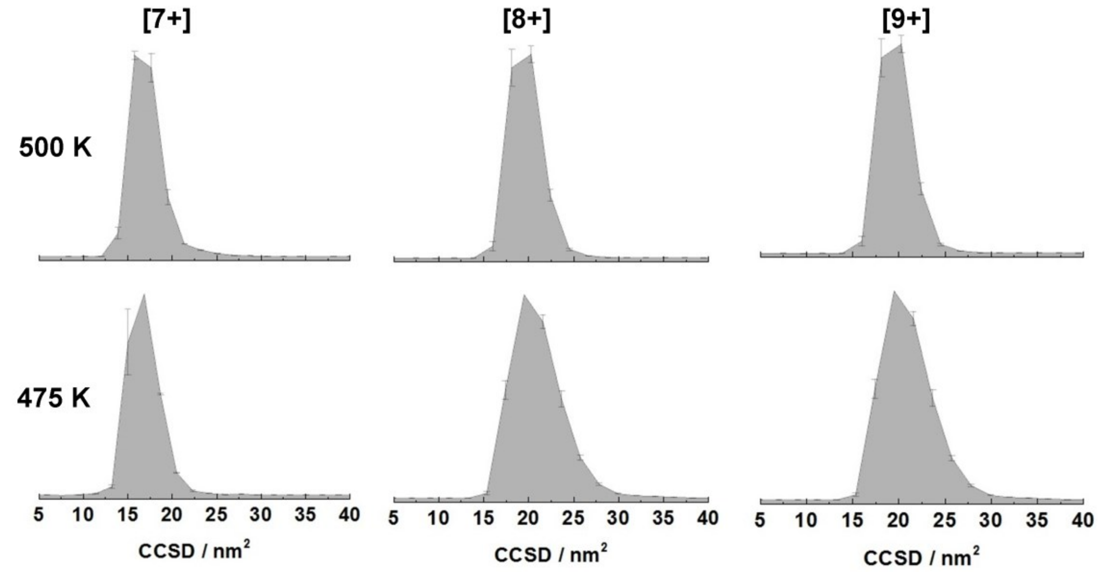

Figure 4.10 Collision cross section distributions (CCSD) of the 7+, 8+ and 9+ ejected TTR monomer at 475 K and 500 K. The width of CCSD becomes narrower at 500 K in comparison to CCSD width at 475 K.

less unfolded monomer, (c) the width of the CCSD decreases further as the analysis temperature raises – suggestive of decreased number of conformationaly related monomeric species. Testing these hypotheses would prove additional evidence for the TID dissociation mechanism being temperature dependent. If all three assumptions discussed above were to be confirmed experimentally, it could be speculated that TID dissociation initially follows the 'typical' dissociation route and adapts more 'atypical' dissociation route as the analysis temperature in increased.

4.3.6 Insights into strength of non-covalent interactions between protein subunits from VT-IM-MS experiments

Multimeric protein complex dissociation is highly controlled by the strength on the non-covalent interactions between the subunit interfaces.[51] The increase of T_{GPD} with increasing molecular mass of the complex was a clear trend observed from VT-MS experiments. The size of the multimeric protein complex will correlate somewhat to the interface area in-between the subunits. Since the T_{GPD} was observed to be influenced by the molecular weight; here, two proteins relatively close in mass with similar T_{GPD}: TTR (55 kDa, T_{GPD} = 468.2 ± 0.7) and avidin (64 kDa, T_{GPD} = 474.0) are compared. The average interface surface area per subunit, average number of hydrogen bonds per subunit and average number of possible salt bridges per subunit was calculated using the

'Protein interfaces, surfaces and assemblies' service PISA at the European Bioinformatics Institute for structures of TTR (PDB: 1BMZ, 1DVQ, 3U2I) and avidin (PDB: 1AVE, 1VYO, 1RAV) deposited in the Protein Data Bank. The average values based on three structures for each protein complex are reported in Table 4.2.

The average interface surface area for each TTR subunit was calculated to be 17.11 ± 2.28 nm^2 with an average of 20 ± 2 hydrogen bonds and 1 ± 1 possible salt bridge. Values determined for an avidin subunit were slightly higher, with an interface surface area of 25.63 ± 0.50 nm^2, average of 36 ± 8 hydrogen bonds and 7 ± 5 possible salt bridges. The large standard deviation on the number of hydrogen bonds and possible salt bridges originate from variety in the structures examined. Despite a higher number of non-covalent interactions between the subunits, avidin unfolds to a lesser extent near the T_{GPD} prior to ejection in comparison to TTR. The most abundant, 14+ charge state of TTR has increased its CCS by 25.0 % at 475 K in comparison to avidin with only 15.9 % increase in CCS of the 15+ charge state.

Table 4.2 Comparison of TTR's and avidin's, dissociation temperature T_{GPD}, average interface surface area per subunit, average number of hydrogen bonds per subunit, average number of possible salt bridges per subunit and the percentage increase in the CCS at 475 K.

Protein complex	TTR	avidin
Mass / kDa	55	64
T_{GPD} / K	468.2 ± 0.7	474.0
Average interface surface per subunit / nm^2	17.11 ± 2.28	25.63 ± 0.50
Average number of H-bonds per subunit	20 ± 2	36 ± 8
Average number of salt bridges per subunit	1 ± 1	7 ± 5
Percentage increase in the CCS at 475 K	[13+] +22.5 % [14+] +25.0 % [15+] +25.4 %	[14+] +8.7 % [15+] +15.9 %

Avidin has a larger area of the interface between subunits and more non-covalent interactions per subunit than TTR. Interestingly, the extent of unfolding is lesser by approximately 10 % in contrast to TTR ions carrying the same amount of charge. More non-covalent interactions might hinder extensive unfolding and keep the subunit compact prior to reaching the dissociation energy barrier. At the same time, fewer interactions and extensive unfolding of TTR subunits, suggests that the non-covalent interactions between the subunits must be stronger holding them within the complex prior its ejection. Measuring the extent of unfolding with VT-MS experiments could provide insights into the strength of non-covalent interactions between subunits when high resolution data is not available/possible.

4.4 Conclusions

VT-MS and VT-IM-MS methodology was applied to study four multimeric protein complexes, their dissociation and related conformational change at elevated temperatures ranging from 300 K to 550 K. The presented data pinpoints the importance of analysis temperature for protein structural and thermal stability studies, and highlights the difference between gas phase and solution thermal stability. VT-MS was employed to probe dissociation of large multimeric protein complexes and as such decouple gas phase complex dissociation temperature (T_{GPD}) from solution melting temperature (T_m).

VT-IM-MS provided insights into conformational changes occurring during the TID complex dissociation process. Complexes were found to undergo an initial compaction at 350 K and 400 K noted by a decrease in median CCS. At these temperatures, each protein complex is losing its quaternary structure, collapsing into more compact structures with lower number of conformational possibilities present as reflected by narrow CCSD profiles. Subsequent unfolding and eventual release of a monomer at temperatures above 450 K were marked by significant increase in median CCS and widening of CCSD associated with a series of unfolding events the protein complexes undergo prior to reaching the dissociation energy barrier. The degree of compaction and unfolding was found to vary across charge states; however, a common trend was seen for the higher charge states to experience greater degree of extension and having lower energy requirement for unfolding initiation.

The TID mechanism was observed to initially proceed *via* the so called ‘typical’ (CID) dissociation route *i.e.* a release of a highly charged unfolded monomer as proven by VT-MS dissociation profiles and extent of unfolding determined *via* VT-IM-MS.

Interestingly, it was found that at higher analysis temperature, slightly less unfolded monomer with lower average charge is ejected from the complex, suggesting that the TID dissociation process might be adapting more 'atypical' dissociation route. More experiments at temperatures above 550 K need to be carried out to confirm this theory. Nevertheless, correlating TID temperatures and CID energies could serve as a framework for thermal stability screening to be performed on instruments with CID capabilities. The TID experiments provide fundamental insights into the protein folding, subunit interactions and fundamental thermodynamic parameters.

4.5 References

(1) Taylor, K.; Barran, P. E.; Dorin, J. R. *Biopolymers* **2008**, *90*, 1.
(2) Pedreno, S.; Pisco, J. P.; Larrouy-Maumus, G.; Kelly, G.; de Carvalho, L. P. S. *Biochemistry* **2012**, *51*, 8027.
(3) Sacchi, S.; Caldinelli, L.; Cappelletti, P.; Pollegioni, L.; Molla, G. *Amino Acids* **2012**, *43*, 1833.
(4) Jurneczko, E.; Barran, P. E. *Analyst* **2011**, *136*, 20.
(5) Peters, S. J.; Smales, C. M.; Henry, A. J.; Stephens, P. E.; West, S.; Humphreys, D. P. *Journal of Biological Chemistry* **2012**, *287.*
(6) Ryslava, H.; Doubnerova, V.; Kavan, D.; Vanek, O. *Journal of proteomics* **2013**, *92*, 80.
(7) Menendezarias, L.; Argos, P. *Journal of Molecular Biology* **1989**, *206*, 397.
(8) Heringa, J.; Argos, P.; Egmond, M. R.; Devlieg, J. *Protein Engineering* **1995**, *8*, 21.
(9) Kelly, S. M.; Price, N. C. *Current Protein & Peptide Science* **2000**, *1*, 349.
(10) Benjwal, S.; Verma, S.; Rohm, K. H.; Gursky, O. *Protein Science* **2006**, *15*, 635.
(11) Johnson, C. M. *Archives of Biochemistry and Biophysics* **2013**, *531*, 100.
(12) Dupeux, F.; Roewer, M.; Seroul, G.; Blot, D.; Marquez, J. A. *Acta Crystallographica Section D-Biological Crystallography* **2011**, *67*, 915.
(13) Mao, Y.; Woenckhaus, J.; Kolafa, J.; Ratner, M. A.; Jarrold, M. F. *Journal of the American Chemical Society* **1999**, *121*, 2712.
(14) Jarrold, M. F. *Accounts of Chemical Research* **1999**, *32*, 360.
(15) Teplow, D. B.; Lazo, N. D.; Bitan, G.; Bernstein, S.; Wyttenbach, T.; Bowers, M. T.; Baumketner, A.; Shea, J.-E.; Urbanc, B.; Cruz, L.; Borreguero, J.; Stanley, H. E. *Accounts of Chemical Research* **2006**, *39*, 635.
(16) Berezovskaya, Y.; Porrini, M.; Barran, P. E. *International Journal of Mass Spectrometry* **2013**, *345*, 8.
(17) Adams, N. G.; Smith, D. *International Journal of Mass Spectrometry and Ion Processes* **1976**, *21*, 349.
(18) Smith, S. C.; McEwan, M. J.; Giles, K.; Smith, D.; Adams, N. G. *International Journal of Mass Spectrometry and Ion Processes* **1990**, *96*, 77.
(19) Giles, K.; Adams, N. G.; Smith, D. *Journal of Physical Chemistry* **1992**, *96*, 7645.
(20) McCullough, B. J.; Kalapothakis, J.; Eastwood, H.; Kemper, P.; MacMillan, D.; Taylor, K.; Dorin, J.; Barran, P. E. *Anal Chem* **2008**, *80*, 6336.
(21) Wyttenbach, T.; Kemper, P. R.; Bowers, M. T. *Int J Mass Spectrom* **2001**, *212*, 13.
(22) Dwivedi, P.; Wu, C.; Matz, L. M.; Clowers, B. H.; Siems, W. F.; Hill, H. H., Jr. *Analytical Chemistry* **2006**, *78*, 8200.
(23) Wu, C.; Siems, W.; Asbury, R.; Hill, H. *Analytical Chemistry* **1998**, *70*, 4929.
(24) May, J. C.; Russell, D. H. *Journal of the American Society for Mass Spectrometry* **2011**, *22*, 1134.

(25) Verbeck, G. F.; Gillig, K. J.; Russell, D. H. *European Journal of Mass Spectrometry* **2003**, *9*, 579.

(26) Silveira, J. A.; Servage, K. A.; Gamage, C. M.; Russell, D. H. *Journal of Physical Chemistry A* **2013**, *117*, 953.

(27) Shen, H.-B.; Chou, K.-C. *Journal of Proteome Research* **2009**, *8*, 1577.

(28) Krissinel, E.; Henrick, K. *Journal of Molecular Biology* **2007**, *372*, 774.

(29) Krissinel, E. *Journal of Computational Chemistry* **2010**, *31*, 133.

(30) Ruotolo, B. T.; Hyung, S. J.; Robinson, P. M.; Giles, K.; Bateman, R. H.; Robinson, C. V. *Angewandte Chemie-International Edition* **2007**, *46*, 8001.

(31) Sobott, F.; McCammon, M. G.; Robinson, C. V. *International Journal of Mass Spectrometry* **2003**, *230*, 193.

(32) Pagel, K.; Hyung, S.-J.; Ruotolo, B. T.; Robinson, C. V. *Analytical Chemistry* **2010**, *82*, 5363.

(33) Hall, Z.; Politis, A.; Bush, M. F.; Smith, L. J.; Robinson, C. V. *Journal of the American Chemical Society* **2012**, *134*, 3429.

(34) Hall, Z.; Hernandez, H.; Marsh, J. A.; Teichmann, S. A.; Robinson, C. V. *Structure* **2013**, *21*, 1325.

(35) Zhou, M.; Dagan, S.; Wysocki, V. H. *Angewandte Chemie-International Edition* **2012**, *51*, 4336.

(36) Zhou, M.; Huang, C.; Wysocki, V. H. *Analytical Chemistry* **2012**, *84*, 6016.

(37) Zhou, M.; Dagan, S.; Wysocki, V. H. *Analyst* **2013**, *138*, 1353.

(38) Sterling, H. J.; Kintzer, A. F.; Feld, G. K.; Cassou, C. A.; Krantz, B. A.; Williams, E. R. *Journal of the American Society for Mass Spectrometry* **2012**, *23*, 191.

(39) Bush, M. F.; Hall, Z.; Giles, K.; Hoyes, J.; Robinson, C. V.; Ruotolo, B. T. *Analytical Chemistry* **2010**, *82*, 9557.

(40) Hyung, S.-J.; Robinson, C. V.; Ruotolo, B. T. *Chemistry & Biology* **2009**, *16*, 382.

(41) Aquilina, J. A.; Robinson, C. V. *Biochemical Journal* **2003**, *375*, 323.

(42) Sinelnikov, I.; Kitova, E. N.; Klassen, J. S. *Journal of the American Society for Mass Spectrometry* **2007**, *18*, 617.

(43) Lundberg, E.; Olofsson, A.; Westermark, G. T.; Sauer-Eriksson, A. E. *Febs Journal* **2009**, *276*, 1999.

(44) Nordlund, H. R.; Hytonen, V. P.; Horha, J.; Maatta, J. A. E.; White, D. J.; Halling, K.; Porkka, E. J.; Slotte, J. P.; Laitinen, O. H.; Kulomaa, M. S. *Biochemical Journal* **2005**, *392*, 485.

(45) Sinha, S.; Mitra, N.; Kumar, G.; Bajaj, K.; Surolia, A. *Biophysical Journal* **2005**, *88*, 1300.

(46) Boeri Erba, E.; Ruotolo, B. T.; Barsky, D.; Robinson, C. V. *Anal Chem* **2010**, *82*, 9702.

(47) Wanasundara, S. N.; Thachuk, M. *Journal of the American Society for Mass Spectrometry* **2007**, *18*, 2242.

(48) Benesch, J. L. P.; Aquilina, J. A.; Ruotolo, B. T.; Sobott, F.; Robinson, C. V. *Chemistry & Biology* **2006**, *13*, 597.

(49) Shelimov, K. B.; Clemmer, D. E.; Hudgins, R. R.; Jarrold, M. F. *Journal of the American Chemical Society* **1997**, *119*, 2240.

(50) Reimann, C. T.; Sullivan, P. A.; Axelsson, J.; Quist, A. P.; Altmann, S.; Roepstorff, P.; Velazquez, I.; Tapia, O. *Journal of the American Chemical Society* **1998**, *120*, 7608.

(51) Vogt, G.; Woell, S.; Argos, P. *Journal of Molecular Biology* **1997**, *269*, 631.

5

Probing Antibody Thermal Stability with VT-(IM)-MS

Aggregation of biologics such as mAbs can not only affect the efficacy of the therapeutic treatment but can also induce adverse effects. Efforts are made to shift the equilibrium away from the aggregation-prone state by increasing the thermodynamic stability of the native state protein and improving its conformational stability. Here, the thermal stability of three intact IgGs and two Fc-hinge fragments is probed using VT-MS and VT-IM-MS. These proteins show similar collapse-unfold type of mechanism as non-covalent complexes investigated in the previous chapter. The differences in the extent of collapse and unfolding are rationalized based on properties attributed to different IgG subclasses and their thermal stability. Moreover, VT-IM-MS shows to be promising tool for thermal stability comparative studies for proteins of therapeutic interest.

5.1 Introduction

Handling of chemical and physical instabilities is one of the obstacles in the development of protein based therapeutics such as mAbs and their derivatives.[1-8] Along with analytical and regulatory aspects, biophysical characteristics such as stability are crucial selection criteria for mAbs designed for clinical use. During manufacturing, purification, formulation and storage, antibodies behave differently in terms of their sensitivity to pH or temperature, aggregation propensity and vulnerability to degradation.[9-11] Low stability of mAbs may be problematic with regards to long-term storage or consistency of production. The most serious result of physical instability is protein aggregation, which can affect not only the efficacy of the therapeutic treatment but also may induce adverse effects such as immunogenicity.[12-15] Efforts are made to enhance stability of mAbs for example through reengineering of the hinge region[16], domain exchange[17], introduction of specific mutations in the CH3 domain[18-20] or within the inter LC-CH1 DSB network[21].

Thermal stability is increasingly accepted as a convenient measure of global stability. The temperature induced unfolding of mAbs measured by differential scanning calorimetry (DSC) has become an essential tool used for monitoring production consistency, clone selection, protein structure characterisation and formulation development.[22] A number of studies have been published investigating IgG unfolding upon exposure to physical stress (heat) and/or chemical stress (solution pH). These studies are briefly overviewed below.

5.1.1 Temperature induced unfolding patterns in IgGs

One of the structural characteristics of an immunoglobulin molecule is its organisation into domains. An IgG molecule consists of 12 similar in size globular domains – 8 formed by the heavy chains and 4 by the light chains, as described in Chapter 3. The stability of such multidomain proteins, is commonly probed with DSC, while the secondary structure content can be investigated with circular dichroism (CD) spectroscopy; providing insights into the global structure as well as behaviour of unfolding domains. Unfolding of IgGs is a complex process, where the denatured state is obtained from the native state *via* several intermediate states as the domains often unfold independently in a non-cooperative manner.[23,24]

The possibility of partly denatured intermediate states of IgGs upon thermal denaturation was first proposed by Rowe and Tanford in 1973.[25] Later it was confirmed that Fab and Fc fragments in IgGs are thermodynamically independent domains.[26] One to three major transitions are generally observed in the DSC thermogram, correlated with independent unfolding of individual domains: CH2 and CH3 domains of the Fc fragment and the Fab domain.[9,22,23,27,28] Previous studies showed that CH2 domain of IgG1 undergoes structural transitions at lower temperature compared to the CH3 domain.[22,29,30] Tischenko *et al.* rationalised this phenomenon in IgG1 molecules based on the strength of interdomain interactions; strong interactions between CH3 domains form a cooperative block, while CH2 interactions are mediated by the *N*-linked oligosaccharides (at Asn279 position).[29] Furthermore, deglycosylation of IgGs was found to result in a significant destabilisation of the CH2 domain and lowered the temperature of its melting but had no effect on the CH3 domain stability.[22,31-36] Kenmert *et al.* referred to thermally-treated IgG-Fc structure as non-native alternatively folded state rather than a molten globule state.[37]

IgG1-Fc fragment unfolding displays a bimodal DSC distribution, the first transition has been associated with CH2 domain unfolding, the second transition represents CH3 domain melt, while the stability of Fab fragment is significantly affected by the sequence of the variable domain.[22] Studies of isolated Fab fragments had shown that diversity within variable antigen binding domains is responsible for stability variations among IgGs of identical subclass; while some Fab fragments may be exquisitely stable others may be relatively unstable.[4,6,31,38-42] Sometimes, Fc fragment and Fab fragment transitions may be overlapping disabling rigours thermodynamic analysis of the individual transitions.[23]

A number of studies have demonstrated that IgG1 is the most thermally stable human subclass followed by IgG2 and IgG4.[10,31] A study performed on mAbs of the same antigen binding specificity had shown lower conformational stability of the IgG4 in comparison to IgG1, resulting in increased levels of soluble aggregates formed.[43] At neutral pH, two transitions were observed for IgG1, while only a single one was noted for IgG4. Reported results indicate that CH2 and CH3 domains unfold simultaneously and weaker non-covalent interactions between the CH3 domains know to exist within IgG4 subclass, may be responsible for its lower melting temperature.[36,43] Additionally, dependent on the nature of denaturation the process may follow different pathways; it was reported that the Fab fragment is more sensitive to the thermal stress, whereas the Fc fragment is strongly affected by lowering of the solution pH.[23] Nevertheless, upon application of either physical or chemical stress, a significant fraction of the secondary structure has been reported to remain intact.[23]

Overall, in each antibody subclass, the amino acid sequence of the variable region and solution conditions affect the unfolding pattern, the number of transitions and their onset temperature observed during heating.[31,43] Stability variations between antibodies of the same subclass are derived from differences in variable domain sequence. Introducing point mutations or reengineering the DSB network are both methods that have been used to increase stability of mAbs making them less prone towards aggregation.[16,23] For example, Peters *et al.* report on the generation of a more thermally stable IgG4 by altering the inter LC-CH1 DSB arrangement to mimic that of IgG1; what resulted in increased Fab fragment stability by up to 6.8 °C.[21] In this chapter, three intact mAbs of the same antigen binding specificity (IgG1, IgG4 and IgG4 with inserted IgG1 upper and core hinge) as well the two Fc-hinge fragments (IgG1 and IgG4) are investigated with VT-MS and VT-IM-MS. Such experiments provide insights to thermal stability along with conformational information and may benefit comparative thermal stability studies of proteins of therapeutic interest.

5.2 Methodology

5.2.1 Sample preparation

Human intact IgG1 ‘C’, IgG4 ‘C’, and IgG4 ‘C’ with IgG1 hinge as well as IgG1 Fc-hinge and IgG4 Fc-hinge fragments were provided by UCB Pharma; protein samples were expressed and purified by Dr Shirley Peters. The upper and core hinge in IgG4 has been replaced with IgG1 upper and core hinge as shown below, to enhance thermal stability of the mAb:

	upper hinge	core	lower hinge
IgG1	**EPKSCDKTHT**	**CPPC**	**PAPELLGGP**
IgG4	**ESKYGPP**	**CPSC**	**PAPEFLGGP**
IgG4 with IgG1 hinge	**EPKSCDKTHT**	**CPPC**	**PAPEFLGGP**

The complete amino acid sequences are available in the Appendix 3. Samples were stored in 50 mM sodium acetate (NaOAc): 125 mM sodium chloride (NaCl) at 4 °C. IgG1 ‘C’, IgG4 ‘C’, and both of the Fc-hinge fragment samples were diluted to a concentration of 30 µM, the stock 6 µM sample the IgG4 ‘C’ with IgG1 hinge was used. On the day of analysis, the buffer was exchanged to 100 mM ammonium acetate (Fisher Scientific, Loughborough, UK) pH 6.8, using micro Bio-Spin Chromatography columns (Micro Bio-Spin 6 Columns, Tris) following the instructions specified by the manufacturer. The desalting procedure was performed twice to achieve desired sample purity. High purity water was obtained from an Arium 611 water purification unit (Sartorius, Göttingen, Germany) fitted with a 0.2 µm filter.

5.2.2 Variable temperature mass spectrometry and variable temperature ion mobility mass spectrometry

The samples were ionised using positive nESI as described in Chapter 2, section 2.1.2. The IM-MS data were acquired on the MoQToF, quadrupole time-of-flight mass spectrometer modified in-house to include a 5.1 cm drift cell, as detailed in section 2.2.1.[44] The voltages along the mass spectrometer were adjusted to preserve native like structures. The capillary potential was held at 1.5 - 1.8 kV, the source temperature was set to 80 °C, and the cone voltage was set to 80 V. The injection energy used was between 30 and 33 V. Other instrumental settings for the MoQToF IM mass spectrometer are listed in Chapter 2, Table 2.3. The drift cell was filled with helium as the buffer gas at a pressure of 3.7 – 3.8 Torr and the pressure was measured using a capacitance manometer (MKS Instruments, UK); the precise pressure was recorded for each and every drift voltage and used in the calculations of CCS. Ion mobility experiments were carried out at drift cell temperatures of 300 K, 350 K, 360 K, 400 K, 475 K, 500 K and 550 K. The cell was heated *via* tantalum wire wound ceramic heaters located in both the cell body (8 heaters) and in the end cap (2 heaters) driven by variable transformers (Variacs). The temperature of the drift cell was monitored using three k-type thermocouples and recorded for each data set. The electric potential across the cell was varied from 60 to 20 V with measurements taken at six different drift voltages. The rotationally-averaged collision cross-sections (CCS) were determined from a plot of arrival time versus P / T and the CCSD were determined as described in Chapter 2, section 2.2.1.4. Data was processed using Mass Lynx V.4.1 Build 10, Microsoft Excel 2003 and Origin 8.5.1 graphing software (OriginLab, Northampton, MA, USA).

5.3 Preliminary Results and Discussion

5.3.1 VT-MS of the intact mAbs

VT-MS experiments were performed on three intact antibodies (denoted here as ‘C’) of a different antigen binding specificity from the mAbs studied in Chapter 3. Mass spectra of (a) IgG1 C, (b) IgG4 C and (c) IgG4 C with IgG1 hinge are shown in Figure 5.1. The upper and core hinge in IgG4 has been replaced with that of IgG1 to enhance thermal stability of the mAb. Solution based melting temperatures (T_m) were 93.3 °C, 84.4 °C and 93.3 °C for IgG1 C, IgG4 C and IgG4 C with IgG1 hinge, respectively.[45] 30 μM (IgG1 and IgG4) and 6 μM (IgG4 with IgG1 hinge) protein samples in 100 mM ammonium acetate at pH 6.8 were ionised using nESI and data were acquired on the in-house modified IM-MS instrument (MoQToF) shown in Figure 2.3. In order to preserve the complexes’ quaternary structure, key source parameters were optimized, in particular the source pressure, capillary, sample and extractor cone and injection energy voltages. The temperature of the drift cell helium gas was raised *via* ten tantalum wire wound ceramic heaters driven by two external variable transformers and the temperature was closely monitored by the capacitance manometer. Mass spectra were recorded at seven discrete temperatures in a range of 300 K to 550 K. Measurement at 360 K (87 °C) was

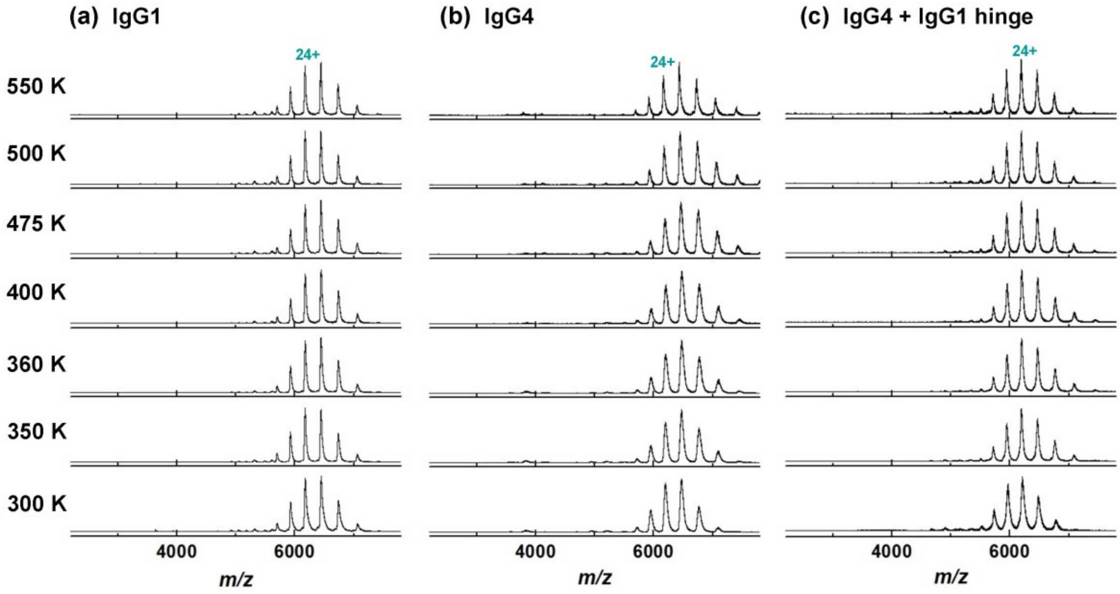

Figure 5.1 nESI mass spectra of intact (a) IgG1 'C', (b) IgG4 'C' and (c) IgG4 'C' with IgG1 hinge in 100 mM ammonium acetate at pH 6.8 acquired on the MoQToF mass spectrometer at buffer gas temperature of 300 K, 350 K, 360 K, 400 K, 475 K, 500 K and 550 K.

acquired to provide more insights into IgG behavior near the solution-phase T_m. The time ions spend in the temperature controlled region of MoQToF is dependent on the ions' mass, charge and the electric potential applied across the drift cell. In the experiment at 300 K presented here, this time varied from 2.2 ms to 5.1 ms for an intact IgG with z = 24+ charge, where the potential difference across the drift cell ranged from 60 to 15 V. The experimental time frame does vary somewhat with temperature, however, this was minimised by adjusting the pressure as a function of temperature to match the drift time at 300 K.

Mass spectra of three intact IgGs at progressively higher temperatures are shown in Figure 5.1. Peaks corresponding to the intact IgG are observed in the ~5800 – 7200 *m/z* range; with the charge state envelope ranging from 21+ to 26+ charge state, centred at the 24+ and 23+ charge states. Upon the increase in drift gas temperature no dissociation into subunits or fragmentation of peptide chains is observed. The chains of IgG1 and IgG4 with IgG1 hinge are covalently linked *via* DSB, hence no dissociation is anticipated. The IgG4 isotype, on the other hand, is capable of forming intra-chain DSB in the hinge region leading to dissociation into two half molecules; however, this was not noted even at 550 K. Furthermore, the charge state distribution (CSD) remains invariant at the range of buffer gas temperatures investigated. At 300 K, IgG1 (a) and IgG4 (b) are centred on 24+ and 23+ charge state, while CSD of IgG1 remains constant thought the experiment within the 300 – 550 K range, the CSD of IgG4 slightly shifts towards 23+ charge state at higher temperature. The CSD of stabilized IgG4 with IgG1 hinge (c) remains centred on 24+ charge state thought the experiment.

An interesting feature observed in the mass spectra at elevated buffer gas temperatures is the significant narrowing of peaks and shift towards lower *m/z*, attributed to more efficient stripping of salt adducts. Similar effect has been noted for the non-covalent complexes investigated in Chapter 4. Figure 5.2 shows a close up of the 24+ charge state of IgG4 species, which displayed the highest degree of salt clean up, particularly at 500 K and 550 K. In combination with in-source salt clean up, VT-MS could serve as a method for obtaining an enhanced resolution for proteins difficult to desolvate, such as virus capsids.

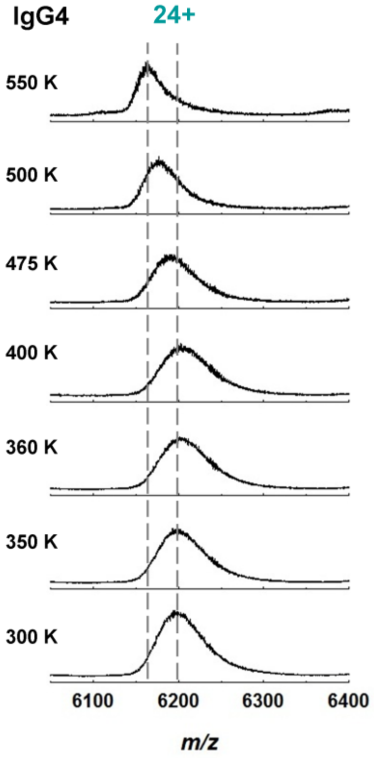

Figure 5.2 Zoom at the 24+ charge state of IgG4 'C' in 100 mM ammonium acetate at pH 6.8 acquired on the MoQToF mass spectrometer at buffer gas temperature of 300 K, 350 K, 360 K, 400 K, 475 K, 500 K and 550 K, displaying an enhanced removal of salt adducts at elevated buffer gas temperature.

5.3.2 VT-MS of the IgG Fc-hinge fragments

VT-MS experiments were also performed on the Fc-hinge fragments of IgG1 and IgG4 subclasses. A core hinge mutation S241P was introduced to the IgG4 Fc-hinge fragment to prevent formation of the intra-chain DSB and subsequent dissociation of the heavy chains. Mass spectra of 30 μM Fc-hinge fragments in 100 mM ammonium acetate at pH 6.8 in the 300 K – 550 K temperature range, presented in Figure 5.3, were acquired in a similar fashion to that described in the previous section.

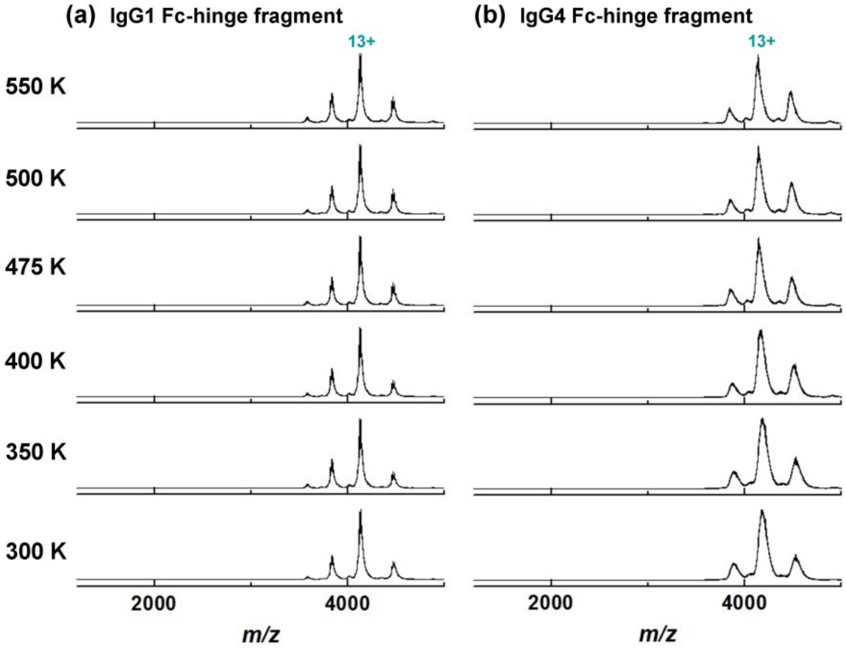

Figure 5.3 nESI mass spectra of (a) IgG1 'C' Fc-hinge fragment and (b) IgG4 'C' Fc-hinge fragment in 100 mM ammonium acetate at pH 6.8 acquired on the MoQToF mass spectrometer at buffer gas temperature of 300 K, 350 K, 400 K, 475 K, 500 K and 550 K.

Fc-hinge fragments of both isotypes exhibit narrow CSD (~*m/z* 3600 – 4500) centred on the 13+ charge state. Similarly to the intact IgGs, Fc-hinge fragments display preservation of CSD at progressively increasing buffer gas temperature and lack of dissociation into subunits. At 300 K, IgG4 *m/z* peaks (b) are significantly broader in comparison to the IgG1 (a), while their resolution somewhat improves at higher buffer gas temperatures.

5.3.3 VT-IM-MS of the intact mAbs

Structural changes due to increased temperature of analysis environment of three intact mAbs were investigated. VT-IM-MS experiments were carried out at seven discrete temperatures ranging from 300 K to 550 K. CCSD landscapes and their transformations, derived from arrival time distributions (ATD) of IgG1, IgG4 and IgG4 with IgG1 hinge acquired at a range of temperatures are presented in Figure 5.4. Despite the lack of dissociation, structural transformation trends observed for IgGs are similar to those reported for non-covalent complexes studied in Chapter 4. IM data acquired at 350 K, 360 K and 400 K show a minor decrease in the CCS of IgG1 and IgG4 in comparison to CCS determined at 300 K, suggesting a structural collapse. The extent of the collapse was noted to be greater for higher charge states. As the buffer gas temperature is increased to 475 K and above, CCS increase as IgG chains begin to unfold. Furthermore, above 400 K CCSD profiles become significantly broader suggesting presence of closely related unfolding intermediate states. Interestingly, no decrease in the CCS associated with a thermally induced collapse was observed for the IgG4 with IgG1 hinge. This re-engineered mAb mimics thermal stability of IgG1 in solution (T_m = 93.3 °C); but does not display the same denaturation pathway in the gas-phase. Moreover, the CCSD of the hybrid antibody presents over an even broader conformational landscape at temperatures above 300 K. This data suggests that the increased thermal stability correlates to higher structural flexibility. Another explanation is that the re-engineered hinge is less able to preserve a compact configuration of this hybrid mAb.

As discussed in Chapter 4, the decrease in the CCS is associated with loss of structure and solution T_m. Figure 5.5 shows CCSD of the most abundant (24+) charge state of all three IgGs along with the percentage change in the median CCS with respect to CCS at 300 K. It can be seen that the greatest decrease in the CCS, hence the maximum collapse, is detected at a higher temperature for IgG1 (400 K) than for IgG4 (360 K). This correlates well with the solution phase studies, where IgG1 was found to be more thermally stable than IgG4.[45] Again, IgG4 with an IgG1 hinge is the outlier from the trend as no compaction reflected by a decrease in CCS was noted. A list of median CCS is provided in the Appendix 6.

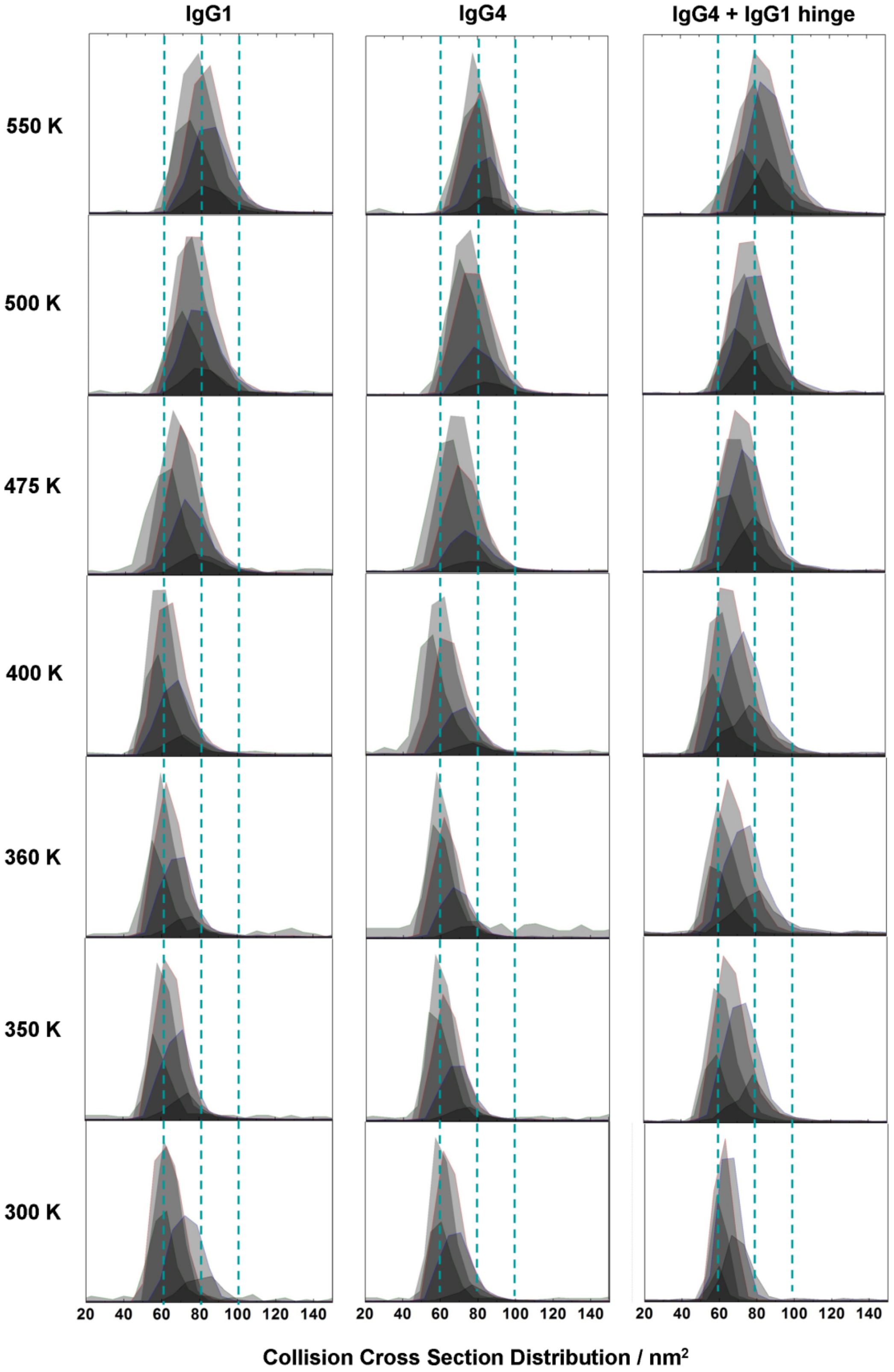

Figure 5.4 Total collision cross section distributions (CCSD) of intact IgG1 'C', IgG4 'C' and IgG4 'C' with IgG1 hinge in 100 mM ammonium acetate at pH 6.8 acquired on the MoQToF mass spectrometer (DV = 35 V) at buffer gas temperature of 300 K, 350 K, 360 K, 400 K, 475 K, 500 K and 550 K. CCSD of individual charge states have been normalised to spectral intensity.

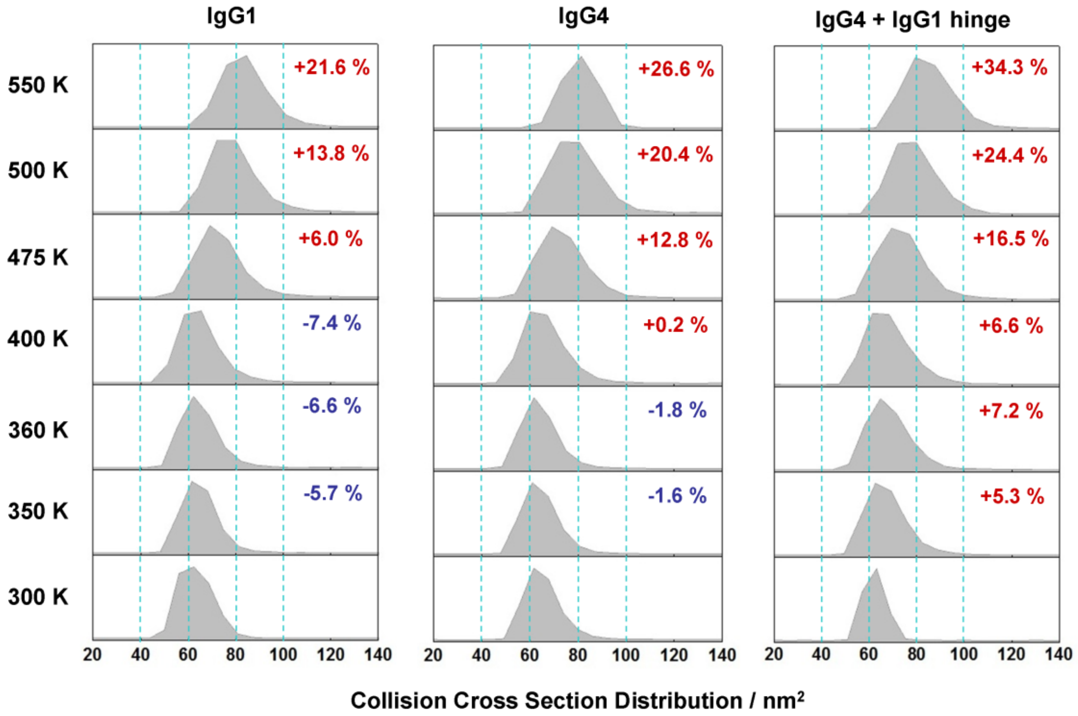

Figure 5.5 Collision cross section distributions (CCSD) of the most abundant charge state (24+) of (a) IgG1 ‘C’, (b) IgG4 ‘C’ and (c) IgG4 ‘C’ with IgG1 hinge in 100 mM ammonium acetate at pH 6.8 acquired on the MoQToF mass spectrometer (DV = 35 V) at a 300 – 550 K buffer gas temperature range; along with percentage change in the median CCS with respect to CCS at 300 K.

Moreover, IgG1 undergoes greater degree of compaction in comparison to IgG4; at 400 K up to 7.4 % decrease in median CCS of 24+ charge state is noted, compared to only 1.8 % decrease for 24+ charge state of IgG4 (Figure 5.5). This behaviour might be related to the intrinsic flexibility of the hinge region. The hinge of an intact IgG1 is know to be more flexible than that of IgG4, hence IgG1 might be capable of adopting more compact structures upon heat exposure.[46] One would expect similar compaction behaviour of the hybrid mAb possessing IgG1 hinge, however, such compaction was not observed calling for further investigation.

Worth mentioning are the differences observed in the extent of unfolding among the IgG subclasses at high buffer gas temperatures. The onset of IgG4 unfolding occurs at lower temperature and proceeds to a greater extent (+26.6 % at 550 K) in comparison to IgG1 (+21.6 % at 550 K). This observation can be rationalized by the strength of non-covalent interaction between CH3 domains of heavy chains; which is known to be stronger for the IgG1 isotype.[18,47-50] Strong interactions between CH3 domains of IgG1, hold two heavy chains tightly and prevent extensive unfolding, while weak non-covalent interaction between CH3 domains of IgG4 permit the dissociation of these domains resulting in enhanced unfolding reflected by higher CCS. The unfolding of the hybrid IgG at 550 K progresses to even higher degree (+34.3 % at 550 K), suggesting that the unfolding could be mediated by the strength of non-convent interaction between CH3 domains (weak non-covalent interactions between CH3 domains of IgG4) as well as the hinge flexibility (higher hinge flexibility in IgG1).

Although, VT-IM-MS measurements performed at discrete temperatures will not provide an exact T_m as DSC measurements do; this method may serve as a valuable tool for comparative studies of mAb stability, especially when very limited amount of protein material is available. Measurements taken at smaller temperature intervals near the T_m would certainly improve the assessment of thermal stability and provide a closer estimate of the gas-phase T_m.

5.3.4 VT-IM-MS of the Fc-hinge fragments

VT-IM-MS experiments were also performed on the Fc-hinge fragments of both the IgG1 and IgG4 subclass. CCSD landscapes and their transformations of both Fc-hinge fragments acquired at a range of temperatures are presented in Figure 5.6. Similarly to the intact mAbs, both fragments experience initial structural collapse at 350 K and 400 K, followed by unfolding at higher buffer gas temperatures. Here however, the extent of compaction was noted to be greater for lower charge states and higher for IgG1 Fc-hinge fragment in comparison to IgG4 Fc-hinge fragment. Unfolding continues to be more extensive for higher charge states, similarly to intact mAbs and non-covalent multimeric complexes.

As reported in Chapter 3, over 60 % of the 14+ charge state of the IgG4 Fc-hinge fragment populates the larger conformational family of the two observed (Figures 3.7 and 5.6), as a result of destabilised interactions between the CH3 domains of the heavy

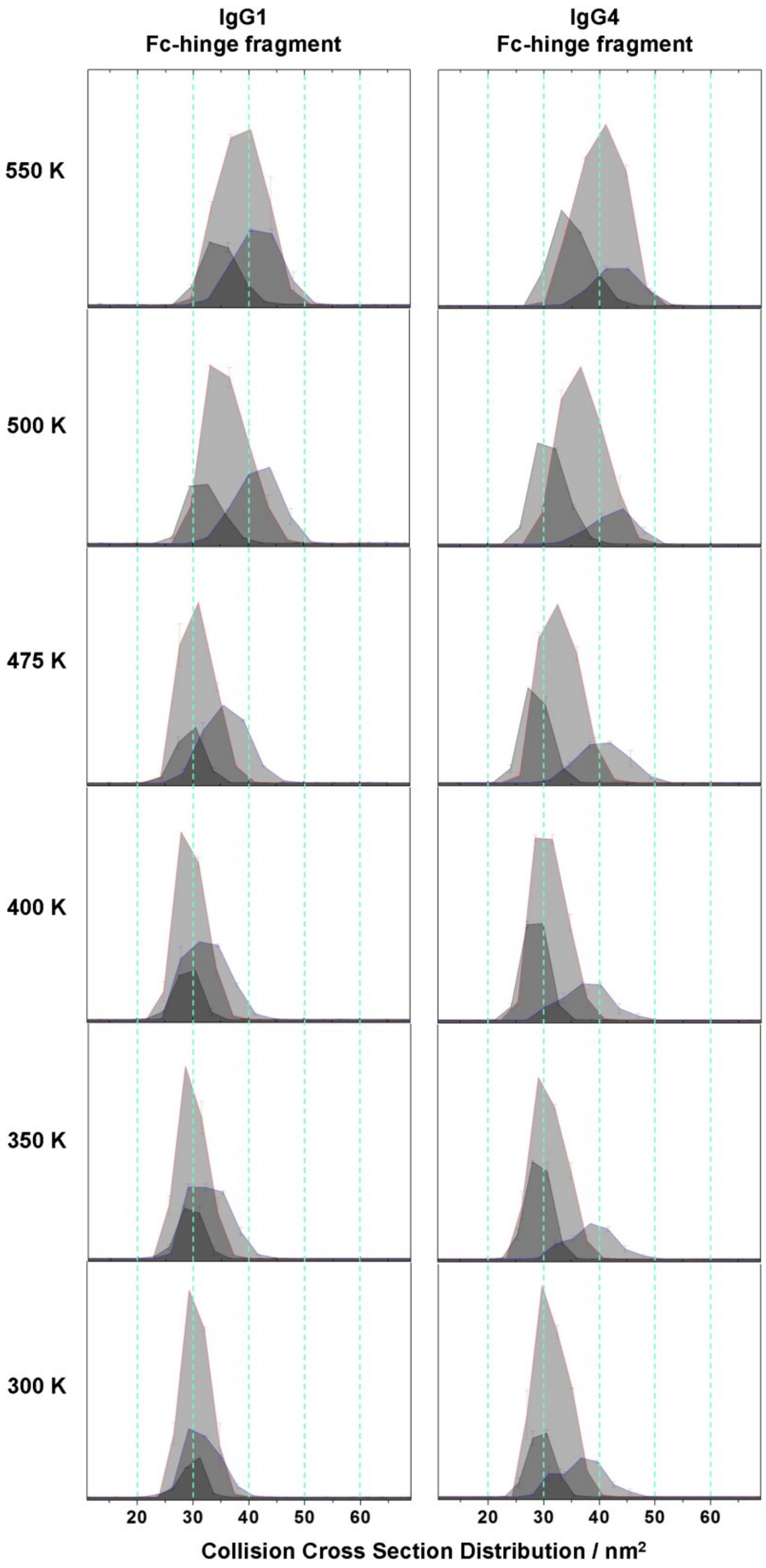

Figure 5.6 **Total collision cross section distributions (CCSD) of IgG1 'C' Fc-hinge fragment and IgG4 'C' Fc-hinge fragment in 100 mM ammonium acetate at pH 6.8 acquired on the MoQToF mass spectrometer (DV = 35 V) at buffer gas temperature of 300 K, 350 K, 400 K, 475 K, 500 K and 550 K. CCSD of individual charge states have been normalised to spectral intensity.**

chains.[50] In contrast, the 14+ charge state of the IgG1 Fc-hinge fragment occupies mainly the smaller conformational family, where CH3 domains are held tightly due to strong non-covalent interactions producing a more compact structure.[47] The crystallographic study reported by Davies *et al.* revealed how Arg409 within CH3 domain of IgG4, can adopt two different conformations affecting the stability of the CH3 interface.[50] One of these conformations is similar to those observed in IgG1, whereas the other conformation weakens the interface by disrupting the water molecule network resulting in reduced hydrogen bonding. VT-IM-MS experiments show that upon increase of buffer gas temperature the distinction between two conformational families of IgG4 Fc-hinge fragment becomes less apparent. The 'destabilised' conformation of IgG4 Fc-hinge fragment experiences unfolding to larger CCS; while the more compact form slowly approaches similar unfolding landscape at 500 K, possibly due to weaker CH3 interface interactions resulting from significantly reduced residual solvent content at this temperature affecting the hydrogen bond network (Figure 5.3). At 550 K, both Fc-hinge fragments display similar CCSD profiles suggesting that both subclasses have unfolded to a comparable degree; a 29.0 % increase in median CCS was noted for the 13+ charge state of IgG1 Fc-hinge fragment and 31.6 % increase for that of IgG4 Fc-hinge fragment. Unfortunately the collected data does not allow distinguishing between CH2 and CH3 domain unfolding and relating gas-phase behaviour of these domains to the solution-phase unfolding. Experiments would have to be performed on isolated domains in order to compare their relative stability.

The amount of thermal unfolding at high temperatures was also noted to be less significant for Fc-hinge fragments than for non-covalent complexes. The extent of mAb fragment (54 kDa) unfolding was compared to unfolding of similar in size non-covalent tetramer transthyretin (TTR, 55 kDa). Both species are composed of four folded domains, however while subunits of TTR are held together by non-covalent interactions, Fc-hinge fragments are covalently linked *via* the hinge (at the CH2 domains) and *via* non-covalent interaction at the CH3 domain interface. TTR's most abundant 14+ charge state experiences about 38.3 % increase in the median CCS at 500 K, while only 16.4 - 16.6 % increase in CCS is noted for the most abundant 13+ charge states of Fc-hinge fragments under the same experimental conditions. At 550 K, unfolding of the Fc-hinge fragment was found to be closer to that of non-covalent TTR at 500 K of the same 13+ charge state: +29.0 % and +31.6 % at 550 K for IgG1 and IgG4 Fc-hinge fragments respectively, and +26.3 % for TTR at 500 K. The differences in the amount of external energy required to reach similar degree of unfolding illustrate the role of DSB of the hinge region and strength of non-covalent interactions at the CH3 domain interface.

5.4 Conclusions

Thermal stability of therapeutic proteins is a crucial aspect of drug development. Enhancing the stability of biologics such as mAbs is aimed to reduce aggregation and improve production consistency. Variable temperature MS and IM-MS was applied to probe the thermal stability with respect to conformation of three intact mAbs: IgG1, IgG4 and thermally enhanced hybrid IgG4 with IgG1 hinge; as well as two Fc-hinge fragments of IgG1 and IgG4. IgG1, IgG4 and their Fc-hinge fragments follow unfolding pathway similar to that of non-covalent complexes investigated in the previous chapter.

Upon temperature increase to 350 – 400 K, IgG1, IgG4 and their Fc-hinge fragments undergo an initial compaction noted by a decrease in median CCS. The hybrid IgG displayed somewhat different unfolding which did not follow any of the trends observed for the other two intact mAbs requiring further investigation. For IgG1 and IgG4, the temperature at which the maximum collapse occurs, correlates with loss of quaternary structure and the solution based T_m. Above 400 K, unfolding of mAb chains was marked by a significant increase in median CCS and widening of CCSD associated with a series of unfolding events. Broader conformational landscapes of the hybrid mAb at temperatures above 300 K, suggest higher structural flexibility contributing to increased thermal stability. Diversity in the extent of collapse and unfolding were rationalised by differences in the hinge flexibility and strength of non-covalent interactions at the CH3 domain interface among IgG subclasses.

This initial investigation still leaves a lot of questions with regards to the hybrid IgG. Nevertheless, VT-IM-MS has been demonstrated as a promising tool for probing the thermal stability of biologics. As the stability of Fab fragment can greatly influence the stability of an intact IgG, if would be worthwhile to apply this method to study mAbs of different antigen binding specificity.

5.5 References

(1) Hoogenboom, H. R. *Nature Biotechnology* **2005**, *23*, 1105.

(2) Holt, L. J.; Herring, C.; Jespers, L. S.; Woolven, B. P.; Tomlinson, I. M. *Trends in Biotechnology* **2003**, *21*, 484.

(3) Todorovska, A.; Roovers, R. C.; Dolezal, O.; Kortt, A. A.; Hoogenboom, H. R.; Hudson, P. J. *Journal of Immunological Methods* **2001**, *248*, 47.

(4) Worn, A.; Pluckthun, A. *Journal of Molecular Biology* **2001**, *305*, 989.

(5) Reiter, Y.; Pastan, I. *Clinical Cancer Research* **1996**, *2*, 245.

(6) Ewert, S.; Honegger, A.; Pluckthun, A. *Methods* **2004**, *34*, 184.

(7) Carter, P. J. *Experimental Cell Research* **2011**, *317*, 1261.

(8) Carter, P.; Merchant, A. M. *Current Opinion in Biotechnology* **1997**, *8*, 449.

(9) Hari, S. B.; Lau, H.; Razinkov, V. I.; Chen, S.; Latypov, R. F. *Biochemistry* **2010**, *49*, 9328.

(10) Ishikawa, T.; Ito, T.; Endo, R.; Nakagawa, K.; Sawa, E.; Wakamatsu, K. *Biological & Pharmaceutical Bulletin* **2010**, *33*, 1413.

(11) Sahin, E.; Grillo, A. O.; Perkins, M. D.; Roberts, C. J. *Journal of Pharmaceutical Sciences* **2010**, *99*, 4830.

(12) Franey, H.; Brych, S. R.; Kolvenbach, C. G.; Rajan, R. S. *Protein Science* **2010**, *19*, 1601.

(13) Rosenberg, A. S. *The AAPS journal* **2006**, *8*, E501.

(14) Chi, E. Y.; Krishnan, S.; Randolph, T. W.; Carpenter, J. F. *Pharmaceutical Research* **2003**, *20*, 1325.

(15) Mahler, H.-C.; Friess, W.; Grauschopf, U.; Kiese, S. *Journal of Pharmaceutical Sciences* **2009**, *98*, 2909.

(16) Lu, Y.; Harding, S. E.; Rowe, A. I.; Davis, K. G.; Fish, B.; Varley, P.; Gee, C.; Mulot, S. *Journal of Pharmaceutical Sciences* **2008**, *97*, 960.

(17) Kolfschoten, M. v. d. N.; Schuurman, J.; Losen, M.; Bleeker, W. K.; Martinez-Martinez, P.; Vermeulen, E.; den Bleker, T. H.; Wiegman, L.; Vink, T.; Aarden, L. A.; De Baets, M. H.; van De Winkel, J. G. J.; Aalberse, R. C.; Parren, P. W. H. I. *Science* **2007**, *317*, 1554.

(18) Labrijn, A. F.; Rispens, T.; Meesters, J.; Rose, R. J.; den Bleker, T. H.; Loverix, S.; van den Bremer, E. T. J.; Neijssen, J.; Vink, T.; Lasters, I.; Aalberse, R. C.; Heck, A. J. R.; van de Winkel, J. G. J.; Schuurman, J.; Parren, P. W. H. I. *Journal of Immunology* **2011**, *187*, 3238.

(19) Rose, R. J.; Labrijn, A. F.; van den Bremer, E. T. J.; Loverix, S.; Lasters, I.; van Berkel, P. H. C.; van de Winkel, J. G. J.; Schuurman, J.; Parren, P. W. H. I.; Heck, A. J. R. *Structure* **2011**, *19*, 1274.

(20) Wozniak-Knopp, G.; Rueker, F. *Archives of Biochemistry and Biophysics* **2012**, *526*, 181.

(21) Peters, S. J.; Smales, C. M.; Henry, A. J.; Stephens, P. E.; West, S.; Humphreys, D. P. *Journal of Biological Chemistry* **2012**, *287*.

(22) Ionescu, R. M.; Vlasak, J.; Price, C.; Kirchmeier, M. *Journal of Pharmaceutical Sciences* **2008**, *97*, 1414.

(23) Vermeer, A. W. P.; Norde, W. *Biophysical Journal* **2000**, *78*, 394.

(24) Johnson, C. M. *Archives of Biochemistry and Biophysics* **2013**, *531*, 100.

(25) Rowe, E. S.; Tanford, C. *Biochemistry* **1973**, *12*, 4822.

(26) Tischenko, V. M.; Zavyalov, V. P.; Medgyesi, G. A.; Potekhin, S. A.; Privalov, P. L. *European Journal of Biochemistry* **1982**, *126*, 517.

(27) Demarest, S. J.; Hopp, J.; Chung, J.; Hathaway, K.; Mertsching, E.; Cao, X.; George, J.; Miatkowski, K.; LaBarre, M. J.; Shields, M.; Kehry, M. R. *Journal of Biological Chemistry* **2006**, *281*, 30755.

(28) Saito, S.; Hasegawa, J.; Kobayashi, N.; Kishi, N.; Uchiyama, S.; Fukui, K. *Pharmaceutical Research* **2012**, *29*, 397.

(29) Tischenko, V. M.; Abramov, V. M.; Zav'yalov, V. P. *Biochemistry* **1998**, *37*, 5576.

(30) Kameoka, D.; Masuzaki, E.; Ueda, T.; Imoto, T. *Journal of Biochemistry* **2007**, *142*, 383.

(31) Garber, E.; Demarest, S. J. *Biochemical and Biophysical Research Communications* **2007**, *355*, 751.

(32) Wang, X.; Kumar, S.; Buck, P. M.; Singh, S. K. *Proteins-Structure Function and Bioinformatics* **2013**, *81*, 443.

(33) Pepinsky, R. B.; Silvian, L.; Berkowitz, S. A.; Farrington, G.; Lugovskoy, A.; Walus, L.; Eldredge, J.; Capili, A.; Mi, S.; Graff, C.; Garber, E. *Protein Science* **2010**, *19*, 954.
(34) Liu, H.; Bulseco, G.-G.; Sun, J. *Immunology Letters* **2006**, *106*, 144.
(35) Mimura, Y.; Church, S.; Ghirlando, R.; Ashton, P. R.; Dong, S.; Goodall, M.; Lund, J.; Jefferis, R. *Molecular Immunology* **2000**, *37*, 697.
(36) Ghirlando, R.; Lund, J.; Goodall, M.; Jefferis, R. *Immunology Letters* **1999**, *68*, 47.
(37) Kanmert, D.; Brorsson, A.-C.; Jonsson, B.-H.; Enander, K. *Biochemistry* **2011**, *50*, 981.
(38) Shimba, N.; Torigoe, H.; Takahashi, H.; Masuda, K.; Shimada, I.; Arata, Y.; Sarai, A. *Febs Letters* **1995**, *360*, 247.
(39) Knappik, A.; Pluckthun, A. *Protein Engineering* **1995**, *8*, 81.
(40) Wall, J. G.; Pluckthun, A. *Protein Engineering* **1999**, *12*, 605.
(41) Knappik, A.; Ge, L. M.; Honegger, A.; Pack, P.; Fischer, M.; Wellnhofer, G.; Hoess, A.; Wolle, J.; Pluckthun, A.; Virnekas, B. *Journal of Molecular Biology* **2000**, *296*, 57.
(42) Rothlisberger, D.; Honegger, A.; Pluckthun, A. *Journal of Molecular Biology* **2005**, *347*, 773.
(43) Neergaard, M. S.; Nielsen, A. D.; Parshad, H.; Van de Weert, M. *Journal of Pharmaceutical Sciences* **2014**, *103*, 115.
(44) McCullough, B. J.; Kalapothakis, J.; Eastwood, H.; Kemper, P.; MacMillan, D.; Taylor, K.; Dorin, J.; Barran, P. E. *Analytical Chemistry* **2008**, *80*, 6336.
(45) Peters, S., Personal communication, 2013.
(46) Roux, K. H.; Strelets, L.; Michaelsen, T. E. *Journal of Immunology* **1997**, *159*, 3372.
(47) Rispens, T.; Davies, A. M.; Ooijevaar-de Heer, P.; Absalah, S.; Bende, O.; Sutton, B. J.; Vidarsson, G.; Aalberse, R. C. *The Journal of biological chemistry* **2014**, *289*, 6098.
(48) Rispens, T.; Ooievaar-De Heer, P.; Vermeulen, E.; Schuurman, J.; Kolfschoten, M. v. d. N.; Aalberse, R. C. *Journal of Immunology* **2009**, *182*, 4275.
(49) Davies, A. M.; Rispens, T.; den Bleker, T. H.; McDonnell, J. M.; Gould, H. J.; Aalberse, R. C.; Sutton, B. J. *Molecular Immunology* **2013**, *54*, 1.
(50) Davies, A. M.; Rispens, T.; Heer, P. O.-d.; Gould, H. J.; Jefferis, R.; Aalberse, R. C.; Sutton, B. J. *Journal of Molecular Biology* **2014**, *426*, 630.

6

Application of MS, IM-MS and HDX-MS for Probing Mechanisms of Allosteric Inhibition of Enzymes

Natural feedback allosteric inhibition of metabolic enzymes is one of nature's ways of regulating biochemical pathways. Here, MtATP-phosphoribosyltransferase (MtATP-PRT) is investigated, an enzyme catalysing the first step of the biosynthesis of L-histidine in Mycobacterium tuberculosis. Native MS is applied to provide insights into L-histidine binding and the inhibition mechanism of MtATP-PRT. IM-MS and analytical ultracentrifugation (AUC) are employed to probe conformational changes induced by environmental factors and ligand binding. Moreover, these structural changes are mapped with hydrogen deuterium exchange (HDX) MS.

6.1 Introduction

6.1.1 Enzyme activity and inhibition

Enzymes are a category of globular proteins which act as a catalyst in the biochemical reaction in the living organisms. Regulation of these enzymatic activities is crucial for proper functioning of cells. An enzyme's structure is highly important for its activity and may be affected by external factors such as temperature or pH. Additionally, enzyme activity can be influenced by the binding of other molecules such as cofactors (non-protein element - metal cation or small organic molecule), activators (molecules which increase enzymes activity) or inhibitors (molecules which decrease enzymes activity).

The active site of an enzyme (indicated in light blue in Figure 6.1) is where the substrate *i.e.* the reacting molecule binds, and lowers the reaction activation energy resulting in product formation at an increased reaction rate. The activity of the enzyme can be blocked or decreased by an inhibitor binding at the active site (competitive inhibition) or at the allosteric site (allosteric inhibition) (Figure 6.1). Binding at the allosteric site often induces conformational changes to the enzyme structure that prohibit substrate from binding and subsequent product formation. The ability to undergo such changes resulting from ligand binding to sites other that the active site is a powerful way of regulating protein function. Naturally occurring allosteric sites in metabolic enzymes controlled through feedback effectors are nature's way of controlling biochemical pathways.

Studying feedback allosteric inhibition mechanisms can not only prove to be useful for enzyme regulation but these natural inhibitors may also serve as templates for chemically diverse, small molecule inhibitors sought after as regulators for synthetic biology, as therapeutics for diseases or as probes in both chemical genetics and chemical biology.[1-3] Additionally, the allosteric sites become attractive drug targets when the active site of an enzyme are "not targetable" or have poor "ligandability".[4-6] Some examples of important enzymes that have been successfully targeted at their allosteric

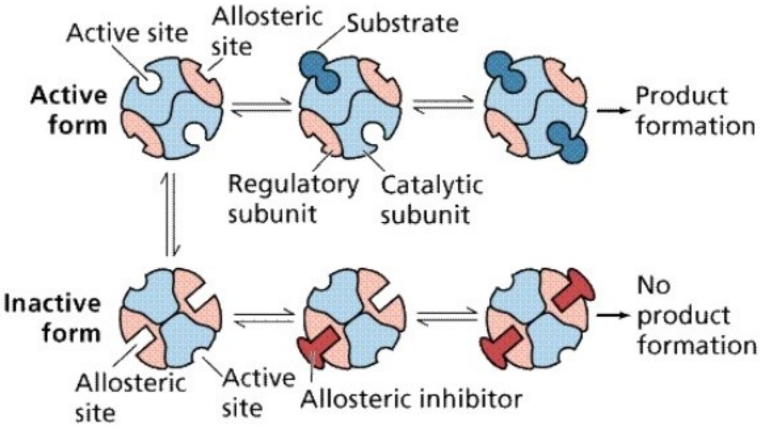

Figure 6.1 In their active form, enzymes act as a catalyst in biochemical reactions. Binding of a substrate (dark blue) to an active site (light blue) leads to eventual product formation at an increased reaction rate. Enzymes can be inactivated by binding of an allosteric inhibitor (red) to an allosteric site (pink), inducing conformational changes and stopping product formation by disabling substrate binding. Image reproduced from Purves *et al.*[7]

site include pyruvate kinesin[8], mitotic kinesin[9] or the Cdc34 ubiquitin-conjugating enzyme[10]. A classic example of an allosterically regulated enzyme is MtATP-phosphoribosyltransferase (MtATP-PRT).

6.1.2 Mycobacterium tuberculosis ATP-phosphoribosyltransferase (MtATP-PRT): function and structure

MtATP-PRT belongs to the phosporibosyltransferase superfamily of enzymes which catalyse the condensation of 5-phospo-alpha-D-ribose-1-diphosphate with nitrogenous bases in presence of metal ions.[11] MtATP-PRT catalyses the first step in the biosynthesis of L-histidine in *Mycobacterium tuberculosis i.e.* condensation of adenosine triphosphate (ATP) with phosphoribosyl pyrophosphate (PRPP) in the presence of Mg^{2+} cation. Being a feedback allosterically regulated enzyme, it is inhibited by the end product of the pathway, L-histidine.[12-14] Due to its essentiality in the cell, MtATP-PRT has been suggested as a potential target for the development of novel anti-tuberculosis agents, an infectious disease affecting over 2 billion people and responsible for 2 million deaths a year.[13,15] No *priori* toxicity associated with potential inhibitors has been suggested as this pathway is absent in humans, making it a suitable drug target.[12]

In terms of the tertiary and quaternary structure, two types of ATP-PRT exist. The more abundant homo-hexameric form encountered in bacteria, fungi and plants[13,16] and the hetero-octameric form present in some bacteria.[17,18] MtATP-PRT is a homohexameric protein with a total mass of about 190 kDa.[12] A cartoon representation of MtATP-PRT x-ray crystal structure along the 3-fold axis (Figure 6.2a) and 2-fold axis where the C-terminus is shown in the front plane (Figure 6.2b) is illustrated below.[13]

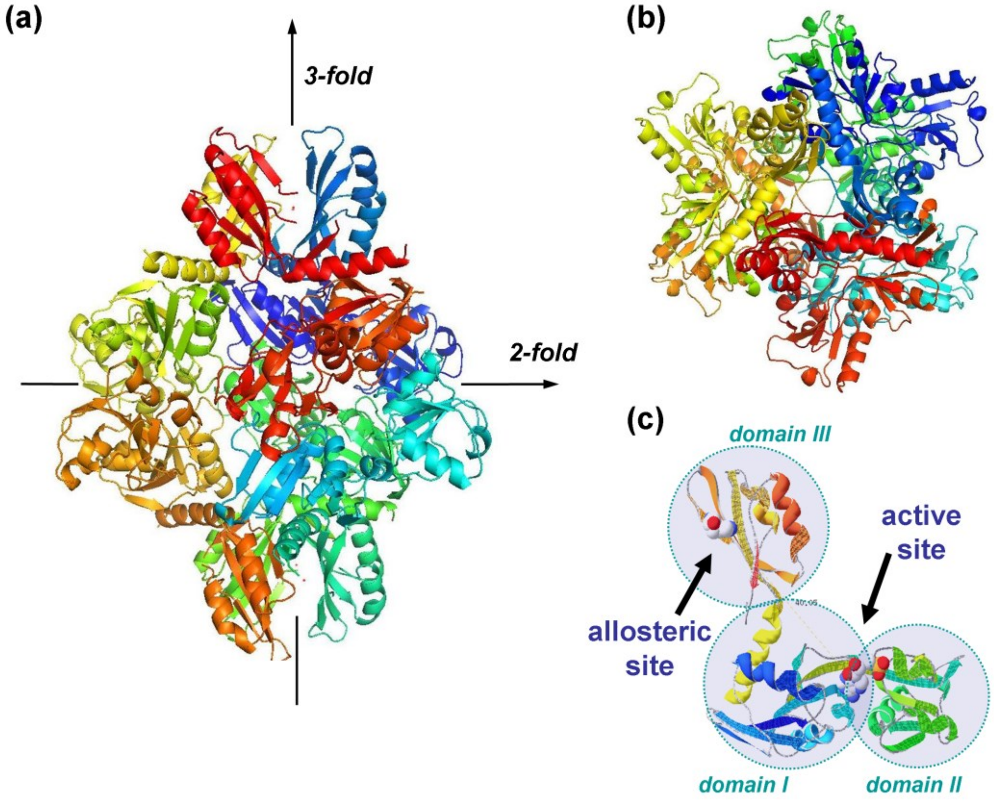

Figure 6.2 Graphical representation of the hexameric apo MtATP-PRT x-ray crystal structure along the (a) 3-fold symmetry axis and (b) 2-fold symmetry axis. Data available in PDB consists of MtATP-PRT dimer (PDB:1NH7); here the structure has been assembled into a hexamer using the online 'Protein interfaces, surfaces and assemblies' service PISA at the European Bioinformatics Institute website.[19,20] (c) MtATP-PRT monomer consists of three contiguous domains indicated with teal circles: I, II and III (PDB:1NH8). Location of the allosteric site (with L-histidine) and the active (with AMP) site are indicated with black arrows.

A crystallographic study by Cho *et al.*[13] revealed MtATP-PRT monomer as an elongated molecule composed of 10 α-helices and 15 β-strands situated across three continuous domains (Figure 6.2c). Domain I (residues 1-90, 175-184 and 194-211) consists of a central β-sheet (four parallel β-strands: β1, β3-5 and two anti-parallel strands: β2 and β11) surrounded by three α-helices (α1-3). Domain II (residues 91-174) has four parallel β-strands (β7-10), one anti-parallel β-strand (β6) and two α-helices (α4-5). Domain III (residues 212-284) is composed of one β-sheet (four anti-parallel β-stands: β12-15) and two α-helices (α9-10). The catalytic core of MtATP-PRT is located in a highly negatively charged cavity between domains I and II. Whereas, L-histidine is held at the allosteric site by interactions with the carboxyl group of aspartic acid at position 218 (Asp218), the hydroxyl group of threonine at position 238 (Thr238) and the backbone amide oxygen from alanine at position 273 (Ala273) in domain III.[13]

6.1.3 Proposed MtATP-PRT allosteric inhibition mechanisms with L-histidine

Cho *et al.*[13] determined crystal structures of apo MtATP-PRT at pH 6.5; and in complex with L-histidine and AMT (a competitive inhibitor to ATP) at pH 5.6. The authors suggested that MtATP-PRT is an active dimer that assembles into an inactive hexamer upon L-histidine binding (Figure 6.3a).[13] It was found that L-histidine binds ~30Å from the active site inducing a significant conformational change and supporting the allosteric inhibition model. The major conformational change in the L-histidine bound form is a significant twist of the domain III, where the allosteric site is located, with respect to domain I and II causing steric hindrance in the active site. Residues from two adjacent domain III were identified to be involved in binding and bringing three dimers together to deactivate the enzyme. These interactions include an ordered hydrogen bonding network with residues Asp218 and Ala273 from one subunit and residues Leu234, Glu235, Ser236, Thr238 and Leu253 of the second subunit. Six L-histidine molecules were found to bind to domain III clusters at both ends of three dimers, to stabilize the hexameric form. Binding of L-histidine reorients some of the key residues in the active site (Tyr116, Arg135, Asp154 and Arg160). Additionally, an increase in inhibition was noted upon binding of AMP, which establishes additional inter-subunit interactions that stabilize the L-histidine bound form.

The other inhibition mechanism was proposed by Pedreño *et al.*[12], and has been supported by gel filtration, steady-state and pre-steady-state kinetics, pH studies and ^{1}H NMR spectroscopy studies.[12] Gel filtration studies showed, that MtATP-PRT is present mostly in the hexameric form in solution, independent of protein sample concentration

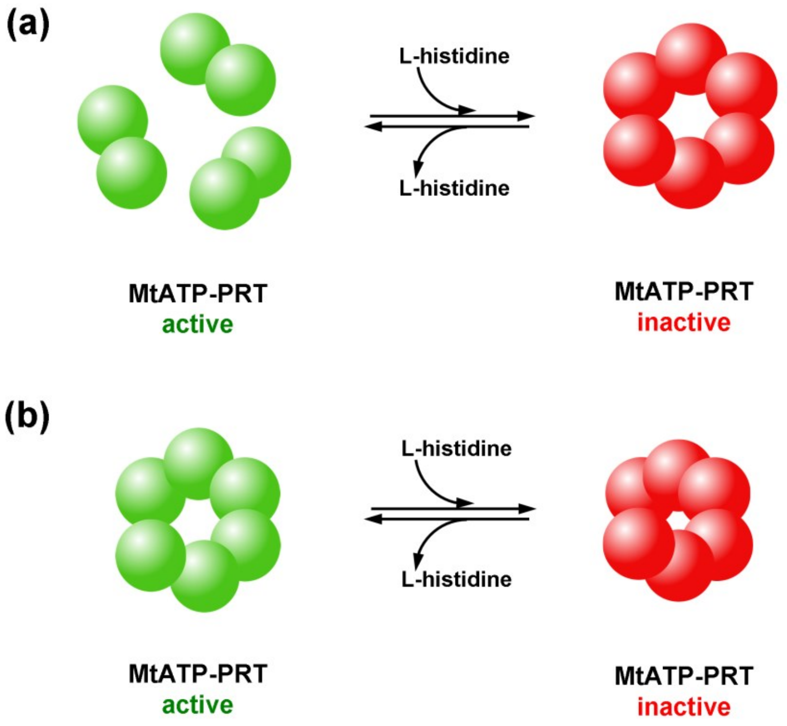

Figure 6.3 Proposed mechanisms of MtATP-PRT allosteric inhibition with L-histidine postulated by Cho *et al.*[13] (a) and Pedreño *et al.*[12] (b). Mechanism 1: (a) MtATP-PRT is an active dimer assembling to an inactive hexamer upon L-histidine binding; mechanism 2: (b) MtATP-PRT is a functional hexamer and conformational changes have to be invoked to explain the allosteric inhibition.

(within 0.1 – 10 mg/mL range), and both in the presence and absence of the L-histidine or ATP (Figure 6.3b). Similarly, no shift in the oligomeric state has been observed for the hexameric homologous enzyme from *S. enterica*.[21,22] These findings are in contrast with results reported by Cho *et al*.[13] Pedreño *et al*.[12] speculate that the observed differences are possibly due to different experimental conditions, and that lower pH values can lead to dissociation of MtATP-PRT into dimers as there is no evidence that the dimer represents a kinetically competent form of MtATP-PRT (the activity drastically drops below pH 8). Similar loss of activity below pH 8 have been reported for ATP-PRT from *C. glutamicum*.[23] A proposed mechanism (Figure 6.3b) envisions MtATP-PRT as a functional hexamer where conformational changes have to be invoked to explain the allosteric inhibition.

Steady-state kinetic studies indicated that MtATP-PRT has very low activity at neutral and acid pH (below pH 8).[12] Hence, the experiments were carried out at pH 8 and above. Although studies at high pH have no physiological importance as the cytoplasm will not reach pH 9, the results may hint at potential mechanism for preparing L-histidine analogues that bind tightly. Moreover, pre-steady-state analysis revealed that binding of ATP, the first substrate, is essential for inhibition by L-histidine.[12]

The ionic state of L-histidine was also found to influence the inhibition and binding to MtATP-PRT.[12] L-histidine exists in four ionic states across the pH range. Three half-equivalence points (pK_as) along the L-histidine titration curve (Figure 6.4) are observed at pH 1.82, pH 6.10, and pH 9.17. ^{1}H NMR studies showed that saturation transferred to L-histidine when bound to MtATP-PRT is influenced by pH and was found to be maximal at high pH. Neutral imidazole and deprotonated α-amino group favour L-histidine binding (~pH 9 and above). On the other hand, the pH dependence of inhibition is the opposite of what was observed for binding *i.e.* inhibition is weaker at higher pH values, as deprotonation of α-amino group decreases inhibition potency. Therefore, the ionic form of L-histidine that best inhibits MtATP-PRT most effectively is different from the form that binds the strongest; suggesting that the protonation state of the ligand is highly important in the transmission of the inhibitory signal from the allosteric site to the catalytic site.

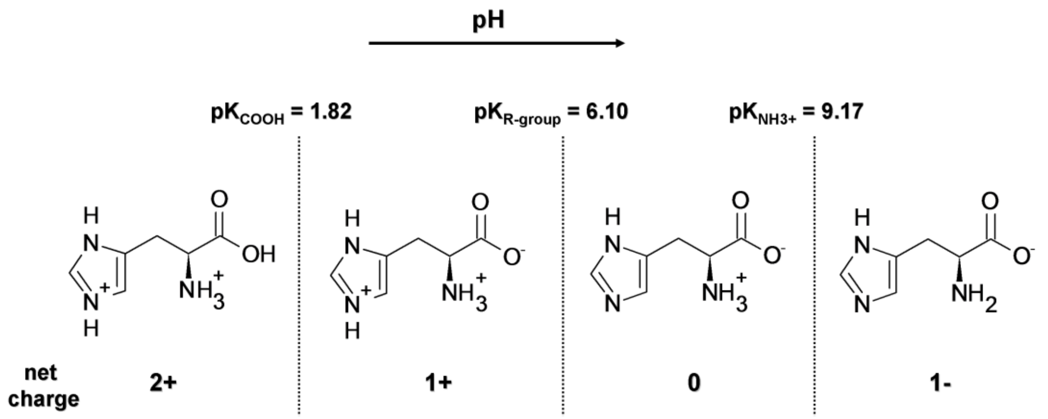

Figure 6.4 Ionic states of L-histidine. Below pH 1.8, all possible sites of L-histidine are protonated (net charge = 2+); between pH 1.8 and pH 6.1 carboxylic acid loses its proton making L-histidine singly charged (1+); between pH 6.1 and pH 9.2 L-histidine is a zwitterion with an overall charge of 0. Above pH 9.17 L-histidine loses the α-amino proton and now carries negative charge (1-). pK_{COOH} = 1.82; p$K_{R\text{-group}}$ = 6.10; pK_{NH3+} = 9.17. The pI value (where half of the species are in the zwitterion form) of L-histidine is 7.59.

To unambiguously and independently define the mechanism of inhibition other experimental methods that probe native conformations and conformational changes need to be employed. In this chapter, the structure of MtATP-PRT and mechanism of its feedback inhibition with L-histidine is explored. Native mass spectrometry (MS), ion mobility mass spectrometry (IM-MS) and analytical ultracentrifugation (AUC) are employed to study conformational changes induced by environmental changes (pH) and by binding of L-histidine. These structural changes are subsequently mapped with hydrogen deuterium exchange mass spectrometry (HDX-MS), and in agreement the with the reported x-ray crystallography data.[13]

6.2 Methodology

6.2.1 Protein expression and purification

The samples were provided by Dr. Luiz de Carvalho from the MRC National Institute of Medical Research, Mill Hill, London, UK. MtATP-PRT was expressed and purified by João Pedro Pisco and Gérald Larrouy-Maumus. The *rv2121c* (*hisG*) gene sequence from *M. tuberculosis* H37Rv was codon adapted to *E. coli*, and its nucleotide sequence was synthetically prepared and ligated into the pJ411 plasmid (DNA 2.0). DNA sequence was confirmed by sequencing. This construct contained a noncleavable N-terminal hexahistidine tag to facilitate purification. The N-terminal hexahistidine tag was shown not to affect the structure or activity of MtATP-PRT. During MtATP-PRT purification, all steps were performed at 4 °C. Frozen BL21(DE3)pLysS (pJ411::*hisG*) cells were thawed on ice, and lysed by sonication, in the presence of buffer A (20 mM triethanolamine (TEA) (pH 7.8), 300 mM NaCl, and 50 mM imidazole) containing lysozyme and complete EDTA-free protease inhibitor cocktail. Soluble protein was obtained by centrifugation at 25000g for 30 min. The soluble fraction was loaded into a 50 mL Ni-NTA column and the protein separated by a gradient using buffer B (20 mM TEA (pH 7.8), 300 mM NaCl, and 500 mM imidazole). Peak fractions were analyzed by SDS−PAGE. Fractions containing only MtATP-PRT were pooled together, concentrated, dialyzed in 20 mM TEA (pH 7.8), and stored in 50 % glycerol at −20 °C or, alternatively, stored at −80 °C after being flash-frozen in liquid nitrogen.

6.2.2 Sample preparation

On the day of analysis, buffer was exchanged to 100 mM ammonium acetate buffer (Fisher Scientific, Loughborough, UK) of specified pH, using micro Bio-Spin Chromatography columns (Micro Bio-Spin 6 Columns, Tris) following the instructions specified by the manufacturer. The desalting procedure was performed four to five times to achieve desired sample quality. pH of the buffer was adjusted with hydrochloric acid or ammonia supplied by VWR International Ltd (UK). Solution pH readings were taken using a pH meter (Jenway 3305). High purity water was obtained from an Arium 611 water purification unit (Sartorius, Göttingen, Germany) fitted with a 0.2 µm filter. L-histidine and 3-(2-thienyl)-L-alanine were obtained from Sigma-Aldrich. Charge reduction experiments were carried out by addition of 10% (v) triethylamine acetate buffer (TEAA) (Fluka, Steinheim, Switzerland) prior to MS analysis.

6.2.3 Native mass spectrometry

Mass spectra were recorded on a Q-TOF mass spectrometer (Ultima API US, Waters, Manchester, UK) modified for transmission of high mass molecules. MtATP-PRT samples were ionised using positive nESI as described in Chapter 2, section 2.1.2. The samples were prepared in 100 mM ammonium acetate buffer with pH values of 5, 6.8, 8, 9, and 10. The source voltages and pressures were tuned to enable maximum ion transmission; the source backing pressure was elevated to $\sim 8.5 \times 10^{-1}$ mBar. The sample cone voltage was varied from 40 to 200 V and the source temperature was kept at 30 °C to prevent sample aggregation in the glass capillary. Ligand binding experiments with L-histidine and 3-(2-thienyl)-L-alanine were performed at different ligand concentrations and at a range of incubation time points as described in the Results and Discussion. Other instrumental settings for the Ultima API US mass spectrometer are listed in Chapter 2, Table 2.1 External calibration of the spectra was achieved using solutions of cesium iodide (2 mg.mL^{-1} in 50 : 50 water:isopropanol). Data were acquired and processed with MassLynx software (Waters, Manchester, UK).

6.2.4 Ion mobility mass spectrometry: DT-IM-MS

The samples were ionised using positive nESI as described in Chapter 2, section 2.1.2. The IM-MS data were acquired on the MoQToF, quadrupole time-of-flight mass spectrometer, detailed in section 2.2.1.[24] The samples were prepared in 100 mM ammonium acetate buffer at pH 6.8 and pH 9.0. The capillary potential was held at 1.3 - 1.7 kV, the source temperature was set to 30 °C, and the cone voltage was set to 80 V. The injection energy used was between 33 and 35 V. Other instrumental settings for the MoQToF IM mass spectrometer are listed in Chapter 2, Table 2.3. The drift cell was filled with helium gas at a pressure of 3.5 – 3.6 Torr at temperature of 300 - 302 ± 0.5 K. The electric potential across the cell was varied from 60 to 20 V, with measurements taken at six different drift voltages. The rotationally-averaged collision cross-sections (CCS) were determined from a plot of arrival time versus P / T and the CCSD were determined as described in Chapter 2, section 2.2.1.4.

6.2.5 Ion mobility mass spectrometry: TWIMS-MS

The IM-MS data were acquired on the Synapt G2S HDMS (Waters, Manchester, UK) at the Waters Corporation, Floats Road, Manchester, UK. In-house made nano-capillaries were used as described previously. The samples were prepared in 100 mM ammonium acetate buffer at pH 6.8 and pH 9.0. Gentle conditions were applied to preserve the native-like structure: capillary voltage 1.6 kV, sampling cone 99 V, source temperature 20 °C, trap collision energy 5.6 V, and transfer collision energy 2 V. The pressure of the backing region was 8.3 mbar. For IM, the helium cell and the IMS gas flows were 180 and 90 mL/min, respectively, the IMS wave velocity was 617 m/s, and the IMS wave height was 40 V. Nitrogen was the carrier gas. Data were acquired and processed with MassLynx software (Waters, Manchester, UK).

6.2.6 Determination of theoretical CCS

The theoretical CCS calculations were carried out by Dr Massimiliano Porrini from the Institute Européen de Chimie et Biologie (IECB) in Pessac, France. The input coordinates files were those taken from the crystallographic structures, PDB identifiers 1NH7 and 1NH8 for apo MtATP-PRT and Mt-ATP-PRT – L-histidine complex, respectively. After adding hydrogen atoms, the x-ray crystal structures were minimized *in vacuo* with the sander module of Amber11[25], implementing a radial cut-off of 999 Å and Amber99SB-ILDN force field[26]. The rotationally averaged CCS were calculated with the trajectory method of MOBCAL code[27] appropriately modified to handle large systems such as MtATP-PRT studied here.

6.2.7 Collision-induced-dissociation mass spectrometry (CID-MS)

The IM-MS data were acquired on the Synapt G2 HDMS (Waters, Manchester, UK) at the Manchester Institute of Biotechnology, The University of Manchester, UK. The samples were prepared in 100 mM ammonium acetate buffer at pH 6.8 in the presence and the absence of L-histidine and ionised as described previously. Gentle source conditions were applied to preserve the native-like structure: capillary voltage 1.6 kV, sampling cone 99 V, source temperature 20 °C. The pressure of the backing region was 7.5 mbar. For the IM, the helium cell and the IMS gas flows were 180 and 90 mL/min, respectively, the IMS wave velocity was 550 m/s, and the IMS wave height was 40 V. Nitrogen was the carrier gas. CID activation was induced by elevating the trap collision energy. MS and IM-MS data were acquired at several discrete trap collision energy values of 10 V, 30 V, 50 V, 80 V, 100 V, 120 V, 150 V and 180 V. Data were acquired and processed using MassLynx software (Waters, Manchester, UK).

6.2.8 Hydrogen deuterium exchange mass spectrometry (HDX-MS)

HDX-MS experimental set up and data analyses were carried out with help of Dr Rebecca J. Burnley at UCB Pharma, Slough, UK. HDX-MS analysis was achieved using a Waters HDX module with nanoAcquity UPLC and Synapt G2 mass spectrometer. Sample handling steps were performed by a LEAP-PAL robotics system. 30 μM protein solutions were diluted 20 fold into 10 mM phosphate in either H_2O or D_2O, pH/pD 7, and the mixture incubated at 20 °C for 0 minutes (H_2O), or 1, 10, 30 or 120 minutes (D_2O), before the quench step. HDX quenching was achieved by mixing the reaction solution 1:1 with cooled 3.4 M Gdn-HCl, 500 mM TCEP, 200 mM phosphate (pH 2.5, 0 °C). 37.5 pmol was injected into the HDX module (0 °C), and washed over the pepsin column (Applied Biosystems, 3 cm Porozyme immobilised pepsin column) with 0.1% HCOOH in H_2O, pH 2.5, at 200 $\mu L.min^{-1}$. Resulting peptides were trapped on a VanGuard C18 trap column. Peptide separation was achieved on a C18 column (BEH C18, 100 × 1.0 mm, 1.7 µM) with the following gradient: 0 min: 8% B, 7 min: 32% B, 8 min: 85% B (mobile phase A: 0.1% HCOOH in H_2O, pH 2.5; mobile phase B: 0.1% HCOOH in MeCN). The mass spectrometer was operated in ToF only mode, with MS^e data acquisition (trap collision energy ramp 14-35V). Calibration was achieved from the MS/MS spectrum of GluFib peptide. PLGS v2.5 and DynamX Data Analysis v2.0 software (Waters Corporation, Manchester, UK) were used for data analysis. The deuterium update protein maps were created in the PyMOL Molecular Graphics System, V1.5.0.4 (Schrödinger, LLC., Portland, OR, USA).

6.2.9 Analytical ultracentrifugation

Sedimentation velocity analysis were carried out by Dr. Thomas Jowitt at the Biomolecular Analysis Core Facility, Faculty of Life Sciences, the University of Manchester, UK. His-tagged MtATP-PRT was purified and buffer exchanged by running peak fractions twice on a Superdex200 10/300 gel filtration column attached to a multi-angle laser light scattering system (MALLS) in ammonium acetate buffer at either pH 6.8 or pH 9.0. The peak fractions for each pH separation corresponding to hexameric protein were pooled and the concentration assayed using a spectrometer reading at 280 nm and a molar extinction coefficient of 20190 M^{-1} cm^{-1} for monomeric protein. The final concentrations were ~40 µM (hexamer) and to this 12-fold molar excess L-histidine from a 50 mM stock in HCl was added to one 0.5 ml fraction for both pH 6.8 and pH 9.0. Samples were loaded (400 µl) into 2-sector sedimentation velocity cells with sapphire windows and loaded into a XL-I ultracentrifuge (Beckman). Sedimentation was monitored every 1 minute at 45,000 rpm, 20 °C using interference optics and data analysed using the direct boundary modelling software Sedfit and represented using GUSSI.

6.3 Results and Discussion

6.3.1 MtATP-PRT exists mainly in the hexameric form under physiological conditions

Changes in pH which can accompany process undergoing the living cells, may alter protein structure and hence its activity. Firstly, the oligomeric state of apo MtATP-PRT has been investigated as a function of buffer pH. nESI-MS of 20 µM MtATP-PRT (based on hexamer concentration) in 100 mM ammonium acetate at pH 5, pH 6.8, pH 8, pH 9 and pH 10 acquired on the Ultima API US Q-ToF mass spectrometer are shown in Figure 6.5. Peaks corresponding to the hexameric form of MtATP-PRT are observed in the ~6500 – 7500 *m/z* range; with the charge state envelope ranging from 25+ to 29+ charge state, centred at the 27+ charge state. At pH 6.8, around *m/z*

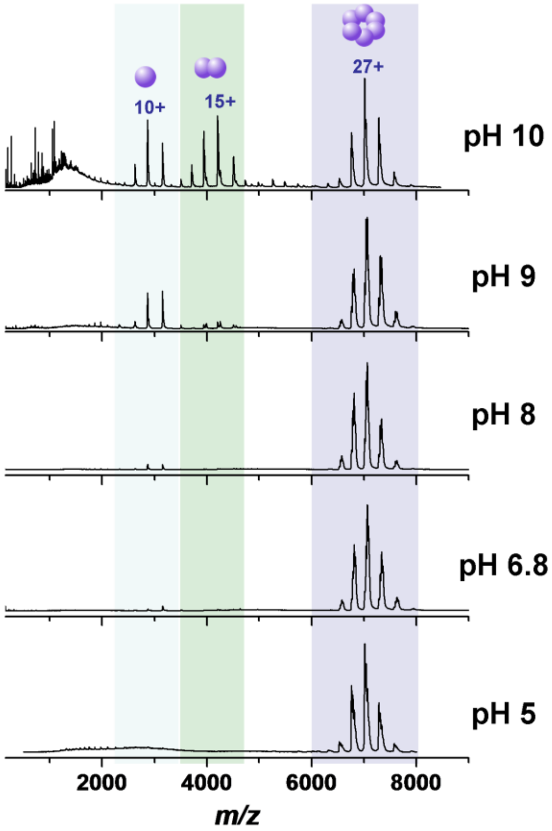

Figure 6.5 nESI mass spectra of 20 µM MtATP-PRT (hexamer concentration) in 100 mM ammonium acetate at pH 5, pH 6.8, pH 8, pH 9 and pH 10 (from bottom to top) acquired on Ultima API US Q-ToF mass spectrometer, showing the effect of pH on the oligomeric state of the enzyme.

3000 a minor amount of monomeric MtATP-PRT is present. The population of monomeric species increases along with the pH and becomes more prominent at pH 10 (centred on the 10+ charge state). Additionally at pH 8, dimeric MtATP-PRT is detectable (~3900 – 4600 *m/z*, centred at 15+ charge state) and similarly increases in intensity with increasing basicity of the buffer. Under deprotonated conditions *i.e.* high pH, carboxyl termini may lose their interaction with an adjacent subunit leading to conformational changes or dissociation into subunits. These MS experiments indicate that MtATP-PRT is present in solution mainly in a hexameric form in the absence of any ligands, in agreement with results reported by Pedreño *et al.*[12]. Under highly basic conditions (around pH 9 and above), the presence of monomeric and dimeric MtATP-PRT is noted.

For mass determination experiments, high cone voltages (268 V) were applied. The experimentally determined mass of the MtATP-PRT monomer of 31516 ± 11 Da, matches closely the theoretical average mass determined for MtATP-PRT monomer (31515.6 Da). The experimentally determined mass of the MtATP-PRT hexamer is 189374 ± 23 Da, which is slightly higher than the theoretical mass (189090 Da). This difference is attributed to retention of residual solvent and salt despite the application of high source acceleration voltages.

6.3.2 Insights into ligand binding stoichiometry from native MS experiments

6.3.2.1 Stoichiometry of L-histidine binding

X-ray crystallography experiments indicated up to 6 L-histidine molecules can bind to one MtATP-PRT hexamer.[13] 12 equivalents of L-histidine were added to 1 equivalent of MtATP-PRT hexamer in 100 mM ammonium acetate at pH 6.8 and incubated for 1 hour at room temperature (Figure 6.6). The mass of MtATP-PRT hexamer (189 kDa) exceeds by over 1000-fold the mass of L-histidine (155.15 Da). This large discrepancy in mass precludes the resolution of bound from unbound species with the instrumentation used here. Despite this, upon addition of L-histidine and application of gentle source conditions, a shift in the peak centre of the protein complex peaks is observed. Mass spectra acquired at a cone voltage of 115 V in the presence of the ligand, display a mass shift of ~1.2 kDa, corresponding to binding of 8 L-histidine molecules, a number greater than the one determined based on the crystallography data, implying super-stoichiometric and perhaps non-specific binding (Figure 6.6a). Nevertheless, under gentle dissolvation conditions which allow for preservation of non-covalent interactions and retention of the ligand, a significant amount of residual solvent is still present and the binding stoichiometry cannot be exactly determined. Even at higher cone voltages which aid the desolvation process, a significant amount of solvent is present what could bias the stoichiometry of binding determination. Efforts to shift charge state distribution (CSD) to a higher *m/z* range by addition of charge reducing agents such as TEAA and EDDA[28], did not improve resolution sufficiently to determine the binding stoichiometry. Additionally, elevated acceleration voltages (up to 268 V) led to in-source ligand dissociation. As shown in Figure 6.6b, at high cone voltages, a significant shift in the charge state envelope is observed from 27+ charge state (no ligand) to 24+ charge state (1H :12L) at CV = 268 V. This shift in the CSD was found to be pH dependent and it

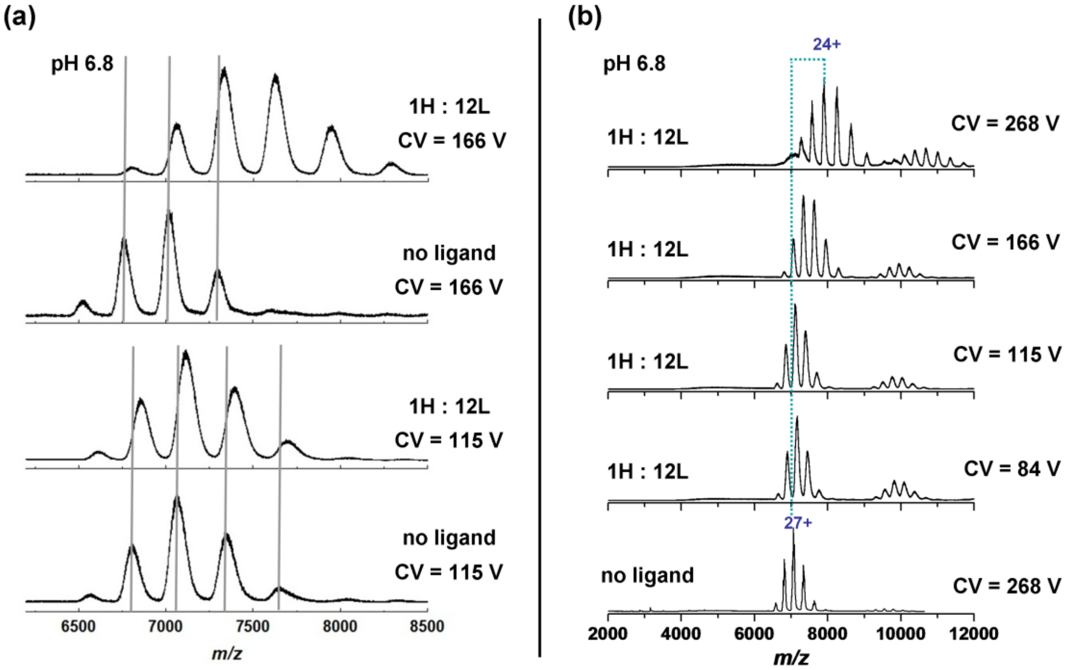

Figure 6.6 (a) Mass spectra of MtATP-PRT in presence and in absence of 12 equivalents of L-histidine (1H:12L) in 100 mM ammonium acetate at pH 6.8 acquired on Ultima API US Q-ToF mass spectrometer at 115 V and 166 V cone voltage (CV), showing the mass shift associated with ligand binding. Moreover, a shift in charge state envelope is noted at higher CV. Grey lines are used to help visualize the mass shift (based on apex of 'no ligand' peaks). (b) Dissociation of L-histidine upon increased cone voltage; 1 equivalent of MtATP-PRT incubated with 12 equivalents of L-histidine in 100 mM ammonium acetate pH 6.8 acquired at various cone voltages ranging from 84 – 268 V on Ultima API US Q-ToF mass spectrometer.

can be postulated that as the ligand dissociates from the complex, it takes the charge with it, reducing the charge of the protein as will be discussed later.

Binding of a given ligand to its target can be influenced by the presence of other ligands already bound to the molecule. The Hill number (nH) provides a way to quantify the degree of cooperativity of ligand binding.[29,30] If nH is greater than one, this is termed positive cooperative binding, where the binding of the first ligand then increases the affinity of the substrate for other ligands. On the other hand, nH values below one indicate negative cooperative binding, where the binding of a given ligand then decreases the affinity of subsequent ligands. L-histidine was found to inhibit MtATP-PRT with a nH of 1.5.[12] This suggests that all six active sites could be inhibited with only four L-histidine molecules.[31] Nevertheless, MtATP-PRT can still accommodate six ligands in the six binding sites. In some cases were partial occupancy is detected different binding affinities can also be observed, therefore, it is possible that the first four L-histidine molecules have different affinity from the final two.[31]

A titration experiment was performed, where 1-40 equivalents of L-histidine were added to one equivalent of MtATP-PRT hexamer in 100 mM ammonium acetate at pH 6.8. High acceleration voltage (CV = 268 V) was applied during acquisition of all mass spectra shown in Figure 6.7. As mentioned earlier, in-source dissociation leads to a charge state shift attributed to the loss of charge from the protein complex as the ligand departs. This observation was exploited here to obtain insights into ligand binding affinities. Interestingly, the amount of ligand present in the sample influences the extent of CSD shift observed. No differences in mass between apo MtATP-PRT and those containing L-histidine were noted, suggesting that all L-histidine molecules have dissociated during the desolvation process at high acceleration voltage. For the MtATP-PRT samples containing 1-4 L-histidine equivalents, only a small shift in the CSD (from being centered at 27+ to 26+) is noted and all four mass spectra display the same charge state profiles. As the amount of L-histidine is increased to 5-6 equivalents, protein complex is stripped of an additional charge resulting in CSD shift from central 27+ to 25+ charge state. When more L-histidine is titrated in, 12 and 40 equivalents, a further shift in the CSD is observed to centre on the 24+ and 23+ charge states, respectively.

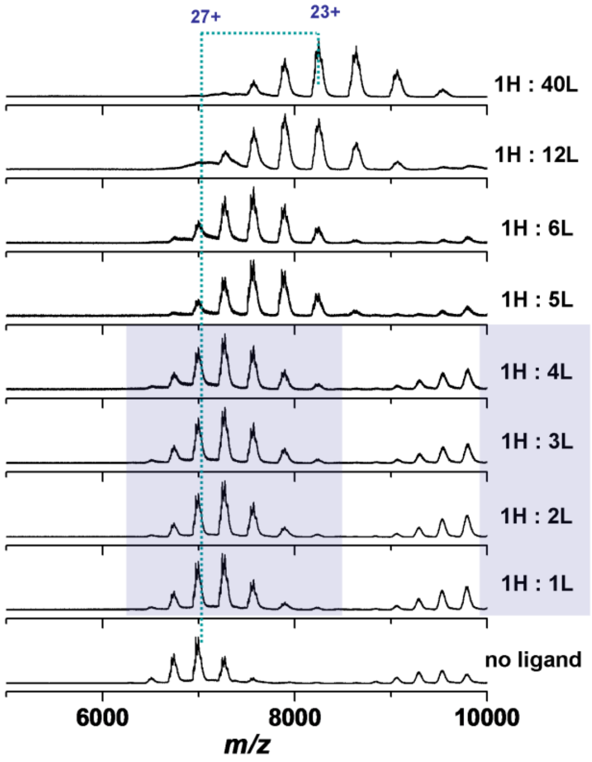

Figure 6.7 Titration of L-histidine into MtATP-PRT at 1-40 L-histidine equivalents to 1 MtATP-PRT hexamer in 100 mM ammonium acetate pH 6.8 acquired at a constant cone voltage (268 V) on Ultima API US Q-ToF mass spectrometer. A greater shift in the CSD profiles is observed along with increasing concentration of L-histidine.

Differences in CSD profiles upon ligand dissociation may be deriving from the strength of the non-covalent interactions and charge transfer during desolvation. As reported earlier, the ionic form of L-histidine that binds to MtATP-PRT is different from the form that inhibits it.[12] Kinetic studies suggest that the first four ligands could inhibit all six active sites inducing conformational change.[12,31] A possible explanation for the observed differences in CSD may be the involvement of the first four ligands bound (and in particular with the protonated forms) facilitating inhibition by inducing the subsequent conformational change as opposed to the remaining two which bind, however may not necessarily be crucial for the inhibition. Upon dissociation of the fifth and sixth ligand, more charge is taken from the protein complex during desolvation suggesting that less external energy is required for the dissociation of the ligand along with extra protons. The presence of excess L-histidine causes additional charge reduction of MtATP-PRT and may be associated with non-specific binding.

6.3.2.2 The effect of buffer pH and incubation time on L-histidine binding

The ionic state of L-histidine has been found to influence the inhibition of as well as its binding to MtATP-PRT.[12] The effect of the buffer pH and incubation time on binding to MtATP-PRT as well as charge stripping upon ligand dissociation have been investigated. 20 μM MtATP-PRT was incubated for 30 and 240 minutes at room temperature with 12 L-histidine equivalents at pH 6.8 (a), pH 8 (b), pH 9 (c) and pH 10 (d). nESI-MS acquired at high acceleration voltage (CV = 268 V) on the Ultima API US Q-ToF mass spectrometer are shown in Figure 6.8.

L-histidine exists in four ionic states across the pH range (Figure 6.4). Three half-equivalence points along the L-histidine titration curve (Figure 6.4) are situated at pH 1.82, pH 6.10, and pH 9.17. Between pH 6.10 and pH 9.17, L-histidine carries an average net charge of 0. Binding experiments carried out within this ionic range *i.e.* at pH 6.8 (a) and pH 8 (b), show a reduction in the CSD by 3 charge states upon L-histidine dissociation represented by a shift from the central charge state located at 27+ to 24+, this suggests that the ligand is dissociating with a bound proton. As the basicity of the buffer is increased to pH 9 (c) this charge stripping is reduced. Even though under these conditions, L-histidine is still within the 0 net charge bracket, it is now less prone to extract additional positive charge from the protein complex upon dissociation, which could be explained by a conformational change at the binding site or by the binding site no longer containing a labile hydrogen. As a result less extensive charge stripping, a CSD shift from central 27+ to 25+ charge state, is observed. Upon further increase of buffer pH to pH 10 (d), L-histidine crosses the final half-equivalence point and acquires average net charge of -1. Here, the CSD shift becomes even less evident, shifting from central 27+ to 26+ charge state and the average charge of MtATP-PRT post L-histidine dissociation is reduced by one CS.

It has been reported that the form of L-histidine that best inhibits MtATP-PRT is different from the form that binds best; suggesting that the ionic state of the ligand is highly responsible for the transmission of the inhibitory signal from the allosteric site to the active site.[12] This presented MS data also shows a dependence of the buffer pH on the amount of charge L-histidine can accommodate and remove from the protein complex upon in-source dissociation. Under basic conditions, a reduction of the protein

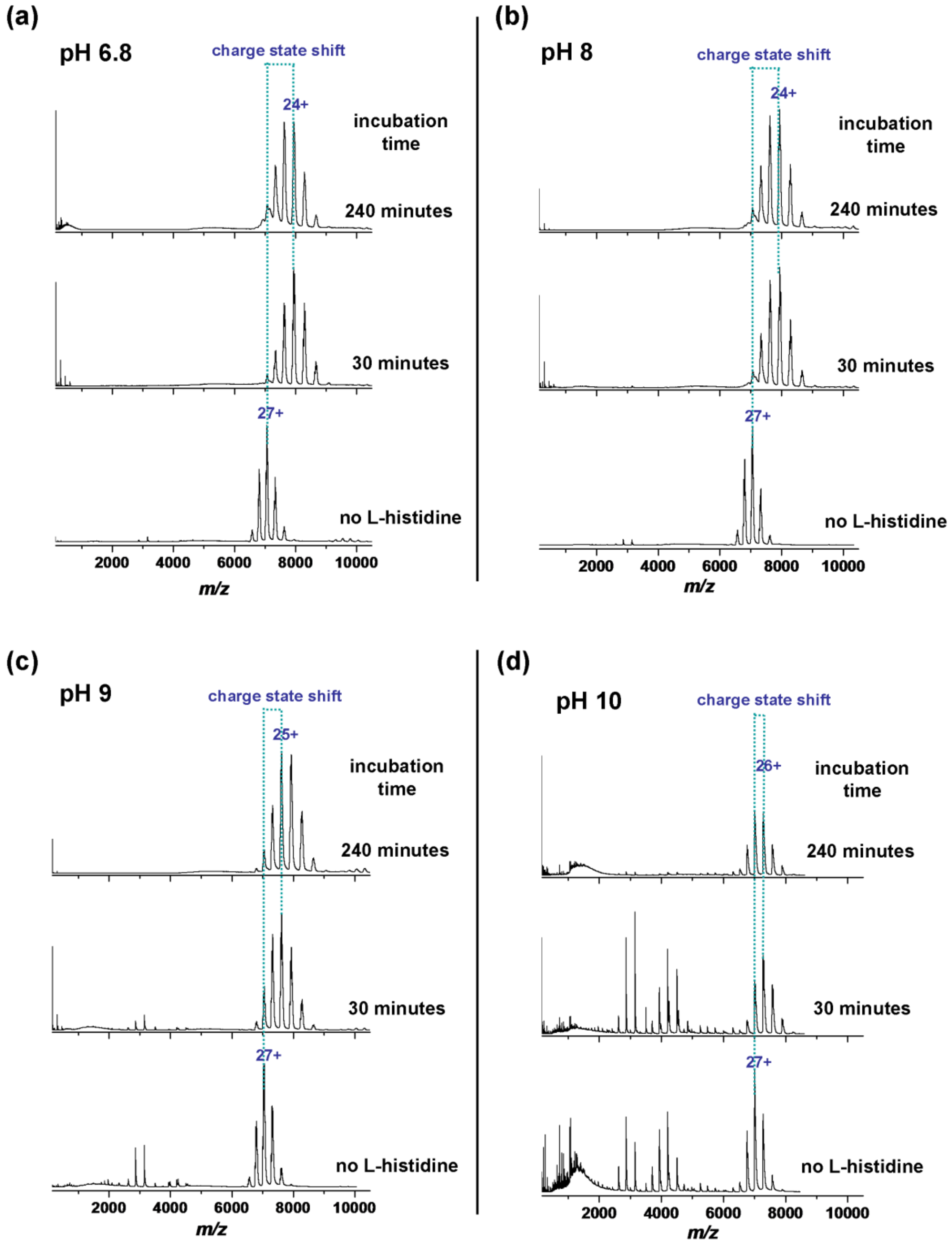

Figure 6.8 **nESI mass spectra of 20 μM apo MtATP-PRT (hexamer concentration) and MtATP-PRT incubated with 12 equivalents of L-histidine for 30 minutes and 240 minutes in 100 mM ammonium acetate at (a) pH 6.8, (b) pH 8, (c) pH 9 and (d) pH 10, acquired on Ultima API US Q-ToF mass spectrometer (at cone voltage 268 V).**

charge state post ligand dissociation is less apparent in comparison to the shift observed under more neutral conditions. It could be speculated that α-amino group or/and imidazole nitrogen could be responsible for sequestering the charge from the MtATP-PRT surface. Titration experiments (Figure 6.7) had shown that it is mainly the L-histidine molecules which bind non-specifically, that are responsible for the majority of charge reduction of MtATP-PRT upon dissociation. At pH 6.8 and pH 8, the population of L-histidine with neutral imidazole and deprotonated amino group would be more predisposed to accept extra charge, which would result in a greater CSD shift as opposed to the same scenario at higher pH. Furthermore, it is important to keep in mind that the pH in the desolvating droplet may be different from that in bulk solution, and the change is affected by the solvent composition and initial droplet pH as shown by Zhou *et al.*.[32]

As shown in the previous section, the pH of the buffer solution has an impact on the oligomeric state of MtATP-PRT. MtATP-PRT was mainly present in a hexameric form under buffered conditions in absence of any ligands. Under basic conditions (around pH 9 and above), the presence of monomeric and dimeric MtATP-PRT species was noted. Addition of L-histidine reduces the amount of monomeric and dimeric species after 240 minutes of incubation at room temperature (Figure 6.8c and d). At pH 9, a significant amount of MtATP-PRT monomer and a marginal amount of dimer are present (bottom spectrum in Figure 6.8c). After 30 minutes of incubation with 12 equivalents of L-histidine, the intensity of both lower order species decreases and are not detectable after prolonged incubation period of 240 minutes. At pH 10, an even greater amount of monomeric and dimeric MtATP-PRT is observed. Here, 30 minute incubation with L-histidine does not reduce population of either of the species. A longer incubation period is required to achieve a similar effect and a decrease of these low order oligomeric forms is observed only after 240 minutes.

According to Cho *et al.* [13], MtATP-PRT is an active dimer which assembles into an inactive hexamer upon L-histidine binding which could support the observations at high pH reported above. However, the experiments reported by Cho *et al.* were carried out at pH 6.5 (apo) and pH 5.6 (with L-histidine and AMT), conditions under which MtATP-PRT is believed to be kinetically inactive.[12] Nevertheless, L-histidine appears to have a stabilizing effect on MtATP-PRT at high pH, regardless whether it only binds to and does not inhibit the enzyme.

6.3.2.3 MtATP-PRT binding with 3-(2-thienyl)-L-alanine

L-alanine based ligand, 3-(2-thienyl)-L-alanine was found to bind to MtATP-PRT however, not to inhibit its activity.[31] 20 µM MtATP-PRT was incubated with 12 equivalents of 3-(2-thienyl)-L-alanine at pH 6.8 for 30 and 240 minutes. nESI-MS acquired at high acceleration voltage (CV = 268 V) on the Ultima API US Q-ToF mass spectrometer are shown in Figure 6.9. Similarly as for L-histidine, due to over 1000-fold mass difference between the ligand (171.22 Da) and MtATP-PRT hexamer, again it is not possible to resolve bound and unbound species. Application of high acceleration voltage induces in-source dissociation. Here in contrast to L-histidine, charge stripping and reduction of protein charge state upon ligand dissociation is not present. A minor shift towards higher charge states (centered at 28+) is observed instead. Differences in

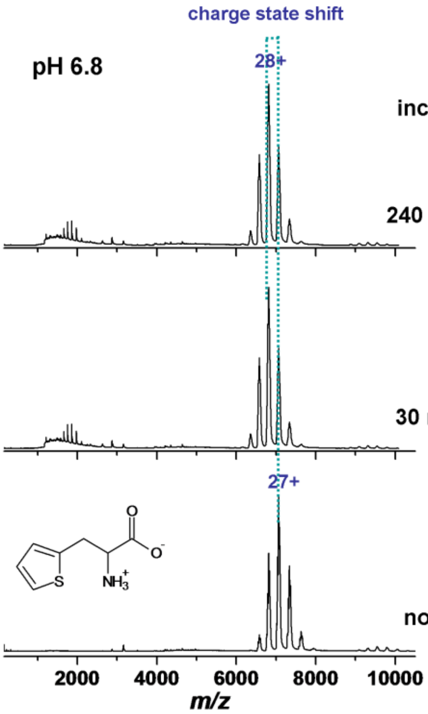

Figure 6.9 nESI mass spectra of 20 µM apo MtATP-PRT (hexamer concentration, bottom spectrum) and MtATP-PRT incubated with 12 equivalents of 3-(2-thienyl)-L-alanine for 30 minutes and 240 minutes in 100 mM ammonium acetate at pH 6.8, acquired on Ultima API US Q-ToF mass spectrometer (CV = 268 V).

the dissociation behavior of the two ligands investigated may be arising from their structural and composition differences. The imidazole nitrogen, suggested to be responsible for charge stripping apparent in experiments with L-histidine by sequesting surface charge upon dissociation is absent in 3-(2-thienyl)-L-alanine. Hence, these results hint towards the imidazole nitrogen to be implicated more in the charge reduction than the α-amino group as suggested above.

6.3.3 Probing conformational changes induced by ligand binding and environmental changes (pH) with IM-MS

Cho and colleagues reported on a large shift of MtATP-PRT domain III with respect to domains I and II in the dimeric form compared with the hexameric MtATP-PRT formed in presence of L-histidine and AMP.[13] Although the dimeric form, observed by Cho *et al.* is not present under experimental conditions applied here (lower pH), the domain shift could still take place, generating an alternative hexamer which could be inhibited. Gel filtration studies by Pedreño *et al.*[12] showed MtATP-PRT to be present mostly in the hexameric form which undergoes subtle conformational changes upon L-histidine addition. Here, IM-MS, both DT-IM-MS and TWIMS-MS, is employed to probe native conformations and conformational changes of MtATP-PRT.

6.3.3.1 Determination of CCS: linear DT-IM-MS

nESI-IM-MS of 30 μM MtATP-PRT and MtATP-PRT in presence of 12 equivalents of L-histidine in 100 mM ammonium acetate at pH 6.8 were acquired on the MoQ-ToF ion mobility mass spectrometer. Source conditions were optimized and low acceleration voltages were applied to preserve protein native-like structure and non-covalent interactions. Arrival time distributions (ATD) were recorded following mobility separation at 300 K and converted into CCSD as described in Chapter 2 section 2.2.1.4. Figure 6.10 shows the CCSD of 27+, 28+ and 29+ charge states of apo MtATP-PRT and MtATP-PRT with L-histidine bound, purple dotted lines are used to help visualize the subtle changes in the CCSD. In the presence of L-histidine, MtATP-PRT CCS become somewhat smaller, suggesting conformational tightening upon ligand binding which may

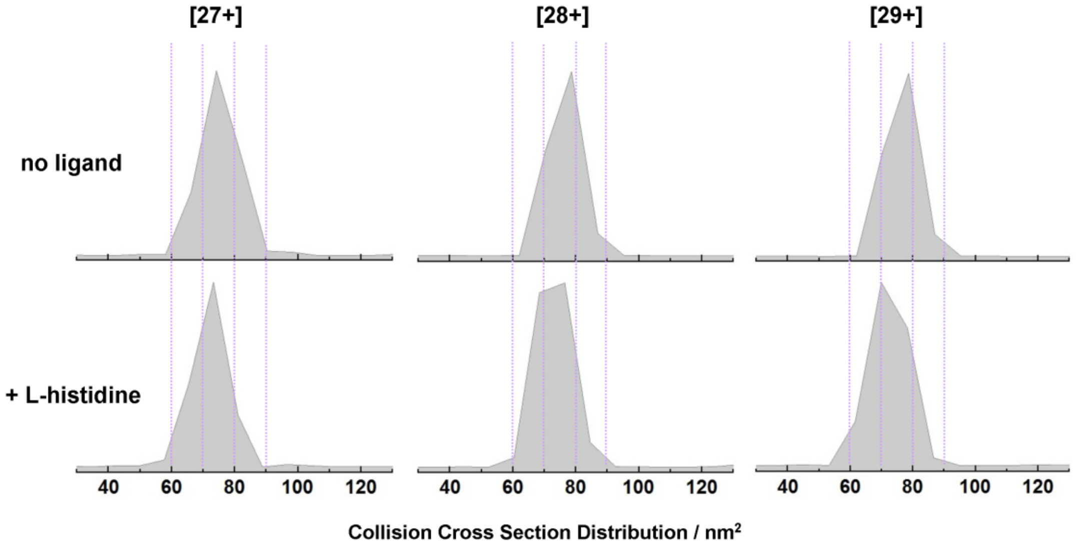

Figure 6.10 Collision cross section distributions (CCSD) of 27+, 28+ and 29+ charge states of 30 μM MtATP-PRT in presence (bottom) and in absence (top) of L-histidine in 100 mM ammonium acetate at pH 6.8, acquired on the MoQToF instrument at DV = 35 V. Purple lines are added to help visualize the subtle changes in CCSD profiles.

be associated with a shift of domain III with respect to domains I and II. No AMP was used in these experiments suggesting that its presence might not be necessary for the allosteric inhibition to take place. Changes in the median CCS from 75.2 nm^2 to 73.6 nm^2, from 76.6 nm^2 to 73.5 nm^2, and 76.4 nm^2 to 72.4 nm^2 were determined upon L-histidine binding for 27+, 28+ and 29+ charge states, respectively. The reported CCS values are based on one experimental repeat. New batch of samples was used to perform replicate experiments; however, these subtle changes in the CCS were no longer observed. Despite many efforts in sample purification and instrumental condition optimization, as will be described later, the results obtained from the first experiment could not be reproduced. Repeat experiments will be performed once the protocol has been optimized. Additionally, dependence of the protein conformation on pH and the effect of ATP on L-histidine binding will be investigated to provide insights into the allosteric inhibition mechanism of MtATP-PRT.

6.3.3.2 Tracing ligand binding and pH dependent conformations: TWIMS-MS

Enzyme activity and structure is dependent on the environmental factors such as temperature or pH of the buffer. Conformational changes of MtATP-PRT due to ligand binding as well as changes due to buffer pH were explored with TWIMS-MS. nESI-IM-MS of 20 μM MtATP-PRT in presence and in absence of L-histidine in 100 mM

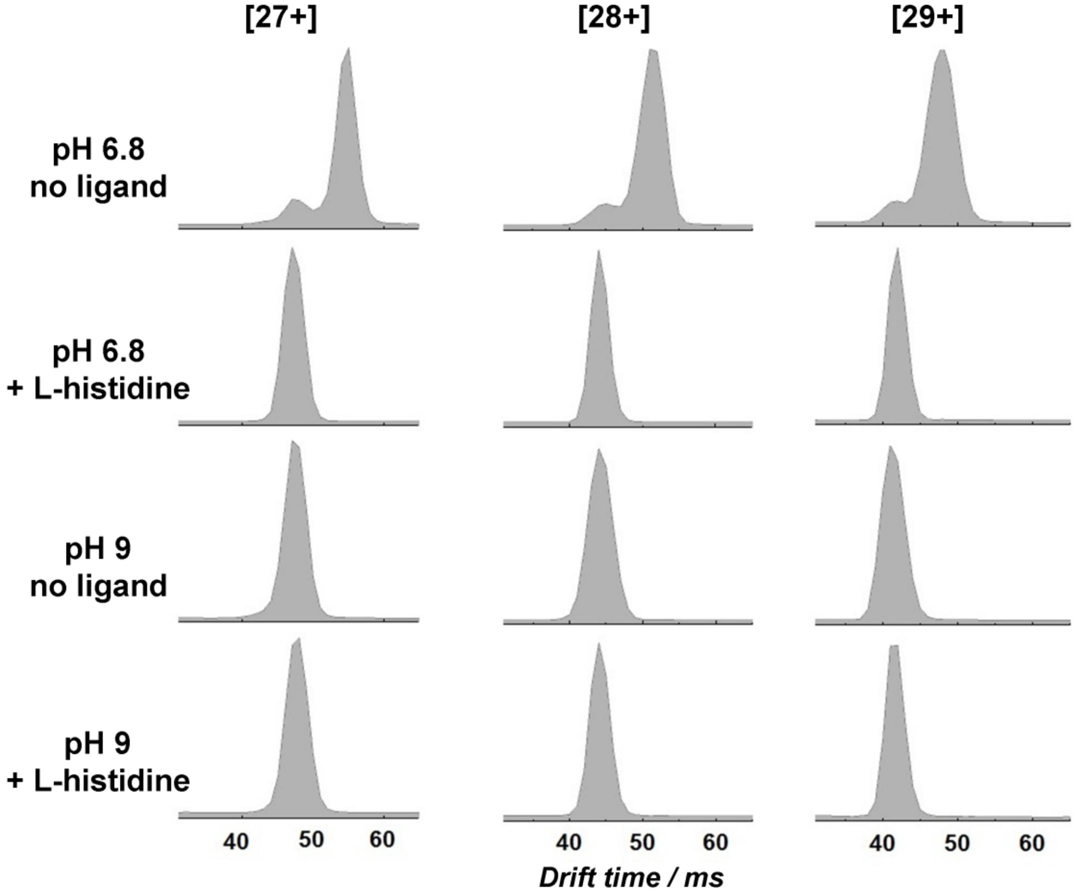

Figure 6.11 Drift time distributions of 27+, 28+ and 29+ charge states of MtATP-PRT in presence and in absence of L-histidine in 100 mM ammonium acetate at pH 6.8 and at pH 9, acquired on the SynapthG2S instrument at wave height of 40 V and wave velocity of 617 m/s.

ammonium acetate at pH 6.8 and pH 9 were acquired on SynaptG2S instrument at Waters Corporation, Manchester. Arrival time distributions for 27+, 28+ and 29+ charge states of apo MtATP-PRT and MtATP-PRT with L-histidine at pH 6.8 and at pH 9 are shown in Figure 6.11. Apo MtATP-PRT at pH 6.8 presents over two conformational families in the ion mobility space. The relaxed conformation with longer drift time (28+ charge state centred at 51.2 ms) is significantly higher in abundance when compared to the tense conformation observed at shorter drift time (28+ charge state centred at 44.1 ms) which constitutes to about 12 % of the total ion population for each charge state. Upon addition of 12 equivalents of L-histidine, the relaxed form of MtATP-PRT is no longed observed. The total ion population shifts to shortened drift times and matches (28+ charge state centred at 44.2 ms) the drift time profile of the tense conformation of apo MtATP-PRT at pH 6.8. This conformational tightening upon ligand binding is in agreement with results reported here earlier with DT-IM-MS and those found in the literature based on gel filtration and x-ray crystallography studies.[12,13] Interestingly, under the same instrumental conditions, apo MtATP-PRT at pH 9 appears to be already in the more compact (tensed) form observed at shorter drift time (28+ charge state centred at 44.0 ms) and matches drift time of the L-histidine bound MtATP-PRT at pH 6.8. Upon addition of L-histidine, the drift time remains constant (28+ charge state centred at 44.1 ms), suggesting absence of the conformational change. This trend is observed across all charge states.

According to the kinetic studies, the enzyme is in its active form at pH 9.[12] The lack of conformational change under these conditions could be arising for the lack of inhibition. Earlier it was proposed that activation or lack of inhibition is dependent on the correct binding and position of the six phosphates from both substrates.[31] However, these substrates are not present in the experiments reported here, revealing that the tightening/activation is independent of substrates and is influenced by the protonation state of the protein and the ligand. Nevertheless, the experiments should be performed in presence of substrates. Attempts to repeat experiments reported here were also not successful, as will be described later, MtATP-PRT appears in the more compact form independent of pH or ligand presence.

6.3.3.3 Conformational differences derived from the x-ray crystal structures: theoretical CCS

The conformational change of MtATP-PRT was confirmed by the theoretical CCS calculated from the available x-ray crystal structures. The input coordinates files were taken from the crystallographic structures, PDB identifiers 1NH7 and 1NH8 for apo MtATP-PRT and Mt-ATP-PRT:L-histidine:AMT complex, respectively. Dimeric form of apo MtATP-PRT available in the PDB was assembled into the hexameric form using the online ‘Protein interfaces, surfaces and assemblies’ service PISA at the European Bioinformatics Institute website.[19,20] After adding hydrogen atoms, the x-ray structures were minimized *in vacuo*. The rotationally averaged CCS were calculated with the trajectory method (TJM) of MOBCAL code[27] appropriately modified to handle large systems such as MtATP-PRT.

The theoretical CCS of hexameric apo MtATP-PRT and Mt-ATP-PRT:L-histidine:AMT complex were found to be 94.0 nm^2 and 90.7 nm^2, respectively. The experimentally determined CCS are significantly smaller than the theoretical CCS by about 23 %. Although, MtATP-PRT is not as flexible as the immunoglobulin molecules presented in Chapter 3, one could still anticipate structural compaction to a certain degree if the x-ray structures were subjected to gas phase molecular dynamics (MD). While, the theoretical CCS values and the experimentally derived CCS are not in close agreement, the trends displayed are similar. The theoretical CCS of apo MtATP-PRT is larger than CCS of inhibited MtATP-PRT by 3.3 nm^2. Similarly, the average change in CCS across charge states as determined with DT-IM-MS measurements (Figure 6.10) was 2.9 nm^2. Nevertheless, it would be worthwhile to subject MtATP-PRT to gas phase MD in order to determine whether its structure undergoes gas phase contraction.

6.3.3.4 Obstacles encountered, proposed solutions and further directions

New batches of sample were used to perform replicate IM-MS experiments; however, no changes in the CCSD upon ligand binding or change of pH were observed. Apo MtATP-PRT at pH 6.8 has shown to occupy the same conformational landscape as MtATP-PRT in presence of L-histidine at pH 6.8 or at pH 9. The very first TWIMS-MS experiments were performed on a Synapt G2S HDMS instrument (at Waters Corporation, Manchester) whilst the repeats were run on three different Synapt G2 HDMS instruments in different laboratories. Initially, it was though that the lack of changes might be due to structural collapse of MtATP-PRT occurring during the desolvation process which could have been originating from differences in the source design between the two instruments (Chapter 2, section 2.2.2.). Careful optimisation of source conditions (elevated pressure and low voltages) did not result in detection of any changes in CCSD. Experiments were performed afresh on the SynaptG2S (at Waters Corporation, Manchester) and MoQToF instruments, however, this time no structural changes were observed upon L-histidine binding. Unsuccessful efforts to replicate the preliminary results by using several different instruments hinted at the fact, that lack of conformational change might be due to the sample itself rather than the instrument and/or conditions utilized.

Purification of MtATP-PRT is facilitated by inclusion of a non-cleavable hexa-histidine tag (HisTag) at the N-terminal. Although, the allosteric site is located within domain III near the C-terminal and far from the HisTag, histidine is the allosteric inhibitor of MtATP-PRT and presence of the HisTag could be affecting its activity. Our collaborator at MRC NIMR, conducted kinetic studies and shown that HisTag does not to affect the structure or activity of MtATP-PRT. Nevertheless, wild type MtATP-PRT was expressed in order to exclude any potential binding of the HisTag histidine to the allosteric site. IM-MS experiments performed on Synapt G2 HDMS instrument, showed no conformational change upon L-histidine addition at pH 6.8. All experiments reported in this chapter, unless otherwise stated, were performed on the HisTag MtATP-PRT. Removal of the histidine tag causes MtATP-PRT to be more prone towards aggregation and maintenance of a stable nano-electrospray becomes challenging.

Another hypothesis proposed explaining lack of conformational changes observed was possibility of enzyme deactivation over time. Potentially, a disulfide bond could be formed between cysteine residues at positions 73 and 175 over time and storage which would alter enzyme activity. These residues are far away from the allosteric site and seem to be distant enough to not form a disulfide bond. Nevertheless, in order to exclude any possible disulfide bond formation, dithiothreitol (DTT) was added to MtATP-PRT sample. Addition of this thiol reducing agent did not alter the structure (as determined with gel filtration) nor activity, indicating that sample did not contain oxidized cysteine residues or disulfide bonds that could inhibit activity.[31] IM-MS experiments were performed on Synapt G2 HDMS instrument on samples treated with DTT, however, still no changes in drift time were noted upon L-histidine addition at pH 6.8.

During sample purification, MtATP-PRT is eluted into buffer containing 500 mM imidazole and subsequently dialyzed into triethanolamine (TEA) buffer prior to storage. Imidazole ring of L-histidine is a crucial structural motif in the inhibition of MtATP-PRT and transmission of the inhibitory signal from the allosteric site to the catalytic site, therefore, presence of imidazole in the buffer solution could have an effect on the conformation of the enzyme. Prior to IM-MS, the buffer is exchanged into 100 mM ammonium acetate using micro Bio-Spin chromatography columns; the procedure is repeated 4-5 time to achieve desired purity. Additionally, MtATP-PRT was purified by running gel filtration (Superdex 200 10/300) to remove any imidazole present. Nevertheless, no conformational changes were observed upon L-histidine addition post the extensive buffer exchange procedure. Currently, efforts are being made to purify the MtATP-PRT without the use of imidazole.

Whether the first IM-MS measurements were one time artefact, the conformational change and enzyme activity across different batches is observed in gel filtration experiments and also hydrogen deuterium exchange (HDX) MS experiments as will be discussed later. Once the conditions, either instrumental or involving sample preparation, allowing for differentiation of the tensed and the relaxed form of MtATP-PRT in IM space are re-established, several additional experiments should be carried out. Firstly, the pH scan experiment which would track the transformation between tensed and relaxed form of MtATP-PRT as a function of buffer pH. Secondly, a titration of L-histidine into MtATP-PRT would help to determine binding stoichiometry and a number of L-histidine molecules necessary to induce conformational change.

6.3.4 Effect of L-histidine on MtATP-PRT dissociation: CID

Disruption of protein structure can provide insights into complex stoichiometry, subunit interactions or complex topology.[33-36] One of the protein activation methods leading to complex dissociation is collision induced dissociation (CID). MtATP-PRT, apo and in complex with L-histidine at pH 6.8, was subjected to CID activation on a Synapt G2 HDMS instrument. The most intense 27+ charge state (*m/z* 7142) was chosen as a precursor ion. CID activation was induced by elevating the trap collision energy. MS and IM-MS data were acquired at several discrete trap collision energy values of 10 V, 30 V, 50 V, 80 V, 100 V, 120 V, 150 V and 180 V. Mass spectra and drift time distributions of apo MtATP-PRT (a,b) and MtATP-PRT in presence of L-histidine (c,d) are shown in Figure 6.12.

As the trap collision energy is increased, onset of apo MtATP-PRT dissociation into monomers (*m/z* 1500 – 3500) is observed around 80 V (Figure 6.12a). As the complex undergoes dissociation, loss of structure is indicated by shift towards longer drift times

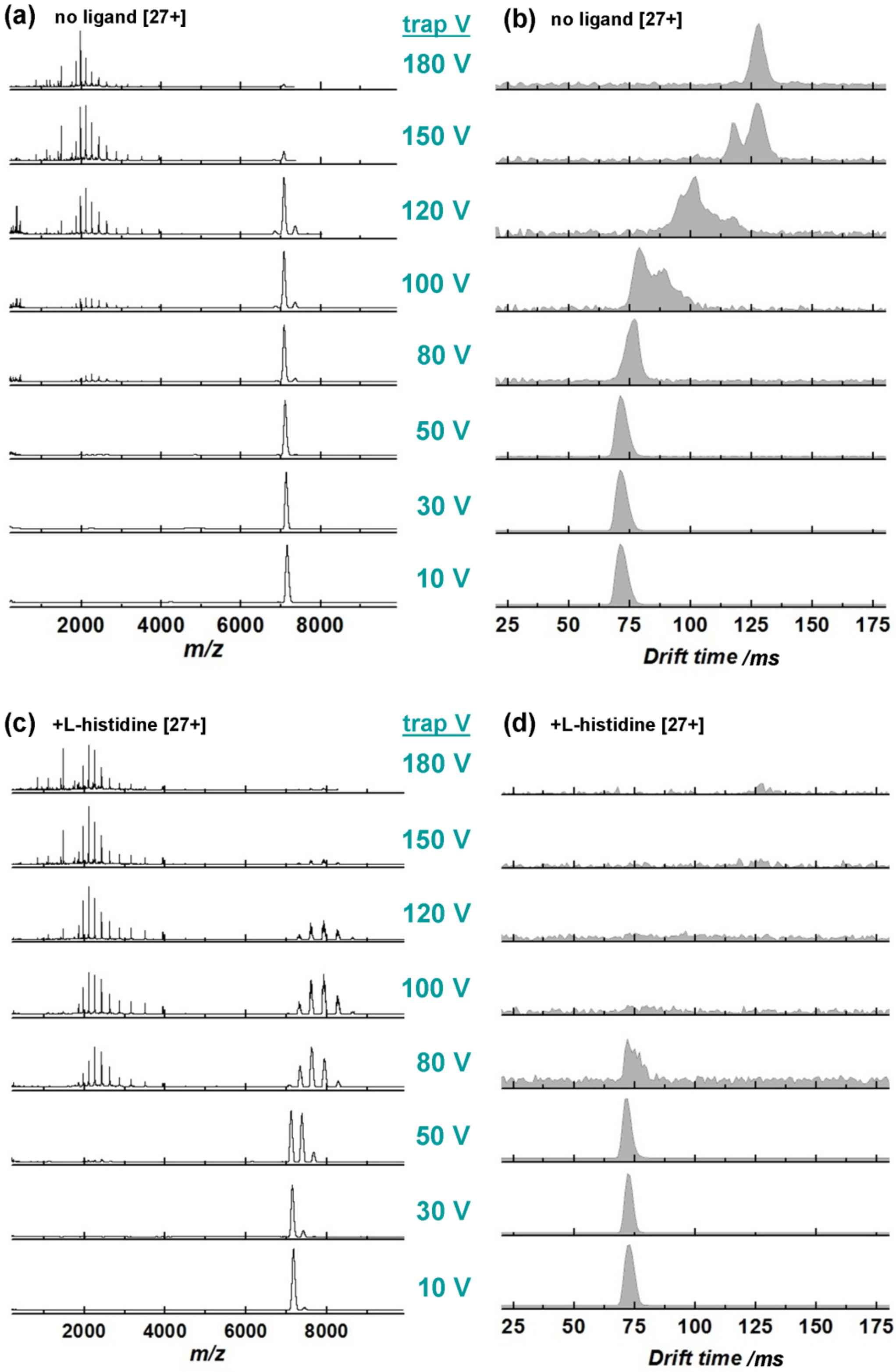

Figure 6.12 Trap CID of 27+ charge state of MtATP-PRT (a,b) and MtATP-PRT in presence of L-histidine (c,d). Mass spectra and drift time distributions were acquired on Synapt G2 HDMS instrument at trap cell voltages of 10 V, 30 V, 50 V, 80 V, 100 V, 150 V and 180 V. Increase in the trap voltage leads to conformational changes associated with subunit unfolding and charge stripping of the MtATP-PRT : L-histidine complex (c).

and broadening of the drift time distribution (Figure 6.12b). Upon increasing trap energy to higher values, the dissociation into subunits becomes more extensive and MtATP-PRT undergoes several intermediate unfolding transitions until finally, at 180 V, only a marginal amount of apo MtATP-PRT hexamer is present over one conformational family with significantly longer drift time (~ 130 ms). It is worth noting, that experiments presented in this section as opposed results reported in section 6.3.3.2 were performed on a different version of the instrument (Synapt G2 and Synapt G2S, respectively) and under application of different ion mobility parameters, hence, the differences is the drift times observed in Figure 6.12 and Figure 6.11. Moreover, the CID experiment was performed on a batch of sample where no conformational difference was observed upon addition of L-histidine, as described earlier.

The presence of L-histidine leads to a different dissociation pattern. At 50 V, charge stripping occurs which has previously been interpreted as due to L-histidine dissociation (Figure 6.12c). A significant amount of MtATP-PRT in lower charge states is detected. As the trap collision energy is increased further to 80 V, charge stripping progresses and the population of lower charge states increases along with a decrease in the intensity of the precursor ion. The CSD continues to shift towards lower charge states and becomes centred at 24+ charge state (at 100 V), similarly to the in-source dissociation experiments (Figure 6.6). Interestingly, the dissociation into monomers appears to be facilitated by ligand induced charge stripping. Population of monomers ejected from MtATP-PRT in presence of L-histidine is higher than that of monomers originating from the apo MtATP-PRT. Dissociation ratios have been calculated (following the procedure presented in Chapter 4, section 3.2) as a function of trap collision energy and are listed in Table 6.1. Upon application of 80 V to the trap cell, about 66 % of apoATP-PRT remains intact as a hexamer in comparison to only 37 % of MtATP-PRT in presence of L-histidine. In conjunction with a titration experiment, inducing such dissociation could facilitate a comparison of binding strength of the first four L-histidine molecules, which have been suggested as being required for the onset of a conformational change, versus the latter two and/or any non-specific binders.

Table 6.1 Trap CID based dissociation ratios of apo MtATP-PRT and MtATP-PRT in presence of L-histidine. The ratio of the summed intensities of charge states corresponding to the intact complex [$I_{complex}$] over the sum of the summed intact complex charge state intensities and summed intensities of monomer charge states produced *via* CID [$I_{complex}$ + $I_{monomer}$] listed as a function of trap collision voltage.

Trap collision voltage /V	Dissociation ratio of MtATP-PRT	Dissociation ratio of MtATP-PRT + L-histidine
10	1.00	1.00
30	1.00	1.00
50	0.98	0.93
80	0.66	0.37
100	0.55	0.33
120	0.25	0.18
150	0.04	0.05
180	0.02	0.02

6.3.5 *Mapping of conformational changes and binding site with HDX-MS*

Conformational changes of MtATP-PRT initially observed by means of IM-MS, were further investigated with HDX-MS. The rate and extent of exchange of labile hydrogen atoms at the backbone amide positions of the protein with deuterium atoms in a surrounding buffer can be measured to provide insights into ligand binding, structural changes as well as protein dynamics. HDX-MS analysis on MtAPT-PRT was achieved using a Waters HDX module with nanoAcquity UPLC and Synapt G2 HDMS equipped with a LEAP-PAL robotics system for sample handling.

6.3.5.1 Sequence coverage

Firstly, MtATP-PRT prepared in ammonium acetate buffer was injected into a pepsin digestion column to determine the sequence coverage. The non-specific cleaving nature of pepsin produces overlapping peptides and increases the sequence coverage of the

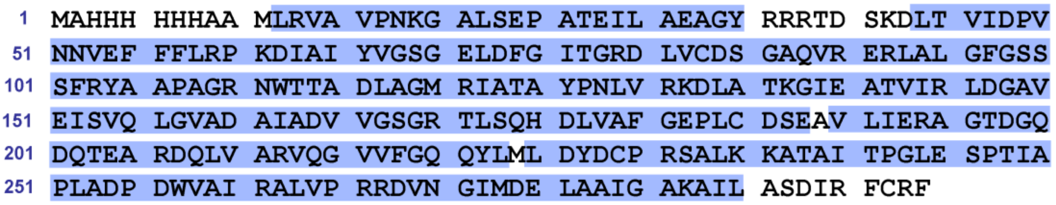

```
  1 MAHHH HHHAA MLRVA VPNKG ALSEP ATEIL AEAGY RRRTD SKDLT VIDPV
 51 NNVEF FFLRP KDIAI YVGSG ELDFG ITGRD LVCDS GAQVR ERLAL GFGSS
101 SFRYA APAGR NWTTA DLAGM RIATA YPNLV RKDLA TKGIE ATVIR LDGAV
151 EISVQ LGVAD AIADV VGSGR TLSQH DLVAF GEPLC DSEAV LIERA GTDGQ
201 DQTEA RDQLV ARVQG VVFGQ QYLML DYDCP RSALK KATAI TPGLE SPTIA
251 PLADP DWVAI RALVP RRDVN GIMDE LAAIG AKAIL ASDIR FCRF
```

Figure 6.13 MtATP-PRT amino acid sequence coverage highlighted in blue, after digestion with pepsin. 85 peptides have been identified covering 90 % of the sequence.

studied protein. Resulting peptides were separated by UPLC, further fragmented and identified by MS. 85 peptides have been identified (list available in Appendix 7) covering 264 out of 294 amino acid residues of the MtATP-PRT sequence *i.e.* 90 % sequence coverage (or 94 % if not considering the polyhistidine tag, residues 1-11). Figure 6.13, highlights residues of MtATP-PRT sequence covered by peptides resulting from pepsin digestion. Residues not converted included MAHHHHHHAAM (1-11), RRRTDSKD (36-43), A (189), M (224), and ASDIRFCRF (286-294). Differences in the numbering system between x-ray crystal structure and HDX data presented here exist, as the HisTag residues in the x-ray crystal structure are not numbered. HDX residue numbers correspond to x-ray residue number plus 10 (HDX residue number = PDB residue number + 10) and will be used throughout the discussion.

6.3.5.2 Changes in deuterium uptake due to L-histidine binding and buffer pH

HDX experiments were carried out on MtATP-PRT in the presence and absence of L-histidine (12 ligand equivalents to 1 hexamer) at pH 6.8 and pH 9 to obtain insights into ligand induced and environment induced subtle conformational changes observed *via* other characterisation techniques. After addition of L-histidine, MtATP-PRT samples were incubated for at least 30 minutes at room temperature and subsequently diluted 20 fold into phosphate buffer in either H_2O (control) or D_2O. The mixtures were incubated at 20 °C for 0 minutes (H_2O), or 1, 10, 30 or 120 minutes (D_2O), prior to exchange quench step and automated injection onto the pepsin column. The D uptake was calculated for each peptide identified at all four labeling time points and compared across experimental conditions *i.e.* ligand presence and pH.

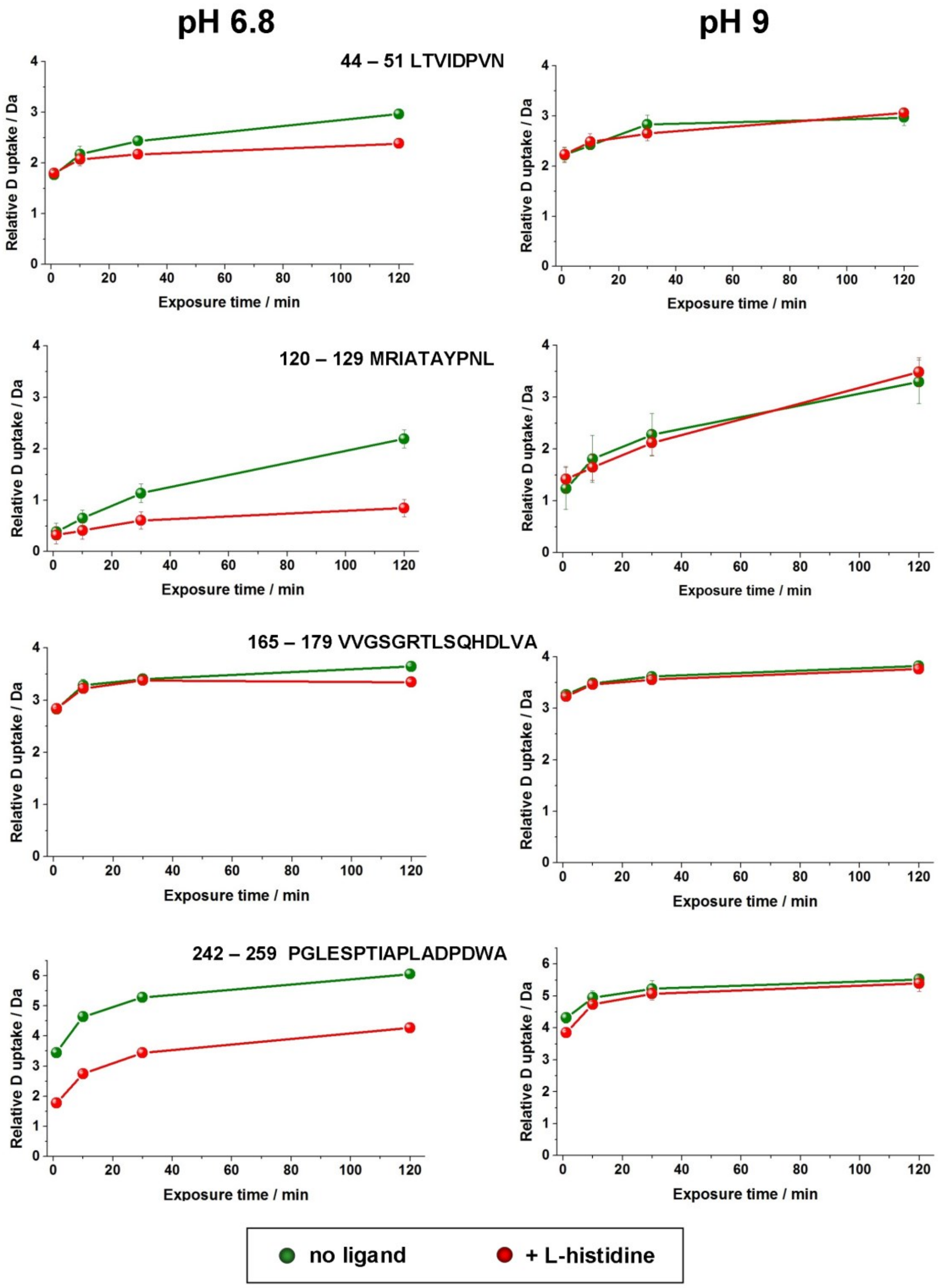

Figure 6.14 **Example deuterium uptake curves of four chosen peptides of MtATP-PRT in presence (red) and in absence (green) of L-histidine at pH 6.8 (left) and pH 9 (right). Deuterium uptake was determined at four exposure time points: 1 minute, 10 minutes, 30 minutes and 120 minutes. D uptake data for all peptides identified is provided in the Appendix 7.**

Highly dynamic and disordered protein regions or those with increased solvent accessibility undergo rapid deuteration, whereas less solvent accessible regions or buried by the ligand binding may be protected within the complex and exchange at a slower rate. Example D uptake curves of four chosen peptides of MtATP-PRT (green) and MtATP-PRT : L-histidine complex (red) are shown in Figure 6.14. The amount of D uptake varies along the MtATP-PRT sequence. Peptides L44-N51, V165-A179 and P242-A259 of which all are located on the surface of domains I, II and III , respectively, experience higher extent of deuteration on a short time scale (1 min) in comparison to peptide M120-L129 which is somewhat buried within domain II. Upon addition of L-histidine at pH 6.8, the amount of D uptake instantly decreases in the region within domain III (P242-A259, Figure 6.14 bottom plot) recognized as the allosteric site of L-histidine binding. As L-histidine binds, amide hydrogen atoms become protected from the deuterated solvent which significantly slows down the HDX reaction, hence the difference in D uptake is observable within the first minute of reaction. Although, the D absolute uptake increases with the HDX reaction time, the relative difference between two species remains constant, suggesting it is protection of a particular residue/s that is responsible for the decrease in observed uptake.

Changes in HDX between ligand free and ligand bound MtATP-PRT are also observed on long time scales (120 min of HDX). Peptide M120-L129, located near the AMP binding site and proposed ATP and PRPP binding site, shows no significant change in D uptake at 1 minute of HDX. At longer HDX times, however, a decrease in D uptake is noted for L-histidine bound form. Such differences originate from conformational changes induced by ligand binding which restrict protein dynamics and limit deuteration at extended exposure times rather than from direct interaction with the binding molecule.

Interestingly, no differences in D uptake were observed between apo and L-histidine bound MtATP-PRT at pH 9. No significant changes were observed around the allosteric region due to L-histidine binding nor near the active site, suggesting that the conformational changes observed at pH 6.8 are not present at pH 9, in agreement with conclusions drawn from IM-MS data (section 6.3.3.). Average D uptake values along with standard deviation values (based on three experimental replicas) across four samples and four time points for each peptide identified are provided in Appendix 7.

(a) pH 6.8

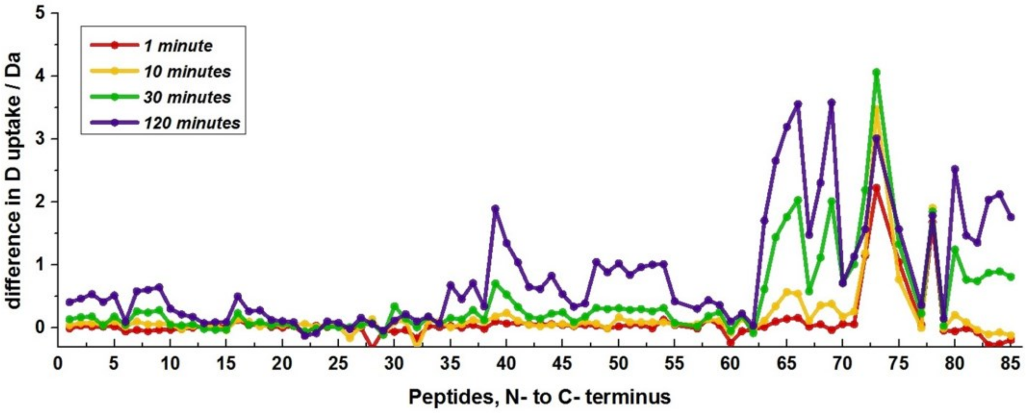

(b) pH 9

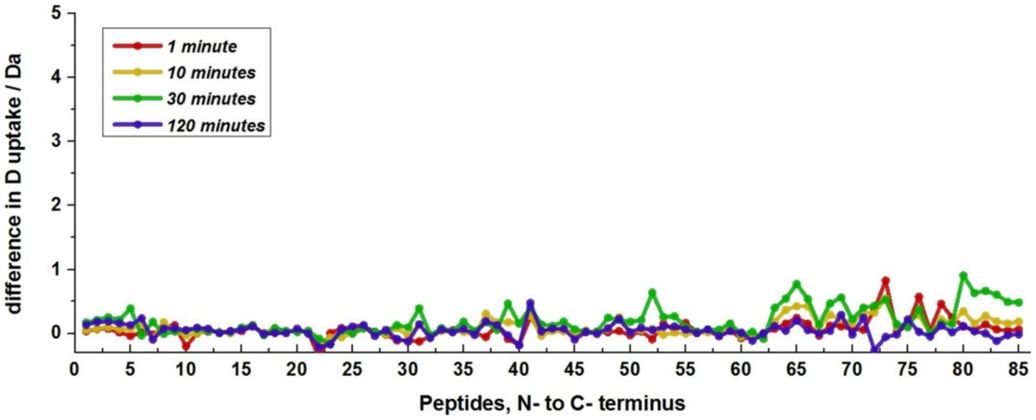

Figure 6.15 Difference in the absolute D uptake between L-histidine free and L-histidine bound MtATP-PRT at pH 6.8 (a) and pH 9 (b), measured at four deuterium exposure time points: 1 minute (red), 10 minutes (yellow), 30 minutes (green) and 120 minutes (blue); providing information about regions of ligand binding and conformational changes.

HDX experiments were also carried out on the WT MtATP-PRT (no HisTag present) showing the same trends. Due to a large number of peptides, the collected data is better represented in form of butterfly plots. The difference in absolute D uptake between apo MtATP-PRT and MtATP-PRT in presence of L-histidine at four exposure time points is plotted in Figure 6.15 for each peptide along x-axis from N- to C- terminal, at pH 6.8 (a) and pH 9 (b). It becomes clearly visible how changes occurring on a fast timescale (observable < 1 min, red trace) associated with direct L-histidine binding take place within domain III (peptides 70-85) at pH 6.8 (Figure 6.15a); whereas the other changes occur on longer timescales (most obvious at 120 minutes, blue trace), suggesting an induced conformational change near the active site (peptides 35-60, 80-85) proceeding at a slower rate. Anand *et al.* have suggested HDX changes at different time points as a way of differentiating between small molecule binding and protein structural events.[37,38] At pH 9, the differences in D uptake upon L-histidine are more subtle (Figure 6.15 b). A minor variation in D uptake is noted around domain III (peptides 63-85) indicating some binding is occurring; however, no significant changes on longer time scale associated with conformational changes are observed around the active site. The datasets obtained under different buffer conditions cannot be compared to each other, due to the pH dependence of the intrinsic HDX rate.[39,40] Nevertheless, data obtained under identical buffer conditions serve to map regions of ligand binding and conformational changes.[41,42]

When high resolution structural data is available for a given protein, HDX information can be transposed onto the structure to help visualize and understand structural changes and dynamics.[43] The percentage differences in D uptake between apo and L-histidine bound MtATP-PRT at pH 6.8 were calculated and applied onto available x-ray crystal structures 1NH7 (apo MtATP-PRT) and 1NH8 (MtATP-PRT + AMP + L-histidine) as shown in Figure 6.16. Residues D226-A259 located in the region of significant changes within the first minute of HDX are highlighted in red, and encompass residues identified to be involved in direct binding with L-histidine: D228, L244, S246, T248, L263, and A283 (black). Residues, for which differences in HDX were found on a longer time scale (120 min), are highlighted in three shades of blue of increasing intensity corresponding to greater changes. The greatest change (difference of 20 % and higher) in HDX between L-histidine free and L-histidine bound MtATP-PR evident on a longer time scale were located near the allosteric site (V210-L223 and L275-L285). Slightly less extensive but still notable (10 to 20 %) changes where found in regions surrounding the active site positioned in the cavity between domains I and II (L44-F55, L117-L129, I152-D164); which in Figure 6.16 are marked in teal-green for residues involved in direct binding of AMP and lime-green for residues proposed to be involved in ATP and PRPP binding. Cho *et al.*[13] reported on a major conformational change upon L-histidine binding originating from a significant twist of the domain III with respect to domain I and II causing steric hindrance in the active site. HDX data supports this hypothesis owing to over 30 % change in HDX detected within the α-helix between domains I and III (R212-L223); and envisions conformational changes induced by allosteric inhibitor binding, resulting in limited access to the active site and/or reorienting residues

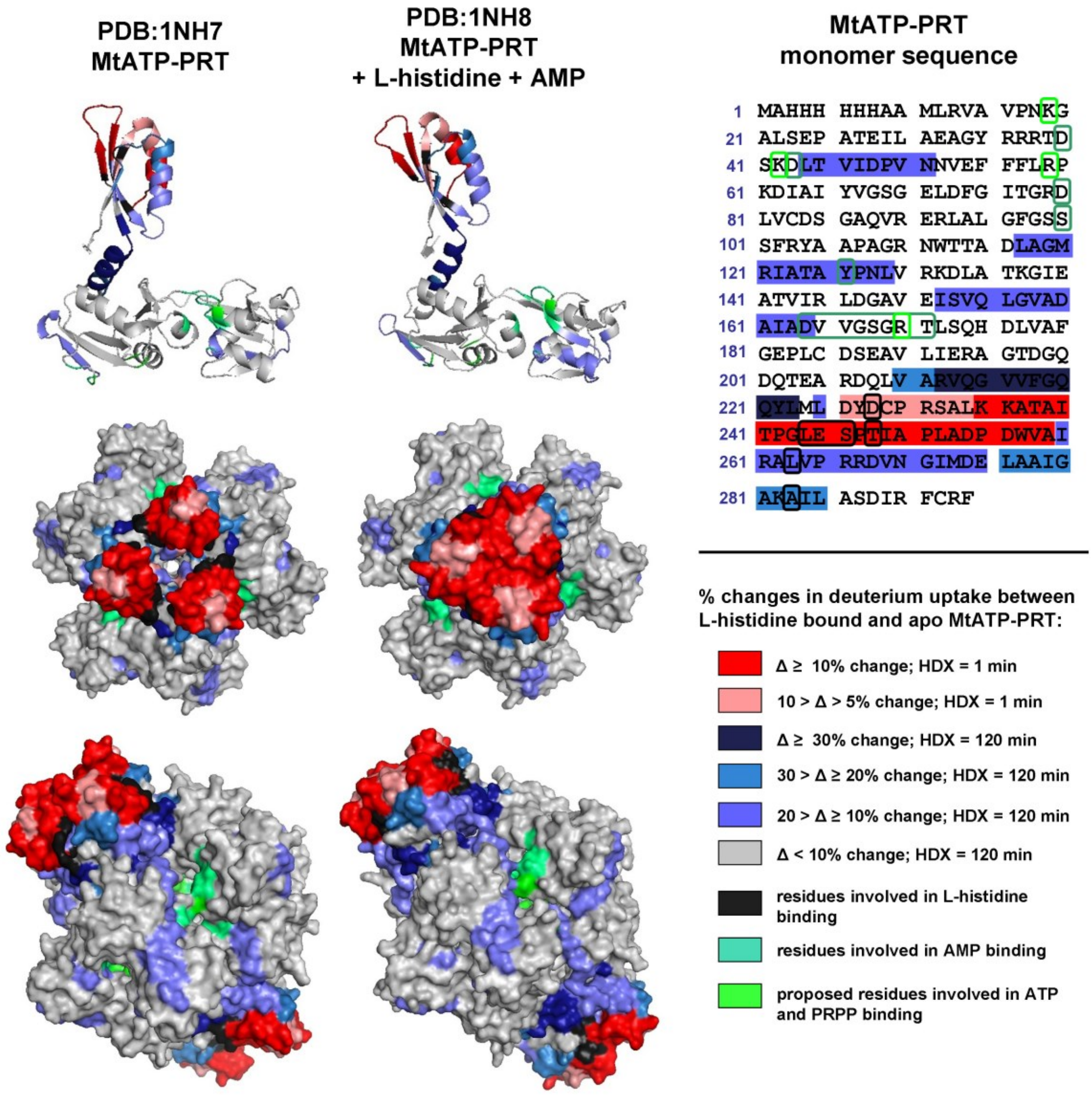

Figure 6.16 Percentage differences in deuterium uptake visualized on the PDB: 1NH7 and 1NH8 crystal structures and the MtATP-PRT monomer sequence. Residues with significant changes in HDX on short time scale are highlighted in red, residues where changes occur on a longer time scale (120 min) are highlighted in shades of blue. Residues involved in direct interactions with L-histidine, residues involved in binding of AMP and residues proposed to be involved in ATP and PRPP binding as reported by Cho *et.al.*[13] are shown in black, teal-green and lime-green, respectively.

responsible for interactions with both of the substrates: ATP and PRPP. Table 6.2 lists residues and peptides experiencing notable changes in D uptake between ligand free and ligand bound MtATP-PRT states; as well as residues involved in interactions with inhibitors and substrates determined by Cho *et al*..[13]

Table 6.2 List of MtATP-PRT residues with altered D uptake due to L-histidine binding determined *via* HDX experiments; along with list of MtATP-PRT involved in binding with L-histidine, AMT and residues predicted to interact with ATP and PRPP.

HDX DATA

Residues	Change in D uptake	Peptide number
L44-F55	long time scale: 120 min	7-9
L117-L129	intermediate time scale: 30 min	39-41
V130-E151	intermediate and long time scale: 30-120 min	44-45
I152-D164	intermediate and long time scale: 30-120 min	48-53
V210-L234	intermediate and long time scale: 30-120 min (significant)	63-71
D226-A259	instant within 1 minute	72, 73, 75, 78
Y227-K235	intermediate and long time scale: 30-120 min	74
V258-L285	intermediate and long time scale: 30-120 min	80-85

X-RAY CRYSTALLOGRAPHY DATA[13]

Residues (HDX numbering)	Type of interaction
D228, L244, S246, T248, L263, A283	L-histidine
D40, D43,D80, S100, Y126,D164-T171	AMP
K19, K42, R59, R170	ATP and PRPP (predicted)

One of the factors affecting the HDX rate is the solvent accessibility. Amide hydrogen atoms on the surface of protein are more prone to undergo exchange at faster rates; therefore, residues at the subunit interfaces would be expected to incorporate lower amounts of deuterium on a short time scale. The percentage of absolute D uptake was calculated for MtATP-PRT in the presence and absence of L-histidine at pH 6.8 at 1 minute and 120 minutes exchange time points and was applied onto the MtATP-PRT monomer structure. The MtATP-PRT monomer is presented in Figure 6.17, at various angles: three snapshots along the 3-fold axis and one along 2-fold symmetry plane. An increased percentage of absolute D uptake is visualized with increasing intensity of blue. Additionally, the interface residues were identified using the online ‘Protein interfaces, surfaces and assemblies’ service PISA[19,20] based on the 1NH7 (violet) and 1NH8 (purple) crystal structures as shown in the top row of Figure 6.17. Some of the crucial residues at the subunit interfaces were not covered by peptides resulting from pepsin digestion (brown). Nevertheless, it is seen that a lower amount of D is incorporated into

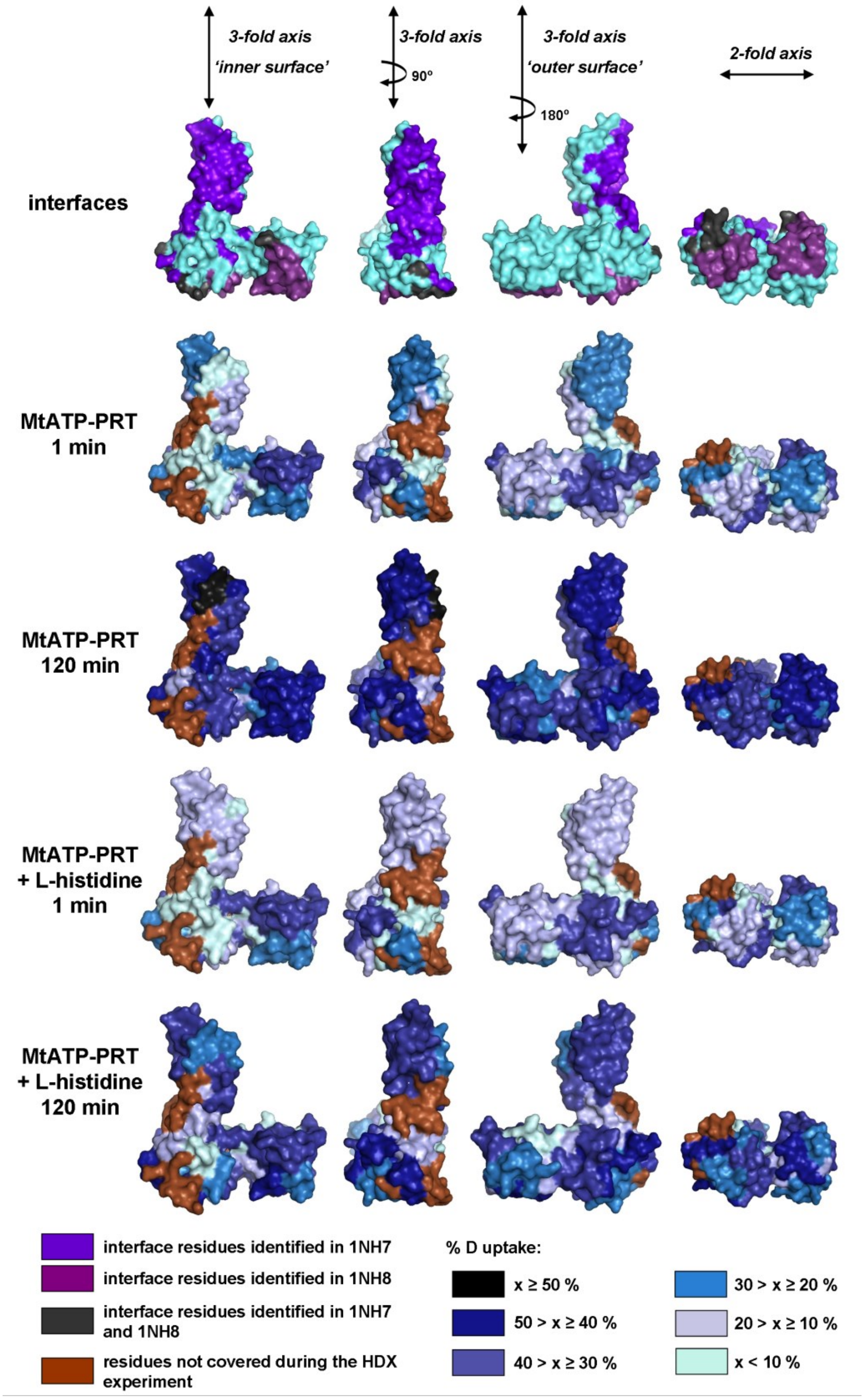

Figure 6.17 Percentage D uptake of MtATP-PRT in presence and in absence of L-histidine at pH 6.8 after 1 minute and 120 minutes of exposure to deuterated buffer represented on MtATP-PRT monomer (PDB:1NH7) viewed from different angles. The top row highlights interface residues based on PDB:1NH7 (violet) and PDB:1NH8 (purple). The increasing intensity of blue correlates with increase in D uptake. Residues not covered during the HDX experiment are highlighted in brown.

the surface residues facing the intra-subunit cavity *i.e.* ‘inner surface’, as opposed to the residues on the ‘outer surface’ within the first minute of HDX. Such pattern is observed both, in the presence and absence of L-histidine, and is supportive of the mechanism proposed by Pedreño *et al.*[12] which envisions MtATP-PRT as a functional hexamer where conformational changes have to be invoked to explain the allosteric inhibition (Figure 6.3b). Moreover, upon the addition of L-histidine , the percentage of absolute D uptake on a long time scale at the ‘inner surface’ is lower in comparison to D uptake in the absence of ligand further supporting conformational rearrangement to a more compact structure and reducing solvent penetration of the intra-subunit cavity.

6.3.6 Conformational changes probed with solution-phase technique: AUC

Analytical ultracentrifugation (AUC) is a powerful method for analysis of macromolecules in solution.[44-46] Sedimentation velocity analysis is an AUC method *via* which the movement of molecules through high centrifugal fields is explored to define their size, shape and interactions. Sedimentation velocity experiments determine sedimentation coefficient ($s_{20,w}$) expressed in Svedberg (1 S = 10^{-13} s) and defined as ratio of a particle's sedimentation velocity to the acceleration that is applied to it. The sedimentation coefficient depends on the molecular weight of the protein where larger species sediment faster, but also on their molecular conformation. Unfolded proteins or ones with highly elongated conformations will experience more hydrodynamic friction, and thus will have smaller sedimentation coefficients than folded, globular proteins of the same molecular weight.

Sedimentation coefficient distributions of MtATP-PRT acquired at pH 6.8 (a) and pH 9 (b) are shown in Figure 6.18. The sedimentation coefficient values ($s_{20,w}$) of MtATP-PRT at pH 6.8 in presence and in absence of L-histidine were determined to be 8.22 ± 0.26 S and 8.58 ± 0.14 S, respectively (Figure 6.18a). An increase in $s_{20,w}$ upon binding of L-histidine is indicative of conformational changes and the adoption of a more compact structure. Furthermore, the width of $s_{20,w}$ distribution can reflect on the protein dynamics and population of closely related structures. The minimum width of the sedimentation boundary is related to the diffusion coefficient of the molecule; however,

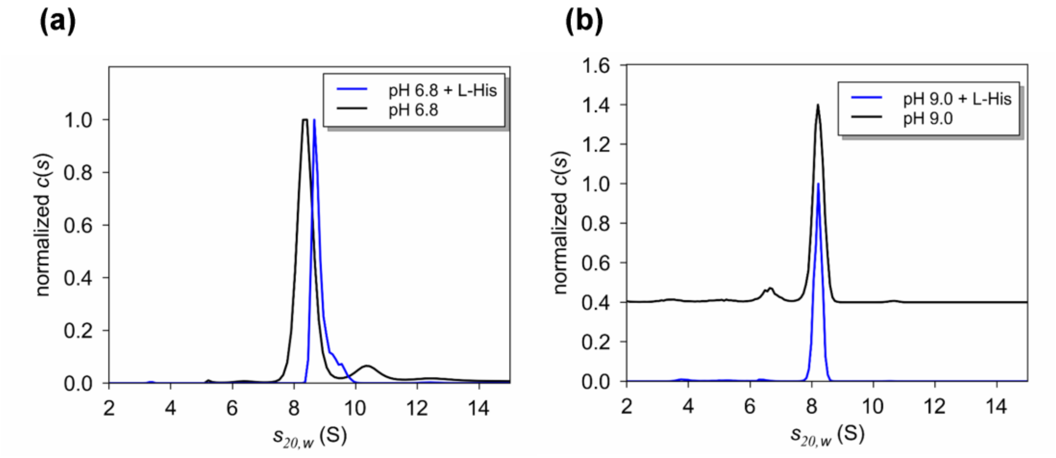

Figure 6.18 Sedimentation coefficient distributions ($s_{20,w}$) of MtATP-PRT in 100 mM ammonium acetate at pH 6.8 (a) and pH 9 (b), in presence (blue trace) and in absence of L-histidine (black trace). More compact proteins experience less hydrodynamic friction, and thus have larger sedimentation coefficient.

presence of multiple species with similar sedimentation coefficients will cause the boundary to be broader. A narrowing of the $s_{20,w}$ distribution is observed upon L-histidine addition, suggesting that its presence may be causing MtATP-PRT to be more structurally constrained.

The sedimentation coefficient values of MtATP-PRT at pH 9 in presence and in absence of L-histidine were determined to be 8.09 ± 0.18 S and 8.15 ± 0.14 S, respectively (Figure 6.18 b). Here, the difference in $s_{20,w}$ between ligand free and ligand bound MtATP-PRT is significantly smaller, suggesting close structural resemblance of the two species. In agreement with IM-MS and HDX-MS results, under these conditions MtATP-PRT does not appear to undergo conformational tightening upon L-histidine addition. Minor differences in $s_{20,w}$ of apo MtATP-PRT at pH 6.8 and pH 9 is most likely due to an affect of the buffer pH on the hydrodynamic friction during the sedimentation process rather than conformational changes. It is worth nothing that the small population of lower order species at $s_{20,w} = 6.41$ S observed at pH 9, is no longer detected after the addition of L-histidine. Native MS experiments showed, monomeric and dimeric MtATP-PRT present at pH 9 to similarly decrease in intensity after incubation with L-histidine (Figure 6.8 c). In summary, AUC data is in agreement with results obtained from IM-MS and HDX-MS studies *i.e.* detection of subtle conformational tightening of MtATP-PRT at pH 6.8 upon L-histidine addition noted, however, no evident conformational changes are present at pH 9.

6.4 Conclusions

A set of MS based techniques has been employed to investigate allosteric inhibition mechanism of MtATP-PRT, a 190 kDa homohexameric enzyme catalysing the first step of the biosynthesis of L-histidine in *Mycobacterium tuberculosis*. Native MS revealed MtATP-PRT to exist in the hexameric state under physiological conditions. The binding stoichiometry could not be conclusively determined from the mass shift due to a significant mass difference between the ligand and the protein as well as a considerable amount of residual solvent and buffer present under the gentle desolvation conditions used to preserve non-covalent interactions. Nevertheless, in-source dissociation MS experiments suggest that the first four L-histidine molecules binding may have different affinity from the subsequent two.

Conformational changes induced by L-histidine binding and the influence of buffer pH were probed with IM-MS, HDX-MS and AUC. Results obtained from all three techniques support the occurrence of subtle conformational changes upon ligand binding at pH 6.8. Linear drift-tube IM-MS experiments showed a decrease in the median CCS from 76.6 nm^2 to 73.5 nm^2 (for the 28+ charge state) and this change was also confirmed by the theoretical CCS calculated from the available crystal structures. No such changes in conformation were found to take place at pH 9. Sedimentation velocity analysis confirmed the conformational tightening upon ligand binding observed *in vacuo*.

Furthermore, HDX was used for mapping of the conformational changes and the results are in agreement with x-ray crystallography data. Changes in the deuterium uptake between apo MtATP-PRT and L-histidine bound MtATP-PRT occurring on a short time scale were found within domain III and are associated with L-histidine binding to the allosteric site. Changes occurring on longer time scales related to conformational changes induced by ligand binding were identified around the active site and near the residues involved in AMT binding and residues proposed to be involved in binding of ATP and PRPP substrates.

The collected data supports the mechanism proposed by Pedreño *et al.*, which envisions MtATP-PRT as a functional hexamer where conformational changes have to be invoked to explain the allosteric inhibition. Still, more experiments need to be carried out for further elucidation of the inhibition mechanism and determination of the binding stoichiometry (such as IM- and CID-based titration). In future, a combination of methods employed here, will be used to scan libraries of MtATP-PRT inhibitor ligands with the aim to discover potential novel anti-tuberculosis agents.

6.5 References

(1) Krishnan, N.; Koveal, D.; Miller, D. H.; Xue, B.; Akshinthala, S. D.; Kragelj, J.; Jensen, M. R.; Gauss, C.-M.; Page, R.; Blackledge, M.; Muthuswamy, S. K.; Peti, W.; Tonks, N. K. *Nature chemical biology* **2014**, *10*, 558.
(2) Gilmartin, A. G.; Faitg, T. H.; Richter, M.; Groy, A.; Seefeld, M. A.; Darcy, M. G.; Peng, X.; Federowicz, K.; Yang, J.; Zhang, S.-Y.; Minthorn, E.; Jaworski, J.-P.; Schaber, M.; Martens, S.; McNulty, D. E.; Sinnamon, R. H.; Zhang, H.; Kirkpatrick, R. B.; Nevins, N.; Cui, G.; Pietrak, B.; Diaz, E.; Jones, A.; Brandt, M.; Schwartz, B.; Heerding, D. A.; Kumar, R. *Nature Chemical Biology* **2014**, *10*, 181.
(3) Scheuermann, T. H.; Li, Q.; Ma, H.-W.; Key, J.; Zhang, L.; Chen, R.; Garcia, J. A.; Naidoo, J.; Longgood, J.; Frantz, D. E.; Tambar, U. K.; Gardner, K. H.; Bruick, R. K. *Nature Chemical Biology* **2013**, *9*, 271.
(4) Edfeldt, F. N. B.; Folmer, R. H. A.; Breeze, A. L. *Drug Discovery Today* **2011**, *16*, 284.
(5) Surade, S.; Blundell, T. L. *Chemistry & Biology* **2012**, *19*, 42.
(6) Hardy, J. A.; Wells, J. A. *Current Opinion in Structural Biology* **2004**, *14*, 706.
(7) Purves, W. K.; Orians, G. H. *The science of biology*; Sinauer Associates Inc., Sunderland, Massachusetts, 1987.
(8) Fenton, A. W. *Allostery: Methods and Protocols* **2012**, *796*, 369.
(9) Luo, L.; Parrish, C. A.; Nevins, N.; McNulty, D. E.; Chaudhari, A. M.; Carson, J. D.; Sudakin, V.; Shaw, A. N.; Lehr, R.; Zhao, H.; Sweitzer, S.; Lad, L.; Wood, K. W.; Sakowicz, R.; Annan, R. S.; Huang, P. S.; Jackson, J. R.; Dhanak, D.; Copeland, R. A.; Auger, K. R. *Nature Chemical Biology* **2007**, *3*, 722.
(10) Ceccarelli, D. F.; Tang, X.; Pelletier, B.; Orlicky, S.; Xie, W.; Plantevin, V.; Neculai, D.; Chou, Y.-C.; Ogunjimi, A.; Al-Hakim, A.; Varelas, X.; Koszela, J.; Wasney, G. A.; Vedadi, M.; Dhe-Paganon, S.; Cox, S.; Xu, S.; Lopez-Girona, A.; Mercurio, F.; Wrana, J.; Durocher, D.; Meloche, S.; Webb, D. R.; Tyers, M.; Sicheri, F. *Cell* **2011**, *145*, 1075.
(11) Sinha, S. C.; Smith, J. L. *Current Opinion in Structural Biology* **2001**, *11*, 733.
(12) Pedreno, S.; Pisco, J. P.; Larrouy-Maumus, G.; Kelly, G.; de Carvalho, L. P. S. *Biochemistry* **2012**, *51*, 8027.
(13) Cho, Y.; Sharma, V.; Sacchettini, J. C. *Journal of Biological Chemistry* **2003**, *278*, 8333.
(14) Bell, R. M.; Parsons, S. M.; Dubravac, S. A.; Redfield, A. G.; Koshland, D. E. *Journal of Biological Chemistry* **1974**, *249*, 4110.
(15) Cho, Y.; Ioerger, T. R.; Sacchettini, J. C. *Journal of Medicinal Chemistry* **2008**, *51*, 5984.
(16) Lohkamp, B.; McDermott, G.; Campbell, S. A.; Coggins, J. R.; Lapthorn, A. J. *Journal of Molecular Biology* **2004**, *336*, 131.
(17) Vega, M. C.; Zou, P. J.; Fernandez, F. J.; Murphy, G. E.; Sterner, R.; Popov, A.; Wilmanns, M. *Molecular Microbiology* **2005**, *55*, 675.
(18) Champagne, K. S.; Sissler, M.; Larrabee, Y.; Doublie, S.; Francklyn, S. S. *Journal of Biological Chemistry* **2005**, *280*, 34096.
(19) Krissinel, E.; Henrick, K. *Journal of Molecular Biology* **2007**, *372*, 774.
(20) Krissinel, E. *Journal of Computational Chemistry* **2010**, *31*, 133.

(21) Voll, M. J.; Appella, E.; Martin, R. G. *Journal of Biological Chemistry* **1967**, *242*, 1760.
(22) Martin, R. G. *Journal of Biological Chemistry* **1963**, *238*, 257.
(23) Zhang, Y.; Shang, X.; Deng, A.; Chai, X.; Lai, S.; Zhang, G.; Wen, T. *Biochimie* **2012**, *94*, 829.
(24) McCullough, B. J.; Kalapothakis, J.; Eastwood, H.; Kemper, P.; MacMillan, D.; Taylor, K.; Dorin, J.; Barran, P. E. *Analytical Chemistry* **2008**, *80*, 6336.
(25) Case, D. A.; Darden, T. A.; III, T. E. C.; Simmerling, C. L.; Wang, J.; Duke, R. E.; Luo, R.; Walker, R. C.; Zhang, W.; Merz, K. M.; Roberts, B.; Wang, B.; Hayik, S.; Roitberg, A.; Seabra, G.; Kolossvary, I.; F.Wong, K.; Paesani, F.; Vanicek, J.; Liu, J.; X.Wu; Brozell, S. R.; Steinbrecher, T.; H. Gohlke; Cai, Q.; Ye, X.; Wang, J.; Hsieh, M.-J.; Cui, G.; Roe, D. R.; Mathews, D. H.; Seetin, M. G.; Sagui, C.; Babin, V.; Luchko, T.; Gusarov, S.; Kovalenko, A.; Kollman, P. A. University of California, San Francisco, 2010.
(26) Lindorff-Larsen, K.; Piana, S.; Palmo, K.; Maragakis, P.; Klepeis, J. L.; Dror, R. O.; shaw, D. E. *Proteins-Structure Function and Bioinformatics* **2010**, *78*, 1950.
(27) Shvartsburg, A. A.; Schatz, G. C.; Jarrold, M. F. *Journal of Chemical Physics* **1998**, *108*, 2416.
(28) Dyachenko, A.; Gruber, R.; Shimon, L.; Horovitz, A.; Sharon, M. *Proceedings of the National Academy of Sciences of the United States of America* **2013**, *110*, 7235.
(29) Coval, M. L. *Journal of Biological Chemistry* **1970**, *245*, 6335.
(30) Heck, H. D. A. *Journal of the American Chemical Society* **1971**, *93*, 23.
(31) de Carvalho, L. P. S., Personal communication, 2013.
(32) Zhou, S. L.; Prebyl, B. S.; Cook, K. D. *Analytical Chemistry* **2002**, *74*, 4885.
(33) Benesch, J. L. P. *Journal of the American Society for Mass Spectrometry* **2009**, *20*, 341.
(34) Benesch, J. L. P.; Aquilina, J. A.; Ruotolo, B. T.; Sobott, F.; Robinson, C. V. *Chemistry & Biology* **2006**, *13*, 597.
(35) Benesch, J. L.; Robinson, C. V. *Current Opinion in Structural Biology* **2006**, *16*, 245.
(36) Wysocki, V. H.; Jones, C. M.; Galhena, A. S.; Blackwell, A. E. *Journal of the American Society for Mass Spectrometry* **2008**, *19*, 903.
(37) Krishnamurthy, S.; Moorthy, B. S.; Lin, L.; Anand, G. S. *Biochimica Et Biophysica Acta-Proteins and Proteomics* **2013**, *1834*, 1215.
(38) Nambi, S.; Badireddy, S.; Visweswariah, S. S.; Anand, G. S. *Journal of Biological Chemistry* **2012**, *287*, 18115.
(39) Bai, Y. W.; Milne, J. S.; Mayne, L.; Englander, S. W. *Proteins-Structure Function and Genetics* **1993**, *17*, 75.
(40) Hui, X.; Hoerner, J. K.; Eyles, S. J.; Dobo, A.; Voigtman, E.; Mel'Cuk, A. I.; Kaltashov, I. A. *Protein Science* **2005**, *14*, 543.
(41) Zhang, Q.; Chen, J.; Kuwajima, K.; Zhang, H.-M.; Xian, F.; Young, N. L.; Marshall, A. G. *Scientific Reports* **2013**, *3*.
(42) Chalmers, M. J.; Busby, S. A.; Pascal, B. D.; West, G. M.; Griffin, P. R. *Expert Review of Proteomics* **2011**, *8*, 43.
(43) Konermann, L.; Pan, J. X.; Liu, Y. H. *Chemical Society Reviews* **2011**, *40*, 1224.
(44) Lebowitz, J.; Lewis, M. S.; Schuck, P. *Protein Science* **2002**, *11*, 2067.
(45) Howlett, G. J.; Minton, A. P.; Rivas, G. *Current Opinion in Chemical Biology* **2006**, *10*, 430.
(46) Laue, T. M.; Stafford, W. F. *Annual Review of Biophysics and Biomolecular Structure* **1999**, *28*, 75.

7

Conclusions and Outlook

Mass spectrometry in conjunction with ion mobility and hydrogen deuterium exchange have been used to probe structure, dynamics, interactions and stability of several large proteins and multimeric protein complexes. Conformational changes of these proteins induced by ligand binding or elevated temperature or pH were probed. This chapter summarizes the principal findings presented in this thesis and provides directions for further investigation.

Mass spectrometry evolved into a powerful tool for the analysis of protein architecture, dynamics and interactions with significant benefits for structural biology and drug discovery. Intact proteins and their complexes can be analysed with molecular weight even on a mega Dalton scale, and the results can be related to data obtained *via* other biophysical techniques to create a fuller picture of their structure. In the presented work, mass spectrometry in conjunction with ion mobility and hydrogen deuterium exchange was used to investigate a broad spectrum of protein behaviour ranging from gas-phase dynamics of therapeutic antibodies, temperature induced dissociation mechanism of non-covalent protein complexes, through probing of thermal stability of mAbs to mapping of conformational changes in enzymes upon allosteric inhibition. Proteins and protein complexes studied here ranged in mass from 55 kDa to 190 kDa. The key conclusions derived from the described studies are summarized below and directions for further research are proposed.

In Chapter 3, higher order structure and dynamics of intact monoclonal antibodies (mAbs) and their fragments were explored with IM-MS and MD. In comparison to other protein complexes of similar size, mAbs displayed significantly broader conformational landscape attributed to their intrinsic flexibility and structural dynamics. MD simulations revealed dynamics between linked folded domains of mAbs and indicated that desolvation causes a contraction mainly in the hinge region and loss of cavities between the folded domains of mAbs; while much of the secondary structure as well as the tertiary fold are retained. Experimentally observed differences in IM-MS data among the two IgG subclasses (IgG1 and IgG4) were rationalized based on the distinct features in the hinge region and the non-covalent interactions at the CH3-CH3 domain interface. While significant gas-phase contraction is observed during nESI process raising caveats about the use of MS to probe higher order structure in flexible proteins; presented data have shown that the linked folded domains of mAbs ‘dance’ in the absence of solution as they do in the condensed phase. In future, it would be worthwhile to explore dynamic behaviour of other IgG subclasses to further pinpoint the effect of structural differences on the conformational landscapes derived from IM-MS experiments. Moreover, performing IM-MS experiments at low buffer gas temperature would allow ‘freezing’ mAb molecules and potentially provide more insights into their conformational diversity.

In Chapter 4, four non-covalent protein complexes were examined at several discrete temperatures ranging from 300 K to 550 K. Increased buffer gas temperature leads to complex dissociation and structural changes occurring along the way. Variable temperature MS (VT-MS) measurements allowed decoupling of melting temperature (T_m) associated with loss of structure in solution measurements, from the protein complex gas-phase dissociation temperature (T_{GPD}). The thermally induced dissociation (TID) mechanism was found to follow a 'typical' CID-like dissociation route. VT-IM-MS data have shown that complexes undergo an initial collapse at 350 K and 400 K. Subsequent unfolding and eventual release of a highly charged monomer from the complex at temperatures above 450 K were marked by increase in median CCS. Broadening of the CCSD was associated with a series of unfolding events prior to complex dissociation. Interestingly, at higher analysis temperature, the ejected monomer carrying lower average charge, was slightly less unfolded and had a narrowed CCSD profile, suggesting that the TID dissociation process might be adopting more 'atypical' dissociation route. In future, experiments at temperatures above 550 K shall be carried out to confirm this hypothesis. Within the temperature range where the initial loss of structure and dissociation occurs, the TID process was shown to follow the 'typical' CID route, hence correlating the TID temperature and CID energies would allow for T_{GDP} to be performed on commonly available instruments with CID capabilities. The presented data portrays the importance of analysis temperature for protein structural, and highlighted the difference between gas phase and solution thermal stability.

The VT-IM-MS methodology employed in Chapter 4, was further applied to probe thermal stability of mAbs, albeit without dissociation. Chapter 5 describes conformational changes occurring in intact mAbs and their fragments at elevated temperatures up to 550 K, aimed to predict thermal stability of therapeutic proteins. IgG1, IgG4 and their Fc-hinge fragments followed unfolding mechanism similar to that of non-covalent protein complexes. Although no dissociation of these covalent molecules is present, mAbs were noted to undergo initial collapse at 350 - 400 K and subsequent unfolding of domains as the buffer gas temperature is increased. The temperature at which the maximum collapse was observed is speculated to be correlated to the solution T_m. Differences in the extent of collapse and unfolding among IgG subclasses occur to be controlled by the differences in the hinge flexibility and strength of non-covalent interactions at the CH3 domain interface. A hybrid IgG (IgG4 with

IgG1 hinge) engineered for enhanced thermal stability, displayed an unfolding pathway which did not resemble the one of other IgGs investigated. No compaction was noted and broader conformational landscapes of this hybrid mAb at temperatures above 300 K acquired suggest higher structural flexibility contributing to increased thermal stability. The unanswered questions about the gas-phase behaviour and unfolding route of this hybrid IgG leave room for further investigation. Nevertheless, VT-IM-MS is a promising tool for probing thermal stability of therapeutic proteins and benefit drug development process aimed at enhancing stability of biologics to reduce aggregation. Furthermore, VT-(IM)-MS methodology could be applied to study extremophile proteins such as thermophilic or antifreeze proteins.

The final results Chapter 6, sets out to probe conformational changes of metabolic enzymes induced by natural feedback allosteric inhibition, and to further elucidate the inhibition mechanism. MtATP-phosphoribosyltransferase (MtATP-PRT) inhibition with L-histidine was probed using native MS, IM-MS and HDX-MS. MtATP-PRT was found to exist in the hexameric state under physiological conditions and to undergo subtle conformational changes upon ligand binding and changes in pH. Ligand induced changes were found to occur only at pH 6.8 as opposed to pH 9. This conformational tightening observed *in vacuo* was further confirmed *via* SV-AUC experiments. HDX-MS methodology was employed to map the conformational changes and the results were found in agreement with x-ray crystallography data. Changes in the deuterium uptake between apo MtATP-PRT and L-histidine bound MtATP-PRT occurring on a short time scale were associated with L-histidine binding to the allosteric site while changes occurring on longer time scales were caused by conformational changes induced by ligand binding. The predicted inhibition mechanism envisions MtATP-PRT as a functional hexamer where conformational changes have to be invoked to explain the allosteric inhibition. Once the protein purification protocol has been established, more experiments will need to be performed to further investigate binding stoichiometry, importance of substrate presence on the inhibition and influence of the buffer pH. In the near future, a combination of MS, IM-MS and HDX-MS, will be applied to scan libraries of MtATP-PRT inhibitor ligands with the aim to discover potential novel anti-tuberculosis agents.

MS has proved to be a valuable tool for investigation of protein structures in solvent-free environment with clear application and benefits to medical and pharmaceutical research. Further method development will help to understand and provide more insight into properties of these biomacromolecules.

Appendix 1: Amino Acid Abbreviations and Properties

Table of amino acids listing their three and one letter code, monoisotopic and average masses.

Amino Acid	Three Letter Code	One Letter Code	Molecular Formula	Monoisotopic Mass	Average Mass
Glycine	Gly	G	$C_2H_5NO_2$	75.03203	75.06660
Alanine	Ala	A	$C_3H_7NO_2$	89.04768	89.09318
Serine	Ser	S	$C_3H_7NO_3$	105.0426	105.0926
Proline	Pro	P	$C_5H_9NO_2$	115.0633	115.1305
Valine	Val	V	$C_5H_{11}NO_2$	117.0790	117.1463
Threonine	Thr	T	$C_4H_9NO_3$	119.0582	119.1192
Cysteine	Cys	C	$C_3H_7NO_2S$	121.0197	121.1582
Leucine	Leu	L	$C_6H_{13}NO_2$	131.0946	131.1729
Isoleucine	Ile	I	$C_6H_{13}NO_2$	131.0946	131.1729
Asparagine	Asn	N	$C_4H_8N_2O_3$	132.0535	132.1179
Aspartic Acid	Asp	D	$C_4H_7NO_4$	133.0375	133.1027
Glutamic Acid	Gln	Q	$C_5H_9NO_4$	147.0532	147.1293
Lysine	Lys	K	$C_6H_{14}N_2O_2$	146.1055	146.1876
Glutamine	Glu	E	$C_5H_{10}N_2O_3$	146.0691	146.1445
Methionine	Met	M	$C_5H_{11}NO_2S$	149.0510	149.2113
Histidine	His	H	$C_6H_9N_3O_2$	155.0695	155.1546
Phenylalanine	Phe	F	$C_9H_{11}NO_2$	165.0790	165.1891
Arginine	Arg	R	$C_6H_{14}N_4O_2$	174.1117	174.2010
Tyrosine	Tyr	Y	$C_9H_{11}NO_3$	181.0739	181.1885
Tryptophan	Trp	W	$C_{11}H_{12}N_2O_2$	204.0899	204.2252

Appendix 2: Amino Acid R Groups

Non Polar Amino Acids

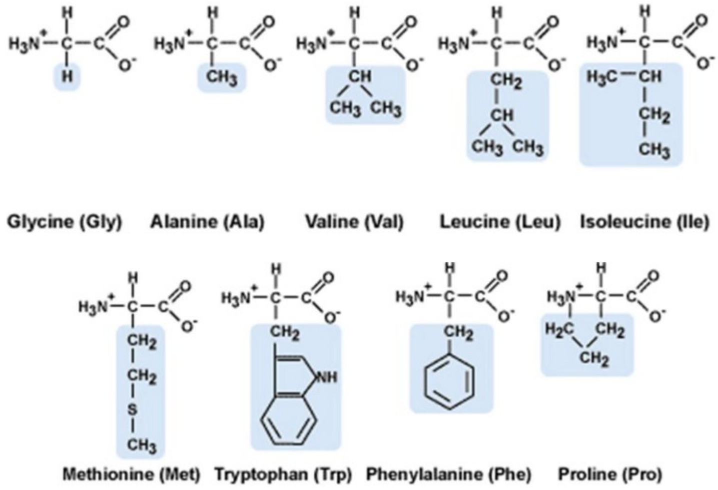

Polar Amino Acids

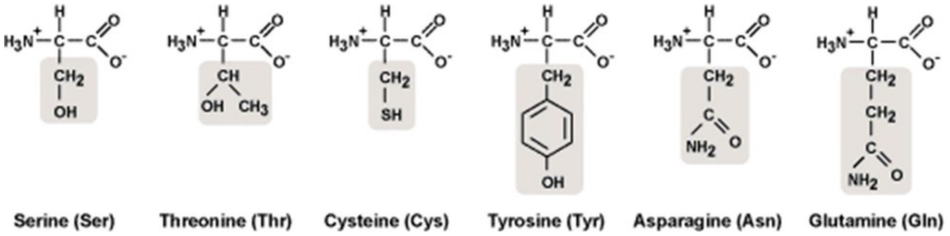

Electrically Charged Amino Acids

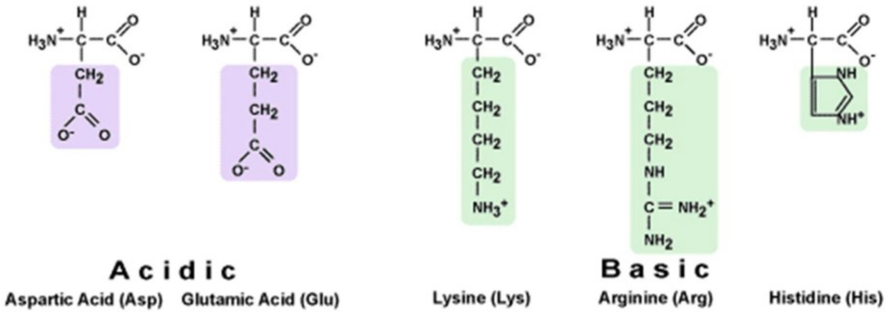

Figure taken from the website of the Department of Biology, Pennsylvania State University https://wikispaces.psu.edu/display/bio110/Carbon+and+Life

Appendix 3: Sequences and Theoretical Masses of Proteins Studied in this Thesis

(variable domains of IgGs provided below are indicated in black)

IgG 'A' anti-TNF

IgG1 - Heavy chain
QVQLVQSGAEVVKPGSSVKVSCKASGYTFTDYNVDWVKQAPGQGLQWIGNINPNNGG
TIYNQKFKGKGTLTVDKSTSTAYMELSSLTSEDTAVYYCARSAFYNNYEYFDVWGQG
TTVTVSSASTKGPSVFPLAPSSKSTSGGTAALGCLVKDYFPEPVTVSWNSGALTSGV
HTFPAVLQSSGLYSLSSVVTVPSSSLGTQTYICNVNHKPSNTKVDKKVEPKSCDKTH
TCPPCPAPELLGGPSVFLFPPKPKDTLMISRTPEVTCVVVDVSHEDPEVKFNWYVDG
VEVHNAKTKPREEQYNSTYRVVSVLTVLHQDWLNGKEYKCKVSNKALPAPIEKTISK
AKGQPREPQVYTLPPSRDELTKNQVSLTCLVKGFYPSDIAVEWESNGQPENNYKTTP
PVLDSDGSFFLYSKLTVDKSRWQQGNVFSCSVMHEALHNHYTQKSLSLSPGK

IgG4 - Heavy chain
QVQLVQSGAEVVKPGSSVKVSCKASGYTFTDYNVDWVKQAPGQGLQWIGNINPNNGG
TIYNQKFKGKGTLTVDKSTSTAYMELSSLTSEDTAVYYCARSAFYNNYEYFDVWGQG
TTVTVSSASTKGPSVFPLAPCSRSTSESTAALGCLVKDYFPEPVTVSWNSGALTSGV
HTFPAVLQSSGLYSLSSVVTVPSSSLGTKTYTCNVDHKPSNTKVDKRVESKYGPPCP
SCPAPEFLGGPSVFLFPPKPKDTLMISRTPEVTCVVVDVSQEDPEVQFNWYVDGVEV
HNAKTKPREEQFNSTYRVVSVLTVLHQDWLNGKEYKCKVSNKGLPSSIEKTISKAKG
QPREPQVYTLPPSQEEMTKNQVSLTCLVKGFYPSDIAVEWESNGQPENNYKTTPPVL
DSDGSFFLYSRLTVDKSRWQEGNVFSCSVMHEALHNHYTQKSLSLSLGK

IgG1 and IgG4 - Light chain (κ)
DIMMTQSPSTLSASVGDRVTITCKSSQSLLYSNNQKNYLAWYQQKPGQAPKLLISWA
STRESGVPSRFIGSGSGTEFTLTISSLQPDDVATYYCQQYYDYPWTFGQGTKVEIKR
TVAAPSVFIFPPSDEQLKSGTASVVCLLNNFYPREAKVQWKVDNALQSGNSQESVTE
QDSKDSTYSLSSTLTLSKADYEKHKVYACEVTHQGLSSPVTKSFNRGEC

	Intact IgG1 A	Intact IgG4 A
Average mass	147 199.13 Da	146 868.42 Da
Monoisotopic mass	147 106.78 Da	146 776.18 Da
Theoretical pI	7.78	7.09

IgG ‘B’ anti-Her

IgG1 - Heavy chain

EVQLVESGGGLVQPGGSLRLSCAASGFNIKDTYIHWVRQAPGKGLEWVARIYPTNGY
TRYADSVKGRFTISADTSKNTAYLQMNSLRAEDTAVYYCSRWGGDGFYAMDYWGQGT
LVTVSSASTKGPSVFPLAPSSKSTSGGTAALGCLVKDYFPEPVTVSWNSGALTSGVH
TFPAVLQSSGLYSLSSVVTVPSSSLGTQTYICNVNHKPSNTKVDKKVEPKSCDKTHT
CPPCPAPELLGGPSVFLFPPKPKDTLMISRTPEVTCVVVDVSHEDPEVKFNWYVDGV
EVHNAKTKPREEQYNSTYRVVSVLTVLHQDWLNGKEYKCKVSNKALPAPIEKTISKA
KGQPREPQVYTLPPSRDELTKNQVSLTCLVKGFYPSDIAVEWESNGQPENNYKTTPP
VLDSDGSFFLYSKLTVDKSRWQQGNVFSCSVMHEALHNHYTQKSLSLSPGK

IgG4 - Heavy chain

EVQLVESGGGLVQPGGSLRLSCAASGFNIKDTYIHWVRQAPGKGLEWVARIYPTNGY
TRYADSVKGRFTISADTSKNTAYLQMNSLRAEDTAVYYCSRWGGDGFYAMDYWGQGT
LVTVSSASTKGPSVFPLAPCSRSTSESTAALGCLVKDYFPEPVTVSWNSGALTSGVH
TFPAVLQSSGLYSLSSVVTVPSSSLGTKTYTCNVDHKPSNTKVDKRVESKYGPPCPS
CPAPEFLGGPSVFLFPPKPKDTLMISRTPEVTCVVVDVSQEDPEVQFNWYVDGVEVH
NAKTKPREEQFNSTYRVVSVLTVLHQDWLNGKEYKCKVSNKGLPSSIEKTISKAKGQ
PREPQVYTLPPSQEEMTKNQVSLTCLVKGFYPSDIAVEWESNGQPENNYKTTPPVLD
SDGSFFLYSRLTVDKSRWQEGNVFSCSVMHEALHNHYTQKSLSLSLGK

IgG1 and IgG4 - Light chain (κ)

DIQMTQSPSSLSASVGDRVTITCRASQDVNTAVAWYQQKPGKAPKLLIYSASFLYSG
VPSRFSGSRSGTDFTLTISSLQPEDFATYYCQQHYTTPPTFGQGTKVEIKRTVAAPS
VFIFPPSDEQLKSGTASVVCLLNNFYPREAKVQWKVDNALQSGNSQESVTEQDSKDS
TYSLSSTLTLSKADYEKHKVYACEVTHQGLSSPVTKSFNRGEC

	Intact IgG1 B	Intact IgG4 B
Average mass	145 337.32 Da	145 006.61 Da
Monoisotopic mass	145 246.13 Da	144 915.53 Da
Theoretical pI	7.99	7.52

IgG ‘C’ anti-KC1

IgG1 - Heavy chain

QVQLQESGPGLVRPSQTLSLTCTVSGYSITSDHAWSWVRQPPGRGLEWIGYISYSGI
TTYNPSLKSRVTMLRDTSKNQFSLRLSSVTAADTAVYYCARSLARTTAMDYWGQGSL
VTVSSASTKGPSVFPLAPSSKSTSGGTAALGCLVKDYFPEPVTVSWNSGALTSGVHT
FPAVLQSSGLYSLSSVVTVPSSSLGTQTYICNVNHKPSNTKVDKKVEPKSCDKTHTC
PPCPAPELLGGPSVFLFPPKPKDTLMISRTPEVTCVVVDVSHEDPEVKFNWYVDGVE
VHNAKTKPREEQYNSTYRVVSVLTVLHQDWLNGKEYKCKVSNKALPAPIEKTISKAK
GQPREPQVYTLPPSRDELTKNQVSLTCLVKGFYPSDIAVEWESNGQPENNYKTTPPV
LDSDGSFFLYSKLTVDKSRWQQGNVFSCSVMHEALHNHYTQKSLSLSPGK

IgG4 - Heavy chain

QVQLQESGPGLVRPSQTLSLTCTVSGYSITSDHAWSWVRQPPGRGLEWIGYISYSGI
TTYNPSLKSRVTMLRDTSKNQFSLRLSSVTAADTAVYYCARSLARTTAMDYWGQGSL
VTVSSASTKGPSVFPLAPCSRSTSESTAALGCLVKDYFPEPVTVSWNSGALTSGVHT
FPAVLQSSGLYSLSSVVTVPSSSLGTKTYTCNVDHKPSNTKVDKRVESKYGPPCPSC
PAPEFLGGPSVFLFPPKPKDTLMISRTPEVTCVVVDVSQEDPEVQFNWYVDGVEVHN
AKTKPREEQFNSTYRVVSVLTVLHQDWLNGKEYKCKVSNKGLPSSIEKTISKAKGQP
REPQVYTLPPSQEEMTKNQVSLTCLVKGFYPSDIAVEWESNGQPENNYKTTPPVLDS
DGSFFLYSRLTVDKSRWQEGNVFSCSVMHEALHNHYTQKSLSLSLGK

IgG4 with IgG1 hinge - Heavy chain

QVQLQESGPGLVRPSQTLSLTCTVSGYSITSDHAWSWVRQPPGRGLEWIGYISYSGI
TTYNPSLKSRVTMLRDTSKNQFSLRLSSVTAADTAVYYCARSLARTTAMDYWGQGSL
VTVSSASTKGPSVFPLAPSSRSTSESTAALGCLVKDYFPEPVTVSWNSGALTSGVHT
FPAVLQSSGLYSLSSVVTVPSSSLGTKTYTCNVDHKPSNTKVDKRVEPKSCDKTHTC
PPCPAPEFLGGPSVFLFPPKPKDTLMISRTPEVTCVVVDVSQEDPEVQFNWYVDGVE
VHNAKTKPREEQFNSTYRVVSVLTVLHQDWLNGKEYKCKVSNKGLPSSIEKTISKAK
GQPREPQVYTLPPSQEEMTKNQVSLTCLVKGFYPSDIAVEWESNGQPENNYKTTPPV
LDSDGSFFLYSRLTVDKSRWQEGNVFSCSVMHEALHNHYTQKSLSLSLGK

IgG1 and IgG4 - Light chain (κ)

DIQMTQSPSSLSASVGDRVTITCRASQDISSYLNWYQQKPGKAPKLLIYYTSRLHSG
VPSRFSGSGSGTDFTFTISSLQPEDIATYYCQQGNTLPYTFGQGTKVEIKRTVAAPS
VFIFPPSDEQLKSGTASVVCLLNNFYPREAKVQWKVDNALQSGNSQESVTEQDSKDS
TYSLSSTLTLSKADYEKHKVYACEVTHQGLSSPVTKSFNRGEC

	Intact IgG1 C	Intact IgG4 C	Intact IgG4 C w/IgG1 C hinge
Average mass	145 255.38 Da	144 924.67 Da	145 649.44 Da
Monoisotopic mass	145 164.37 Da	144 833.77 Da	145 558.16 Da
Theoretical pI	8.26	7.90	7.90

IgG 'C' anti-KC1 Fc-hinge fragment

Fc-hinge fragment IgG1

**EPKSCDKTHTCPPCPAPELLGGPSVFLFPPKPKDTLMISRTPEVTCVVVDVSHEDPE
VKFNWYVDGVEVHNAKTKPREEQYNSTYRVVSVLTVLHQDWLNGKEYKCKVSNKALP
APIEKTISKAKGQPREPQVYTLPPSRDELTKNQVSLTCLVKGFYPSDIAVEWESNGQ
PENNYKTTPPVLDSDGSFFLYSKLTVDKSRWQQGNVFSCSVMHEALHNHYTQKSLSL
SPGK**

Fc-hinge fragment IgG4

**ESKYGPPCPSCPAPEFLGGPSVFLFPPKPKDTLMISRTPEVTCVVVDVSQEDPEVQF
NWYVDGVEVHNAKTKPREEQFNSTYRVVSVLTVLHQDWLNGKEYKCKVSNKGLPSSI
EKTISKAKGQPREPQVYTLPPSQEEMTKNQVSLTCLVKGFYPSDIAVEWESNGQPEN
NYKTTPPVLDSDGSFFLYSRLTVDKSRWQEGNVFSCSVMHEALHNHYTQKSLSLSLG
K**

	Fc-hinge IgG1 C	Fc-hinge IgG4 C
Average mass	52 167.16 Da	51 510.16 Da
Monoisotopic mass	52 134.11 Da	51 477.49 Da
Theoretical pI	7.22	6.13

Transthyretin (TTR)

composed of 4 identical subunits, each with the following sequence:

**GPTGTGESKCPLMVKVLDAVRGSPAINVAVHVFRKAADDTWEPFASGKTSESGELHG
LTTEEEFVEGIYKVEIDTKSYWKALGISPFHEHAEVVFTANDSGPRRYTIAALLSPY
SYSTTAVVTNPKE**

	Monomer	Tetramer
Average mass	13 761.41 Da	54 991.58 Da
Monoisotopic mass	13 752.89 Da	54 957.52 Da
Theoretical pI	5.238	

Avidin

composed of 4 identical subunits, each with the following sequence:

**ARKCSLTGKWTNDLGSNMTIGAVNSRGEFTGTYITAVTATSNEIKESPLHGTQNTIN
KRTQPTFGFTVNWKFSESTTVFTGQCFIDRNGKEVLKTMWLLRSSVNDIGDDWKATR
VGINIFTRLRTQKE**

cabrohydrate moiety 1640 (4-5 x mannose + 3 x N-acetylglucosamine)

	Monomer	Tetramer + carbohydrate
Average mass	14343.17 Da	63 932.68 Da
Monoisotopic mass	14334.25 Da	63 870.00 Da
Theoretical pI	10.281	

Concanavalin A (conA)

composed of 4 identical subunits, each with the following sequence:

**ADTIVAVELDTYPNTDIGDPSYPHIGIDIKSVRSKKTAKWNMQDGKVGTAHIIYNSV
DKRLSAVVSYPNADATSVSYDVDLNDVLPEWVRVGLSASTGLYKETNTILSWSFTSK
LKSNSTHQTDALHFMFNQFSKDQKDLILQGDATTGTDGNLELTRVSSNGSPEGSSVG
RALFYAPVHIWESSAATVSFEATFAFLIKSPDSHPADGIAFFISNIDSSIPSGSTGR
LLGLFPDAN**

	Monomer	Tetramer
Average mass	25 572.38 Da	102 235.48 Da
Monoisotopic mass	25 556.76 Da	102 172.95 Da
Theoretical pI	4.881	

Serum Amyloid P Component (SAP)

composed of 5 identical subunits, each with the following sequence:

**HTDLSGKVFVFPRESVTDHVNLITPLEKPLQNFTLCFRAYSDLSRAYSLFSYNTQGR
DNELLVYKERVGEYSLYIGRHKVTSKVIEKFPAPVHICVSWESSSGIAEFWINGTPL
VKKGLRQGYFVEAQPKIVLGQEQDSYGGKFDRSQSFVGEIGDLYMWDSVLPPENILS
AYQGTPLPANILDWQALNYEIRGYVIIKPLVWV**

	Monomer	Pentamer
Average mass	23 358.53 Da	116 220.58 Da
Monoisotopic mass	23 243.95 Da	116 147.71 Da
Theoretical pI	6.291	

His-Tag Mt-ATP-phosphoribosyltransferase

composed of 6 identical subunits, each with the following sequence:

**MAHHHHHHAAMLRVAVPNKGALSEPATEILAEAGYRRRTDSKDLTVIDPVNNVEFFF
LRPKDIAIYVGSGELDFGITGRDLVCDSGAQVRERLALGFGSSSFRYAAPAGRNWTT
ADLAGMRIATAYPNLVRKDLATKGIEATVIRLDGAVEISVQLGVADAIADVVGSGRT
LSQHDLVAFGEPLCDSEAVLIERAGTDGQDQTEARDQLVARVQGVVFGQQYLMLDYD
CPRSALKKATAITPGLESPTIAPLADPDWVAIRALVPRRDVNGIMDELAAIGAKAIL
ASDIRFCRF**

	Monomer	Hexamer
Average mass	31 648.04 Da	189 798.15 Da
Monoisotopic mass	31 628.31 Da	189 679.80 Da
Theoretical pI	5.557	

* Theoretical pI values were calculated using the online protein isoelectric point calculator available at http://isoelectric.ovh.org/

Appendix 4: Collision Cross Section Distributions

Avidin tetramer

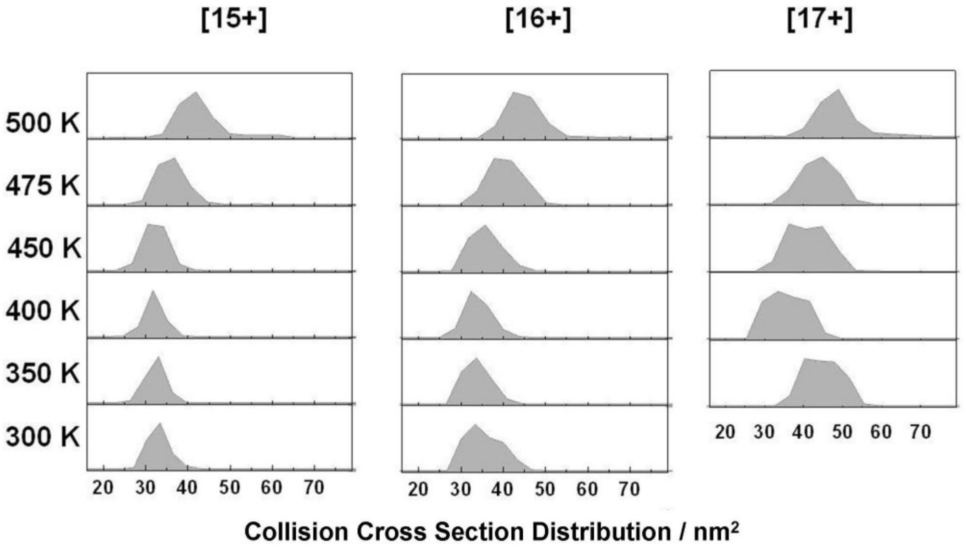

Concanavalin A tetramer

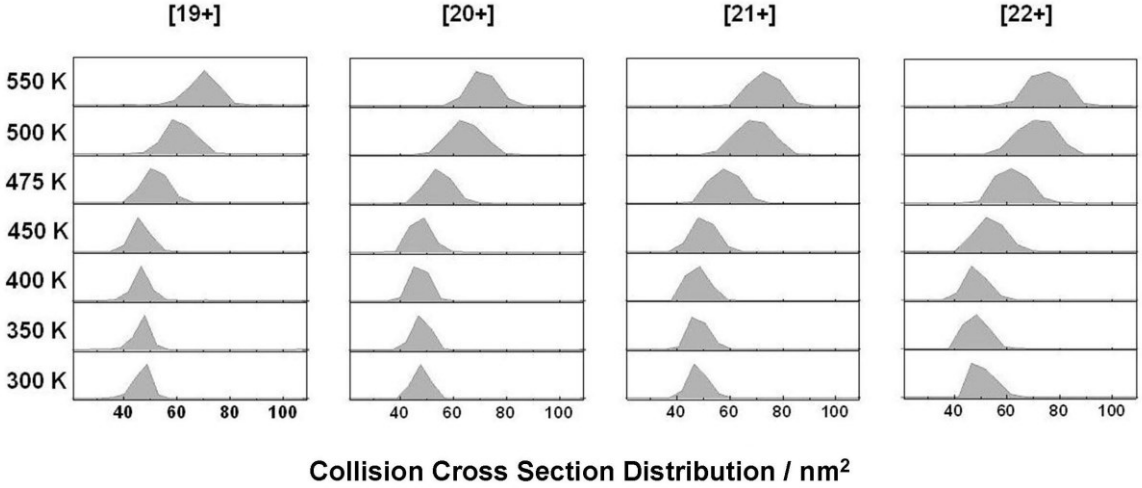

Concanavalin A dimer

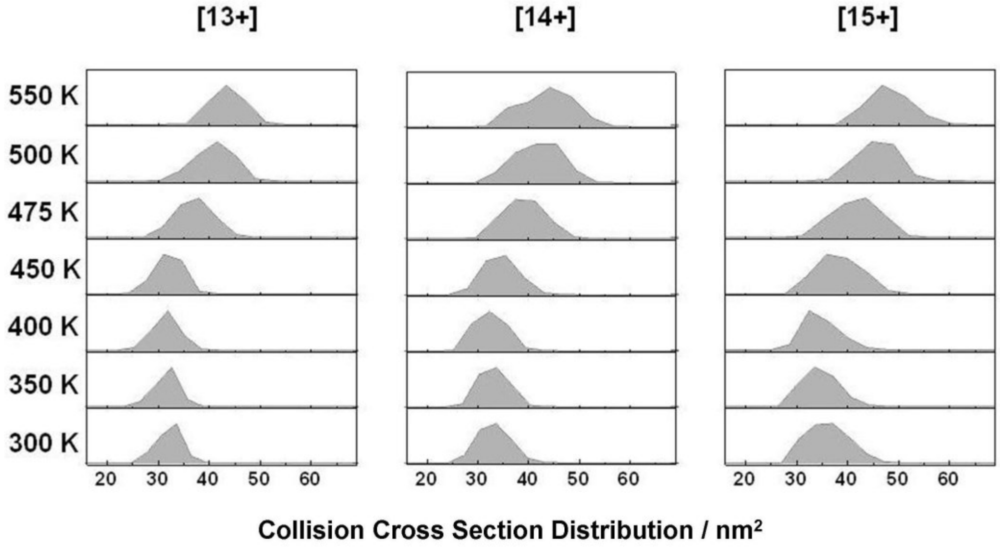

Concanavalin A monomer

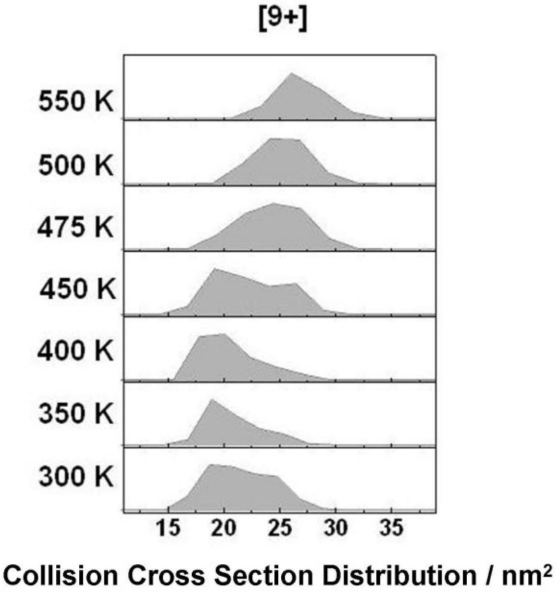

Appendix 5: Median Collision Cross Sections of Protein Complexes at Various Analysis Temperatures

Median collision cross sections (CCS) of transthyretin (TTR) and serum amyloid P component (SAP) at various buffer gas temperatures (T / K) along with relative change in CCS (Δ) for each charge state (CS) with respect to CCS at 300 K. Reported values are averages based on two experimental repeats.
P = pentamer, T = tetramer, M = monomer

	TTR			**SAP**		
T	**CS**	**CCS /nm^2**	**Δ/%**	**CS**	**CCS /nm^2**	**Δ/%**
300 K	T [13+]	31.28 ± 0.15	-	P [22+]	59.08 ± 1.01	-
	T [14+]	32.02 ± 0.52	-	P [23+]	61.41 ± 0.86	-
	T [15+]	33.50 ± 1.30	-	P [24+]	62.86 ± 0.76	-
	-	-	-	P [25+]	63.26 ± 1.02	-
	-	-	-	P [26+]	63.67 ± 0.60	-
350 K	T [13+]	30.73 ± 0.01	-1.74	P [22+]	58.86 ± 0.22	-3.65
	T [14+]	31.39 ± 0.13	-1.97	P [23+]	61.39 ± 0.70	-3.27
	T [15+]	32.30 ± 0.15	-3.60	P [24+]	63.24 ±0.37	-1.86
	-	-	-	P [25+]	63.99 ± 0.26	-0.39
	-	-	-	P [26+]	66.42 ± 0.90	+2.71
400 K	T [13+]	30.57 ± 0.06	-2.25	P [22+]	58.77 ± 0.16	-1.08
	T [14+]	31.12 ± 0.01	-2.81	P [23+]	60.27 ± 1.23	-2.66
	T [15+]	32.28 ± 0.11	-3.64	P [24+]	63.76 ± 2.56	-0.38
	-	-	-	P [25+]	65.47 ± 2.74	+1.09
	-	-	-	P [26+]	71.93 ± 5.09	+8.20
450 K	T [13+]	30.80 ± 0.13	-1.52	P [22+]	60.05 ± 0.88	+0.73
	T [14+]	32.10 ± 0.13	-0.25	P [23+]	64.70 ± 0.18	+3.06
	T [15+]	35.94 ± 0.29	+7.27	P [24+]	69.02 ± 0.11	+6.81
	-	-	-	P [25+]	71.82 ± 0.03	+11.05
	-	-	-	P [26+]	75.31 ± 0.29	+16.69

T	CS	CCS /nm^2	Δ/%	CS	CCS /nm^2	Δ/%
457 K	T [13+]	38.31 ± 0.34	+22.49	P [22+]	66.00 ± 0.22	+12.61
	T [14+]	40.02 ± 0.13	+24.98	P [23+]	68.63 ± 0.16	+11.23
	T [15+]	42.01 ± 0.54	+25.40	P [24+]	71.76 ± 0.01	+14.80
	M [7+]	16.83 ± 0.06	-	P [25+]	74.14 ± 0.33	+18.38
	M [8+]	20.94 ± 0.28	-	P [26+]	77.79 ± 0.43	+25.15
	M [9+]	22.57 ± 0.06	-	-	-	
500 K	T [13+]	39.48 ± 2.19	+26.24	P [22+]	70.76 ± 0.32	+19.07
	T [14+]	44.28 ± 1.15	+38.29	P [23+]	73.34 ± 0.41	+18.14
	T [15+]	47.02 ± 1.14	+40.34	P [24+]	76.14 ± 0.19	+20.43
	M [7+]	16.90 ± 0.08	-	P [25+]	76.43 ± 0.25	+21.76
	M [8+]	19.60 ± 0.01	-	P [26+]	80.66 ± 1.12	+28.05
	M [9+]	21.31 ±0.01	-	M [10+]	25.77 ± 0.54	
	M [10+]	21.59 ± 0.95	-	M [11+]	29.75 ± 0.33	
	-	-	-	M [12+]	32.65 ± 0.42	
	-	-	-	M [13+]	34.22 ± 1.14	
550 K	-	-	-	P [22+]	77.35 ± 0.80	+31.16
	-	-	-	P [23+]	76.56 ± 0.52	+23.98
	-	-	-	P [24+]	81.83 ± 0.04	+29.99
	-	-	-	P [25+]	77.51 ± 1.07	+23.19
	-	-	-	P [26+]	89.70 ± 0.86	+44.21
	-	-	-	M [10+]	28.35 ± 0.01	-
	-	-	-	M [11+]	29.92 ± 0.02	-
	-	-	-	M [12+]	32.22 ± 0.05	-
	-	-	-	M [13+]	33.22 ± 0.01	-

Median collision cross sections (CCS) of avidin and concanavalin A (conA) at various buffer gas temperatures (T / K) along with relative change in CCS (Δ) for each charge state (CS) with respect to CCS at 300 K.
T = tetramer, D = dimer, M = monomer

	Avidin			**ConA**		
T	**CS**	**CCS /nm^2**	**Δ/%**	**CS**	**CCS /nm^2**	**Δ/%**
300 K	T [15+]	32.78	-	T [19+]	47.47	-
	T [16+]	34.76	-	T [20+]	47.98	-
	-	-	-	T [21+]	48.20	-
	-	-	-	T [22+]	50.66	-
	-	-	-	D [13+]	32.45	-
	-	-	-	D [14+]	33.19	-
	-	-	-	D [15+]	35.82	-
	-	-	-	M [9+]	20.87	-
350 K	T [15+]	32.34	-1.34	T [19+]	47.42	-0.11
	T [16+]	33.77	-2.85	T [20+]	48.14	+0.33
	T [17+]	46.33	-	T [21+]	48.44	+0.50
	-	-	-	T [22+]	48.69	-3.89
	-	-	-	D [13+]	31.98	-1.45
	-	-	-	D [14+]	33.17	-0.06
	-	-	-	D [15+]	34.66	-3.24
	-	-	-	M [9+]	20.07	-3.83
400 K	T [15+]	31.86	-2.81	T [19+]	46.76	-1.50
	T [16+]	33.75	-2.91	T [20+]	47.50	-1.00
	T [17+]	40.95	-	T [21+]	47.73	-0.98
	-	-	-	T [22+]	48.34	-4.58
	-	-	-	D [13+]	31.58	-2.68
	-	-	-	D [14+]	32.52	-2.02
	-	-	-	D [15+]	34.32	-4.19
	-	-	-	M [9+]	19.88	-4.74

T	CS	CCS /nm^2	Δ/%	CS	CCS /nm^2	Δ/%
450 K	T [15+]	32.62	-1.65	T [19+]	46.63	-1.77
	T [16+]	35.79	+2.96	T [20+]	47.47	-1.06
	T [17+]	41.23	-	T [21+]	50.38	+4.52
	-	-	-	T [22+]	54.25	+7.09
	-	-	-	D [13+]	32.16	-0.89
	-	-	-	D [14+]	34.46	+3.83
	-	-	-	D [15+]	38.26	+6.81
	-	-	-	M [9+]	21.68	+3.88
457 K	T [15+]	35.62	+8.66	T [19+]	52.20	+9.96
	T [16+]	40.29	+15.91	T [20+]	54.54	+13.67
	T [17+]	43.81	-	T [21+]	58.33	+21.02
	M [7+]	16.95	-	T [22+]	62.36	+22.90
	M [8+]	19.28	-	D [13+]	37.18	+14.58
	M [9+]	21.66	-	D [14+]	39.35	+18.56
	M [10+]	22.60	-	D [15+]	42.02	+17.31
	M [11+]	22.40	-	M [9+]	24.56	+17.68
500 K	T [15+]	40.81	+24.50	T [19+]	61.13	+28.78
	T [16+]	44.33	+27.53	T [20+]	64.57	+34.58
	T [17+]	47.33	-	T [21+]	69.28	+43.73
	M [7+]	17.14	-	T [22+]	72.10	+42.32
	M [8+]	18.31	-	D [13+]	41.36	+27.46
	M [9+]	20.08	-	D [14+]	42.05	+26.69
	M [10+]	20.65	-	D [15+]	45.88	+28.08
	M [11+]	20.99	-	M [9+]	25.06	+20.08
	-	-	-	M [10+]	27.84	-
	-	-	-	M [11+]	29.38	-
	-	-	-	M [12+]	31.20	-
	-	-	-	M [13+]	33.18	-
	-	-	-	M [14+]	35.14	-

	CS	CCS /nm^2	Δ/%	CS	CCS /nm^2	Δ/%
	-	-	-	M [15+]	35.26	-
	-	-	-	M [16+]	28.47	-
	-	-	-	M [18+]	39.93	-
550 K	-	-	-	T [19+]	70.01	+47.48
	-	-	-	T [20+]	71.12	+48.23
	-	-	-	T [21+]	73.05	+51.56
	-	-	-	T [22+]	74.93	+47.91
	-	-	-	D [13+]	43.31	+33.47
	-	-	-	D [14+]	44.00	+32.57
	-	-	-	D [15+]	47.45	+32.47
	-	-	-	M [9+]	26.72	+28.03
	-	-	-	M [10+]	28.15	-
	-	-	-	M [11+]	29.69	-
	-	-	-	M [12+]	32.72	-
	-	-	-	M [13+]	34.86	-
	-	-	-	M [14+]	38.37	-
	-	-	-	M [15+]	40.43	-
	-	-	-	M [16+]	37.79	-
	-	-	-	M [18+]	39.74	-

Appendix 6: Median Collision Cross Sections of IgGs and Fc-hinge Fragments at Various Analysis Temperatures

Median collision cross sections (CCS) of IgGs ‘C’ at various buffer gas temperatures (T / K) along with relative change in CCS (Δ) for each charge state (CS) with respect to CCS at 300 K, based on one experimental repeat. *CS = charge state

		IgG1		IgG4		IgG4 + IgG1 hinge	
T	**CS**	**CCS /nm^2**	**Δ/%**	**CCS /nm^2**	**Δ/%**	**CCS /nm^2**	**Δ/%**
300 K	**22**	60.99		58.20		58.57	
	23	63.42		60.26		59.83	
	24	67.43		63.77		61.98	
	25	72.58		67.21		65.11	
	26	81.57		75.30		70.15	
350 K	**22**	58.40	-4.25	57.10	-1.89	57.42	-1.96
	23	60.21	-5.06	59.31	-1.58	60.47	1.07
	24	63.58	-5.71	62.91	-1.35	65.24	5.26
	25	67.34	-7.22	68.01	1.19	71.73	10.17
	26	71.78	-12.00	72.26	-4.04	77.43	10.38
360 K	**22**	56.57	-7.25	58.16	-0.07	58.25	-0.55
	23	60.16	-5.14	58.99	-2.11	60.90	1.79
	24	63.00	-6.57	62.60	-1.83	66.47	7.24
	25	67.02	-7.66	67.97	1.13	72.55	11.43
	26	71.65	-12.16	73.53	-2.35	78.92	12.50
400 K	**22**	56.66	-7.10	54.62	-6.15	57.02	-2.65
	23	59.44	-6.28	59.59	-1.11	60.70	1.45
	24	62.42	-7.43	63.92	0.24	66.05	6.57
	25	65.63	-9.58	70.76	5.28	72.45	11.27
	26	69.37	-14.96	75.18	-0.16	76.10	8.48
475 K	**22**	60.49	-0.82	64.13	10.19	64.17	9.56
	23	67.90	7.06	68.85	14.25	68.67	14.78
	24	71.45	5.96	71.91	12.76	72.23	16.54
	25	73.39	1.12	74.96	11.53	75.89	16.56
	26	78.77	-3.43	76.18	1.17	81.35	15.97
500 K	**22**	69.67	14.23	71.06	22.10	71.03	21.27
	23	73.49	15.88	74.11	22.98	73.76	23.28
	24	76.76	13.84	76.80	20.43	77.12	24.43
	25	79.26	9.20	80.30	19.48	80.02	22.90
	26	80.30	-1.56	84.91	12.76	83.67	19.27
550 K	**22**	73.18	19.99	76.33	31.15	72.69	24.11
	23	76.51	20.64	78.40	30.10	77.76	29.97
	24	82.02	21.64	80.72	26.58	83.26	34.33
	25	83.74	15.38	83.38	24.06	86.74	33.22
	26	83.65	2.55	86.99	15.52	87.76	25.10

Median collision cross sections (CCS) of Fc-hinge fragments at various buffer gas temperatures (T / K) along with relative change in CCS (Δ) for each charge state (CS) with respect to CCS at 300 K, based on one experimental repeat. *CS = charge state

		IgG1 Fc-hinge fragment		**IgG4 Fc-hinge fragment**	
T	**CS**	**CCS /nm^2**	**Δ/%**	**CCS /nm^2**	**Δ/%**
300 K	**12**	30.26		29.44	
	13	30.28		30.67	
	14	31.05		35.54	
350 K	**12**	29.52	-2.45	28.89	-1.87
	13	29.64	-2.11	30.39	-0.91
	14	31.46	1.32	38.37	7.96
400 K	**12**	29.12	-3.77	28.45	-3.36
	13	29.45	-2.74	30.20	-1.53
	14	30.79	-0.84	35.88	0.96
475 K	**12**	29.88	-1.26	28.43	-3.43
	13	30.85	1.88	31.71	3.39
	14	35.44	14.14	38.13	7.29
500 K	**12**	32.51	7.44	30.43	3.36
	13	35.30	16.58	35.70	16.40
	14	41.28	32.95	42.48	19.53
550 K	**12**	36.44	20.42	34.38	16.78
	13	39.05	28.96	40.36	31.59
	14	42.35	36.39	42.55	19.72

Appendix 7: MtATP-PRT HDX data

List of peptides identified

peptide #	Start residue	End residue	Maximum D uptake	Sequence
1	12	27	13	LRVAVPNKGALSEPAT
2	12	28	14	LRVAVPNKGALSEPATE
3	12	30	16	LRVAVPNKGALSEPATEIL
4	13	28	13	RVAVPNKGALSEPATE
5	13	30	15	RVAVPNKGALSEPATEIL
6	29	35	6	ILAEAGY
7	44	51	6	LTVIDPVN
8	44	52	7	LTVIDPVNN
9	44	55	10	LTVIDPVNNVEF
10	45	55	9	TVIDPVNNVEF
11	46	55	8	VIDPVNNVEF
12	47	55	7	IDPVNNVEF
13	56	62	5	FFLRPKD
14	56	64	7	FFLRPKDIA
15	57	65	7	FLRPKDIAI
16	63	71	8	IAIYVGSGE
17	63	73	10	IAIYVGSGELD
18	63	74	11	IAIYVGSGELDF
19	65	74	9	IYVGSGELDF
20	66	73	7	YVGSGELD
21	66	74	8	YVGSGELDF
22	66	80	14	YVGSGELDFGITGRD
23	67	80	13	VGSGELDFGITGRD
24	72	80	8	LDFGITGRD
25	73	79	6	DFGITGR
26	73	80	7	DFGITGRD
27	81	88	7	LVCDSGAQ
28	81	91	10	LVCDSGAQVRE
29	84	93	9	DSGAQVRERL
30	89	102	13	VRERLALGFGSSSF
31	92	102	10	RLALGFGSSSF
32	94	101	7	ALGFGSSS
33	94	102	8	ALGFGSSSF
34	96	102	6	GFGSSSF
35	102	111	8	FRYAAPAGRN
36	103	111	7	RYAAPAGRN
37	103	117	13	RYAAPAGRNWTTADL
38	112	119	7	WTTADLAG
39	117	129	11	LAGMRIATAYPNL
40	120	129	8	MRIATAYPNL
41	121	129	7	RIATAYPNL
42	130	140	10	VRKDLATKGIE

peptide #	Start residue	End residue	Maximum D uptake	Sequence
43	130	141	11	VRKDLATKGIEA
44	130	142	12	VRKDLATKGIEAT
45	142	151	9	TVIRLDGAVE
46	143	149	6	VIRLDGA
47	143	151	8	VIRLDGAVE
48	152	159	7	ISVQLGVA
49	152	160	8	ISVQLGVAD
50	152	161	9	ISVQLGVADA
51	154	161	7	VQLGVADA
52	157	163	6	GVADAIA
53	157	164	7	GVADAIAD
54	160	179	19	DAIADVVGSGRTLSQHDLVA
55	162	179	17	IADVVGSGRTLSQHDLVA
56	164	179	0	DVVGSGRTLSQHDLVA
57	165	179	14	VVGSGRTLSQHDLVA
58	180	186	5	FGEPLCD
59	180	188	7	FGEPLCDSE
60	190	209	19	VLIERAGTDGQDQTEARDQL
61	191	199	8	LIERAGTDG
62	192	209	17	IERAGTDGQDQTEARDQL
63	210	218	8	VARVQGVVF
64	210	221	11	VARVQGVVFGQQ
65	210	222	12	VARVQGVVFGQQY
66	210	223	13	VARVQGVVFGQQYL
67	212	218	6	RVQGVVF
68	212	221	9	RVQGVVFGQQ
69	212	223	11	RVQGVVFGQQYL
70	225	233	7	LDYDCPRSA
71	225	234	8	LDYDCPRSAL
72	226	246	18	DYDCPRSALKKATAITPGLES
73	226	259	28	DYDCPRSALKKATAITPGLESPTIAPLADPDWVA
74	227	234	6	YDCPRSAL
75	235	246	10	KKATAITPGLES
76	235	259	0	KKATAITPGLESPTIA
77	237	245	7	ATAITPGLE
78	242	259	14	PGLESPTIAPLADPDWVA
79	249	257	6	IAPLADPDW
80	258	273	14	VAIRALVPRRDVNGIM
81	260	273	12	IRALVPRRDVNGIM
82	260	275	14	IRALVPRRDVNGIMDE
83	276	285	9	LAAIGAKAIL
84	277	285	8	AAIGAKAIL
85	279	285	6	IGAKAIL

D uptake – MtATP-PRT at pH 6.8

Average relative D uptake at 1 minute, 10 minutes, 30 minutes and 120 minutes of exposure along with standard deviation values (SD).

pH 6.8	**D UPTAKE /Da**							
peptide #	**1 min**	**SD**	**10 min**	**SD**	**30 min**	**SD**	**120 min**	**SD**
1	3.04	0.04	3.04	0.05	3.38	0.08	4.08	0.09
2	3.06	0.04	3.04	0.03	3.38	0.05	4.07	0.10
3	2.86	0.05	2.84	0.04	3.12	0.05	3.79	0.08
4	3.05	0.03	3.02	0.05	3.30	0.06	4.01	0.10
5	2.98	0.08	2.99	0.07	3.27	0.08	3.95	0.14
6	0.30	0.04	0.33	0.05	0.46	0.04	0.75	0.04
7	1.77	0.09	2.17	0.16	2.43	0.09	2.96	0.09
8	1.90	0.06	2.48	0.04	2.86	0.06	3.39	0.08
9	1.85	0.03	2.29	0.05	2.69	0.04	3.27	0.09
10	1.73	0.12	2.08	0.05	2.25	0.09	2.43	0.24
11	1.19	0.03	1.50	0.06	1.70	0.04	1.89	0.06
12	1.10	0.08	1.42	0.05	1.54	0.05	1.69	0.08
13	0.91	0.02	1.04	0.02	1.21	0.02	1.39	0.02
14	1.18	0.11	1.62	0.05	1.86	0.03	2.12	0.03
15	1.06	0.10	1.62	0.11	1.94	0.09	2.21	0.11
16	1.16	0.10	1.51	0.06	1.87	0.07	2.37	0.06
17	0.61	0.03	0.93	0.03	1.18	0.07	1.73	0.04
18	0.48	0.06	0.69	0.05	1.02	0.07	1.57	0.13
19	0.62	0.04	0.91	0.03	1.27	0.03	1.74	0.04
20	0.53	0.01	0.84	0.02	1.20	0.03	1.65	0.07
21	0.68	0.03	1.05	0.02	1.45	0.03	2.02	0.06
22	0.94	0.12	1.69	0.12	2.12	0.02	2.54	0.15
23	1.13	0.09	1.63	0.10	2.05	0.03	2.34	0.04
24	0.92	0.07	1.16	0.06	1.23	0.06	1.32	0.15
25	0.72	0.02	0.92	0.01	1.00	0.01	1.06	0.01
26	0.74	0.11	0.86	0.07	1.04	0.10	1.03	0.06
27	1.96	0.03	1.96	0.03	2.05	0.07	2.23	0.04
28	3.00	0.04	3.54	0.12	3.72	0.15	3.72	0.08
29	2.51	0.14	2.70	0.16	2.83	0.12	2.91	0.18
30	2.28	0.20	2.54	0.13	3.02	0.28	3.40	0.19
31	1.86	0.03	2.16	0.01	2.50	0.06	3.05	0.03
32	1.97	0.03	2.04	0.07	2.17	0.02	2.57	0.04
33	1.24	0.03	1.49	0.04	1.86	0.06	2.39	0.07
34	1.60	0.01	1.74	0.01	1.86	0.02	2.00	0.02
35	2.25	0.06	2.41	0.06	2.56	0.05	3.05	0.13
36	2.31	0.04	2.46	0.01	2.56	0.03	2.87	0.02
37	3.69	0.04	4.02	0.02	4.42	0.05	5.17	0.08
38	1.17	0.05	1.30	0.02	1.62	0.07	2.15	0.04
39	0.55	0.08	0.88	0.06	1.70	0.12	3.17	0.08
40	0.39	0.16	0.65	0.16	1.13	0.18	2.19	0.18
41	0.39	0.24	0.59	0.20	0.98	0.21	1.92	0.20

peptide #	1 min	SD	10 min	SD	30 min	SD	120 min	SD
42	1.35	0.04	2.08	0.04	2.37	0.03	2.88	0.05
43	1.95	0.06	2.79	0.05	3.04	0.05	3.55	0.04
44	2.08	0.15	3.15	0.19	3.54	0.14	4.33	0.10
45	2.17	0.09	2.86	0.08	3.47	0.06	4.27	0.13
46	1.33	0.05	1.56	0.06	1.80	0.08	2.17	0.07
47	2.01	0.04	2.63	0.06	3.12	0.04	3.75	0.02
48	1.37	0.03	1.75	0.03	2.07	0.01	2.91	0.03
49	1.45	0.11	1.83	0.07	2.19	0.06	2.97	0.08
50	1.70	0.17	2.16	0.36	2.43	0.04	3.29	0.10
51	0.70	0.03	1.00	0.03	1.27	0.05	1.86	0.05
52	0.40	0.06	0.38	0.04	0.61	0.07	1.29	0.07
53	0.45	0.08	0.44	0.02	0.68	0.08	1.48	0.12
54	6.01	0.07	6.14	0.07	6.72	0.12	7.97	0.11
55	4.44	0.11	4.84	0.09	5.23	0.10	6.00	0.07
57	2.83	0.04	3.28	0.12	3.40	0.07	3.64	0.03
58	0.71	0.03	0.70	0.05	0.82	0.09	1.28	0.04
59	0.56	0.04	0.66	0.04	0.96	0.05	1.46	0.07
60	6.35	0.18	6.93	0.10	7.17	0.16	7.62	0.15
61	1.16	0.09	1.48	0.12	1.87	0.15	2.40	0.08
62	5.97	0.06	6.40	0.04	6.60	0.13	7.01	0.12
63	0.24	0.02	0.32	0.02	0.86	0.02	2.02	0.02
64	0.58	0.05	0.95	0.07	2.31	0.06	3.89	0.06
65	0.63	0.11	1.19	0.08	2.72	0.03	4.56	0.07
66	0.61	0.04	1.21	0.05	2.93	0.03	4.82	0.15
67	0.15	0.03	0.22	0.02	0.69	0.04	1.66	0.03
68	0.57	0.06	0.99	0.07	1.94	0.07	3.52	0.14
69	0.49	0.07	1.03	0.07	2.83	0.16	4.75	0.08
70	0.72	0.05	1.08	0.10	2.02	0.07	2.63	0.08
71	0.82	0.03	1.26	0.04	2.44	0.03	3.22	0.03
72	4.31	0.31	5.62	0.18	7.56	0.30	8.65	0.27
73	6.10	0.18	9.13	0.17	11.32	0.26	13.03	0.31
74	0.80	0.09	1.17	0.10	2.05	0.09	2.57	0.09
75	2.55	0.04	3.07	0.17	4.11	0.02	4.83	0.17
77	1.48	0.06	1.75	0.02	2.35	0.02	2.91	0.05
78	3.45	0.09	4.65	0.06	5.29	0.17	6.06	0.15
79	1.20	0.03	1.82	0.14	2.07	0.14	2.38	0.07
80	1.49	0.08	1.81	0.09	3.28	0.07	5.24	0.16
81	1.53	0.03	1.77	0.04	2.84	0.03	4.24	0.07
82	1.68	0.13	2.00	0.17	3.29	0.18	4.65	0.18
83	0.53	0.02	1.50	0.03	2.86	0.02	4.32	0.03
84	0.50	0.02	1.38	0.03	2.61	0.03	3.92	0.04
85	0.42	0.04	1.08	0.06	2.23	0.10	3.26	0.16

D uptake – MtATP-PRT + L-histidine at pH 6.8

Average relative D uptake at 1 minute, 10 minutes, 30 minutes and 120 minutes of exposure along with standard deviation values (SD).

pH 6.8	**D UPTAKE /Da**							
peptide #	**1 min**	**SD**	**10 min**	**SD**	**30 min**	**SD**	**120 min**	**SD**
1	3.05	0.03	3.00	0.03	3.25	0.03	3.67	0.06
2	3.03	0.04	2.97	0.04	3.22	0.02	3.60	0.05
3	2.84	0.03	2.77	0.02	2.94	0.03	3.25	0.06
4	3.03	0.04	2.97	0.03	3.26	0.03	3.60	0.06
5	2.95	0.08	2.89	0.09	3.09	0.08	3.43	0.10
6	0.36	0.06	0.31	0.06	0.41	0.03	0.65	0.04
7	1.80	0.05	2.07	0.13	2.17	0.04	2.38	0.04
8	1.95	0.05	2.43	0.04	2.61	0.04	2.78	0.04
9	1.89	0.11	2.23	0.05	2.41	0.10	2.62	0.06
10	1.76	0.08	2.02	0.17	2.20	0.05	2.13	0.12
11	1.21	0.02	1.53	0.04	1.66	0.05	1.67	0.02
12	1.10	0.06	1.39	0.06	1.48	0.08	1.51	0.06
13	0.87	0.02	1.03	0.02	1.23	0.02	1.32	0.03
14	1.12	0.05	1.58	0.05	1.89	0.05	2.03	0.05
15	1.06	0.08	1.66	0.14	1.96	0.06	2.12	0.09
16	1.04	0.03	1.37	0.02	1.64	0.04	1.87	0.05
17	0.56	0.04	0.83	0.06	1.13	0.03	1.47	0.02
18	0.42	0.07	0.67	0.09	0.93	0.07	1.29	0.06
19	0.61	0.03	0.86	0.03	1.23	0.03	1.62	0.03
20	0.53	0.02	0.80	0.03	1.13	0.01	1.54	0.03
21	0.65	0.03	1.00	0.02	1.42	0.02	1.93	0.04
22	1.05	0.05	1.63	0.04	2.18	0.11	2.67	0.05
23	1.10	0.11	1.61	0.10	2.06	0.09	2.42	0.05
24	0.90	0.05	1.11	0.06	1.21	0.06	1.21	0.07
25	0.69	0.02	0.89	0.01	0.98	0.01	0.98	0.02
26	0.76	0.11	1.02	0.11	1.03	0.11	1.05	0.12
27	1.96	0.02	1.93	0.03	2.01	0.04	2.07	0.04
28	3.33	0.16	3.40	0.05	3.64	0.01	3.66	0.08
29	2.56	0.18	2.80	0.10	2.94	0.08	2.96	0.15
30	2.35	0.07	2.45	0.15	2.68	0.13	3.28	0.14
31	1.89	0.05	2.04	0.02	2.35	0.05	2.83	0.06
32	2.14	0.14	2.38	0.06	2.17	0.07	2.47	0.03
33	1.20	0.04	1.37	0.03	1.68	0.04	2.21	0.06
34	1.59	0.04	1.64	0.03	1.80	0.02	1.93	0.06
35	2.21	0.06	2.40	0.07	2.40	0.03	2.37	0.05
36	2.31	0.04	2.40	0.03	2.43	0.04	2.41	0.04
37	3.64	0.04	3.89	0.02	4.14	0.02	4.46	0.08
38	1.18	0.05	1.21	0.04	1.49	0.03	1.81	0.04
39	0.45	0.04	0.69	0.05	0.99	0.04	1.28	0.04
40	0.32	0.17	0.41	0.17	0.61	0.17	0.85	0.17
41	0.31	0.28	0.48	0.27	0.64	0.27	0.88	0.28

peptide #	1 min	SD	10 min	SD	30 min	SD	120 min	SD
42	1.30	0.03	2.03	0.03	2.20	0.03	2.23	0.04
43	1.90	0.04	2.76	0.04	2.89	0.05	2.93	0.05
44	2.02	0.10	3.10	0.15	3.32	0.18	3.51	0.22
45	2.13	0.08	2.80	0.07	3.23	0.06	3.73	0.07
46	1.30	0.03	1.52	0.06	1.71	0.09	1.83	0.07
47	1.96	0.02	2.53	0.02	2.94	0.03	3.36	0.03
48	1.33	0.01	1.69	0.01	1.75	0.02	1.86	0.03
49	1.46	0.05	1.84	0.06	1.90	0.03	2.09	0.06
50	1.68	0.31	1.99	0.03	2.11	0.04	2.27	0.06
51	0.65	0.03	0.91	0.01	0.98	0.01	1.02	0.01
52	0.35	0.03	0.29	0.03	0.31	0.03	0.33	0.04
53	0.45	0.02	0.36	0.02	0.42	0.07	0.48	0.05
54	5.88	0.09	6.05	0.04	6.40	0.05	6.96	0.12
55	4.39	0.11	4.78	0.08	5.15	0.07	5.58	0.10
57	2.84	0.03	3.23	0.03	3.38	0.03	3.34	0.05
58	0.57	0.05	0.57	0.04	0.64	0.04	0.84	0.05
59	0.52	0.02	0.55	0.03	0.71	0.04	1.09	0.04
60	6.58	0.16	7.01	0.16	7.22	0.11	7.52	0.13
61	1.21	0.06	1.32	0.10	1.67	0.11	2.17	0.07
62	5.99	0.03	6.42	0.03	6.69	0.03	6.98	0.10
63	0.22	0.01	0.21	0.01	0.24	0.01	0.31	0.01
64	0.49	0.03	0.60	0.03	0.87	0.02	1.24	0.03
65	0.49	0.04	0.62	0.05	0.96	0.02	1.37	0.04
66	0.45	0.05	0.67	0.04	0.90	0.10	1.26	0.09
67	0.13	0.03	0.11	0.03	0.11	0.02	0.18	0.02
68	0.51	0.08	0.63	0.07	0.82	0.07	1.22	0.06
69	0.52	0.11	0.65	0.07	0.82	0.11	1.16	0.07
70	0.66	0.05	0.90	0.03	1.30	0.03	1.92	0.06
71	0.76	0.03	1.00	0.03	1.43	0.03	2.08	0.05
72	3.16	0.13	4.43	0.34	5.37	0.10	7.08	0.17
73	3.87	0.18	5.65	0.17	7.26	0.21	10.01	0.20
74	0.81	0.08	1.02	0.07	1.41	0.07	2.02	0.09
75	1.50	0.07	2.30	0.07	2.78	0.06	3.26	0.26
77	1.43	0.06	1.76	0.02	2.12	0.06	2.55	0.08
78	1.77	0.04	2.74	0.08	3.44	0.13	4.28	0.11
79	1.24	0.05	1.83	0.05	2.03	0.06	2.24	0.06
80	1.54	0.14	1.60	0.15	2.04	0.10	2.72	0.15
81	1.54	0.02	1.69	0.03	2.07	0.03	2.77	0.05
82	1.75	0.13	2.03	0.12	2.55	0.13	3.30	0.14
83	0.80	0.01	1.61	0.01	1.99	0.03	2.29	0.03
84	0.76	0.01	1.45	0.01	1.72	0.01	1.80	0.03
85	0.61	0.04	1.20	0.05	1.42	0.07	1.50	0.06

D uptake – MtATP-PRT at pH 9

Average relative D uptake at 1 minute, 10 minutes, 30 minutes and 120 minutes of exposure along with standard deviation values (SD).

pH 9	D UPTAKE /Da							
peptide #	1 min	SD	10 min	SD	30 min	SD	120 min	SD
1	4.13	0.13	4.31	0.13	4.88	0.13	5.56	0.39
2	4.30	0.04	4.40	0.09	5.03	0.11	5.74	0.13
3	4.40	0.02	4.60	0.05	5.24	0.06	6.05	0.14
4	4.01	0.15	4.25	0.12	4.81	0.18	5.44	0.22
5	4.71	2.24	4.82	1.85	5.39	1.55	6.08	1.05
6	0.82	0.13	0.96	0.05	1.09	0.17	1.59	0.09
7	2.21	0.15	2.42	0.08	2.83	0.19	2.97	0.16
8	2.43	0.11	2.75	0.12	3.19	0.11	3.47	0.12
9	3.79	0.27	4.01	0.25	4.27	0.23	4.53	0.22
10	2.24	1.09	2.45	0.81	2.82	1.35	3.01	1.51
11	1.55	0.04	1.85	0.05	2.06	0.06	2.34	0.06
12	1.44	0.08	1.72	0.06	1.86	0.08	2.12	0.09
13	1.06	0.02	1.24	0.02	1.39	0.02	1.54	0.03
14	1.49	0.03	1.89	0.03	2.14	0.03	2.41	0.04
15	1.51	0.08	1.99	0.08	2.27	0.07	2.56	0.08
16	1.60	0.26	1.98	0.44	2.37	0.38	2.68	0.23
17	0.89	0.17	1.26	0.15	1.59	0.25	2.13	0.45
18	0.91	0.12	1.31	0.08	1.68	0.15	2.38	0.15
19	1.12	0.04	1.49	0.04	1.94	0.04	2.36	0.06
20	0.89	0.02	1.25	0.03	1.61	0.01	2.03	0.02
21	1.20	0.03	1.64	0.02	2.12	0.04	2.53	0.02
22	1.69	0.24	2.67	0.17	3.42	0.23	3.82	0.24
23	1.75	0.27	2.35	0.24	2.87	0.21	3.33	0.30
24	1.38	0.03	1.49	0.14	1.66	0.16	1.92	0.17
25	0.97	0.03	1.13	0.03	1.23	0.06	1.42	0.08
26	1.05	0.03	1.20	0.12	1.31	0.07	1.54	0.11
27	2.20	0.04	2.10	0.06	2.17	0.09	2.27	0.16
28	3.68	0.22	3.80	0.12	3.96	0.13	4.07	0.34
29	2.90	0.19	3.18	0.22	3.40	0.22	3.46	0.27
30	2.62	0.18	2.92	0.08	3.37	0.12	3.99	0.27
31	2.26	0.05	2.60	0.60	3.16	0.76	3.55	0.67
32	2.30	0.09	2.24	0.02	2.36	0.03	2.65	0.07
33	1.53	0.04	1.74	0.04	2.04	0.05	2.48	0.07
34	1.64	0.02	1.68	0.03	1.77	0.07	1.88	0.04
35	2.80	0.07	2.86	0.06	3.11	0.10	3.54	0.11
36	2.76	0.06	2.80	0.07	2.94	0.07	3.16	0.09
37	4.80	0.25	4.86	1.18	5.48	1.48	6.04	1.69
38	1.70	0.44	1.97	0.75	2.20	0.58	2.59	0.63
39	1.72	0.23	2.32	0.26	3.08	0.27	4.05	0.21
40	1.24	0.40	1.81	0.45	2.28	0.41	3.30	0.42
41	1.36	0.58	1.60	0.26	2.16	0.72	3.19	0.36

peptide #	1 min	SD	10 min	SD	30 min	SD	120 min	SD
42	2.18	0.04	2.59	0.05	2.91	0.03	3.34	0.07
43	2.81	0.05	3.19	0.03	3.46	0.02	3.93	0.06
44	3.23	0.15	3.73	0.14	4.17	0.16	4.86	0.12
45	2.69	0.10	3.18	0.06	3.78	0.07	4.32	0.14
46	1.60	0.09	1.72	0.06	1.89	0.06	2.17	0.07
47	2.45	0.03	2.82	0.02	3.32	0.02	3.70	0.06
48	1.90	0.18	2.26	0.13	2.68	0.13	3.47	0.16
49	2.00	0.51	2.55	0.50	3.01	0.46	3.69	0.49
50	2.31	0.14	2.65	0.13	3.17	0.22	3.95	0.15
51	1.12	0.06	1.38	0.03	1.78	0.11	2.31	0.05
52	0.62	0.11	0.83	0.06	1.61	0.36	1.71	0.08
53	1.10	0.13	1.09	0.10	1.52	0.08	2.11	0.10
54	6.82	0.07	7.00	0.11	7.72	0.10	8.69	0.19
55	5.00	0.03	5.21	0.07	5.67	0.07	6.22	0.15
56	5.05	0.03	5.22	0.05	5.47	0.07	5.83	0.14
57	3.27	0.03	3.48	0.04	3.62	0.04	3.82	0.10
58	0.67	0.04	0.77	0.05	0.94	0.04	1.23	0.06
59	0.73	0.10	0.91	0.06	1.19	0.06	1.66	0.09
60	7.13	0.13	7.29	0.08	7.51	0.13	7.98	0.16
61	1.33	0.07	1.66	0.11	1.94	0.13	2.32	0.06
62	6.65	0.05	6.70	0.07	6.84	0.10	7.15	0.15
63	0.97	0.05	1.31	0.05	2.10	0.08	3.02	0.17
64	1.84	0.07	2.56	0.08	3.85	0.07	4.84	0.10
65	2.09	0.59	2.85	0.50	4.56	0.31	5.62	0.34
66	2.19	0.47	3.07	0.52	4.68	0.27	5.81	0.26
67	1.13	0.19	1.34	0.21	1.67	0.19	2.28	0.07
68	1.40	0.11	1.99	0.19	3.24	0.08	4.19	0.06
69	1.87	0.39	2.63	0.48	4.22	0.33	5.55	0.32
70	1.09	0.03	1.61	0.04	2.41	0.04	2.64	0.07
71	1.57	0.73	2.39	0.71	3.25	0.60	3.86	0.81
72	5.51	0.14	6.81	0.11	8.42	0.27	8.53	0.37
73	8.21	0.23	10.36	0.22	12.37	0.18	13.18	0.38
74	1.01	0.11	1.49	0.12	2.21	0.11	2.48	0.13
75	3.72	0.46	4.17	0.48	4.68	0.60	4.82	0.70
76	5.58	0.05	6.71	0.04	7.77	0.09	8.31	0.17
77	1.77	0.11	2.12	0.08	2.53	0.13	2.86	0.11
78	4.32	0.16	4.95	0.20	5.22	0.26	5.52	0.08
79	1.81	0.63	2.19	0.59	2.23	0.47	2.48	0.56
80	1.74	0.08	2.41	0.20	4.29	0.14	5.67	0.20
81	1.76	0.04	2.18	0.06	3.60	0.11	4.57	0.12
82	1.94	0.13	2.53	0.18	4.03	0.19	5.10	0.32
83	1.11	0.06	2.13	0.08	3.75	0.09	4.67	0.11
84	1.02	0.05	1.94	0.07	3.31	0.12	4.29	0.09
85	0.88	0.06	1.65	0.10	2.85	0.14	3.65	0.12

D uptake – MtATP-PRT + L-histidine at pH 9

Average relative D uptake at 1 minute, 10 minutes, 30 minutes and 120 minutes of exposure along with standard deviation values (SD).

pH 9	**D UPTAKE / Da**							
peptide #	**1 min**	**SD**	**10 min**	**SD**	**30 min**	**SD**	**120 min**	**SD**
1	4.09	0.03	4.26	0.04	4.71	0.05	5.42	0.28
2	4.23	0.02	4.33	0.06	4.82	0.18	5.57	0.05
3	4.33	0.04	4.50	0.06	4.98	0.07	5.87	0.07
4	4.00	0.13	4.18	0.08	4.60	0.20	5.28	0.20
5	4.75	2.40	4.75	1.90	5.00	0.75	5.95	1.58
6	0.80	0.06	0.80	0.14	1.13	0.05	1.36	0.07
7	2.23	0.14	2.49	0.16	2.64	0.14	3.06	0.09
8	2.33	0.05	2.58	0.13	3.20	0.16	3.39	0.09
9	3.67	0.24	3.98	0.25	4.24	0.24	4.45	0.18
10	2.45	1.11	2.48	0.84	2.78	1.32	2.96	1.06
11	1.55	0.04	1.85	0.04	1.99	0.06	2.25	0.05
12	1.41	0.06	1.67	0.07	1.82	0.07	2.05	0.07
13	1.04	0.01	1.22	0.02	1.37	0.02	1.54	0.02
14	1.46	0.02	1.89	0.04	2.12	0.02	2.37	0.02
15	1.47	0.04	1.91	0.11	2.18	0.07	2.50	0.04
16	1.49	0.23	1.85	0.10	2.23	0.18	2.57	0.13
17	0.90	0.10	1.24	0.13	1.62	0.14	2.14	0.24
18	0.90	0.08	1.24	0.07	1.60	0.07	2.37	0.23
19	1.09	0.02	1.45	0.03	1.90	0.03	2.35	0.02
20	0.85	0.02	1.22	0.03	1.58	0.03	1.95	0.02
21	1.17	0.03	1.61	0.02	2.08	0.03	2.54	0.02
22	2.08	0.24	2.80	0.12	3.50	0.16	4.04	0.12
23	1.75	0.27	2.42	0.24	3.03	0.26	3.50	0.18
24	1.29	0.07	1.55	0.09	1.62	0.15	1.85	0.13
25	0.94	0.03	1.13	0.04	1.23	0.07	1.31	0.05
26	0.94	0.06	1.12	0.05	1.23	0.08	1.41	0.10
27	2.17	0.02	2.09	0.02	2.15	0.03	2.31	0.06
28	3.70	0.11	3.82	0.13	3.93	0.15	4.02	0.27
29	3.01	0.27	3.09	0.29	3.27	0.23	3.55	0.14
30	2.73	0.10	2.96	0.16	3.28	0.11	4.12	0.10
31	2.38	0.60	2.46	0.04	2.77	0.04	3.41	0.53
32	2.34	0.15	2.31	0.10	2.38	0.02	2.72	0.05
33	1.49	0.03	1.70	0.03	1.96	0.04	2.42	0.06
34	1.60	0.02	1.66	0.02	1.73	0.03	1.86	0.01
35	2.76	0.11	2.84	0.06	2.93	0.11	3.47	0.10
36	2.74	0.05	2.83	0.08	2.90	0.09	3.18	0.08
37	4.86	1.31	4.55	0.12	5.30	1.86	5.85	0.79
38	1.57	0.51	1.79	0.68	2.15	0.65	2.46	0.69
39	1.81	0.24	2.14	0.27	2.62	0.21	4.08	0.16
40	1.42	0.25	1.65	0.25	2.12	0.24	3.48	0.28
41	1.11	0.53	1.33	0.58	1.76	0.68	2.72	0.12

peptide #	1 min	SD	10 min	SD	30 min	SD	120 min	SD
42	2.14	0.04	2.63	0.13	2.77	0.03	3.31	0.04
43	2.75	0.04	3.15	0.02	3.35	0.04	3.86	0.07
44	3.17	0.13	3.70	0.13	3.99	0.12	4.79	0.14
45	2.69	0.10	3.17	0.07	3.71	0.08	4.41	0.10
46	1.58	0.09	1.67	0.07	1.87	0.09	2.15	0.05
47	2.43	0.01	2.83	0.02	3.29	0.06	3.70	0.02
48	1.88	0.12	2.19	0.13	2.43	0.15	3.39	0.11
49	1.96	0.68	2.29	0.67	2.80	0.71	3.46	0.63
50	2.34	0.19	2.62	0.18	2.99	0.22	3.94	0.19
51	1.09	0.06	1.33	0.03	1.58	0.10	2.23	0.15
52	0.71	0.04	0.76	0.04	0.97	0.09	1.65	0.05
53	0.96	0.10	1.12	0.05	1.26	0.08	2.00	0.14
54	6.77	0.05	6.99	0.07	7.46	0.07	8.58	0.17
55	4.83	0.10	5.22	0.06	5.57	0.06	6.16	0.07
56	5.03	0.02	5.22	0.04	5.45	0.04	5.82	0.07
57	3.23	0.05	3.46	0.03	3.56	0.05	3.76	0.04
58	0.71	0.03	0.81	0.11	0.88	0.19	1.28	0.09
59	0.69	0.08	0.79	0.06	1.03	0.08	1.62	0.08
60	7.20	0.15	7.35	0.08	7.52	0.11	7.97	0.14
61	1.40	0.05	1.72	0.12	1.91	0.11	2.44	0.04
62	6.65	0.03	6.75	0.05	6.93	0.04	7.15	0.03
63	0.90	0.06	1.12	0.06	1.70	0.06	2.90	0.08
64	1.69	0.17	2.20	0.04	3.30	0.07	4.80	0.05
65	1.85	0.65	2.43	0.53	3.79	0.57	5.42	0.35
66	2.04	0.51	2.64	0.55	4.15	0.34	5.75	0.17
67	1.16	0.26	1.24	0.24	1.53	0.20	2.28	0.11
68	1.28	0.06	1.70	0.08	2.77	0.04	4.15	0.08
69	1.75	0.37	2.41	0.42	3.66	0.41	5.26	0.14
70	1.03	0.04	1.46	0.08	2.19	0.02	2.66	0.06
71	1.51	0.68	2.06	0.81	2.85	0.71	3.61	0.67
72	5.13	0.09	6.48	0.18	7.99	0.19	8.79	0.31
73	7.38	0.22	9.82	0.23	11.84	0.21	13.24	0.16
74	0.98	0.12	1.42	0.12	2.07	0.13	2.50	0.12
75	3.59	0.47	3.97	0.49	4.58	0.49	4.60	0.56
76	5.00	0.09	6.42	0.04	7.40	0.03	8.29	0.05
77	1.73	0.08	2.13	0.06	2.52	0.10	2.91	0.09
78	3.86	0.07	4.73	0.09	5.07	0.19	5.40	0.26
79	1.56	0.70	2.03	0.64	2.08	0.65	2.46	0.75
80	1.64	0.17	2.06	0.18	3.39	0.17	5.56	0.23
81	1.71	0.03	2.03	0.02	2.97	0.08	4.53	0.08
82	1.80	0.18	2.25	0.14	3.37	0.16	5.10	0.31
83	1.05	0.03	1.95	0.03	3.14	0.02	4.78	0.03
84	0.98	0.03	1.78	0.01	2.82	0.02	4.32	0.05
85	0.83	0.06	1.47	0.11	2.36	0.10	3.66	0.15

Appendix 8: Metric System Unit Prefixes

Prefix	**Symbol**	**Factor 10^n**
tera	T	10^{12}
giga	G	10^{9}
mega	M	10^{6}
kilo	k	10^{3}
hector	h	10^{2}
deca	da	10^{1}
deci	d	10^{-1}
centi	c	10^{-2}
milli	m	10^{-3}
micro	µ	10^{-6}
nano	n	10^{-9}
pico	p	10^{-12}
femto	f	10^{-15}
atto	a	10^{-18}

Appendix 9: Journal Publications and Work Presented at Conferences and Meetings

Journal publications

The application of ion mobility mass spectrometry and hydrogen deuterium exchange mass spectrometry for probing mechanisms of allosteric inhibition of enzymes. Pacholarz, K.J., Jowitt, T., Burnley, R.J., Ordsmith, V., Porrini, M., Larroy-Maumus, G., Pisco, J.P., Garlish, R.A., Taylor, R.J., de Carvalho, L.P., Barran, P.E.. *Manuscript in preparation*

Insights into disorder–order transitions using variable temperature ion mobility mass spectrometry. Dickinson, E.R., Jurneczko, E., Pacholarz, K.J., Reeves, M., Clarke, D.J., Ball, K., Hupp, T., Nikolova, P.V., Campopiano, D., Barran, P.E.. *Manuscript submitted*

Distinguishing loss of structure from subunit dissociation for protein complexes: a gas-phase route for microcalorimetry. Pacholarz, K.J., Barran. P.E. *Manuscript submitted*

A mass spectrometry based framework to define structural order in proteins. Beveridge, R., Covill, S., Pacholarz, K.J., Kalapothakis, J., McPhee, C., Barran, P.E. *Anal. Chem.,* 2014, **86**, 10979-10991.

Dynamics of intact immunoglobulin G explored by drift-tube ion-mobility mass spectrometry and molecular modeling. Pacholarz, K.J., Porrini, M., Garlish, R.A., Burnley, R.J., Taylor, R.J., Henry, A.J., Barran, P.E. *Angew. Chem.,* 2014*,* **53***,* 7765-7769.

Mass spectrometry based tools to investigate protein-ligand interactions for drug discovery. Pacholarz, K.J., Garlish, R.A., Taylor, R.J., Barran, P.E. *Chem. Soc. Rev.*, 2012, **41**, 4335-4355.

Work presented at conferences and meetings

62nd Conference of American Society of Mass Spectrometry, (15-19/06/2014) Baltomore, USA
"Probing protein stability, unfolding and dissociation with variable temperature mass spectrometry and variable temperature ion mobility mass spectrometry" (**Talk**)

Native Mass Spectrometry and Ion Mobility Workshop (8-9/04/2014) Strasbourg, France
"The application of native MS, IM-MS and HDX-MS to study mechanisms of allosteric inhibition of enzymes: The ATP-Phosporibosyltransferase case" (**Talk**)

UCB PhD Student Science Day (03/10/2013) Oxford, UK
"Signature dynamic of the intact immunoglobulin G isotype revealed by drift-tube ion-mobility mass spectrometry and molecular dynamics" (**Talk**)

Ion Mobility Mass Spectrometry Special Interest Group Inagural Meeting (16/04/2013) Slough, UK
"Variable temperature ion mobility mass spectrometry: the effect of temperature on the gas-phase protein complex structure" (**Talk**)

10th International Congress of Young Chemists - YoungChem (10-14/10/2012) Gdansk, Poland
"Mass Spectrometry for Drug Discovery: Conformation, inhibition and stability studies of the N-terminal domain of MDM2 protein by ion mobility mass spectrometry." (**Talk**)

19th International Mass Spectrometry Conference (15-19/09/2012) Kyoto, Japan
"Variable Temperature Ion Mobility Mass Spectrometry of Large Protein Complexes" (**Poster**)

Scottish Universities Life Science Alliance (SULSA) symposium (11/06/2012), Edinburgh, UK
"Variable Temperature Ion Mobility Mass Spectrometry of Intrinsically Disordered Proteins – New Insights and New Controversies." (**Poster**)

32nd British Mass Spectrometry Society Conference (11-14/09/2011), Cardiff, UK
"Conformation and inhibition studies of the N-terminal domain of MDM2 protein by ion mobility mass spectrometry." (**Poster**)